UNIVERSITY OF CALIFORNIA SAN DIEGO

Seismic Response of Large Embedded Structures and Soil-Structure Interaction

A dissertation submitted in partial satisfaction of the
requirements for the degree of Doctor of Philosophy

in

Structural Engineering

by

John Li

Committee in charge:

Professor Ahmed Elgamal, Chair
Professor Philip E. Gill
Professor Gilberto Mosqueda
Professor P. Benson Shing
Professor Chia-Ming Uang

2019

The Dissertation of John Li is approved, and it is acceptable in quality and form for publication on microfilm and electronically:

Chair

University of California San Diego

2019

Dedication

To my family members

Epigraph

Imagination is more important than knowledge. Knowledge is limited. Imagination encircles the world.

- Albert Einstein

Table of Contents

List of Figures

List of Tables

Acknowledgments

I would like to thank Professor Ahmed Elgamal for his support, guidance and encouragement throughout the PhD program. His persistence and encouragement have challenged me to grow beyond what I thought possible. For his support I express my most sincere gratitude and deepest appreciation.

In addition, my gratitude to my friends in the research group for their support and advice: Ahmed Ebeido, Muhammed Zayed, Kyungtae Kim, Athul Prabhakaran, Abdullah Almutairi, Zhijian Qiu, and Lan Luo. I will always be grateful for your friendship.

The thesis is primarily comprised of material from published work or work in progress that may be published in the future. Chapter 2, 3, and 4 contain slightly modified sections from the report by Li and coauthors: Earth Pressures on Deep Foundation Walls During Seismic Events (NRC Contract No.: NRC-HQ-12-C-04-0066) which details and lays out the current methodology in accessing soil structure interaction.

Chapter 5 has been accepted for publication by Journal of Geotechnical and Geoenvironmental Engineering ASCE and titled as “Three-dimensional Seismic Response of a Large Embedded Structure and Induced Earth Pressure”. The dissertation/thesis author was the primary investigator and author of this paper. Professor Elgamal and Dr. Kim cooperated as co-authors to this journal paper.

Chapter 7 has been submitted for publication to Soil Dynamics and Earthquake Engineering and titled as “Recorded Seismic Response at the Fukushima Daiichi Nuclear Power Plant and Adjacent Downhole Array”. The dissertation/thesis author was the primary investigator and author of this paper. Professor Elgamal and Professor Bewley cooperated as co-authors to this journal paper.

Finally, I would like to express my sincere appreciation to my family with an excellent foundation of support, encouragement, and endless love which has allowed me to successfully pursue my goals.

Vita

06/2013	Bachelor of Science in Structural Engineering University of California San Diego, La Jolla, USA.
12/2015	Master of Science in Structural Engineering University of California San Diego, La Jolla, USA.
12/2019	Doctor of Philosophy in Structural Engineering University of California San Diego, La Jolla, USA.

Publications

1. Li, J., Kyungtae, K. & Elgamal, A. Three-dimensional Seismic Response of a Large Embedded Structure and Induced Earth Pressure. *Journal of Geotechnical and Geoenvironmental Engineering ASCE,* accepted

2. Li, J., & Elgamal, A. Recorded Seismic Response at the Fukushima Daiichi Nuclear Power Plant and Adjacent Downhole Array. *Journal paper,* in preparation

3. Li, J., & Elgamal, A. Recorded Seismic Response of an Advanced Boiling Water Reactor Model and Adjacent Downhole Arrays. *Journal paper,* in preparation

4. Li, J., Lu, J., Kim, K., Elgamal, A. W., Park, E. H., Musgrove, M., Hashash, Y., Wagner, N., Sitar, N., Xu, B., & Rathje, E. *Earth Pressures on Deep Foundation Walls During Seismic Events*. Technical Report, U.S. Nuclear Regulatory Commission, 2016.

5. Li, J (2019). Seismic Response of Large Embedded Structure. PhD Thesis, Dept. of Structural Engineering, University of California San Diego, La Jolla, CA (in preparation)

6. Khosravifar, A., Elgamal, A., Lu, J., & Li, J. (2018). A 3D model for earthquake-induced liquefaction triggering and post-liquefaction response. *Soil Dynamics and Earthquake Engineering*, *110*, 43-52.

ABSTRACT OF THE DISSERTATION

Seismic Response of Large Embedded Structures and Soil-Structure Interaction

by

John Li

Doctor of Philosophy in Structural Engineering

University of California San Diego, 2019

Professor Ahmed Elgamal, Chair

For large relatively stiff structures, soil structure interaction (SSI) plays a major role in dictating the overall seismic response. In light of recent strong seismic excitation affecting such structures, three-dimensional response as well as nonlinear soil behavior are among the areas of increased interest. As such, a series of numerical studies are conducted to shed more light on the involved SSI mechanisms. Amongst those studies is a comparison of the equivalent linear and nonlinear soil formulations in evaluating the seismic response of large embedded structures. Depending on the level of attained nonlinear response, influence of the following modeling considerations is discussed: i) employing the nonlinear versus linear soil formulation, ii) initial own-weight lateral earth pressure stress-state, and iii) the soil-structure interface characteristics. Both formulations generally resulted in remarkably close estimates of structural response.

An opportunity to investigate the SSI mechanisms of large embedded structures due to low amplitude shaking was permitted by the availability of seismic data from an instrumented test site at Higashi-dori, Japan. The compiled data set includes the recorded accelerations for two downhole arrays, and the response of a $1/10^{th}$ scale twin reactor. The extracted site properties are shown to provide a reasonable match to the recorded data. Using these properties parametric computational studies are conducted to illustrate salient mechanisms associated with the seismic response of such large embedded structural systems.

Furthermore, an opportunity to investigate the seismic response of the Fukushima nuclear reactors due to strong shaking was facilitated by data recorded during the magnitude 9.1 Tōhoku earthquake. Linear and nonlinear response of the ground was evaluated using system identification techniques. During the strong shaking, a clear and significant reduction in stiffness was observed within the upper soil strata. Of special interest was the response of Unit 6, which was the most heavily instrumented of the reactors. Response at the base of Unit 6 was compared to that of the nearby downhole array. Amplification of motion along the height of Unit 6 was evaluated, exhibiting the primary role of rocking response.

Chapter 1

Introduction

For large relatively stiff structures, soil structure interaction (SSI) plays a major role in dictating the overall seismic response. In light of recent strong seismic excitation affecting such structures, three-dimensional response as well as nonlinear soil behavior are among the areas of increased interest. As such, a series of numerical studies are conducted to shed more light on the involved SSI mechanisms.

Data related to the seismic response of large embedded structures are an important source of knowledge concerning important facilities such as nuclear power plants (NPP). Generally, such data have not been readily available, but the nuclear industry has sought to generate related insights through alternatives such as large-scale experimentation. Over the last couple of decades, there have been a number of experiments seeking to investigate the seismic response of NPP with some of the most prominent including those at Lotung and Hualien (Luco and Wong 1990; Tang and Stepp 1990; de Barros and Luco 1995; Graves et al. 1996; Ganev et al. 1997; Luco and Francisco 2004) which sought to evaluate the adequacy of soil-structure interaction models and develop guidelines on their usage. More importantly, due to the more recent Tohoku earthquake a unique data set (TEPCO 2011a) has become available. The Tohoku earthquake exceeded the design levels

for a number of the nuclear reactors which eventually led to a station blackout and an eventual nuclear meltdown (FNAIIC 2012). Many of the reactors and nearby downhole arrays were instrumented with sensors which provided valuable insight into the response of large embedded structures and soils due to strong shaking (TEPCO 2011a).

1.1 Primary Contributions

1. Parametric study of large embedded structures and depending on the level of attained nonlinear response, influence of the following modeling considerations: i) employing the nonlinear versus linear soil formulation, ii) initial own-weight lateral earth pressure stress-state, and iii) the soil-structure interface characteristics.
2. Investigation of soil-structure interaction (SSI) mechanisms of large embedded structures due to low amplitude shaking as permitted by the availability of seismic data from an instrumented test site at Higashi-dori, Japan. The compiled data set includes the recorded accelerations, for two downhole arrays, and the response of a $1/10^{th}$ scale twin reactor which allowed for the use of system identification.
3. Examination of the seismic response of the Fukushima nuclear reactors due to the magnitude 9.1 Tōhoku earthquake. Linear and nonlinear response of the ground was evaluated using system identification techniques. During the period of strong shaking, a clear and significant reduction in the soil stiffness was observed within the upper strata. Of special interest was the response of Unit 6, which was the most heavily instrumented of the reactors.

1.2 Outline

This report has been divided into 8 chapters in the following manner:

The first chapter (this chapter) briefly presents the overall objectives and layout of this report.

Chapters 2 and 3 evaluate a number of papers that have provided insights relating to the impact of SSI, which include analytical methods, and field experiments. These papers serve as a benchmark to highlight some of the strengths and limitations of analytical and numerical methods in predicting the response of embedded structures. Experiments that were reviewed in these chapters include the Lotung and Hualien large-scale tests (Luco and Wong 1990; Tang and Stepp 1990; de Barros and Luco 1995; Graves et al. 1996; Ganev et al. 1997; Luco and Francisco 2004).

Chapter 4 presents comparisons between the results for a select number of currently available numerical codes, in order to document the differences and similarities in evaluating seismic site response. The main goal is to provide a convenient resource for checking the response of a user's computer modeling framework against these documented results. This section focuses primarily on the modeling of shear beams which is a fundamental step in evaluating the effects of SSI for more complicated problems.

Chapter 5 discusses an effort related to three-dimensional (3D) finite element simulation which examines the impact of soil-structure interaction for a fully embedded structure. Depending on soil stiffness, the following are explored: 1) change of acceleration response along the height of the embedded structure compared to the free-field, 2) lateral soil pressure profile along the height of the structure, and 3) vertical normal pressure developed along base of the structure. Following this, a preliminary illustrative effort is presented in which an idealized modeling configuration was defined with linear and nonlinear soil response prescribed and then compared. Within this framework, attention is paid to the soil pressure applied on the embedded structure.

Chapter 6 examines the SSI mechanisms of large embedded structures permitted by the availability of seismic data from an instrumented test site at Higashi-dori, Japan (Xu et al. 2003; Xu et al. 2008). The compiled data set includes recorded accelerations for two downhole arrays, and response of a $1/10^{th}$ scale twin reactor. A study is reported herein to examine this data set and develop a representative computational model. The employed system identification techniques are outlined. The extracted site properties are shown to provide a reasonable match to the recorded data. Using these properties, computational studies are conducted to illustrate salient mechanisms associated with the seismic response of such large embedded structural systems.

Chapter 7 discusses an opportunity to investigate seismic response and associated SSI mechanisms due to strong shaking as permitted by the availability of data from the Fukushima Nuclear Power Plant (TEPCO 2011a). The magnitude 9.1 Tōhoku earthquake was one of the most powerful recorded earthquakes to date and exceeded the design levels of the reactors. The provided data set included records at six boiling water reactors, and adjacent ground downhole arrays. The characteristics of seismic response at different depths within the ground can be inferred from the downhole records. Linear and nonlinear response of the ground was evaluated using system identification techniques. During strong shaking, a clear and significant reduction in stiffness was observed within the upper soil strata. Of special interest was the response of Unit 6, which was the most heavily instrumented of the reactors. Response at the base of Unit 6 was compared to that of the nearby downhole array. Amplification of motion along the height of Unit 6 was evaluated, exhibiting the primary role of rocking response. Overall, the reactor structure primarily behaved as a rigid body and the amplification at the top of the reactor was due to the measured rocking response.

Finally, an overall summary is presented in Chapter 8 in which the main conclusions are laid out.

Chapter 2

Literature Review: Analytical Methods

2.1 Introduction

A literature review of a number of notable papers examining analytical methods is presented in the following section. The selected analytical methods help provide valuable insight for assessment of earth pressures and highlights some of the shortcomings that need to be accounted for.

2.2 Analytical Methods

Wood (1973) developed an exact elastic solution for the earth pressure problem of a rigid wall on a rigid foundation. Building on this work, Veletsos et al. (1995) presented a rigorous elastic solution for the case of elastic walls on a rigid foundation. They explored the response of two walls retaining a viscoelastic solid and examined how the response compared against Wood's solution.

Furthermore, they highlighted a number of important parameters when examining earth pressure, which include the ratio of the distance between the rigid walls relative to the height (L/H), the rotational flexibility, and so forth. For the rigid wall case, they demonstrated that their

analytical solution was in good agreement with Wood's solution, as depicted in Figure 2.1. In this figure, a comparison is shown between the normalized predicted earth pressures for varying ratios of L/H, which was demonstrated to be an important factor. When the ratio L/H is small, the pressure transmitted to the wall is primarily by horizontal extension, while in the case where L/H is large, the pressure is transmitted with horizontal shearing action. Additionally, it was concluded that the damping capacity is directly proportional to L/H.

Veletsos et al. (1995) solution demonstrated that pressures exerted on the wall decrease rapidly as the flexibility of the wall increases. When the wall is more flexible, the horizontal extensional stiffness will decrease which consequently reduces the earth pressure exerted on the structure. This same effect was noted by Mononobe and Matsuo (1932) based on the pioneering experimental work that led to the formulation of the so called Mononobe-Okabe analysis method.

Following the work by Veletsos et al. (1995), Psarropoulos et al. (2005) presented a series of general finite element (FE) solutions and compare them against limit equilibrium methods derived using the Mononobe-Okabe solution (M-O) and the linear elasticity solution of Veletsos and Younan (1997). The M-O based methods are an extension of Coulomb's limit-equilibrium analysis while the elasticity solution of Veletsos and Younan (1997) is able to account for wall rotation and flexibility. Veletsos and Younan (1997) demonstrated that by allowing the wall to deform and rotate, the earth pressures will rapidly converge to the M-O solution.

Psarropoulos et al. (2005) demonstrated that the results from the numerical model compared well with the analytical solution by Veletsos and Younan (1997) (Figure 2.2). The main difference between the numerical and analytical results was the base shear and moment. The discrepancy between the results were attributed to the treatment of the tensile stress, which was believed to be unrealistic and thus ignored. These tensile stresses were a result of the assumption

that the soil was completely bonded to the wall, which was shown to be a significant problem for highly flexible walls. When the wall was treated as rigid in both the analytical solution and the numerical model, it was found that the base shear and moment were in close agreement. Furthermore, after having shown that the numerical model matches the results from the analytical solution, the authors explored more complex problems that were difficult to incorporate into analytical solutions. The complexities that were addressed included the variation in soil stiffness with depth and the nonlinearity in both the soil and soil-structure interface. From the numerical simulations, Psarropoulos et al. (2005) demonstrated that when the soil was represented as multiple layers, the earth pressures were slightly reduced when compared to the single layer case. This would suggest that soil heterogeneity and stratification can be potentially beneficial by reducing dynamic earth pressures.

Mylonakis et al. (2007) proposed another approach to evaluate earth pressure which they argued is both more accurate and safer than M-O method. Two different groups of analytical solutions were identified, which included the kinematic and stress solutions. M-O solution falls under the kinematic type, which was argued to be inherently unsafe, because these types of solutions tend to overestimate the active earth pressure and underestimate the passive earth pressure. Stress solutions on the other hand, overestimates the active earth pressure and underestimates the passive earth pressures. Furthermore, additional shortcomings of the M-O method include the difficulty in implementing the solution, the accuracy of the solution in predicting passive earth pressures on rough walls, the assumptions made in the distribution of the tractions on the wall and the necessity to determine how the soil will fail.

Mylonakis et al. (2007) sought to create a method that fell under the umbrella of stress solutions to remedy the previously mentioned shortcomings. The proposed method was compared

against numerical solutions and it was demonstrated that the error in the active earth pressure was within 10% when considering extreme cases such as high friction angles and worse for the passive earth pressure in a range where M-O does not converge. Based on this purely theoretical comparison Mylonakis et al. (2007) claimed that the proposed method was "safer", i.e. more conservative, as depicted in Figure 2.3. It should be noted however, that the proposed method was only shown to be in reasonable agreement with to numerical results, and no comparison with experimental or case history data was attempted. As is discussed later, more recent studies demonstrated that the Mylonakis et al. (2007) solution is actually far too conservative for strong earthquakes (> 0.5 g), and that M-O is a reasonable upper limit for seismic earth pressure for typical applications (see e.g. Sitar et al. 2012).

Ostadan (2005) pointed out that M-O method was not suitable for predicting earth pressures for embedded structures, and instead presents a simple alternative to analyzing earth pressures. As mentioned previously, the M-O method was developed for soil retaining walls. Thus, the assumptions made in the M-O method are not strictly applicable to embedded structures. Instead Ostadan proposed a simple method that took into account the rigidity of the walls due to the floors, wave propagation, frequency content of the design motion, and the properties of the soil. It should be noted that the proposed method does not account for inertial effects of the building and only considers the kinematic interactions. Furthermore, the method assumes the structure to be either on a rigid rock or stiff soil, so effects from rocking are not accounted for. Essential in the development of this method was SASSI2000, which was used for parametric analyses.

From the SASSI2000 simulations, Ostadan (2005) concluded that the pressures on the side walls are highly dependent on the natural frequency of the soil. When the soil resonates with the input motion the expected earth pressures are significantly higher than normal. This observation

suggests that it is necessary to account for the frequency content of the design motion. To incorporate the dependence on the frequency, an acceleration response spectrum should be used to obtain the expected peak acceleration based on the natural frequency of the soil. Subsequently, the peak acceleration can then be used to compute the seismically induced lateral pressure distribution. Despite the simplicity of the method it was in good agreement with finite element solutions for many different soil properties, earthquake motions and wall heights. In general, the pressures predicted by M-O are lower than those predicted using Ostadan's approach. However, it should be noted that Ostadan's method assumes the walls to be rigid and the soil to be linearly elastic, which as demonstrated by Veletsos et al. (1995) will result in large earth pressure and can be overconservative.

2.3 Acknowledgements

This chapter contains slightly modified sections from the report by Li and coauthors: Earth Pressures on Deep Foundation Walls During Seismic Events (NRC Contract No.: NRC-HQ-12-C-04-0066). The dissertation/thesis author was the primary investigator and author of this chapter. Many people took part in the preparation of this report which include Jinchi Lu, Kyungtae Kim, Professor Ahmed Elgamal, Eun Hyun Park, Michael Musgrove, Professor Youssef Hashash, Nathaniel Wagner, Professor Nicholas Sitar, Boqin Xu, and Professor Ellen Rathje.

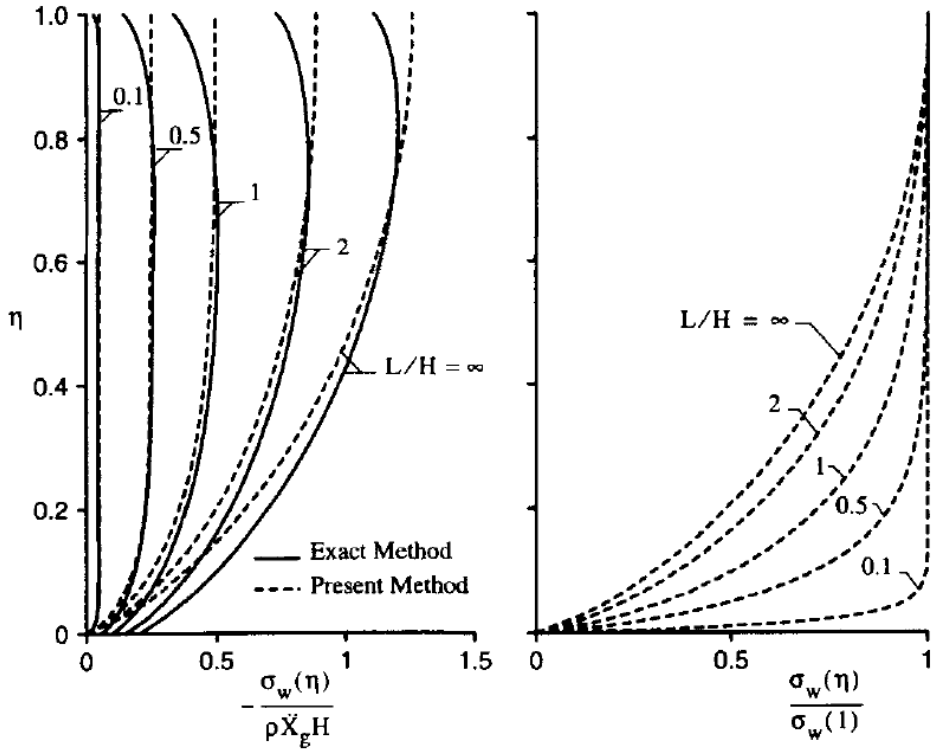

Figure 2.1 Distributions of static wall pressures for systems with fixed-based walls; $m_w = 0, \nu = 0.3$ (Veletsos et al. 1995) (where m_w is the total mass of the wall, ν is the Poisson's ratio of the retained material, η the normalized height, σ_w the pressure on the wall, ρ is the density of the retained material, and $\ddot{X}_g$ is the peak acceleration at the base)

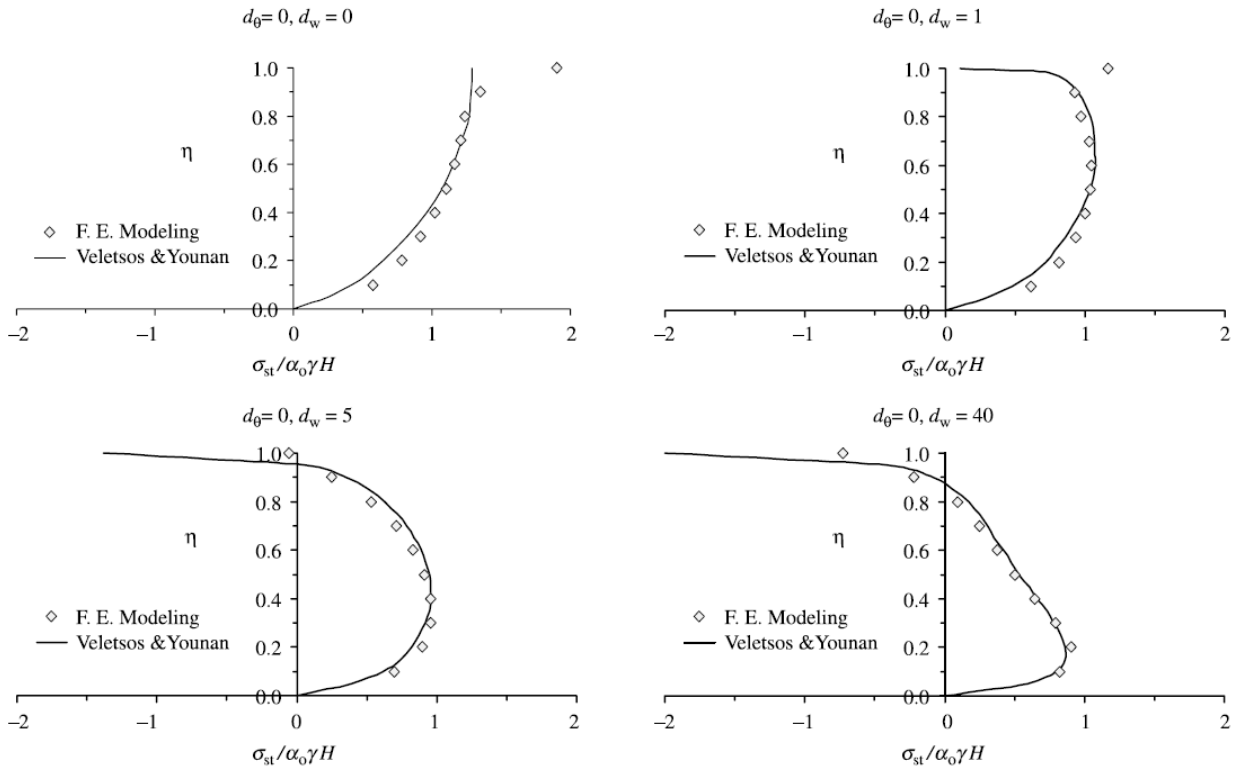

Figure 2.2 Comparison of numerical and analytical distribution of the earth pressures (Psarropoulos et al. 2005) (d_θ is the relative flexibility of the rotational base and the retained wall, and d_w is the relative flexibility of the wall and retained soil, η the normalized height, σ_{st} is the static earth pressure, a_0 is the maximum acceleration at the base in g, γ is the unit weight of the retained soil and H is the height of the wall)

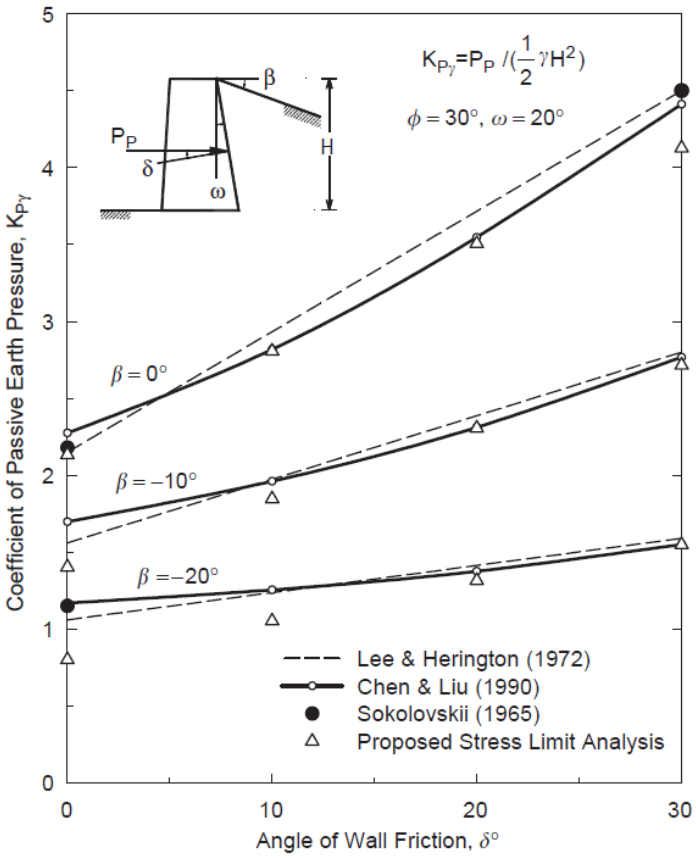

Figure 2.3 Comparison of results for passive earth pressures predicted by different methods (Mylonakis et al. 2007).

Chapter 3

Literature Review: Field Experiments

3.1 Introduction

This section of the literature survey focuses on three field experiments which included Lotung (Tang and Stepp 1990), Hualien (Graves et al. 1996; Ganev et al. 1997; Graves 2004) and Aomori Prefecture (Xu et al. 2003; Xu et al. 2008). These experiments sought to evaluate the adequacy of soil-structure interaction (SSI) models at predicting the response of scaled models of nuclear containment structure. Based on the results from these experiments, it was concluded that current numerical methods were successful at simulating the response reasonably well.

3.2 Lotung

In the 1980's, an experiment was initiated to assess the validity of SSI models and develop guidelines on their usage. Typically, these SSI models would aim to be conservative to account for the difficulties in accurately representing the soil and how it interacts with the structure. A multitude of models were considered, ranging from more complex models that utilized finite elements and substructure impedances, to more simplistic ones such as soil-spring representations.

To gauge the accuracy of these numerical models, a 1/4 and 1/12 scale model of a nuclear containment facility was considered. To ensure the results were realistic, great care was taken in developing the specifications for the model which included the type of material for the prototype and the ability to develop similar levels of stress as the full scaled version. The 1/4 scale model (Figure 3.1) was believed to be the minimum size that could satisfy the criteria that were set. Due to the reduced size of the model, it was concluded that the test site should have soft soils to assure that there would be significant SSI. Consequently, Lotung was selected as the ideal location for this project, due to its high seismic activity, and fairly uniform soil layers.

After the scaled model was constructed, extensive site investigation, and laboratory testing were conducted to provide a total of 13 independent research teams information to submit blind predictions to two low-level forced vibration tests (FVT). As a result of the weak excitation, the response was expected to remain fairly linear and was used to access the properties of the soil. The first of the FVT was performed prior to the addition of the backfill, and only comprised of the scaled model and base mat. The second FVT was initiated following the addition of the backfill. In general, it was found that the comparison between the results obtained from the numerical and experimental models were reasonable, with the maximum deviation being around 20%. A typical comparison of the numerical and experimental results is shown in Figure 3.2. Model B was the original model made prior to the blind predictions, while Model C was an updated model made after comparing the predictions. It was concluded that the numerical and experimental data matched well, with the exception of the steam generator and piping. It was eventually identified that the discrepancy was a result of the boundary conditions that were used for the steam generator. The steam generator was originally believed to be fixed but proved to be far more flexible than

originally assumed. When the boundary conditions were revised, the simulated response for the steam generator improved substantially, as illustrated in Figure 3.3.

Following the FVT, the research group moved on to predicting the response due to seismic loading. In general, it was concluded that the SSI models came reasonably close and tended to be on the conservative side. Figure 3.4 shows some representative comparisons of the spectral acceleration at the top of the scaled model. The differences between the recorded and numerical response were largely attributed to two factors, which were the uncertainties in characterizing the soil and limitations in the SSI models and assumptions made in developing the model. For this experiment, Tang and Stepp identified four uncertainties that contributed to the differences. It was concluded that more information was needed concerning the boundaries of the soil layers, properties of the backfill material, water saturation of the soil and modulus reduction curve. Despite the extensive efforts invested into geotechnical investigations, these uncertainties still remained. In general, it was found that more sophisticated models were more adept at modeling the SSI, while simpler ones tended to be overly conservative. The complex models were able to account for more complex phenomenon such as wave scattering, soil layering and embedment effects, which when accounted for in simpler models, improved their predictive capabilities.

3.3 Hualien

As a result of the soft soils at Lotung, Graves et al. (1996) concluded that the findings were limited to understanding phenomenon such as foundation torsional response. To address these concerns, a 1/4 scale model was to be constructed in stiff soils. It was determined that Hualien was a suitable region with high seismic activity.

For this project, the soil properties were obtained via borings, large penetration tests, and so on. The soil properties from this tests were used to develop a unified soil model that was

provided to every research team. Upon further geotechnical investigations, some of the soil properties were revised and a modified ground model was suggested. It was found that the shear wave velocity of the backfill near the base of the structure was too high and consequently was updated in the modified ground model. Unlike the Lotung experiment, only two analysis methods were considered, which were the flexible volume substructuring approach (SASSI) and the continuum formulation method (CFM).

Similar to the experiments in Lotung, FVT were used to access the dynamic properties of the soil and was completed in two stages. The first stage was completed without the backfill, while the second stage was conducted after the addition of the backfill. From the FVT, it was observed that certain sections of the soil were anisotropic. Fourteen independent groups were provided with the two soil models and were asked to provide blind predictions for the FVT tests. In general, the predictions overestimated the natural frequencies. It was concluded that in the range of small strains, SASSI produced very good results using the modified ground model, while the unified soil model was better for the CFM approach.

As previously mentioned, the shear wave velocity of the backfill in the unified ground model was too high which indicated that the CFM tended to underestimate the stiffness of the soil. The assumptions made by the CFM approach was equivalent to assuming plane strain along the vertical axis. As a result, the shear resistance from rocking was neglected, which would decrease the overall stiffness. Additionally, when performing dynamic analysis for larger earthquakes the weakening soil support needed to be accounted for. Three factors were identified as sources for the degradation which included the nonlinearity of the soil, loss of contact between the soil and structure and the build-up of pore water pressure. It was concluded that there was no indication of pore water pressure build up and that the soil was weakened as a result of the soil nonlinearity. To

account for the weaken soil, the stiffness and damping of the soil were varied parametrically until a good match was obtained (Figure 3.5). The shear strain vs. modulus reduction and shear strain vs. damping were constructed empirically and compared against the Ramberg-Osgood model. From the comparison, it was concluded that the match was inadequate (Figure 3.6). This inadequacy was attributed to local nonlinear effects which was challenging to model and demonstrated that the non-linear elastic theory was unable to adequately capture the soil behavior for this case. In general, it was found that the predicted responses matched reasonably well with the recorded. It was concluded that current models were sufficient in predicting the response, though great care needs to be taken in properly modeling the boundary conditions of the soil layer and soil properties, especially the backfill material.

3.4 Aomori Prefecture

This following section presents a literature review of two documents (Xu et al. 2003; Xu et al. 2008) which summarized the findings from an experiment that was initiated in 1994 by the Nuclear Power Engineering Corporation (NUPEC) but was later succeeded by Japan Nuclear Energy Safety Organization (JNES). The primary focus of the experiment was to investigate the effects of dynamic cross interaction (DCI) effect as well as seismic earth pressures on deeply embedded and/or buried (DEB) nuclear power plant structures. Aomori, Japan was selected as a suitable location for this project which recorded earthquakes for a span of 8 years (1994-2002). The overall plan and schedule of this test can be found in Figure 3.7

Numerical simulations have been primarily developed for lightly embedded structures such as Light Water Reactors (LWRs) and have not been modeled for DEB structures. In this experiment, the structures were embedded 5 meters (~50% of their total height) into the ground. The SSI methods were evaluated in terms of their ability to predict the in-structure response spectra

(ISRS) and seismic induced soil pressures. Additionally, this study sought to gauge the significance of the DCI effect and verify if current numerical methods were adequate.

3.4.1 Experiment Set-Up

In commercial nuclear power plants, structures such as reactors and turbines were commonly constructed adjacent to other structures. The experiment in Aomori (Xu et al. 2003; Xu et al. 2008) examined three configurations (Figure 3.8) which included a single reactor building (Location A), twin reactor (Location B), and a reactor-turbine configuration (Location D). The structures were $1/10^{th}$ scaled models constructed using reinforced concrete. The reactor building was 8m by 8m in plan and 10.5m high, while the turbine building was 6.4m by 10m in plan and 6.75m high. In addition to examining three different layouts, the experiment also took into consideration using excavated and embedded foundations. The excavated variation placed the model 5m below ground level, with open spaces surrounding the structure (Figure 3.9). The embedded model used the same setup as the excavated, but the open space was filled with backfill soil (Figure 3.10). Pre-installed seismometers collected data on real earthquake ground motions which were used to assess the capabilities of analytical tools.

Downhole seismometers were also installed at two free-field locations which were referred to as Old Free-Field Point and New Free-Field Point (Figure 3.8). The free-field analysis addressed issues of wave propagation as well as identified in-situ soil properties (both low strain profile and strain dependent modulus degradation). The soil at Aomori primarily consisted of weathered-pyroclastic and pyroclastic rocks overlain by 5-8 meters of overburden comprised of weathered sandstones and diluvial loams. The water table was located between 7-10 meters below the ground surface.

3.4.2 Modeling Techniques

Field data was collected from numerous earthquake ground motions over the span of 8 years. The recorded data was compared to the results from SASSI and LS-DYNA (version 960), to evaluate how well these computer codes were able to predict the dynamic structural response, such as ISRS at basemat and roof and seismic earth pressures. Furthermore, these numerical codes were used to evaluate if current SSI methods were sufficient in accounting for DCI.

3.4.2.1 SASSI

As mentioned SASSI was one of two programs used to assess the adequacy of numerical methods. It should be noted that SASSI evaluates the problem in the frequency domain, while LS-DYNA works in the time domain. Both excavated and embedded models were developed for this test. The embedded portion of the structure was modeled using finite elements (3-D bricks and shells), while the above ground section was represented using lumped masses and 3-D beam elements. The basemat was modeled using brick elements while the sidewalls and internals employed shell elements. The sidewalls were connected to the superstructure using rigid links to simulate the rigid diaphragm of the floor at grade level. Additionally, a thin weak soil layer was added under the basemat to account for excavation activities that weakened this layer. The finite element models that were developed in SASSI are illustrated in Figure 3.11 - Figure 3.15 The damping implemented into the SASSI model was frequency independent. The properties for the soil fill were assumed to be the same as the free field.

The subtraction method was implemented using SASSI2000. When using the sub-structuring approach, the SSI problem can be divided into several sub-problems which includes a) the site response problem (free field), b) the scattering problem, c) the impedance problem, and d)

the structural response problem. However, the scattering problem was not required since the embedment was not modeled. Additionally, the implemented subtraction method only needed to compute the impedance around the structure as opposed to every node which significantly reduced the run time that was necessary.

3.4.2.2 LS-DYNA

LS-DYNA was specialized for nonlinear problems and can account for material and geometric effects. A typical assumption made in the SASSI model was that there was perfect bonding between the structure and the surrounding soil. SASSI models the soil-structure interface with a closed form solution to address the wave propagations in the half-space. In LS-DYNA the half-space wave propagation problem was modeled using transmitting boundaries to ensure that the outgoing waves was not deflected. Lysmer's dampers were placed at the artificial boundary to reduce unwanted wave reflections. The stress field was given as a function of frequency dependent dampers and springs on the soil boundary. Rayleigh damping was applied to different material parts. Linear response was expected for this experiment due to the weak shaking, and therefore it was safe to assume the soil was bonded to the structure. The finite element mesh used in the LS-DYNA analysis can be found in Figure 3.16 and Figure 3.17.

3.4.3 Analysis of Results

3.4.3.1 Free-Field Analysis – DCI Experiment

Although a couple hundred earthquakes were recorded over the 8-year span, only a few of these exceeded 10 gal. The data set for these eight earthquake events were provided for analysis (Table 3.1). Earthquakes 34, 63, and 89 did not include data at the new free-field point.

3.4.3.1.1 Old Free-Field Point

Due to the alignment of the structures, only the north-south direction was analyzed in this study. Earthquakes 34 and 157 were selected for the free-field analysis. For these earthquakes, it was shown that the Arias intensity was increasing as you approached the ground surface which indicated an upward propagating motion (Figure 3.18 and Figure 3.19). The upward propagating motion was an indication that the motion may be compatible with a 1D site model (Figure 3.20 and Figure 3.21).

To determine the soil properties at the old free-field point, Earthquake 34 was analyzed using the smoothed Fourier ratios technique in combination with the modified Levenburg-Marquadt least square minimization algorithm. The Fourier ratio technique was integrated with the Computer Analysis for Rapid Evaluation of Structures (CARES) program and was used to predict the soil properties that were needed to match the Fourier ratio of the recorded motion at surface and rock. When the soil properties (determined using CARES) were applied to the numerical simulations, it was found that the Arias intensity and Fourier ratio from the numerical simulation were in close agreement with the recorded.

3.4.3.2 New Free Field Point

At the new free-field point, earthquakes 131, 139, and 157 were used to predict the soil properties. These earthquakes were selected for the same reason as the old free-field point, which was their compatibility with the 1D model. After further examination of the Arias Intensities (Figure 3.22 - Figure 3.24), it was determined that Earthquake 139 was the most suitable motion for predicting the low strain soil profile at the new free-field point. Earthquake 139 displayed a clearly defined resonance while the other motions did not. Similar to the old free-field point,

CARES was used to determine the soil properties. The predicted resonance was found to be slightly higher than the recorded. However, it was concluded that the data still fit well when comparing the free-field response spectra.

3.4.3.2.1 Soil Modulus Degradation

Three well publicized and documented test models (GEI 1983; Geomatrix 1991; EPRI 1993) were selected to determine the soil modulus degradation relationships. The comparison of the modulus and damping using these tests models are shown in Figure 3.25 and Figure 3.26. Convolution analysis was used to compute the free field response using the three modulus degradation models. In general, it was found that the responses for the GEI and EPRI 93 were similar to each other and the recorded responses for both the old free-field point and new free-field point (Figure 3.27 - Figure 3.31). On this basis it was concluded that GEI and EPRI were more suitable for this site than Geomatrix.

3.4.3.3 Scaled Models of Nuclear Power Plant Response Analysis – DCI Experiment

Three earthquakes (131, 139, and 157) were analyzed to investigate the impact of DCI on the excavated models. It was found that the presence of an adjacent structure tended to shift the peak frequency upward. Furthermore, when comparing the response spectra for the recorded results, it was shown that the DCI effect will typically lead to a reduction in the response but not always. The exception to this observation was earthquake 157 which showed that the DCI effect led to an amplification which was believed to be a result of the nonlinearity introduced by the larger earthquake. When the structure was embedded, the DCI effect was minimal when compared to the excavated cases. Furthermore, it was shown that predicated results tended to overestimate the response of the structure and was unable to capture the shift in the peak frequency. An example

of how the computed response compared with the recorded response is shown in Figure 3.32 and Figure 3.33.

3.4.3.4 ISRS and Earth Pressure Experiment

To gauge the level of uncertainty in assessing the soil properties, the properties provided by JNES were adjusted using SASSI and LS-DYNA to match the ISRS. The resulting soil properties were referred to as the modified soil column. From the numerical analyses it was concluded that the soil properties provided by JNES were too stiff. It was demonstrated that the peak for the computed ISRS was at a higher frequency than what was recorded. Consequently, it was determined that the shear wave velocity should be reduced. The reduction in the shear wave velocity significantly improved the comparison between the predicted and recorded ISRS and earth pressures. To match the ISRS, the shear wave velocity was reduced by 10% and 5% for SASSI and LS-DYNA respectively.

As mentioned, earth pressures were measured along the structures to assess the ability of SASSI and LS-DYNA to predict the pressures exerted on the structure. Two of the previously mentioned configurations were used for this study: 1) twin reactor case and 2) reactor-turbine case. Figure 3.34 and Figure 3.35 illustrates the comparisons of the pressure data for the twin reactor set up. BAS and BAN referred to the reactor that was south and north respectively. Overall, the predicted pressures tended to be conservative and were much higher than what was recorded. Though the predicted pressures were on the conservative side, it was shown that in general the numerical models were able capture the frequency content.

3.4.4 Summary

After analyzing earthquake data over the 8-year span, the following conclusions were drawn. It was determined that both SASSI and LS-DYNA were sufficient in predicting both IRSR and pressures on the model structures for low-level earthquakes. It should be noted that the recorded earthquakes were mostly in the range of 0.01-0.03g and was unlikely to produce any nonlinear behavior in the soil. In the cases where the expected response was linear, it was concluded that SASSI should be used, since minimal effort was required to develop and run the model when compared to LS-DYNA. More work will be needed to access the viability of these computer codes for nonlinear analysis. When the uncertainties inherent in determining the soil properties were taken into account, it was observed that the comparisons were still within an acceptable range for engineering applications. However, there was some difficulties with matching the ISRS peaks from the structure-structure interaction, which was speculated to be a result of the lack of information of the soil property in between the structures. For this experiment, the soil in between the structure was assumed to have the same properties as the free-field. Furthermore, it was shown that the predicted pressure was able to capture the frequency content of the recorded pressure but tended to be on the conservative side. The experiment demonstrated the role that the DCI effect can play, which was shown to shift the peak frequency upward when examining the response spectra. Additionally, it was shown the DCI effect can amplify the acceleration. It was not clear if current computer codes can adequately capture DCI effects and need to be examined for larger earthquakes.

3.5 Acknowledgements

This chapter contains slightly modified sections from the report by Li and coauthors: Earth Pressures on Deep Foundation Walls During Seismic Events (NRC Contract No.: NRC-HQ-12-C-04-0066). The dissertation/thesis author was the primary investigator and author of this chapter. Many people took part in the preparation of this report which include Jinchi Lu, Kyungtae Kim, Professor Ahmed Elgamal, Eun Hyun Park, Michael Musgrove, Professor Youssef Hashash, Nathaniel Wagner, Professor Nicholas Sitar, Boqin Xu, and Professor Ellen Rathje.

Table 3.1 Earthquake Events Selected for Collaboration (Xu et al. 2003)

Earthquake No.	Earthquake Occurrence Time	Source Location East Longitude	Source Location North Latitude	Earthquake Magnitude (M)	Epicenter/Focal Distance (km)	Max old free field point acceleration GL-1.5m (gal) NS	Max old free field point acceleration GL-1.5m (gal) EW	Max new free field point acceleration GL-3.0m (gal) NS	Max new free field point acceleration GL-3.0m (gal) EW
34	03-05-1991	141'41.0	41'16.0	4	28/46	15.8	9.6		
89	12-28-1994	143'43.3	40'27.1	7.5	213/213	123.0	174.0		
131	02-17-1996	141'23.0	40'47.0	4.6	43/45	15.9	17.3	15.1	13.3
139	02-20-1997	142'52.0	41'45.0	5.6	140/146	9.3	8.9	11.4	11.6
157	01-03-1998	142'04.0	41'28.0	5.1	66/89	28.5	26.7	20.8	30.2
63	01-15-1993	144'23.0	42'51.0	7.8	294/310	109.0	98.0		
164	11-07-1998	142'03.0	41'34.0	4.6	71/95	8.9	8.5	6.3	10.8
172	05-11-1999	143'55.0	42'57.0	6.4	288/305	13.5	13.6	13.3	10.8

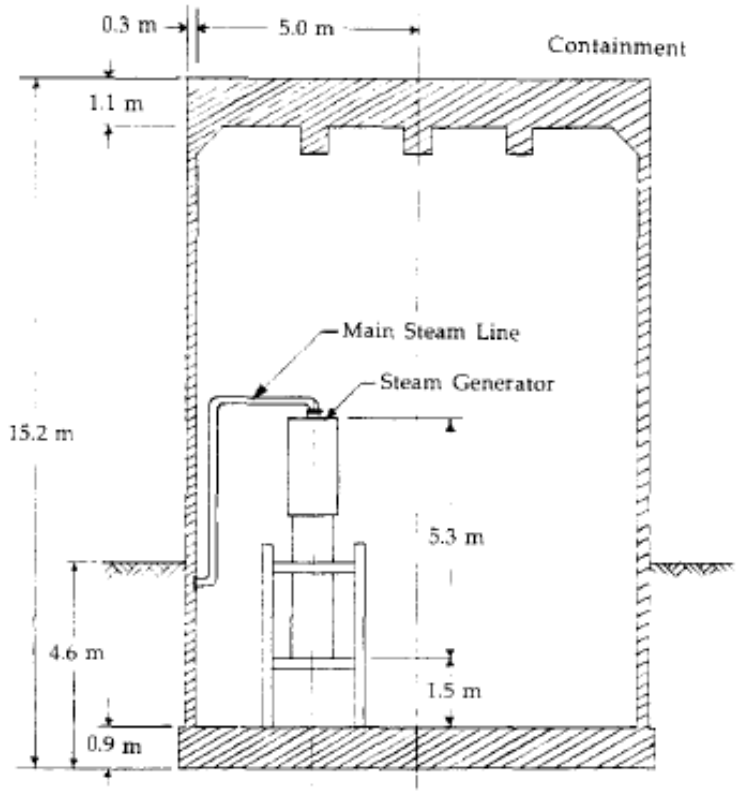

Figure 3.1 The cross-section view of the ¼-scale containment model (Tang and Stepp 1990)

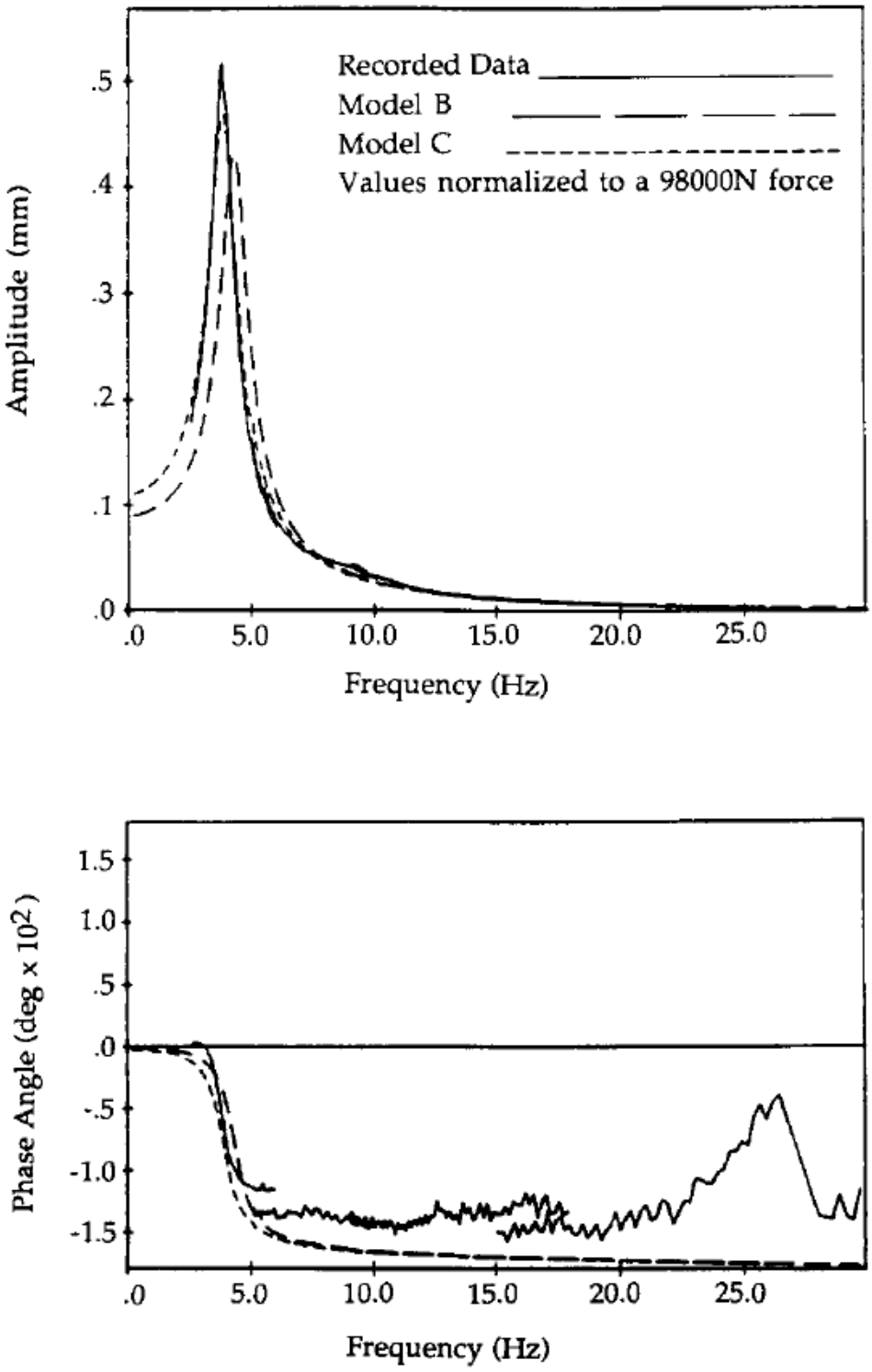

Figure 3.2 Comparison of test and analysis for the top of the 1/4-scale model under force vibration excitation (Tang and Stepp 1990)

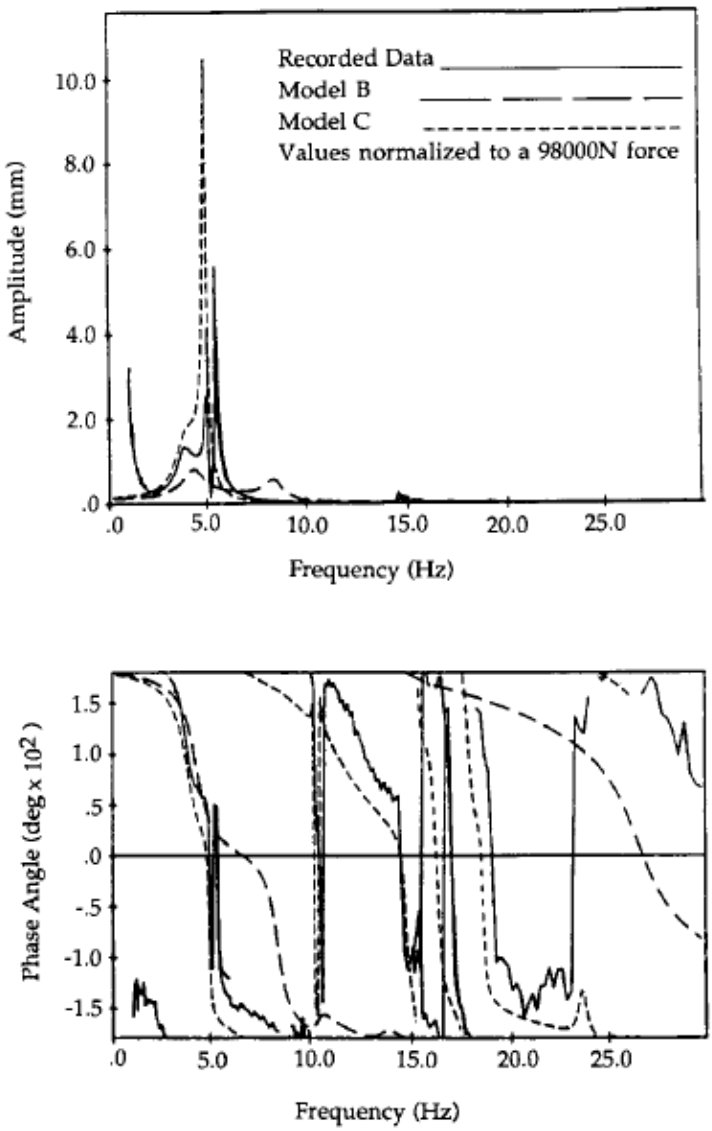

Figure 3.3 Comparisons of test and analysis for the top of the steam generator under forced vibration excitation from (Tang and Stepp 1990)

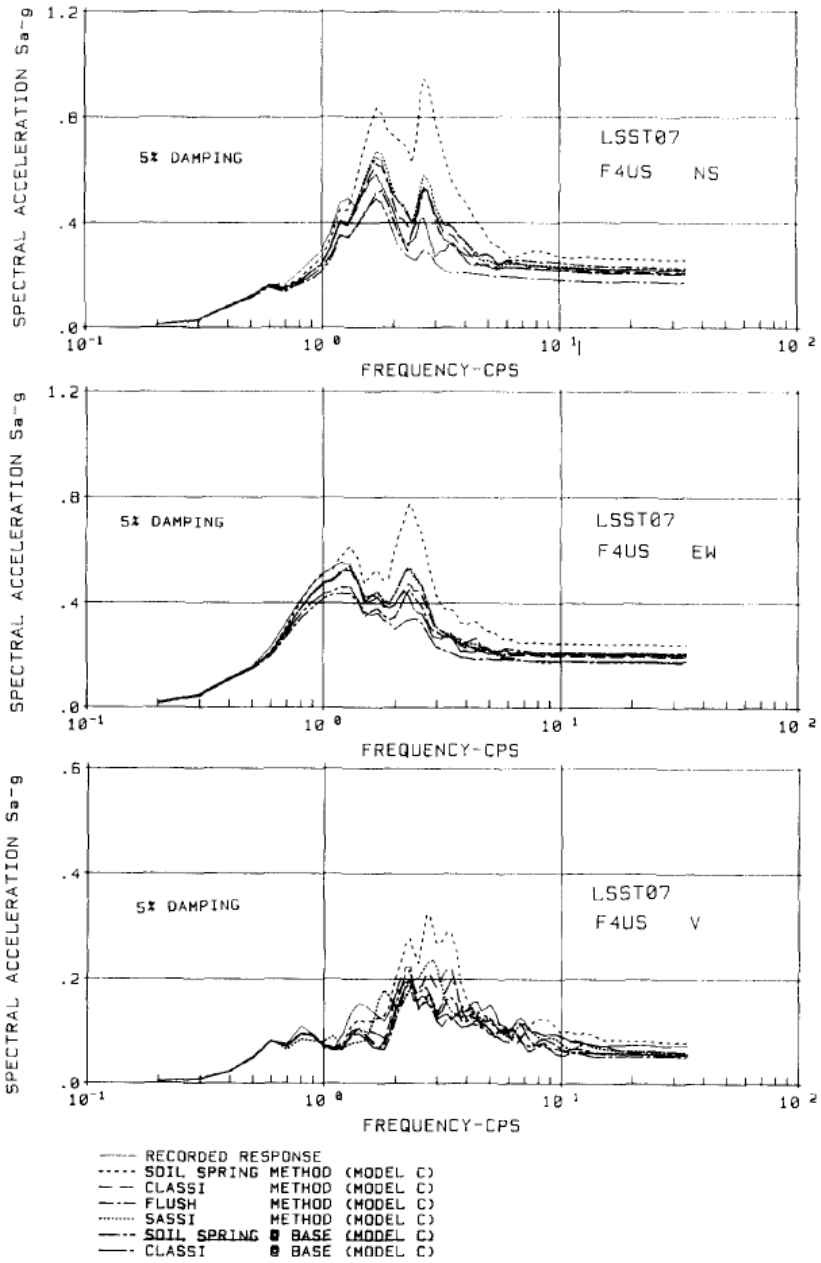

Figure 3.4 Comparison of predicted and measured response spectra at top of the 1/4-scale model of earthquake event 7 (Tang and Stepp 1990); LSST07 refers to earthquake event 7, while F4US refers to the location which is at the top of the containment

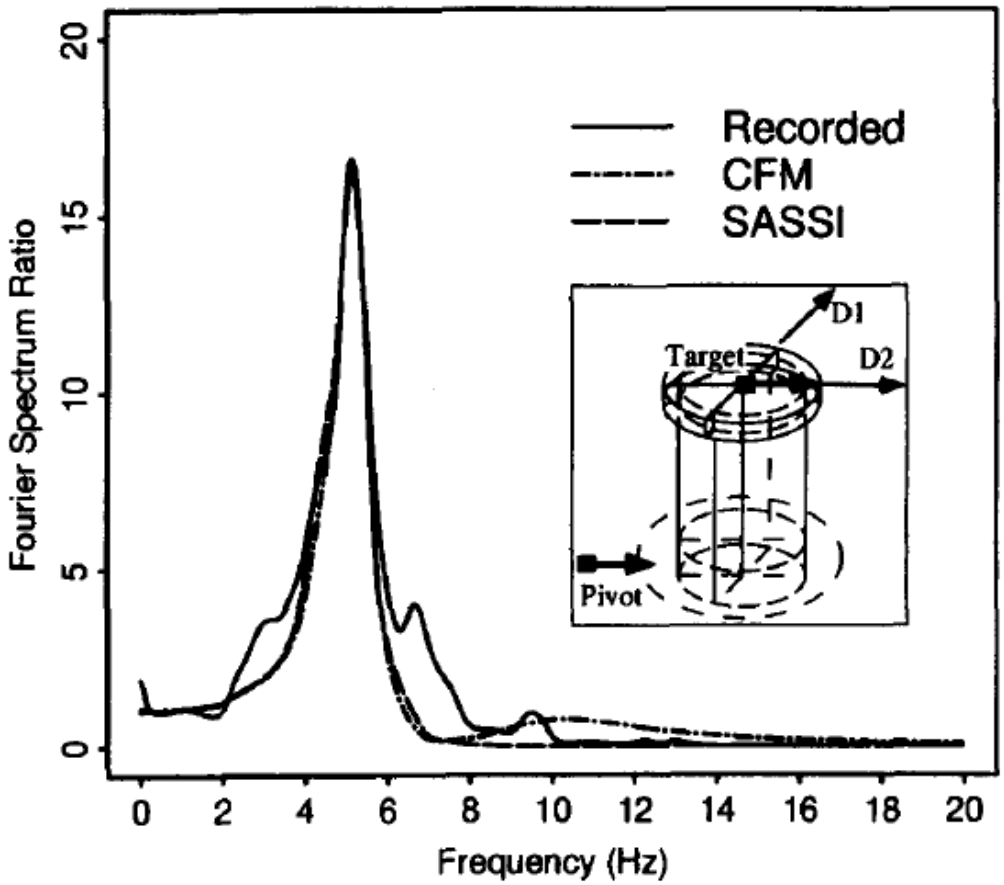

Figure 3.5 Simulation of the D2 component of Event 950501 with CFM and SASSI: Fourier spectrum ratios between the free field and the top of the structure (Ganev et al. 1997)

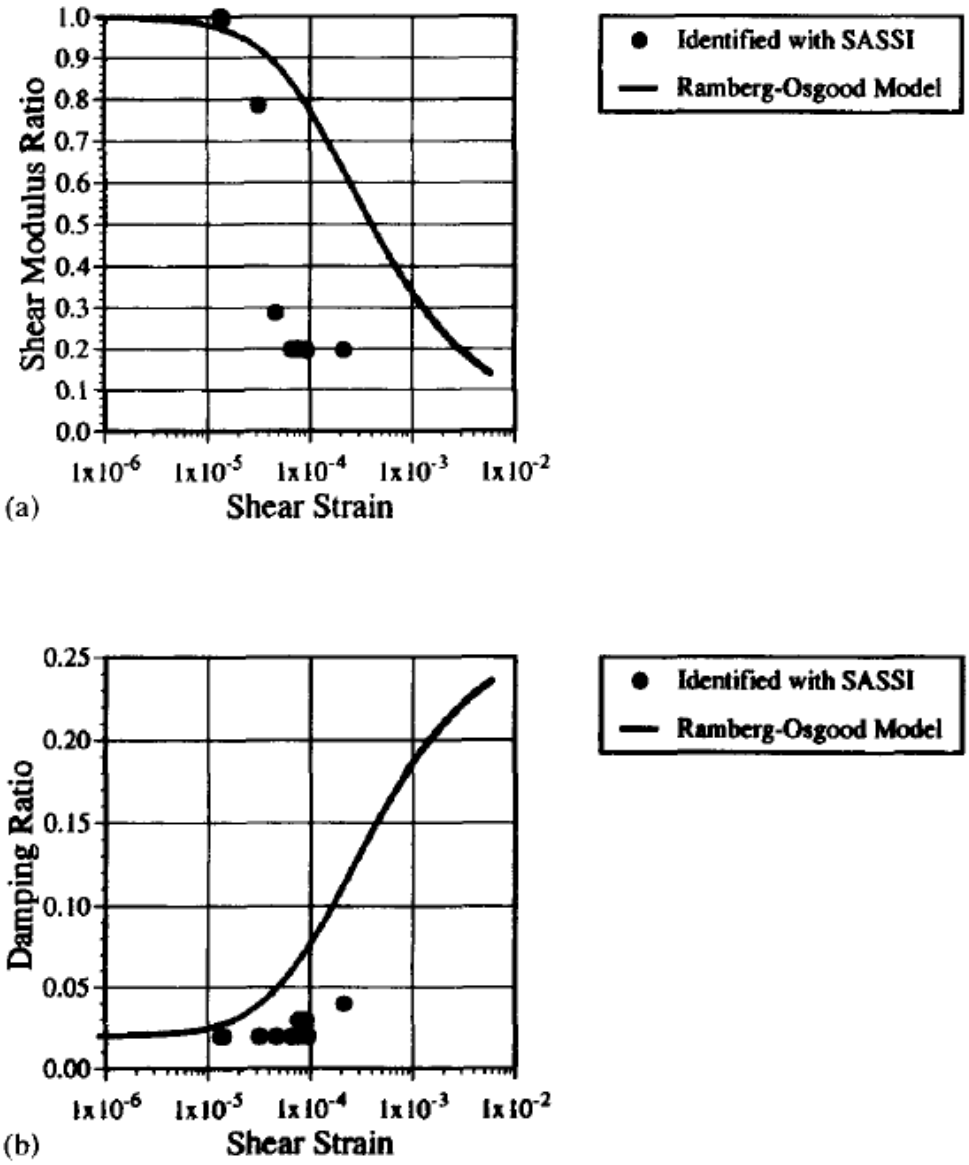

Figure 3.6 Non-linear behavior of the backfill region: (a) shear modulus reduction vs. shear strain, (b) damping ratio vs. shear strain (Ganev et al. 1997)

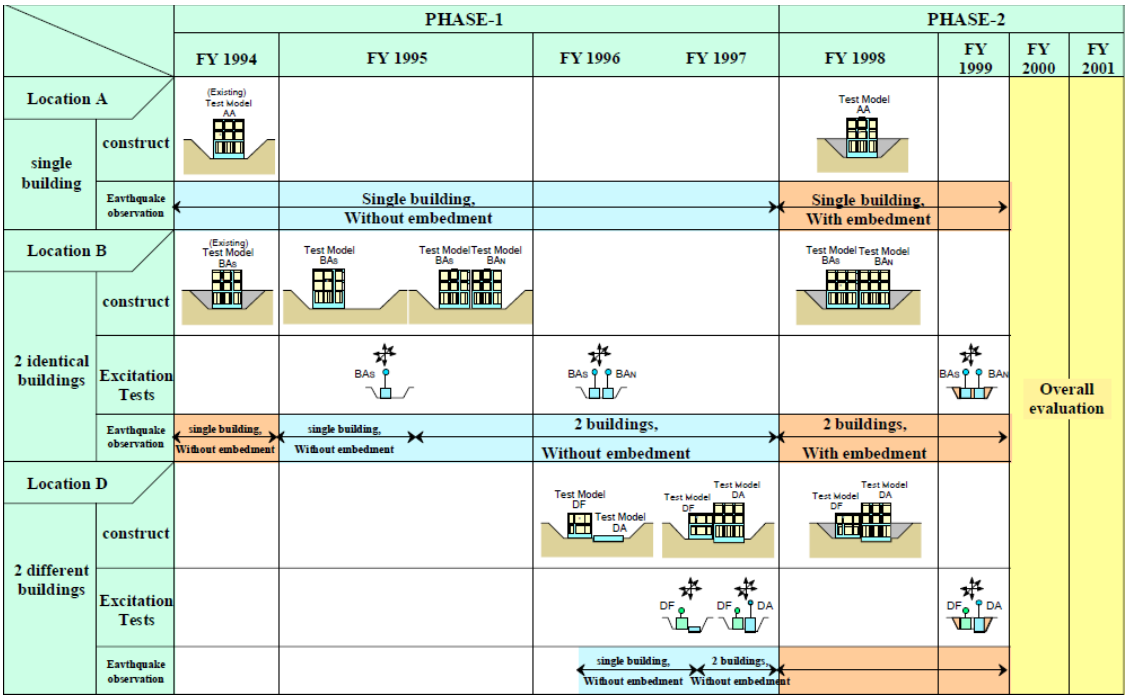

Figure 3.7 Overall Plan for NUPEC Field Tests (Xu et al. 2003)

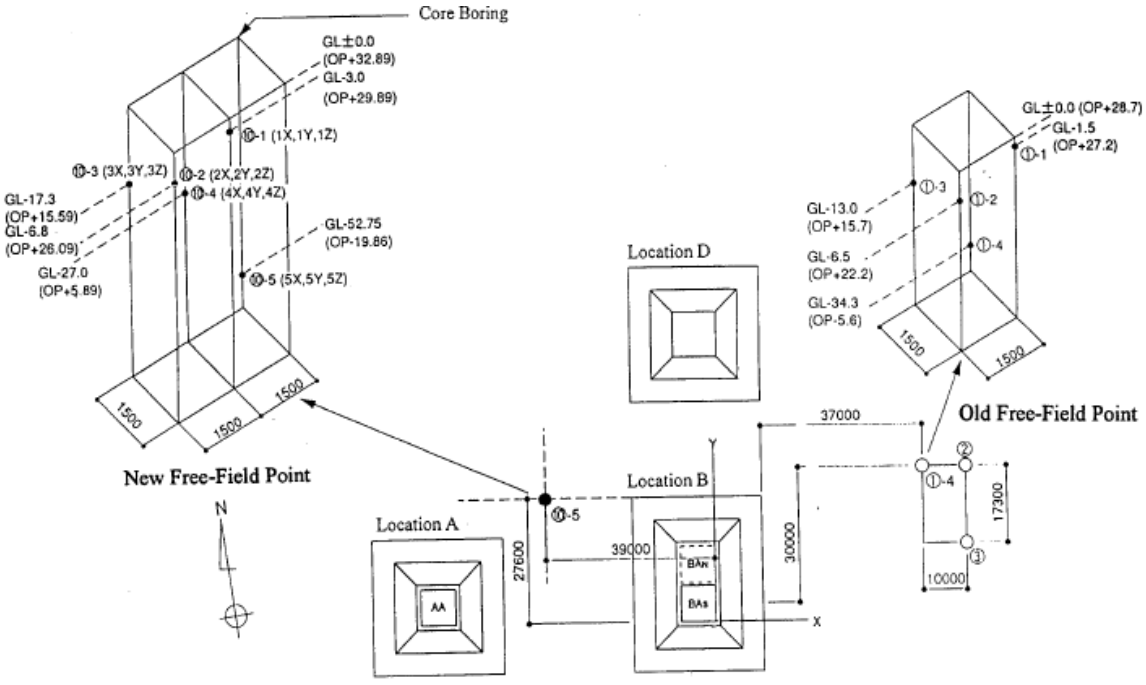

Figure 3.8 Layout of Test Site (Xu et al. 2003)

Figure 3.9 NUPEC Field Test Model of Adjacent Twin Reactor Buildings without Embedment (excavated) (Xu et al. 2003)

Figure 3.10 NUPEC Field Test Model of Adjacent Twin Reactor Buildings with Embedment (Xu et al. 2003)

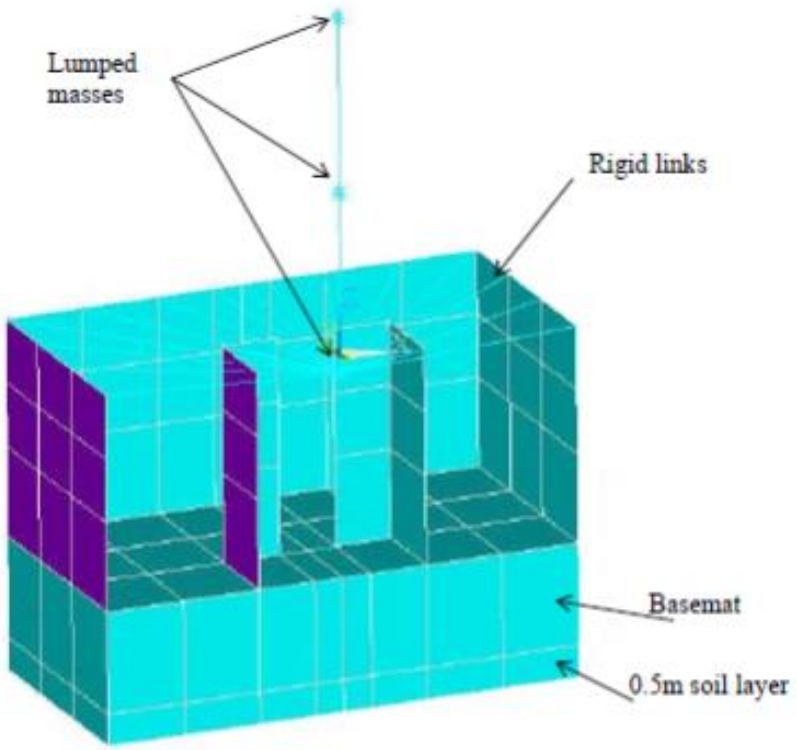

Figure 3.11 BNL SASSI model of the excavated single reactor building (Xu et al. 2008)

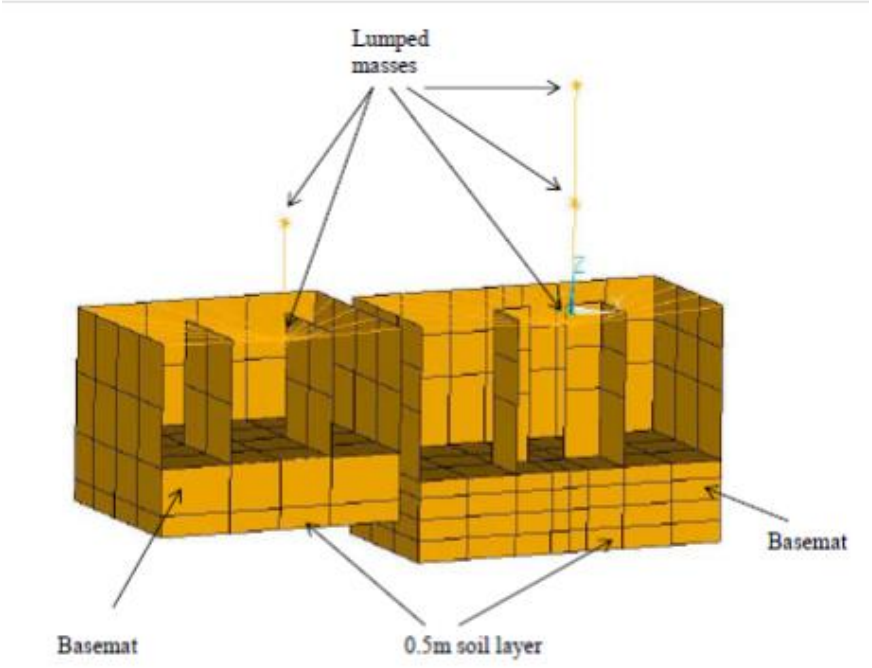

Figure 3.12 BNL SASSI model of the excavated reactor-turbine buildings (Xu et al. 2008)

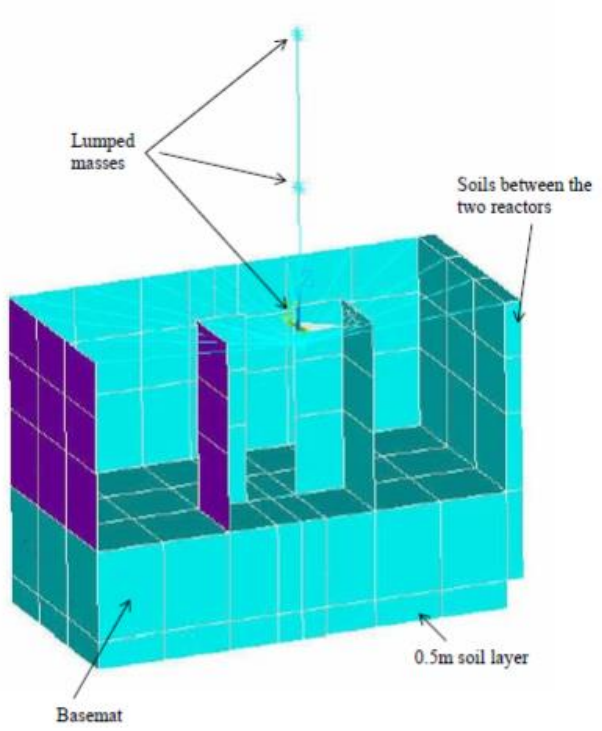

Figure 3.13 BNL SASSI model of the embedded twin-reactor buildings (Xu et al. 2008)

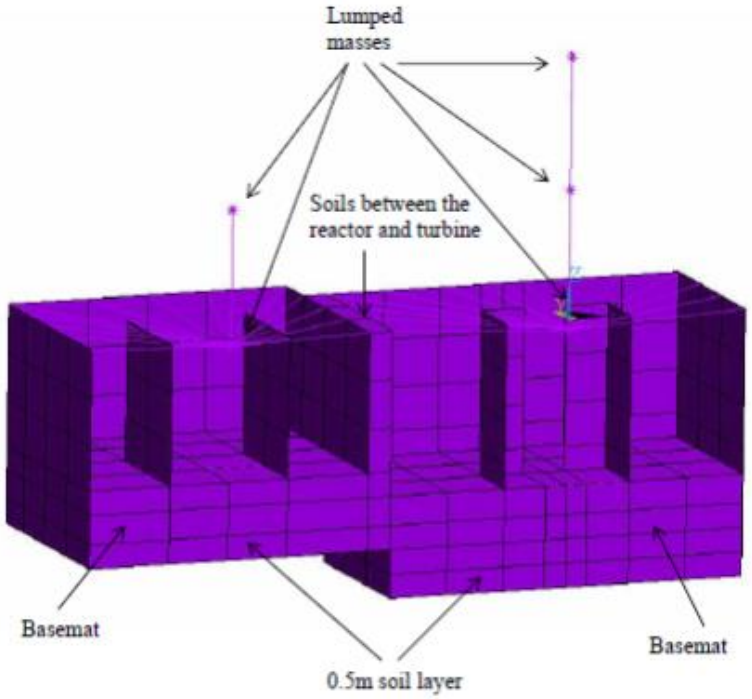

Figure 3.14 BNL SASSI model of the embedded reactor-turbine buildings (Xu et al. 2008)

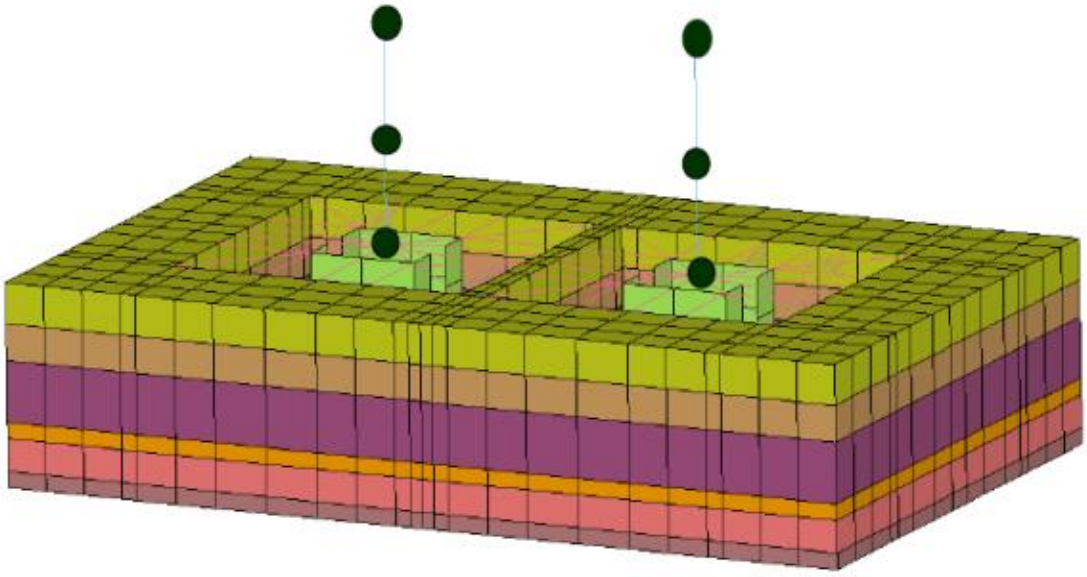

Figure 3.15 SASSI Model for Structures and Surrounding Soil (Xu et al. 2008)

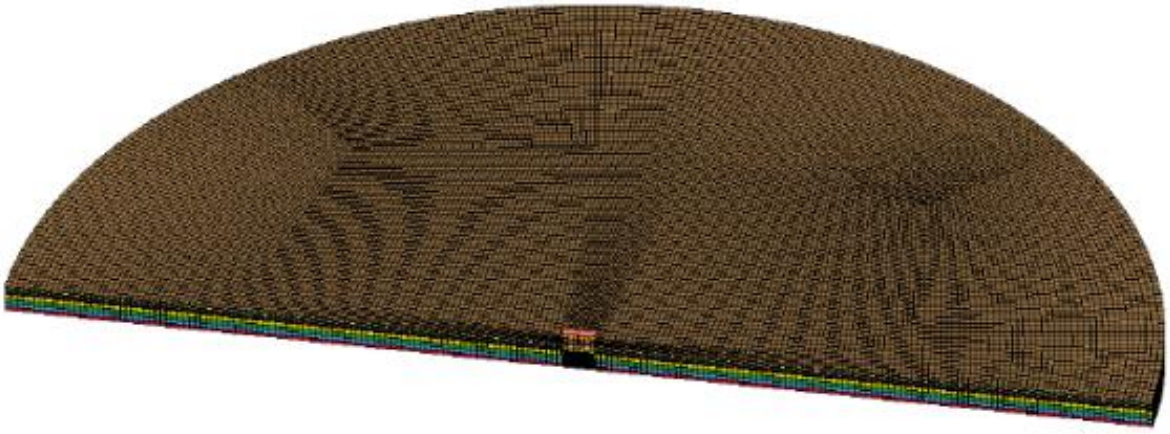

Figure 3.16 LS-DYNA Model for Twin Reactors Test Configuration (Xu et al. 2008)

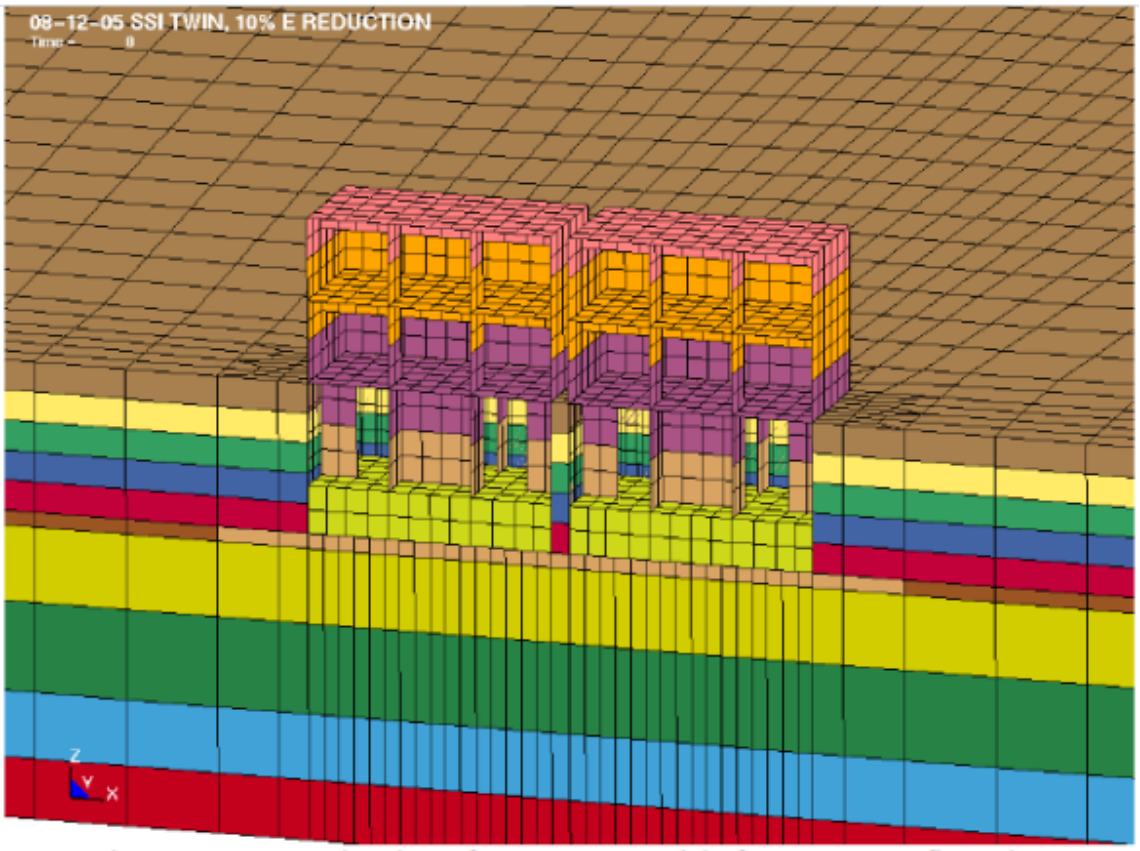

Figure 3.17 Zoom-in View of LS-DYNA Model of reactor-turbine Test Configuration (Xu et al. 2008)

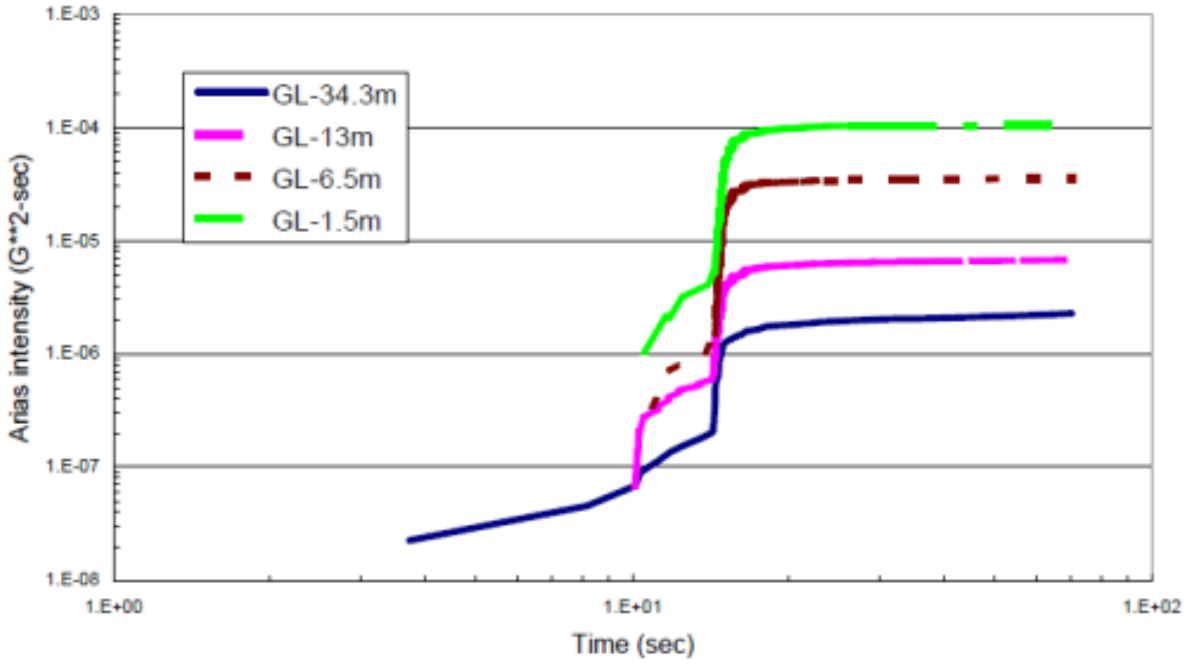

Figure 3.18 Arias intensities for the down-hole array for Earthquake 34x at Old Free-Field Point (Xu et al. 2003) (Note: GL stands for ground level and GL – 34.3m is 34.3m below ground level)

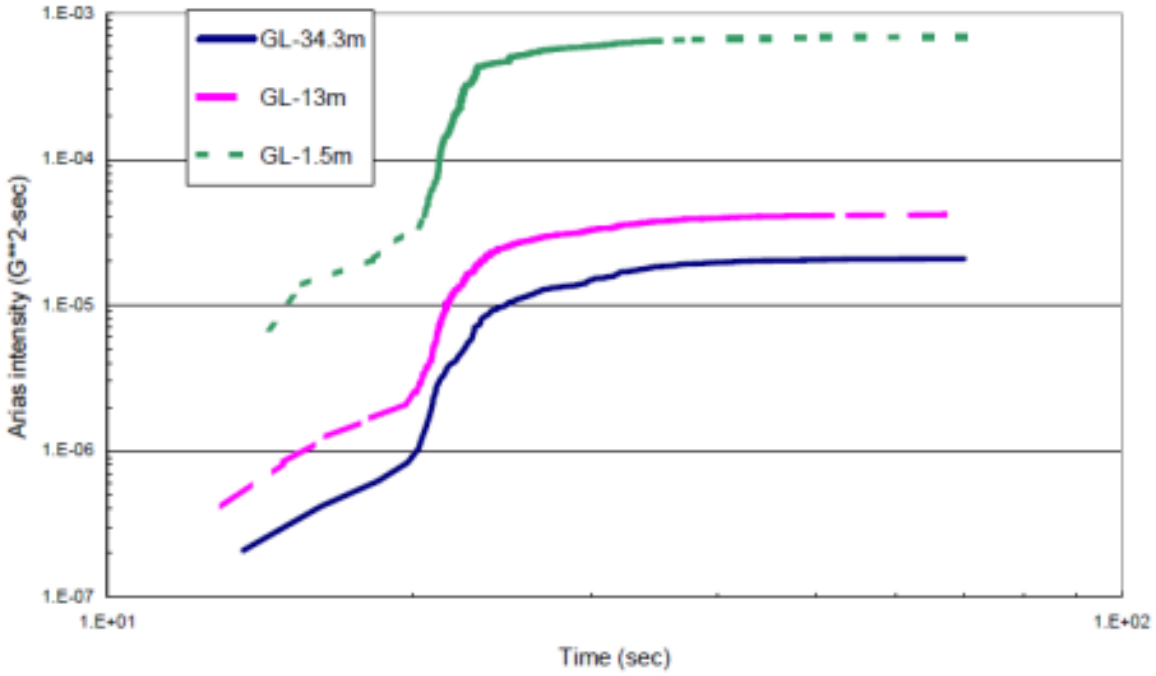

Figure 3.19 Arias intensities for the down-hole array for Earthquake 157 x-direction at Old Free-Field Point (Xu et al. 2003) (Note: GL stands for ground level and GL – 34.3m is 34.3m below ground level)

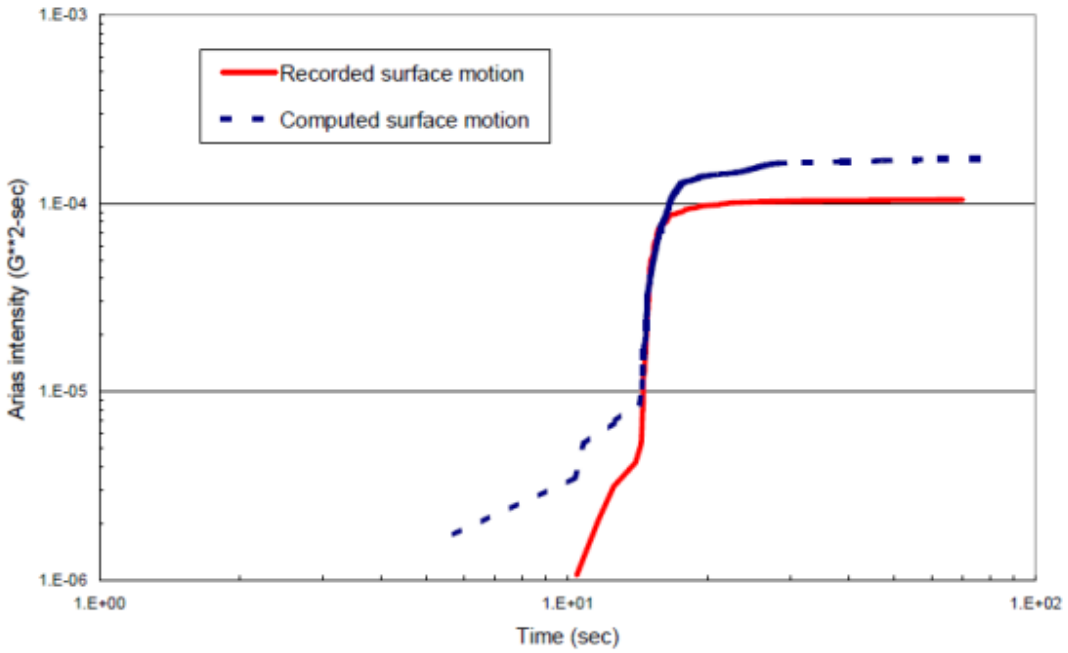

Figure 3.20 Comparison of Arias intensities between computed and recorded surface responses for Earthquake 34x at the Old Free-Field Point (Xu et al. 2003) (Note: GL stands for ground level and GL – 34.3m is 34.3m below ground level)

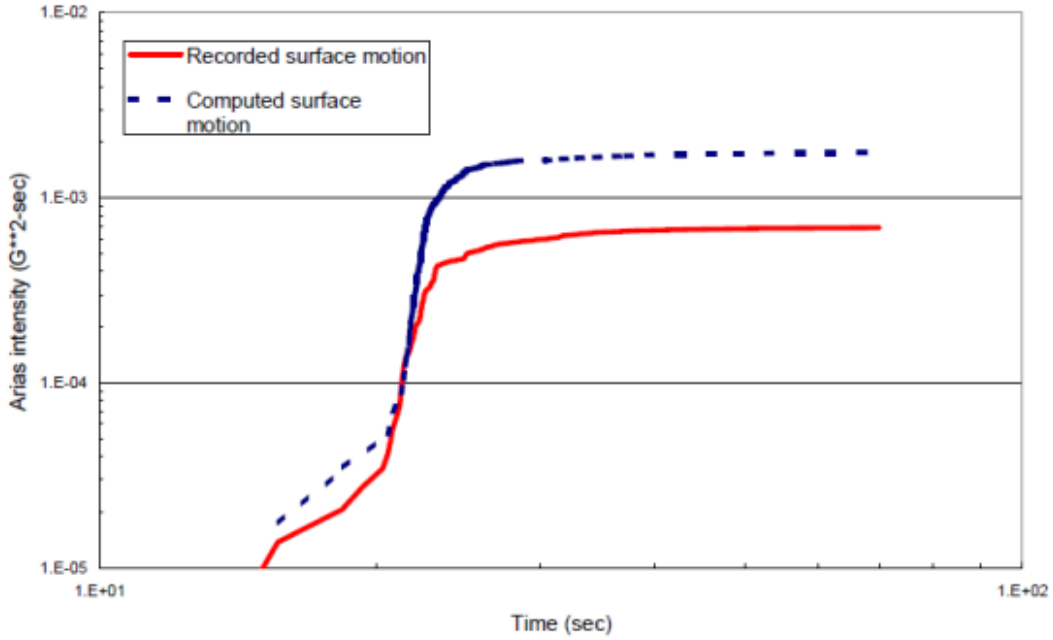

Figure 3.21 Comparison of Arias intensities between computed and recorded surface responses for Earthquake 157 x-direction at the Old Free-Field Point (Xu et al. 2003) (Note: GL stands for ground level and GL – 34.3m is 34.3m below ground level)

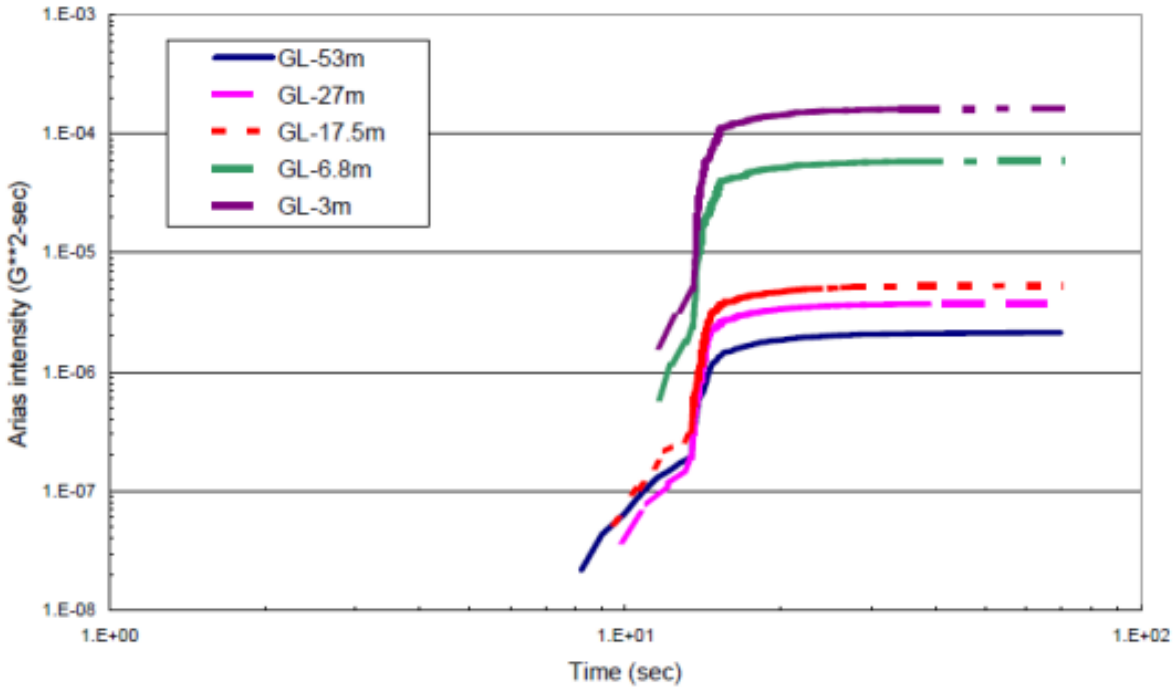

Figure 3.22 Arias intensities for the down-hole array for Earthquake 131x at New Free-Field Point (Xu et al. 2003) (Note: GL stands for ground level and GL – 34.3m is 34.3m below ground level)

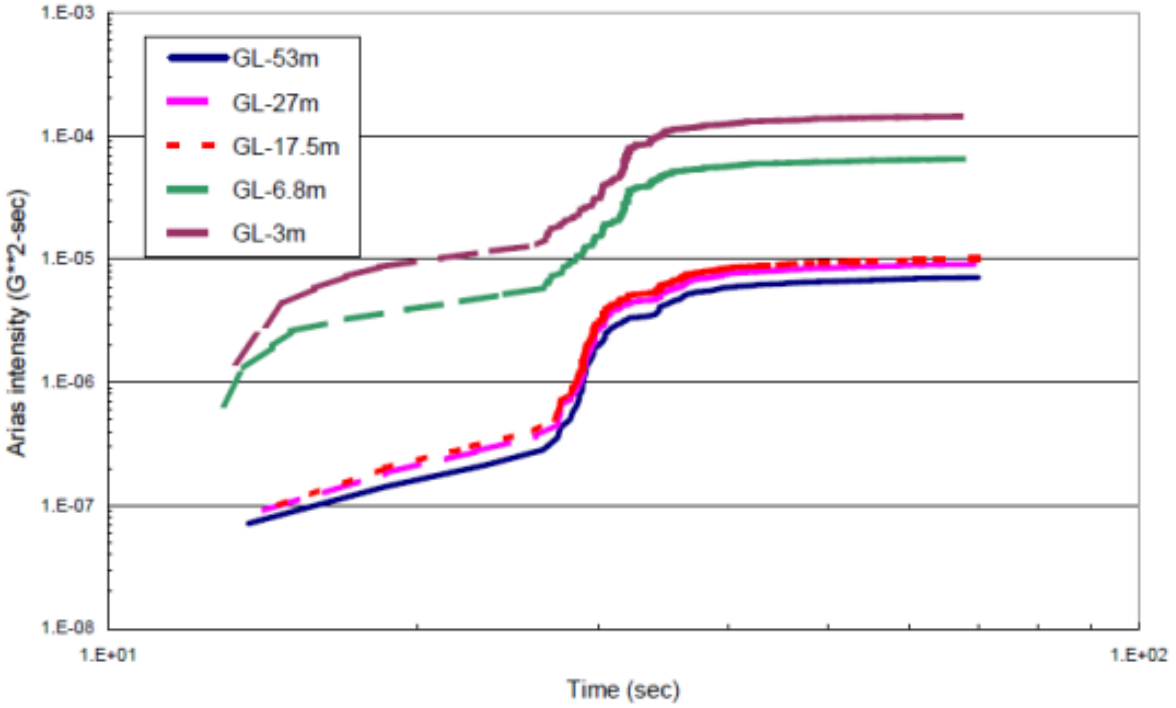

Figure 3.23 Arias intensities for the down-hole array for Earthquake 139 x-direction at New Free-Field Point (Xu et al. 2003) (Note: GL stands for ground level and GL – 34.3m is 34.3m below ground level)

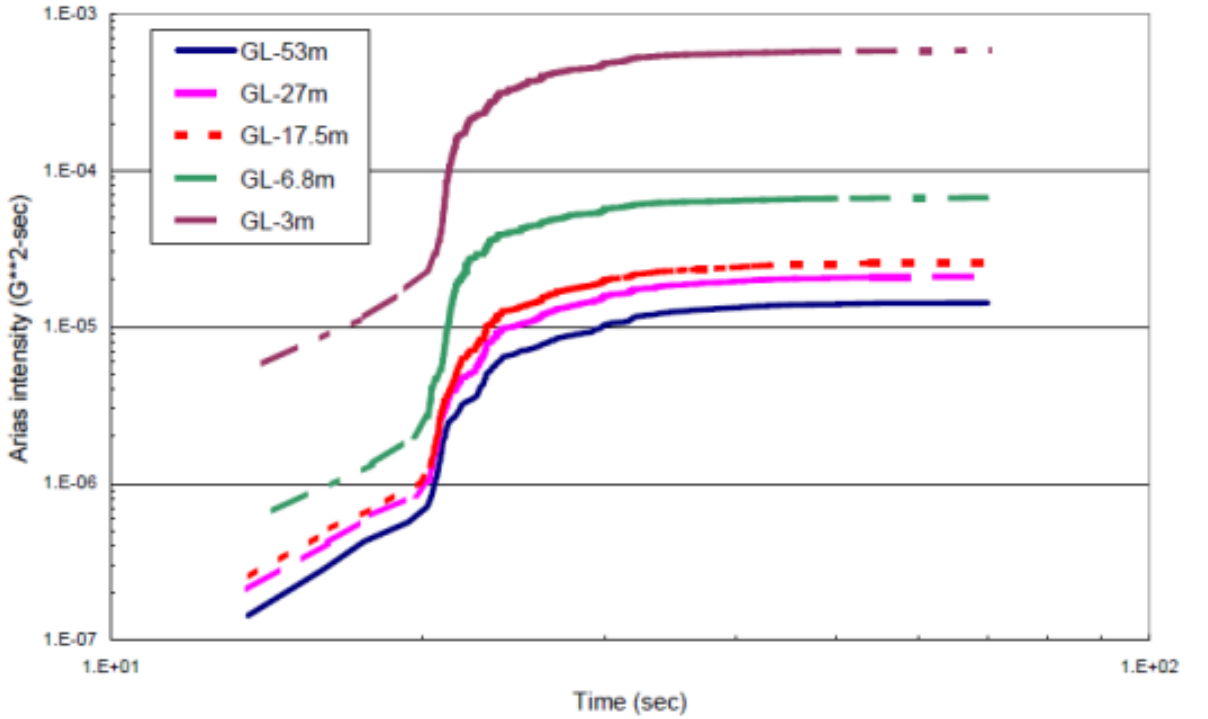

Figure 3.24 Arias intensities for the down-hole array for Earthquake 157 x-direction at New Free0Field Point (Xu et al. 2003) (Note: GL stands for ground level and GL – 34.3m is 34.3m below ground level)

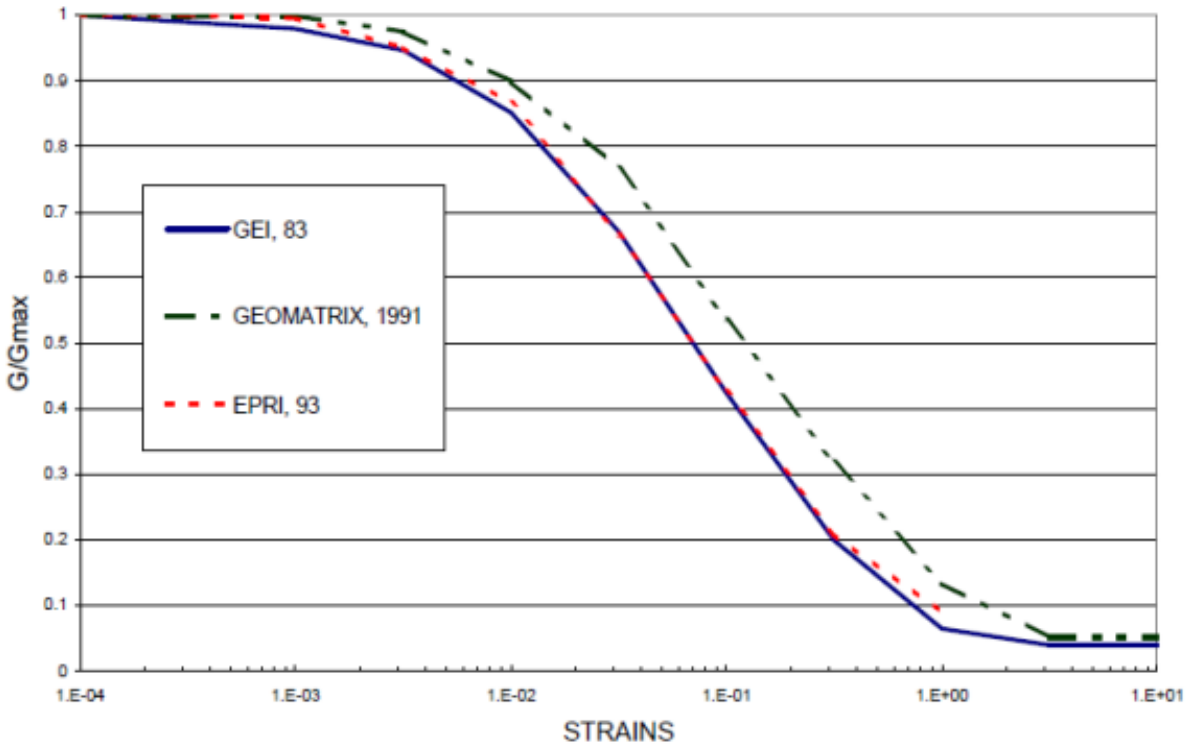

Figure 3.25 Soil modulus strain degradation relationships (Xu et al. 2003)

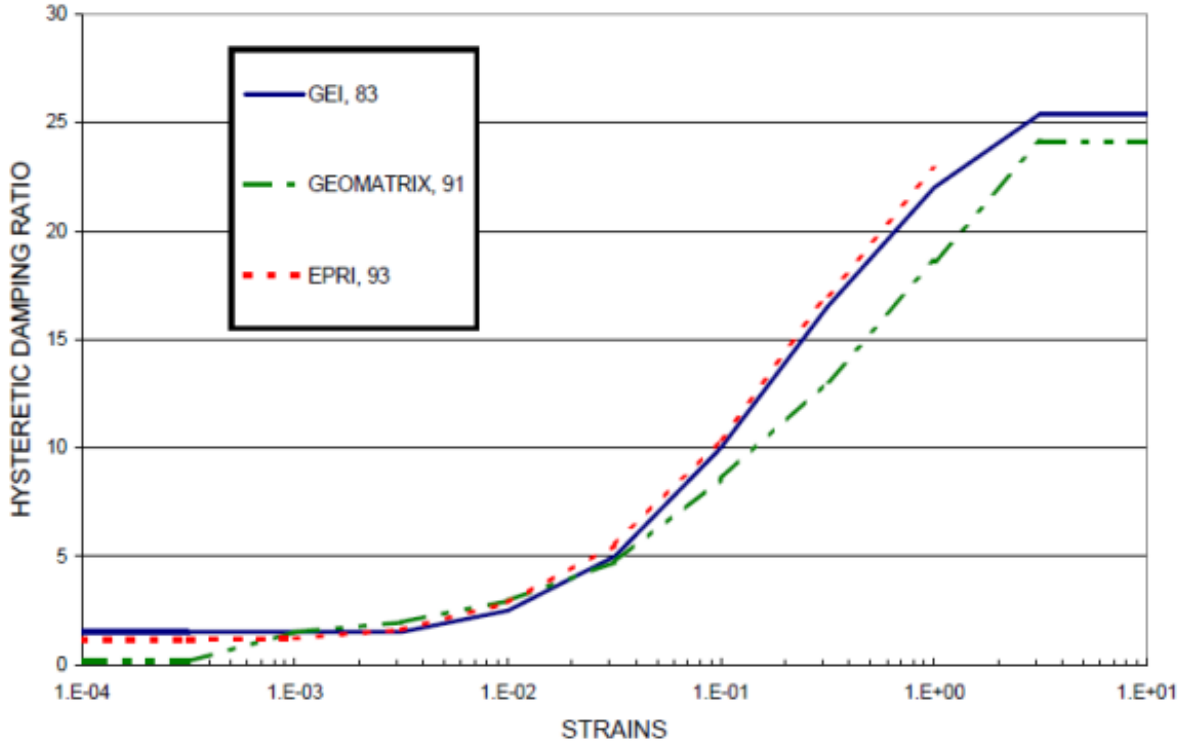

Figure 3.26 Soil hysteretic damping ratios as function of soil strain (Xu et al. 2003)

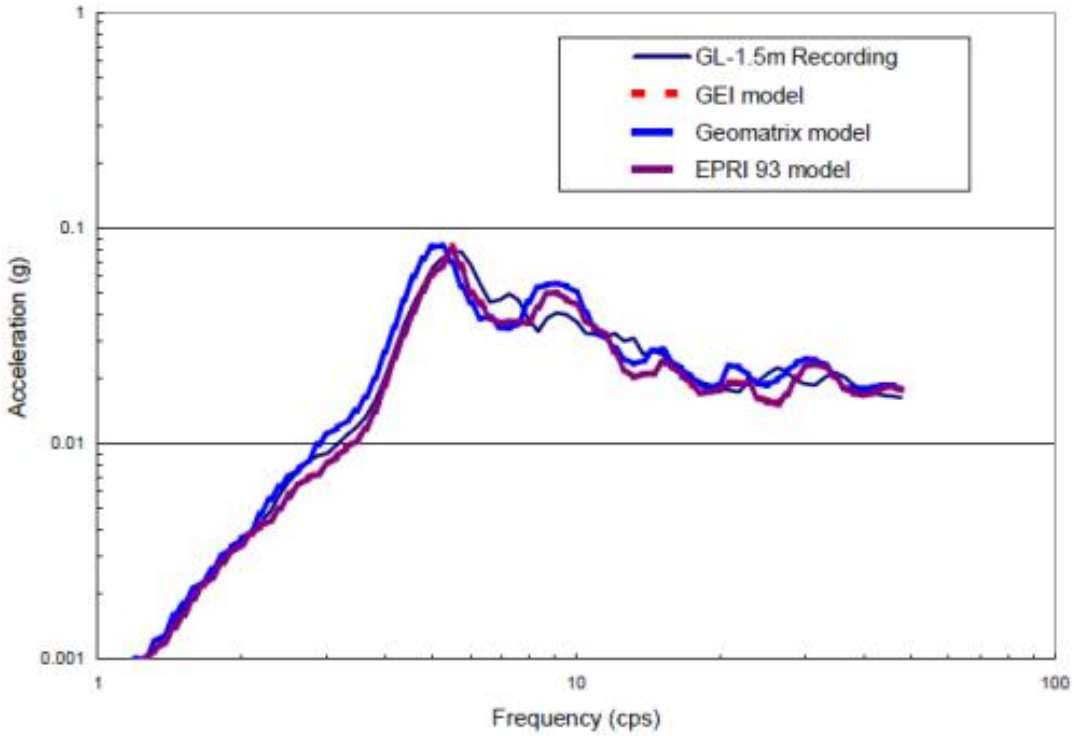

Figure 3.27 Comparison of the use of different degradation models for the old free-field point using Earthquake 34 x-direction (Xu et al. 2003)

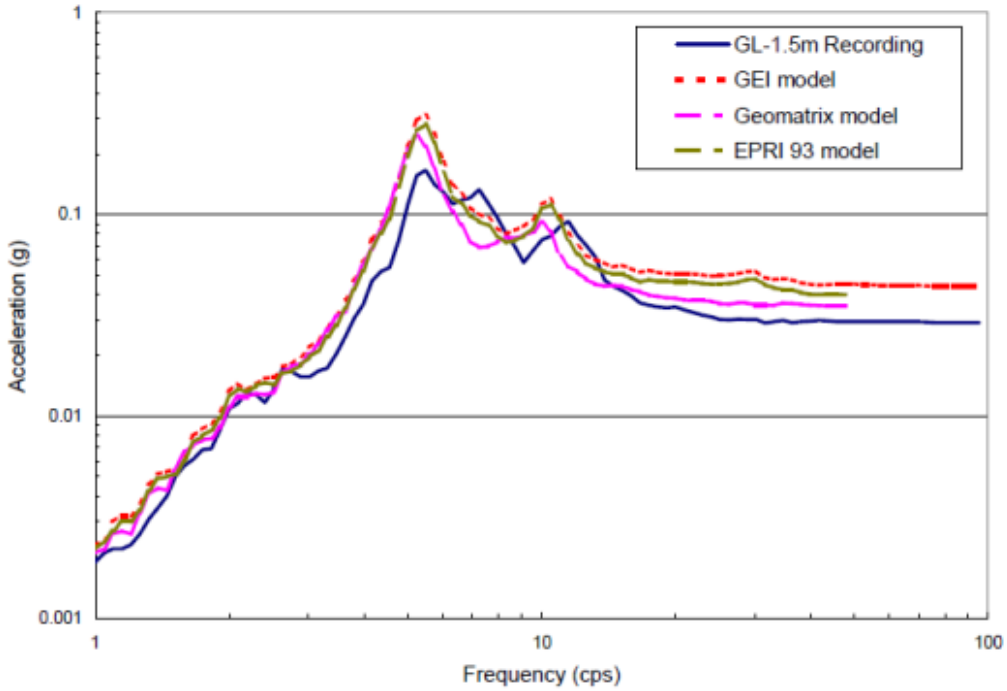

Figure 3.28 Comparison of the use of different degradation models for the Old Free-Field Point using Earthquake 157 x-direction (Xu et al. 2003)

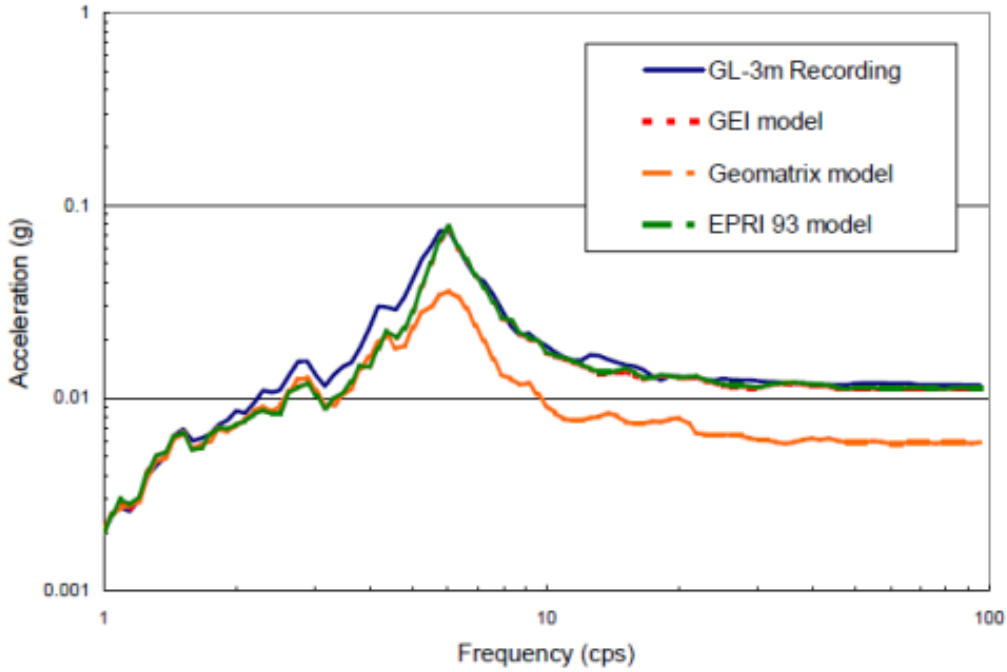

Figure 3.29 Comparison of the use of different degradation models for the New Free-Field Point using Earthquake 139 x-direction (Xu et al. 2003)

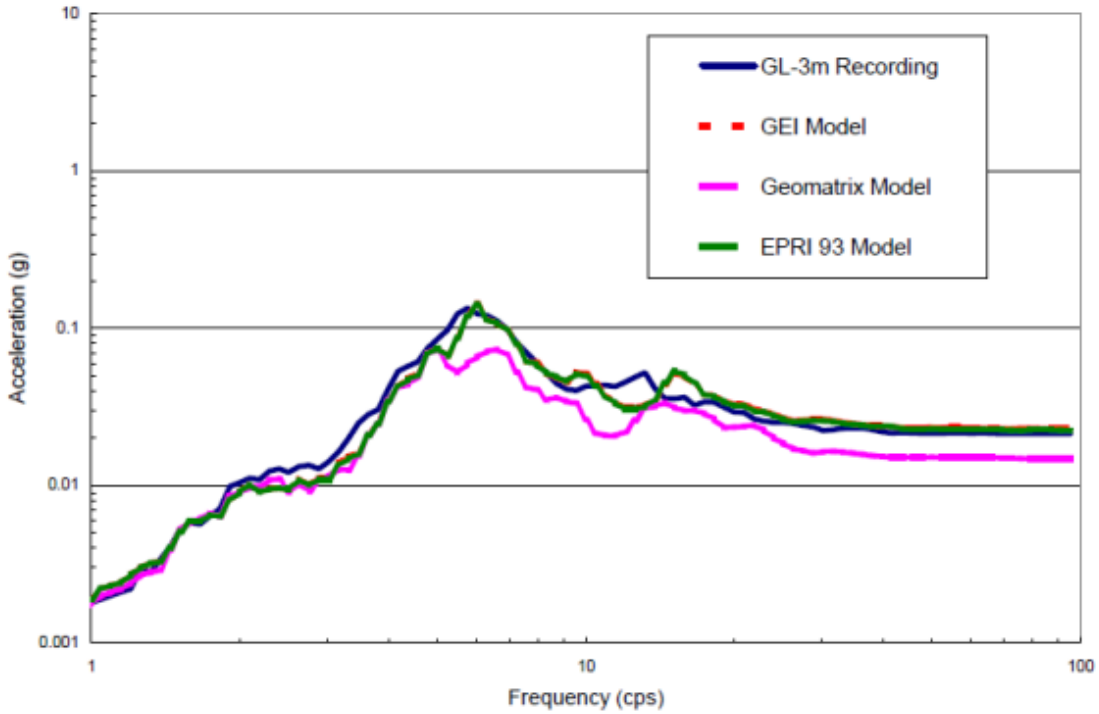

Figure 3.30 Comparison of the use of different degradation models for the New Free-Field Point using Earthquake 157 x-direction (Xu et al. 2003)

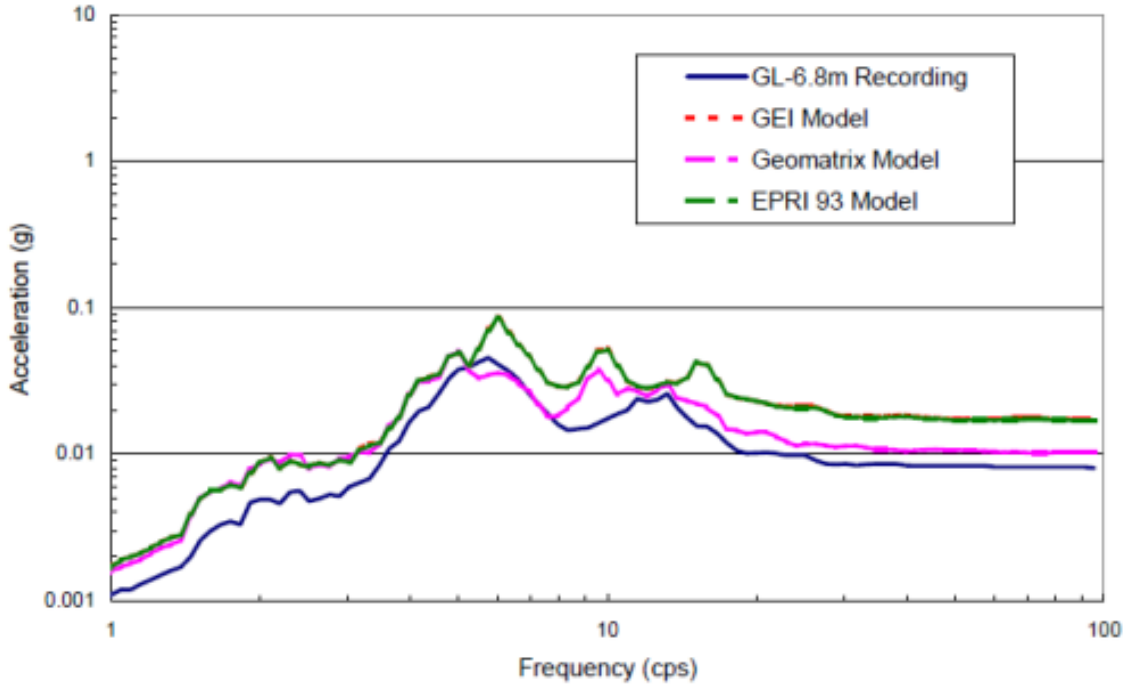

Figure 3.31 Comparison of the use of different degradation models for the New Free-Field Point using Earthquake 157 x-direction (Xu et al. 2003)

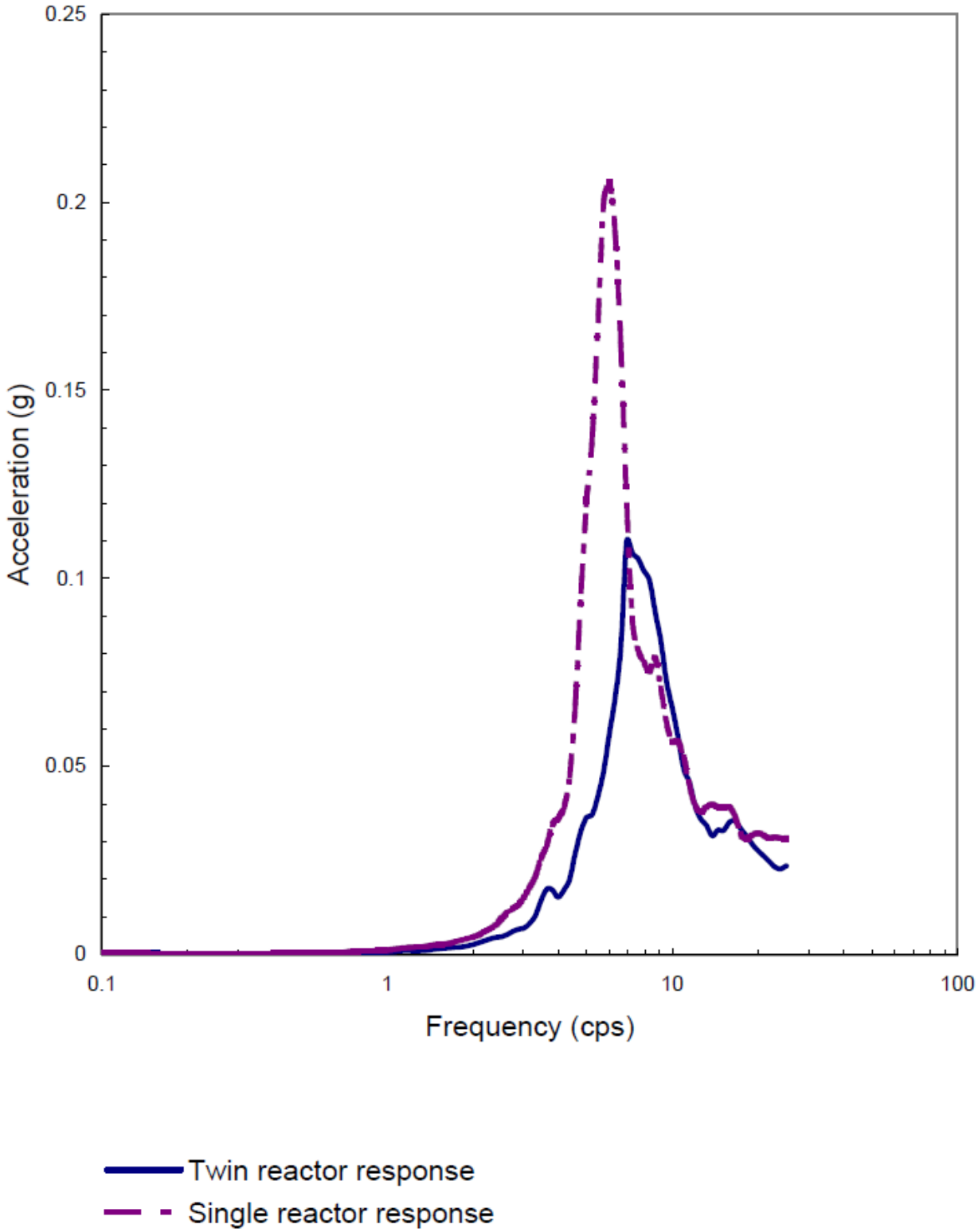

Figure 3.32 Comparison of the recorded response spectra at the roof of excavated reactor buildings in NS direction (No. 131) (Xu et al. 2003)

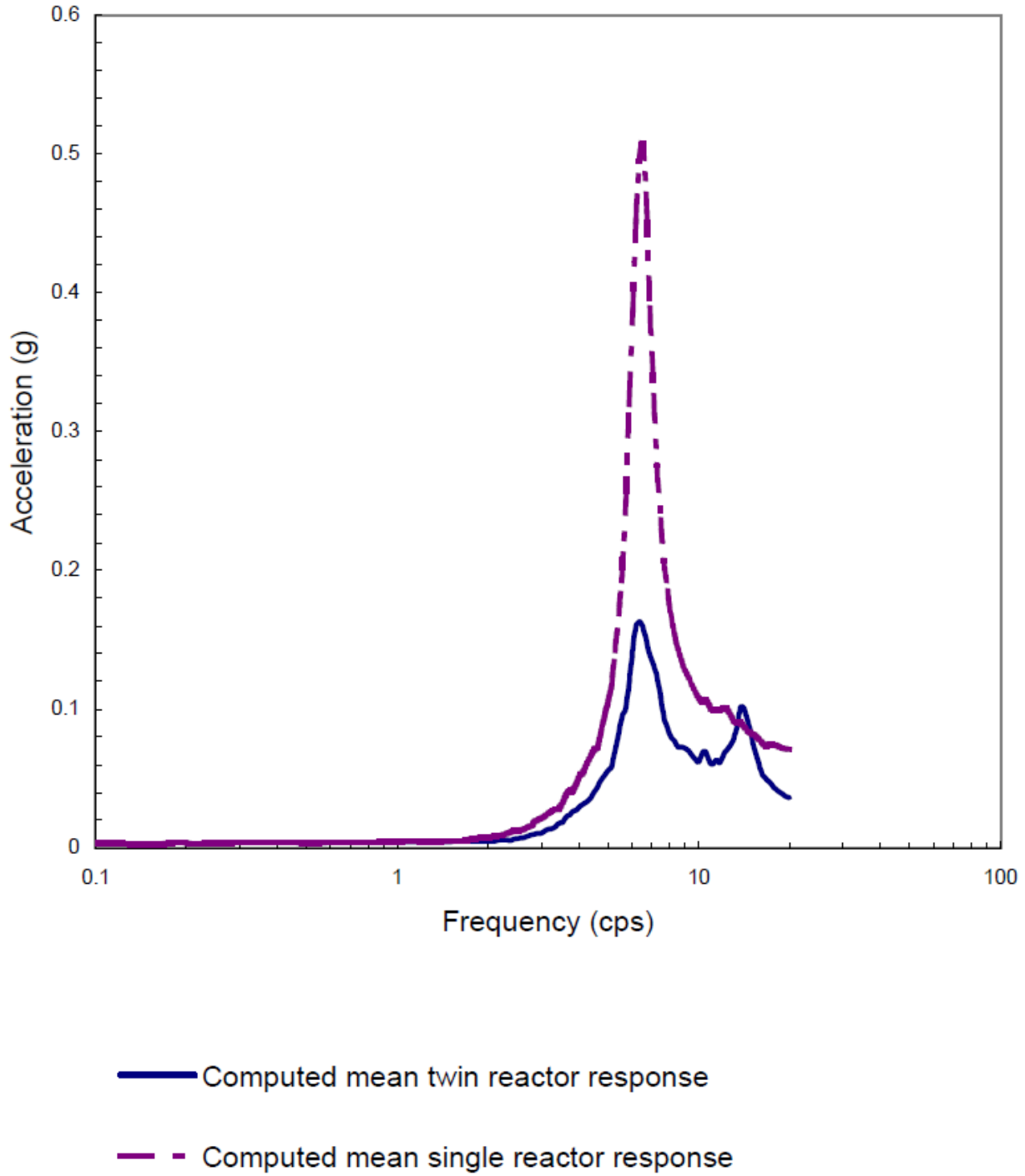

Figure 3.33 Comparison of the predicted response spectra at the roof of excavated reactor buildings in NS direction (No. 131) (Xu et al. 2003)

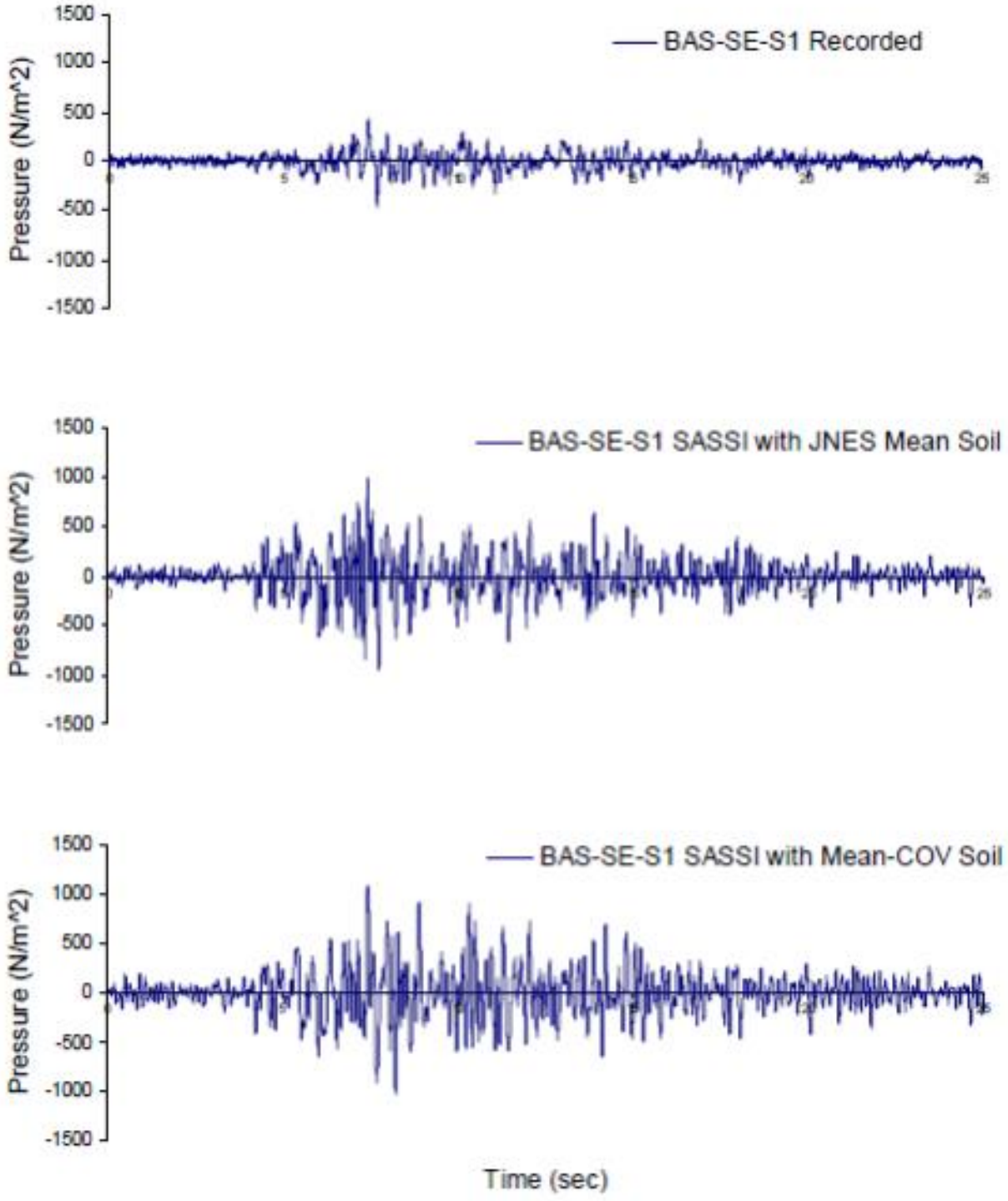

Figure 3.34 Comparison of Seismic Induced Soil Pressure at Sensor BAS-SE-S1(Xu et al. 2008) (This sensor is located on the South wall of the BAS reactor and is near the base of the structure. Mean soil is the best estimate for the soil properties. COV is the measure of the variability of the laboratory tests to obtain the soil properties.)

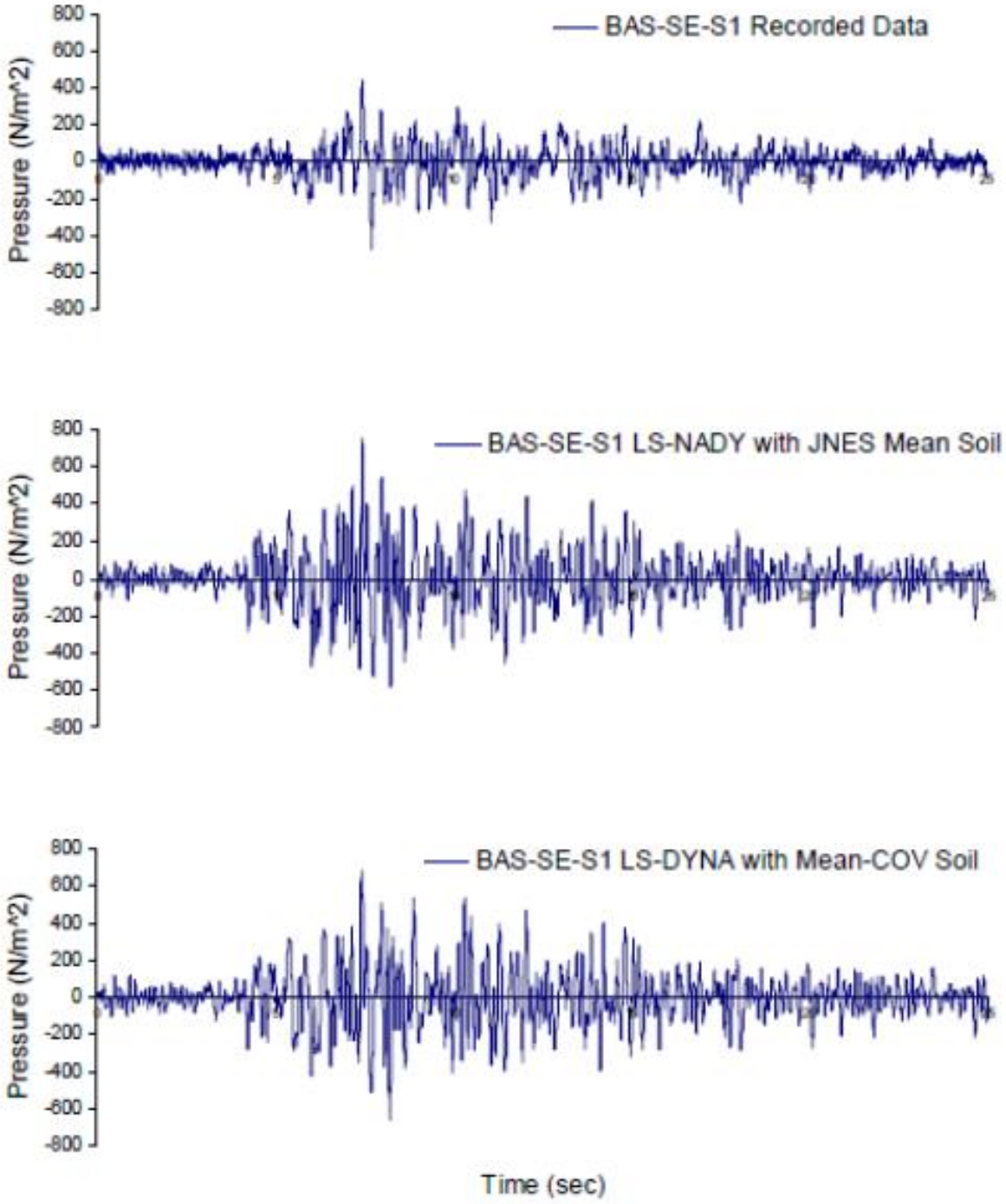

Figure 3.35 Comparison of Seismic Induced Soil Pressure at Sensor BAS-SE-S1 (Xu et al. 2008) (This sensor is located on the South wall of the BAN reactor and is near the base of the structure. Mean soil is the best estimate for the soil properties. COV is the measure of the variability of the laboratory tests to obtain the soil properties.)

Chapter 4

Comparative Study of Numerical Codes

4.1 Introduction

In this chapter, comparisons between the results for a select number of currently available numerical codes are presented in order to document the differences and similarities. The main goal was to provide a convenient resource (readily available online in digital format) for checking the response of a user's computer modeling approach against these documented results. As such, full documentation of every aspect of the underlying numerical techniques was included as well.

For this purpose, a one-dimensional (1D) seismic site response scenario was adopted (Li et al. 2016). Five different numerical codes were employed to conduct a series of linear analyses, while four of these were used for nonlinear analysis. Moreover, four types of viscous damping were used in this study. For each case, the results from a suite of twenty earthquake input motions were documented and compared individually, as well as in terms of the average response (for some codes).

4.2 One-Dimensional Site Response Investigation

4.2.1 Employed Numerical Models

The five codes (Table 4.1) selected for this comparison were DEEPSOIL 6.0 (Hashash et al. 2015), DIANA 9.5 (Manie 2014), LS-DYNA R6.1.0 (LS-DYNA 2012), OpenSees 2.4.3 (Mazzoni et al. 2006), and PLAXIS 2D-AE (Brinkgreve et al. 2011). All five codes were used to perform analysis in the time domain, while only DEEPSOIL was used for frequency domain analysis (Li et al. 2016). DeepSoil 6.0 and PLAXIS 2D-AE were conducted by Professor Hashash and coworkers (Li et al. 2016). The differences between how the soil columns were implemented in each of the numerical codes are presented in the following section.

4.2.2 Modeling Configuration and Input Base Excitation

The modeling parameters utilized in the linear analyses can be found in Table 4.2 - Table 4.4. As shown in Table 4.2, the shear wave velocity for the entire 30 meter soil column was 180 m/s which was very weak and corresponds to Site Class E as defined by NEHRP (BSSC 2004). The first three natural frequencies for this soil column were 1.5 Hz, 4.5 Hz and 7.5 Hz.

DEEPSOIL is a 1D analysis program which utilized a lumped mass model to discretize the soil column. On the other hand, DIANA, LS-DYNA, OpenSees and PLAXIS used finite elements. The mesh used in these codes are shown in Figure 4.1. The differences in how the 1D shear beam models were implemented in the various numerical codes are presented in Table 4.3. As shown, there were some differences in how the boundary conditions were enforced, selection of element, and type of mass matrix used.

As stated, four different damping cases were considered, which all specified the damping to be 5% at the 1st natural frequency. The damping cases were: 1) 5% damping at the 1st natural

frequency using only the stiffness proportional term (stiffness proportional viscous damping), 2) 5% damping at the 1st natural frequency using only the mass proportional term (mass proportional viscous damping), 3) 5% damping at the 1st and 3rd natural frequency using both the stiffness and mass proportional terms (Rayleigh Damping), and 4) frequency independent damping. The types of damping employed by each of the codes can be found in Table 4.4.

This comparison used the Western United States (WUS) input motions (provided by Professor Ellen Rathje) as discussed in the Earth Pressures on Deep Foundation Walls During Seismic Events technical report (Li et al. 2016). This suite of motions includes 10 orthogonal horizontal components (20 motions total) which were selected from the PEER NGA strong motion database to match a deterministic response spectrum.

4.3 Linear Results

4.3.1 Average Response Spectrum

In the following sections, average spectral acceleration using the set of WUS motion are shown for the different damping cases considered. Figure 4.2 - Figure 4.8 plots average response spectrum at ground surface together with +/- one standard deviation and compares it against average response spectrum for the input motions used. The average response spectrum from OpenSees and DIANA were demonstrated to be essentially the same. Representative response computed using the codes mentioned in Table 4.1 can be found in Appendix A. From the comparison of the response spectrums, it was shown that the results from the selected codes were in good agreement with each other.

4.3.2 Discussion of Linear Results

The average response spectrum (Figure 4.2 - Figure 4.8) was demonstrated to behave as expected. The differences between the average acceleration can be explained in terms of the type of damping considered. As previously mentioned, all four damping cases were defined on the basis of specifying 5% damping at the first natural frequency (1.5 Hz). On this basis, it was expected that the response at the 1st natural frequency should be the same amongst the different damping cases. Furthermore, the stiffness proportional term scaled linearly with frequency and as a result should significantly dampen the response at the high frequencies (Figure 4.2 - Figure 4.3). Similarly, when only the mass proportional damping term was used, the response was anticipated to have significant contributions in the high frequency range since the damping decreased with frequency (Figure 4.4 - Figure 4.5).

It was shown that there was reasonable agreement between Rayleigh damping (Figure 4.6 - Figure 4.7) and frequency independent damping (Figure 4.8). Since the Rayleigh damping specified 5% at the 1st and 3rd natural mode,, the peak at the second natural frequency was slightly less than the frequency independent case. When examining the response spectrum for each individual earthquake motion (Appendix A), it was shown that many of the earthquakes were marginally able to excite the model's 4th natural frequency if at all, and as a result did not have much of an impact on the average response. In the event that the motion was able to excite the 4th natural frequency it was observed that Rayleigh damping would underestimate the response when compared against frequency independent damping.

When comparing the results for each individual motions for DIANA, LS-DYNA and OpenSees (Appendix A), it was observed that the responses from these codes were in close agreement. The soil models were implemented in a very similar manner in these codes, and

consequently behaved in a comparable fashion. In the case of LS-DYNA, it was shown that using an 8 Node brick with constant stress and a lumped mass matrix formulation produced very similar results to DIANA and OpenSees. On the other hand, when PLAXIS (using Rayleigh damping) was compared against OpenSees (using Rayleigh damping) it was observed that there were notable differences for some of the input motions. The results from the time and frequency domain analysis using DEEPSOIL (using frequency independent damping) were shown to be close when compared to OpenSees (using Rayleigh damping and frequency independent damping). Overall, the different numerical codes for each damping case, were shown to be consistent.

4.4 Nonlinear Results

4.4.1 Employed Nonlinear Model

All the codes from the linear analysis section except LS-DYNA (due to timely constraints), were used in this comparison of the nonlinear results. The soil properties were similar to the linear analysis. The only difference was the introduction of nonlinear soil models, which are shown in Table 4.5. The material models are discussed in their respective manual, with the exception of DIANA. The soil model used in DIANA was the same as OpenSees and was implemented as a user defined material. The modulus reduction and damping curve (Figure 4.9) that was used for this analysis are provided in Table 4.6. DIANA and OpenSees was able to directly use the modulus reduction curve, while the nonlinear soil properties in DEEPSOIL and PLAXIS were selected to match the curves as best as possible. For DEEPSOIL, the pressure dependence of the model was disabled, while the model in PLAXIS was specified to match the target curve at the mid-depth of the soil column and was still dependent on pressure. The input parameters that were specified in DEEPSOIL and PLAXIS are supplied in Table 4.7. It should be noted that the HS-Small model

(Brinkgreve et al. 2011) in PLAXIS and the Pressure Independent Multi-Yield Material model (Mazzoni et al. 2006) in DIANA and OpenSees used Masing Rules to model the hysteretic behavior of the soil. On the other hand, the Pressure Dependent Modified Kodner-Zelesko model (Hashash et al. 2015) in DEEPSOIL used a non-Masing formulation. Therefore, it was expected that the models may diverge for strong motions because the use of the Masing Rules can result in unrealistically large damping at large strains.

4.4.2 Average Response Spectrum

Similar to the section on linear analysis, the average spectral acceleration using the set of WUS motion are shown for the different damping cases considered. The format of the plots is the same as before. The average response spectrum from OpenSees are presented in the following sections. The response for each earthquake can be found in Appendix A.

4.4.3 Discussion of Nonlinear Results

As to be expected, the average nonlinear response spectrum (Figure 4.10 - Figure 4.13) was significantly reduced when compared against the linear counterpart. Furthermore, it was shown that there was no longer a clear peak in the response spectrum. Analogous to the case with linear analysis, the high frequency response was greatly diminished for the damping cases that included the stiffness proportional term (Figure 4.10). However, when only the mass proportional term was used, there was still significant contributions from the higher frequencies (Figure 4.11). Parallel to the linear analysis, frequency independent damping (Figure 4.13) was shown to be similar to the case where Rayleigh damping specified the damping to be 5% at the 1st and 3rd natural frequency (Figure 4.12). The only discernable difference between these two types of

damping was at frequencies greater than 10 Hz, where the spectral acceleration was higher for the frequency independent damping case.

Similar to the linear analysis, it was demonstrated that DIANA and OpenSees (which shared the same nonlinear model) were in close agreement. The only discrepancy between the results was at very high frequencies when using only mass proportional viscous damping. In this case, OpenSees would typically exhibit a peak that was higher than DIANA. For the other damping cases considered, this very high frequency was not present. Furthermore, DEEPSOIL and PLAXIS was shown to be in reasonable agreement and the observed differences were likely due to the differences in the implementation of soil nonlinearity.

4.5 Acknowledgements

This chapter contains slightly modified sections from the report by Li and coauthors: Earth Pressures on Deep Foundation Walls During Seismic Events (NRC Contract No.: NRC-HQ-12-C-04-0066). The dissertation/thesis author was the primary investigator and author of this chapter. Many people took part in the preparation of this report which include Jinchi Lu, Kyungtae Kim, Professor Ahmed Elgamal, Eun Hyun Park, Michael Musgrove, Professor Youssef Hashash, Nathaniel Wagner, Professor Nicholas Sitar, Boqin Xu, and Professor Ellen Rathje.

Table 4.1 Types of analyses performed for comparative study (20 Motions)

Software	**DEEPSOIL 6.0**	**DIANA 9.5**	**LS-DYNA R6.1.0**	**OpenSees 2.4.3**	**PLAXIS 2D AE**
Linear Elastic – Time Domain	X	X	X	X	X
Linear Elastic – Frequency Domain	X				
Nonlinear – Time Domain	X	X		X	X

Table 4.2 Soil properties

Profile Depth	30 m
Unit Weight	20 kN/m^3
Shear Wave Velocity	180 m/s
Halfspace	Rigid

Table 4.3 Analysis parameters

Software	**DEEPSOIL 6.0**	**DIANA 9.5**	**LS-DYNA R6.1.0**	**OpenSees 2.4.3**	**PLAXIS 2D AE**
Boundary Conditions	Model fixed in Z direction with prescribed acceleration in X direction	Equal degree-of-freedom constraints in X and Y directions, based fixed in Z direction with prescribed acceleration in X direction			Viscous vertical boundaries (non-reflecting), model fixed in Z direction with prescribed acceleration in X direction.
Element Type	N/A	20 Node Brick (CHX60, 3x3x3 Integration)	8 Node Brick (Solid, Constant Stress)	20 Node Brick (20NodeBrick, 3x3x3 Integration)	15 Node Triangular Element (12 Gauss Points)
Element Size	Vertical Height: 1.5 m	Vertical Height: 2 m			Element Area: 0.8996 – 2.032 m^2
Dimensions	1D	3D			2D
Mass Matrix	Lumped	Consistent	Lumped	Consistent	Consistent
Time Integration Scheme	Newmark with $\beta = 0.25;\ \gamma = 0.5$				
Time Step	Same as ground motion.				

Table 4.4 Viscous damping considered for analysis

Software	**DEEPSOIL 6.0**	**DIANA 9.5**	**LS-DYNA R6.1.0**	**OpenSees 2.4.3**	**PLAXIS 2D AE**
Stiffness Proportional Viscous Damping		X	X	X	
Mass Proportional Viscous Damping		X	X	X	
Rayleigh damping		X	X	X	X
Frequency Independent Damping	X			X	

Table 4.5 Soil models used in nonlinear site response analyses

Software	**DEEPSOIL 6.0**	**DIANA 9.5**	**LS-DYNA R6.1.0**	**OpenSees 2.4.3**	**PLAXIS 2D AE**
Soil Model	Pressure Dependent Modified Kodner-Zelesko	Pressure Independent Multi-Yield Material	N/A	Pressure Independent Multi-Yield Material	HS-Small

Table 4.6 Target modulus reduction and damping curves used for the nonlinear analysis

Shear Strain (%)	G/Gmax
0.0001	1
0.0002	1
0.0003	0.999
0.0004	0.995
0.0005	0.99
0.0006	0.985
0.0008	0.971
0.001	0.96
0.0015	0.935
0.002	0.913
0.003	0.873
0.004	0.84
0.005	0.815
0.006	0.79
0.008	0.7455
0.01	0.71
0.015	0.637
0.02	0.582
0.03	0.495
0.04	0.435
0.06	0.345
0.1	0.25
0.15	0.19
0.2	0.155
0.3	0.112
0.4	0.089
0.6	0.063
1	0.04

Shear Strain (%)	Damping (%)
0.0001	2.1
0.0003	2.11
0.0006	2.2
0.001	2.3
0.002	2.5
0.003	3.2
0.006	4.286
0.01	5.357
0.02	7.857
0.03	9.821
0.06	12.857
0.1	15.357
0.2	18.571
0.3	20
0.4	20.893
0.6	22.321
1	23.929

Table 4.7 Parameters used to match closely with target modulus and damping curves

DEEPSOIL	
Parameters	**Value**
Ref. Strain (%)	0.048
Ref. Stress (MPa)	0.18
Beta	1.575
s	0.885
b	0
d	0
MRDF formulation	Darendeli (2001)
P1	0.58
P2	0.046

PLAXIS	
Parameters	**Value**
m	0.544
E_{50}^{ref} (kN/m^2)	1.50E+04
E_{oed}^{ref} (kN/m^2)	1.50E+04
E_{ur}^{ref} (kN/m^2)	5.00E+04
G_0^{ref} (kN/m^2)	9.40E+04
$\gamma 0.7$	1.50E-04
c'ref (kN/m^2)	0
phi (degrees)	34
psi (degrees)	4.25

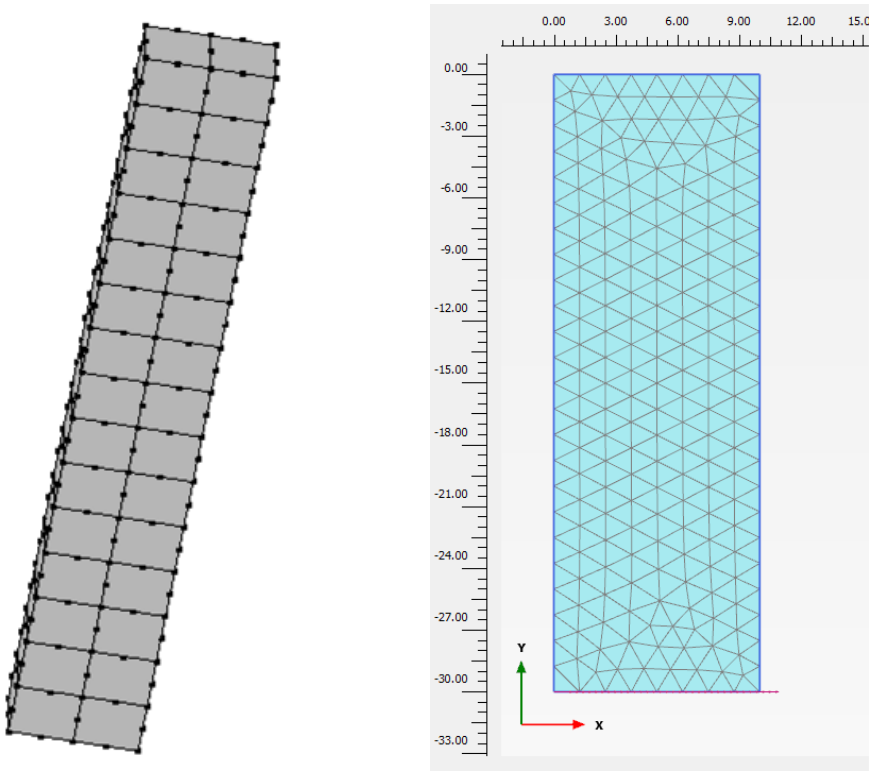

(a) (b)

Figure 4.1 Mesh used in this comparison: (a) OpenSees (DIANA and LS-DYNA has a very similar mesh as well), (b) PLAXIS

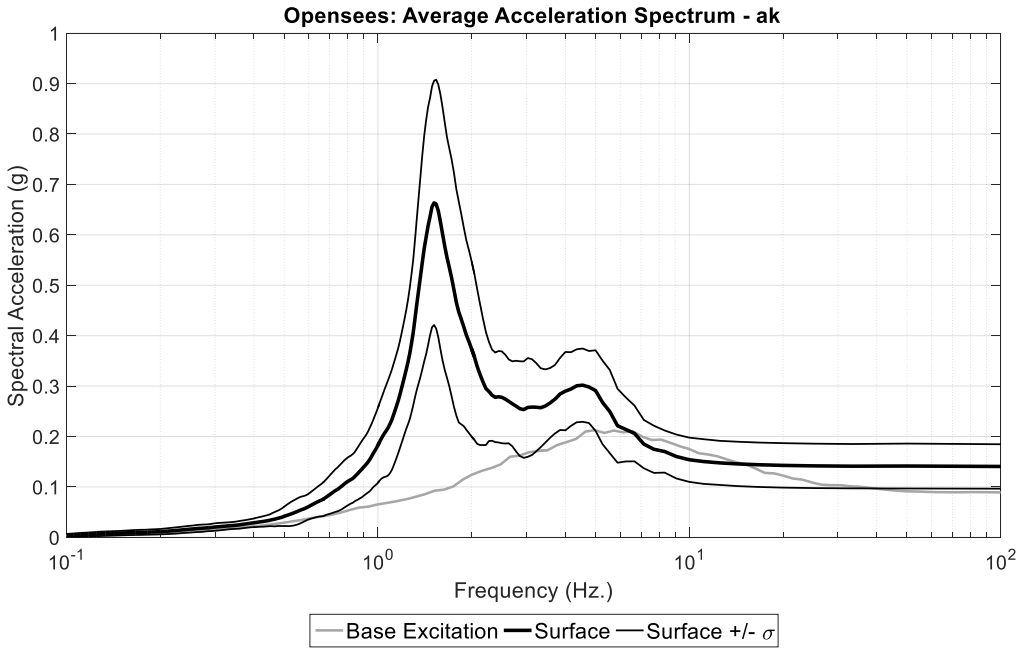

Figure 4.2 Envelope of average acceleration spectrum for analysis using only stiffness proportional damping in OpenSees (Linear)

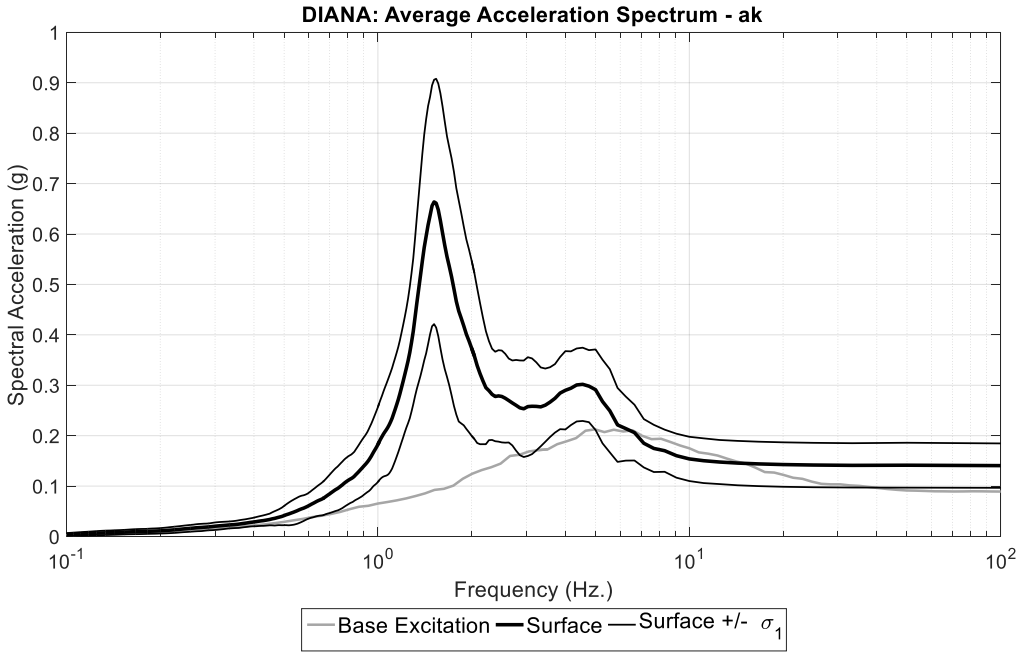

Figure 4.3 Envelope of average acceleration spectrum for analysis using only stiffness proportional damping in DIANA (Linear)

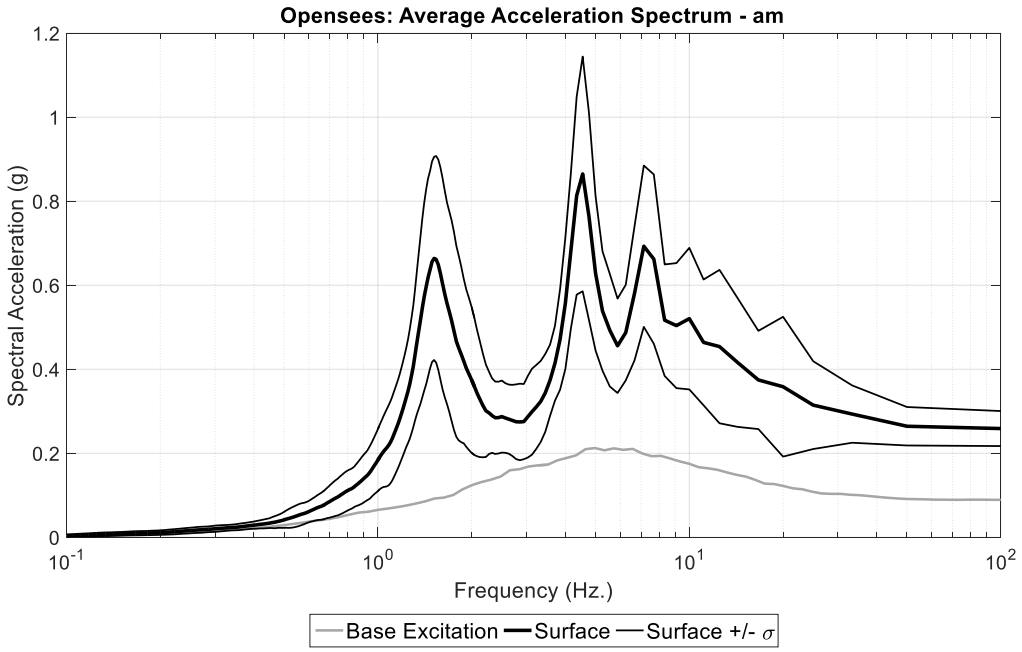

Figure 4.4 Envelope of average acceleration spectrum for analysis using only mass proportional damping in OpenSees (Linear)

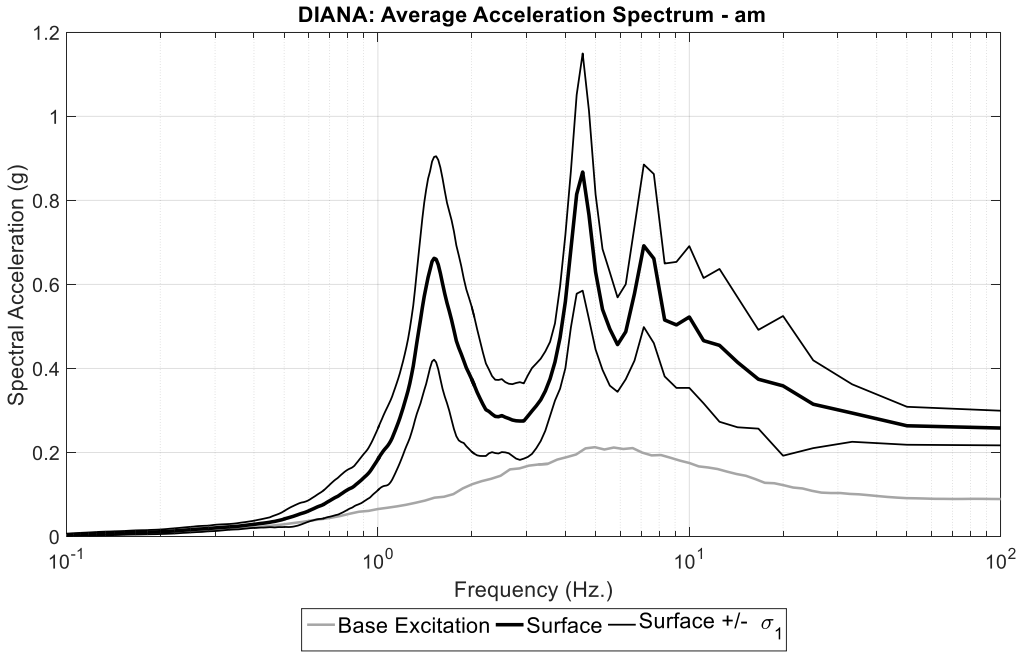

Figure 4.5 Envelope of average acceleration spectrum for analysis using only mass proportional damping in DIANA (Linear)

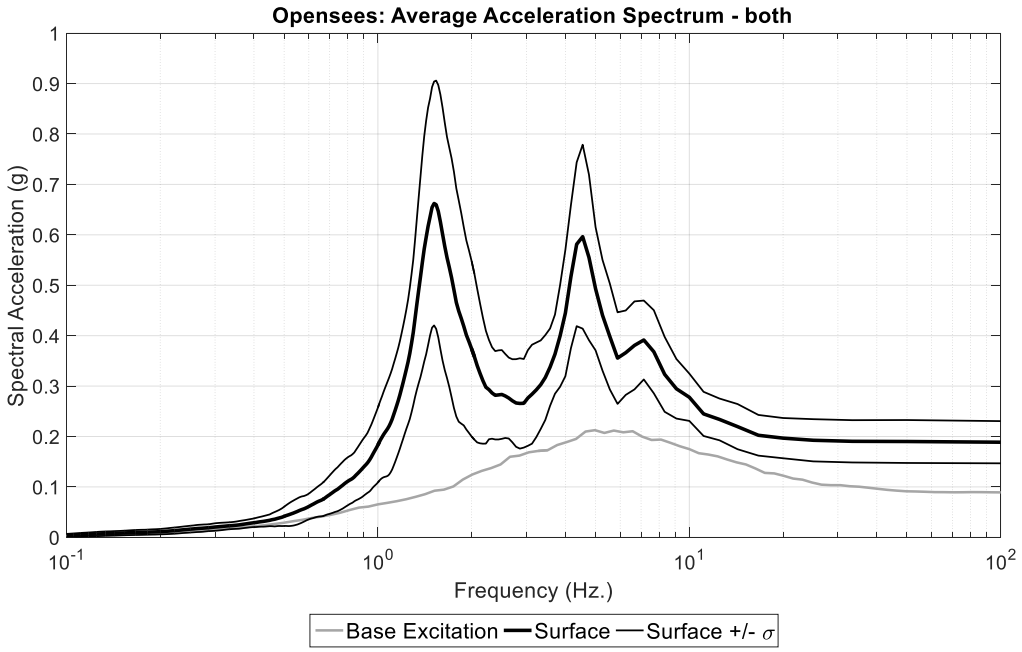

Figure 4.6 Envelope of average acceleration spectrum for analysis using both mass and stiffness proportional damping in OpenSees (Linear)

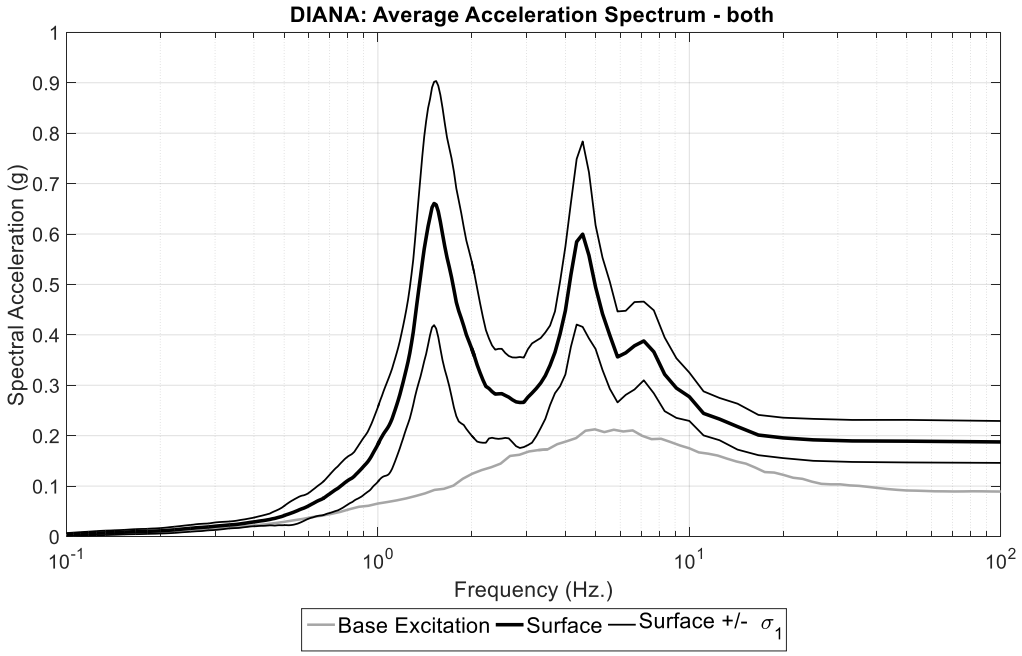

Figure 4.7 Envelope of average acceleration spectrum for analysis using both mass and stiffness proportional damping in DIANA (Linear)

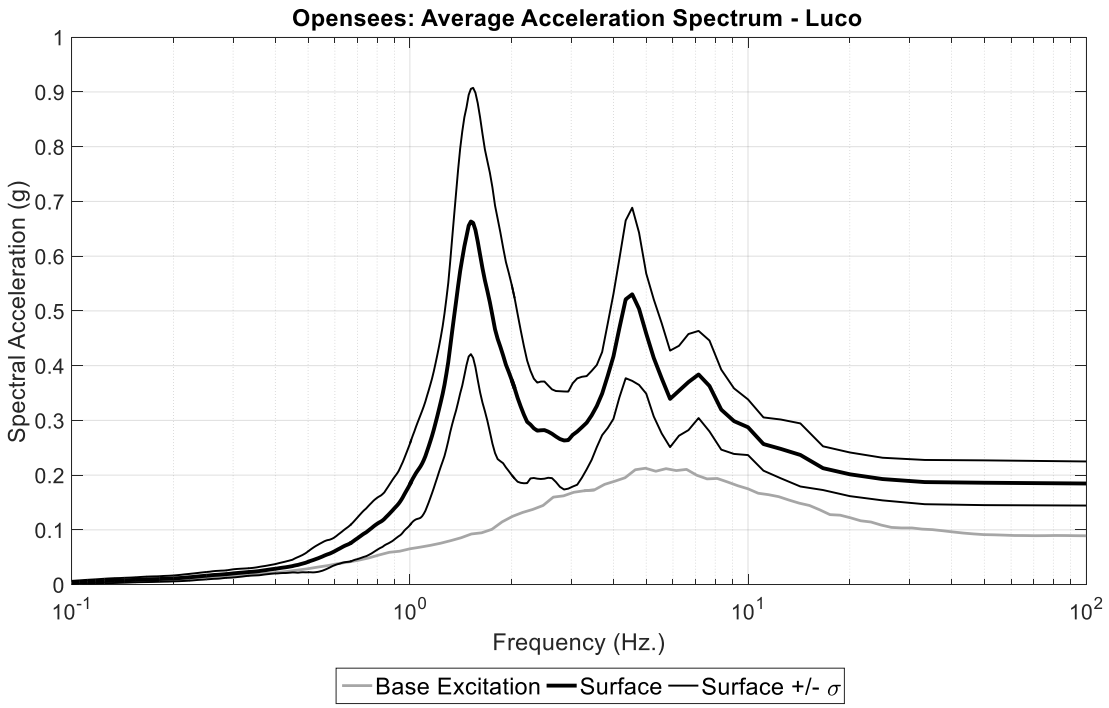

Figure 4.8 Envelope of average acceleration spectrum for analysis using Luco's damping (Luco 2008) in OpenSees (Linear)

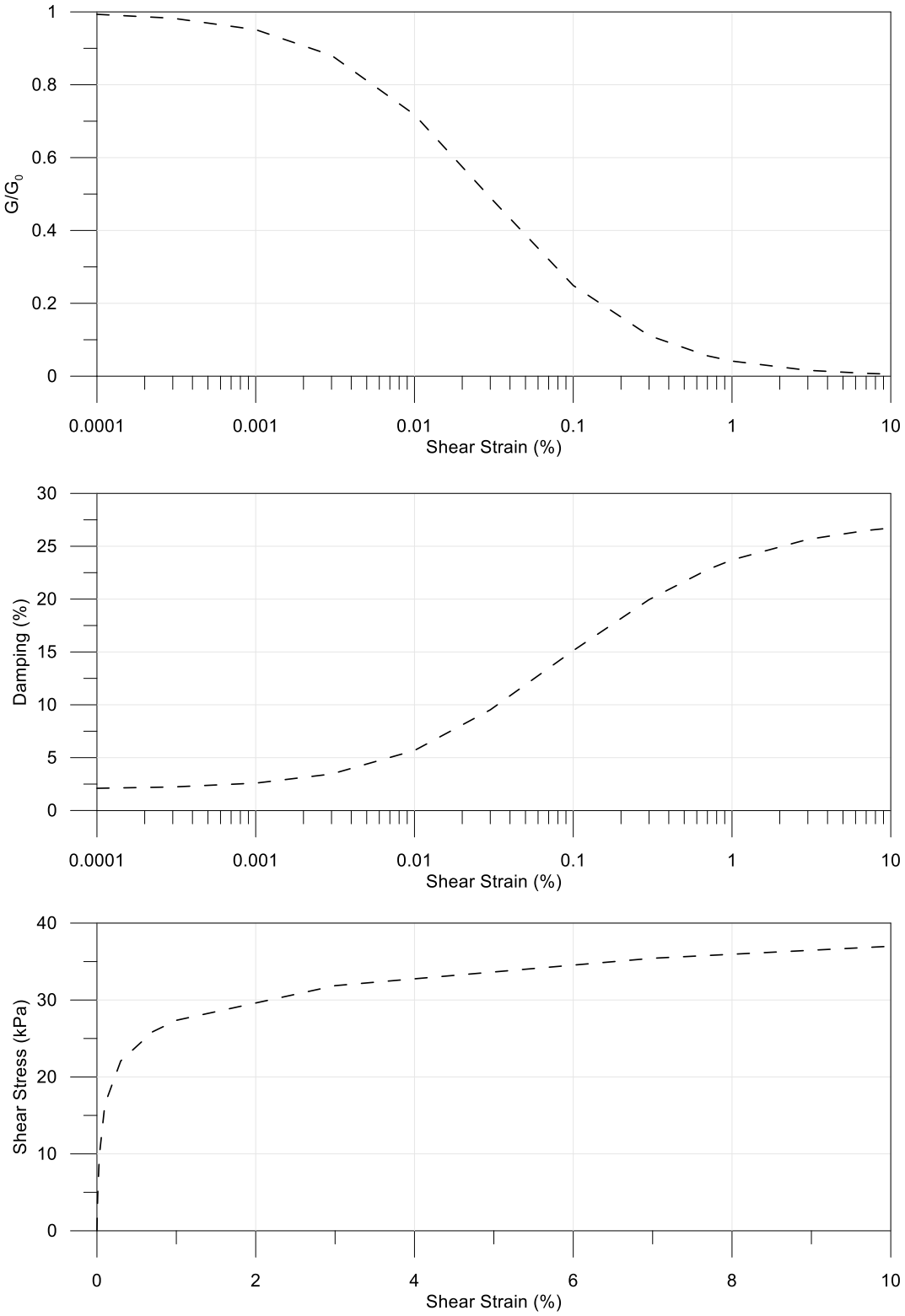

Figure 4.9 Dynamic properties used in nonlinear site response analyses

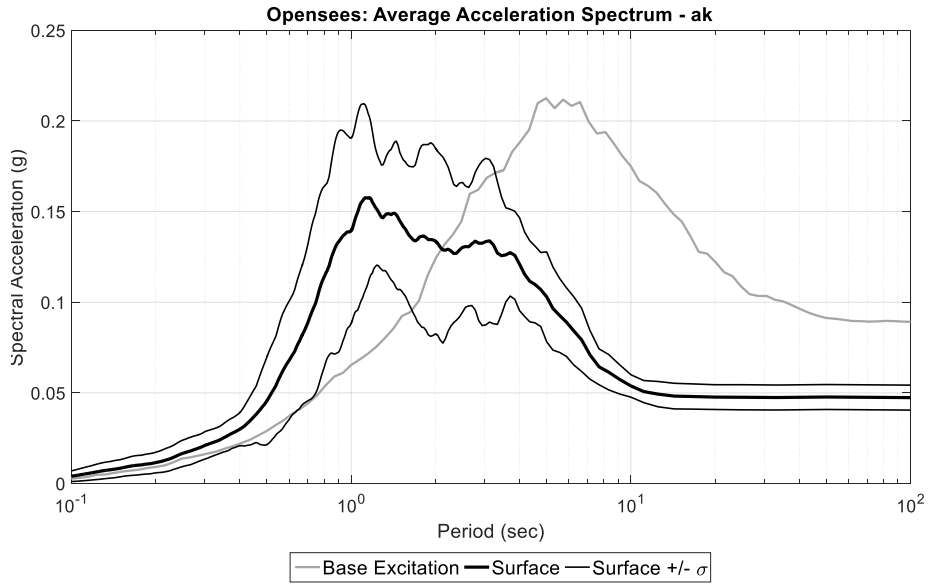

Figure 4.10 Envelope of average acceleration spectrum for analysis stiffness proportional damping in OpenSees (Nonlinear)

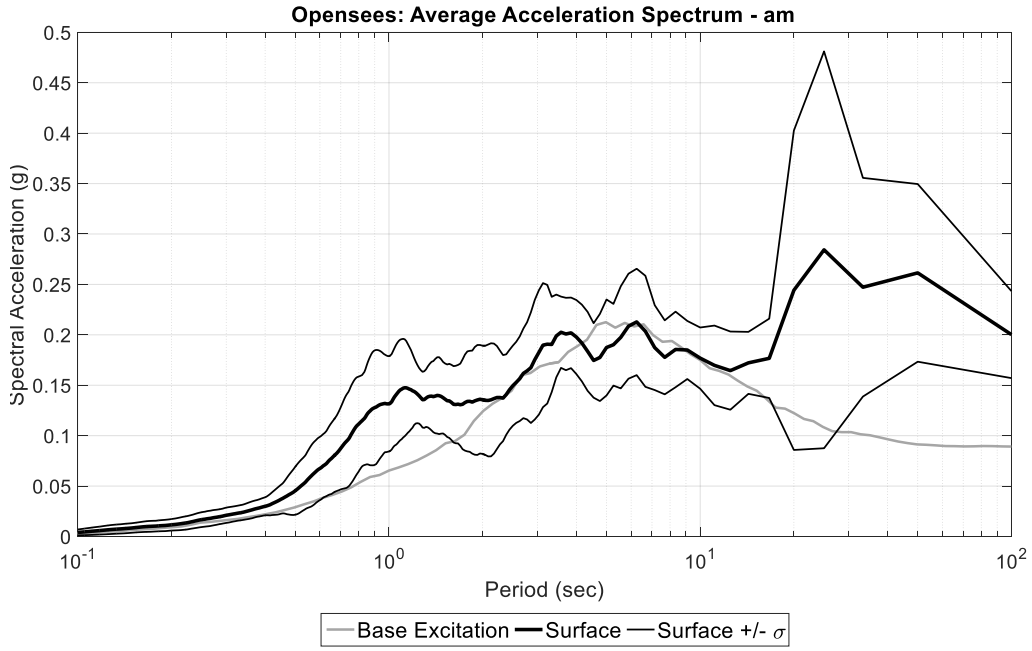

Figure 4.11 Envelope of average acceleration spectrum for analysis using mass proportional damping in OpenSees (Nonlinear)

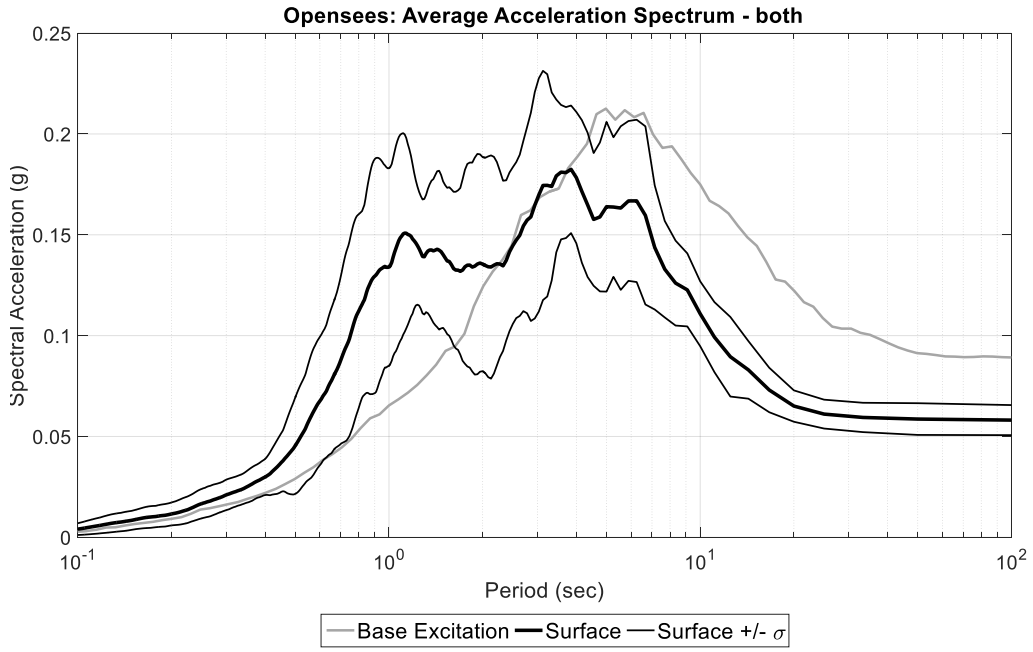

Figure 4.12 Envelope of average acceleration spectrum for analysis using both mass and stiffness proportional damping in OpenSees (Nonlinear)

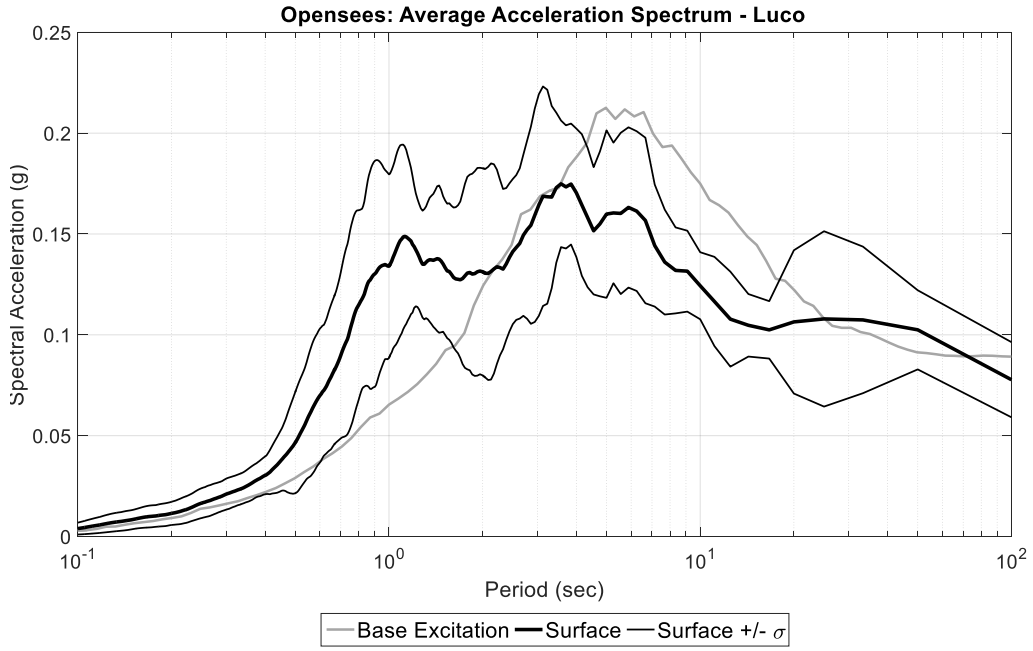

Figure 4.13 Envelope of average acceleration spectrum for analysis using Luco's damping (Luco 2008) in OpenSees (Nonlinear)

Chapter 5

Three-dimensional Seismic Response of a Large Embedded Structure and Induced Earth Pressure

5.1 Abstract

For large embedded structures, soil structure interaction (SSI) plays a major role in dictating the overall seismic response. In light of recent strong seismic excitation affecting such structures, three-dimensional (3D) response as well as nonlinear (NL) soil behavior are among the areas of increased interest. As such, this paper presents a series of 3D NL numerical studies conducted to shed more light on the involved SSI mechanisms. In this parametric study, consideration is given to factors such as the effect of soil own-weight stress-state, the structure-ground interface properties, and the intensity of seismic excitation. For comparison, additional time domain simulations explore the use of linear soil (LS) properties derived from an equivalent linear (EL) site-response analysis. For the purposes of this study, the structure is taken to be

cylindrical and fully embedded into the ground. Depending on the level of attained nonlinear response, influence of the following modeling considerations are discussed: i) employing the NL versus LS formulation, ii) initial own-weight lateral earth pressure stress-state, and iii) the soil-structure interface characteristics. Accelerations along the profile of the structure, as well as earth pressure on the walls and floor are among the main parameters of interest. In the free-field it was observed that the LS representation adequately matches the NL acceleration response up to frequencies of about 10 Hz Furthermore, both formulations generally resulted in remarkably close estimates of the structural response. Nevertheless, exceptions include: i) wall lateral earth pressure and floor pressure were noticeably different, and ii) the potential change in the soil initial stress-state due to seismic excitation was manifested only in the NL modeling scenarios.

5.2 Introduction

Equivalent linear (EL) codes such as SASSI (Lysmer et al. 1981) are widely used to perform soil-structure interaction (SSI) analysis and have been shown to be of significant value for low to moderate levels of earthquake excitation (Ganev et al. 1997; Xu et al. 2008). However, in the aftermath of recent events such as that of the Fukushima Daiichi nuclear power plant incident (Kurukawa 2013), beyond-design basis earthquake excitation has been a concern of growing importance. With increasing demands, nonlinearity due to the soil and soil-structure interface might be expected to play a larger role, mechanisms that the EL approach would face additional challenges in capturing. As such, there has been a growing interest in nonlinear (NL) analysis techniques (Kammerer and Jeremic 2013; Coleman et al. 2016; Solberg et al. 2016), which may be necessary in order to adequately assess the seismic performance of such large embedded facilities.

In this area of research, numerous studies have been conducted to illustrate the underlying mechanisms governing SSI (Hagiwara and Kitadas 2005; Subramanian 2005; Koyanagi et al. 2009; Tabatabaie et al. 2009; Suzuki et al. 2013; Bolisetti and Whittaker 2015). In an effort to evaluate current practice, Xu et al. (2008) examined the computed response of deeply embedded $1/10^{th}$ scale models of a nuclear reactor structure. From their study, the capabilities of the NL and EL numerical tools LS DYNA (LSTC 2001) and SASSI2000 (Lysmer et al. 1999) were evaluated for weak earthquake excitation where significant nonlinearity is not expected. Furthermore, the nonlinear soil-structure interface characteristics were examined by Xu et al. (2006) and Saxena and Paul (2012). It was concluded (Xu et al. 2006) that separation, slip, and uplift diminished with embedment, and were negligible for deeply embedded structures (Xu et al. 2006; Saxena and Paul 2012).

More recently, efforts have been underway to conduct fully nonlinear studies (Solberg et al. 2016, Sinha et al. 2017, Baltaji et al. 2017, Numanoglu et al. 2017, Bolisetti et al. 2018). In these studies, soil behavior was captured by a 3D pressure-independent Masing-type hysteresis model, and spectral accelerations were presented and compared to SASSI-type responses (Solberg et al. 2016, Bolisetti et al. 2018). In addition, the novel domain-reduction approach (Bielak et al. 2003) for handling wave propagation boundary effects is being developed and implemented in such pioneering studies.

Building on these earlier studies, a 3D parametric analysis was conducted, in which a pressure-dependent soil modeling formulation is employed (Yang et al. 2003). Particular attention is dedicated to the seismically induced changes in earth pressure on the walls and floor of the embedded structure. As such, an effort is made to evaluate the relative significance of: i) employing the NL versus LS modeling approaches, ii) the lateral earth pressure initial stress-state

due to own weight, and iii) the soil-structure interface characteristics. On this basis, the following sections: i) outline the employed numerical modeling techniques, ii) present the results of the conducted numerical simulations, and iii) summarize the main conclusions of this study.

5.3 Computational Framework

5.3.1 Three-Dimensional Finite Element Model

The open source finite element (FE) framework OpenSees (Mazzoni et al. 2006), was employed to simulate the seismic response of a large cylindrical stiff structure fully embedded into the ground (Figure 5.1). Symmetry considerations allow for a half mesh configuration, as seismic motion was only imparted in the global X-direction. The soil domain and the structure were modeled using 3D eight node bricks elements.

The dimensions of the FE mesh were chosen to be sufficiently large in order to minimize impact of the boundaries on the structural response. Consequently, the outer perimeter of the mesh essentially replicates the free-field behavior. As such, all lateral boundary nodes at any given depth were restrained to undergo the same motion. To reduce depth of the soil domain, a dashpot wave-transmitting boundary (Lysmer and Kuhlemeyer 1969) was employed at the base of the mesh. The dashpots deployed along this boundary were defined based on postulated bedrock properties with a mass density of 2000 kg/m^3 and shear wave velocity (V_s) of 700 m/s.

5.3.2 Seismic Excitation

To illustrate the response mechanisms of interest, seismic base excitation was defined by the 1952 Taft Earthquake, Kern County N21E component (Figure 5.2), as employed in an earlier study by Seed and Idriss (1973). The motion was treated as “outcrop”, with half the amplitude

applied as a nodal force at the base of the mesh (Lysmer and Kuhlemeyer 1969). Furthermore, to evaluate the impact of increasing shaking amplitude, this record was scaled by a factor of up to 4 times.

5.3.3 Soil Material Properties

Soil properties were defined to model the behavior of a medium dense sand with a corrected Standard Penetration Test (SPT) blow count $(N_1)_{60}$ of 15 (Sabatini et al. 2002). To facilitate comparison, low-strain shear stiffness and the shear stress-strain backbone curve were common to the NL and EL representations as described below.

5.3.3.1 Nonlinear Soil Representation

The PressureDependMultiYield (PDMY) material model (Yang et al. 2003) was used to simulate the NL soil response (Figure 5.3a). This model is based on multi-surface plasticity theory and accounts for dependence of the low-strain shear modulus (G_{max}) and the shear strength (s) on mean confinement (σ_m; see Table 5.1). At any given initial confinement (σ_m), the hyperbolic relationship (Konder and Zelasko 1963) defines the NL soil shear stress-strain response (Figure 5.3b):

$$\tau = \frac{G_{max}\gamma}{1 + \frac{\gamma}{\gamma_r}} \tag{1}$$

where γ is shear strain, and the constant γ_r is defined such that the shear strength s is reached at a user specified γ_s (3% in this study), viz:

$$\gamma_r = \frac{s\gamma_s}{G_{max}\gamma_s - s} \tag{2}$$

5.3.3.2 Definition of LS material properties

For comparison, employing the same FE mesh (Figure 5.1), additional 3D time domain LS simulations were conducted using linear material properties derived from an a priori EL free-field site-response analysis. For that purpose, 1D EL Shake91 (Idriss and Sun 1993) simulations were conducted, in order to obtain the linear site properties that are compatible with the imparted level of base excitation. For these Shake91runs, soil shear response was represented using the same G_{max} and hyperbolic stress-strain relationship (Figure 5.3b) mentioned above (Table 1). On this basis, modulus reduction (G/G_{max}) and damping curves (Ishihara 1996) were obtained. For illustration, the G/G_{max} and damping curves at a representative confinement of 101 kPa (1 atm) are shown in Figure 5.3c and d. In these EL runs, the shear strain ratio was set to the commonly employed value of 0.65. An additional 2% damping was included to account for the Rayleigh damping employed in the conducted NL analyses as discussed below. As such, the LS soil properties derived from Shake91 for each investigated level of shaking are presented in Figure 5.4.

5.3.4 Structural Model and Soil-Structure Interface

For the purpose of this study, a representative geometric configuration (Figure 5.1) was adopted, patterned after an early 2D investigation by Seed and Idriss (1973). The structure was modeled as cylindrical with half the soil mass density (as an equivalent overall density of a basement structure), and height and radius of 22.68 m and 22 m respectively. Stiffness was defined such that the structure is essentially rigid relative to the surrounding soil. To enable potential separation at the soil-structure boundary, zeroLength elements were employed to connect the structure to the adjacent soil. As such, this soil-structure interface was prescribed simply to be rigid in compression, with no resistance to tensile load.

5.3.5 Computational Procedure

Prior to seismic excitation, gravity induced own-weight was applied. To simplify the interpretation of dynamic response, own-weight was imposed such that a vertical-horizontal principal stress state was achieved throughout (Figure 5.5). As such, the resulting lateral stress is uniform at any given depth, with vertical stress varying according to the own-weight of the soil and the structure (Figure 5.5b). Based on the confinement (σ_m) at any location, the soil constitutive model parameters were systematically defined (Table 5.1) for use during seismic excitation.

Dynamic response of this FE model was computed using the TRBDF2 integrator, a combination of the trapezoidal and 3 point backward Euler schemes (Bathe 2007). This integrator attempts to conserve energy and momentum in the model. The implicit analysis was conducted with a step size of 0.005 secs for 10848 time steps, corresponding to 54.26 seconds of seismic response.

To supplement energy dissipation from the NL hysteresis response, a low level of additional viscous Rayleigh damping was employed. For that purpose, the mass and stiffness proportional terms were defined to provide viscous damping of about 2% in the first few modes of the model (in the range of 1.56 *Hz* – 4.20 *Hz*). As mentioned above, this damping was included as the LS low strain value as shown in Figure 5.3d and Figure 5.3b.

5.4 Analysis Results

5.4.1 Free-Field Response

In the results presented below, it was confirmed that response along the FE mesh lateral boundaries (Figure 5.1) was virtually identical to that reproduced by the corresponding 1D soil-

column FE models. As such, it is concluded that free-field behavior is indeed reproduced along these boundaries.

5.4.1.1 Acceleration

At the free-field (lateral boundaries of the FE mesh), peak acceleration computed at the soil base ranged from about 0.10 g - 0.40 g Figure 5.6) for the scaling factors considered. The corresponding NL peak ground acceleration (PGA) was about 0.20 g - 0.70 g (Figure 5.6), with the largest amplification ratio observed for the weakest motion. When comparing to the EL results (Figure 5.6), it can be seen that the response was quite similar for the weaker motion and deviates somewhat with the increase in input shaking amplitudes.

The corresponding response spectra are shown in Figure 5.7. For the weak motion (x1), major amplification is seen around the first resonance of the soil profile (about 1.5 Hz). Some amplification is visible as well at higher frequencies. With the increase in shaking amplitudes, amplification is less pronounced, only appearing around the first resonance and shifting towards a slightly lower frequency of about 1.2 Hz.

It may be observed that the EL results are quite close, but with a tendency to underestimate the response at high frequencies when compared to NL. This phenomenon is a consequence of the EL approach employing the relatively high damping ratio that corresponds to peak shear strain to compute the entire earthquake response (Schnabel et al. 1972), and is consistent with earlier observations (e.g., Yoshida et al 2002). Nevertheless, along the entire depth, peak acceleration (Figure 5.8a) computed using LS was generally close to that of the NL counterpart.

5.4.1.2 Peak Soil Shear Stress and Strain

With the increase in level of shaking, partially as a consequence of the LS secant shear modulus formulation, it was observed that peak LS shear strain (Figure 5.8b) tended to be lower and peak stress (Figure 5.8c) tended to be higher than the NL counterpart. Moreover, in accordance with the observations of Bolisetti et al. (2014), the difference becomes more significant when peak strains exceed the value of about 0.1% (for instance, the 0.2% to 0.3 % range of strain in Figure 5.8b).

5.4.2 Soil-Structure Interaction

5.4.2.1 Acceleration

As illustrated in Figure 5.9, the computed acceleration of the structure using NL and LS were even closer compared to the free-field soil response (Figure 5.6). As demonstrated by Figure 5.6 and Figure 5.9, there was a large reduction in the structure's roof acceleration compared to that of the adjacent free-field ground surface. In fact, peak acceleration of the roof was rather similar to that of the base at the depth of about 23 m (Figure 5.10). In addition, peak ground acceleration gradually increased with distance away from the structure (Figure 5.10), reaching the maximum approximately 20 m meters away from the structure (~ depth of embedment of the structure).

Response spectra of the structure (Figure 5.11) generally peaked near the fundamental frequency of the free-field (Figure 5.7) and spectral response at the top of the structure was similar to that at its base (i.e., motion was not amplified due to the rigid nature of the structure). The structure, being deeply embedded and essentially rigid, displays a response (Figure 5.12) that is: a) highly influenced by the significantly lower levels of seismic excitation at the 23 m embedment

depth, and b) relatively devoid of high frequency amplification, partially due to an averaging mechanism of the ground response along its embedment depth.

5.4.2.2 Response at Peak Lateral Pressure on Structure

Figure 5.13 displays the 4x NL and LS displaced configuration at the instant of peak NL dynamic lateral pressure. At this instant, the soil near ground surface is generally: i) exerting additional pressure on the left side of the structure (180° orientation), and ii) relieving pressure and separating from the structure on the right side (0° orientation). Further, it may be noted (Figure 5.13) that the LS displacements are generally lower.

5.4.2.3 Floor state of stress

With this displaced configuration in mind, Figure 5.14 presents the change in vertical and lateral stress under the footprint of the structure. At the toe area, significant increase in vertical stress is seen as expected for this particular deformed configuration Figure 5.13). Conversely around the heel zone on the other side, vertical stress is fully relieved over a slim section of the structure's base (facilitated by the no tension boundary condition between the structure and the surrounding soil). Along with this vertical stress state, significant lateral tangential resistance is seen along the base of the structure, peaking at the toe and gradually diminishing towards the heel.

It can be seen that the NL and LS scenarios result in noticeable differences in the level of attained peak stresses. Furthermore, compared to the LS case, the NL case appears to result in a more irregular stress distribution pattern, likely influenced by the soil stiffness and strength nonlinearity and pressure dependence (Fig. 3a) of the employed NL model formulation.

5.4.2.4 Lateral Earth Pressure

In terms of total lateral pressure during this time step, changes referenced to the static state are presented in Figure 5.15. It can be seen that the main change in lateral pressure occurs roughly within a 45-degree zone measured from the 0 degree to the 180 degree orientation (in this ½ mesh configuration), with (Figure 5.13): i) increase along the 180 degree side where the soil is pushing on the structure, ii) increase near the bottom of the 0 degree side, where the structure is pushing on the soil, and iii) decrease along the upper zones of the zero degree side where the soil is moving away from the structure. Within the 45 degree to 135 degree zone, the pressure rapidly decreases until the 90° orientation, where the pressure barely changed compared to the static state.

In general, the pressure distribution pattern was similar for NL and LS, except for the 0°-45° orientation zone, where higher NL stresses prevailed near the toe. At this highly stressed location, the NL pressure dependent soil response (Fig. 3a) might have contributed to this outcome in view of the associated increase in lateral confinement. Such behavior is only exhibited by the NL model, and cannot be captured by the LS formulation.

5.4.2.5 Lateral Earth Pressure Force

Changes in lateral load on the structure may be portrayed in the form of the resultant earth pressure force. As shown in Figure 5.16, this resultant force and ratio of point of action to the height, depict an oscillation pattern that closely follows that of the structure's displacement and rotation. In the shown 0 and 180 degree orientations, changes in resultant force and point of action are seen to be reciprocal along these two opposite sides, in that when one is decreasing, the other is increasing and vice versa. For the 1x case, peak force increased by as much as 10 %, and point of action of the resultant force changes mainly in the narrow band of about 1/3 of the height. For

the 4x scenario, resultant force increased by as much as about 50 %, with the corresponding point of action moving upwards around 40% of the height. Instance of reduction in total force were generally associated with the lowest point of action at around 20 % of the height.

5.4.3 Influence of the Soil Initial Static Stress State

So far, the presented results were based on an initial static lateral stress state where own-weight soil horizontal stress was approximately equal to the vertical stress (i.e., for application of the static own weight, the initial static lateral coefficient of earth pressure K_0 = 1.0 approximately). In this section, the influence of having a lower coefficient of earth pressure is highlighted. For that purpose, a representative normally consolidated K_0 =0.5 (Lambe and Whitman 1969) is adopted for the initial own-weight application phase.

In general, seismic excitation will result in densification of such normally consolidated cohesionless soil, gradually causing the lateral stress to approach the soil own-weight vertical stress (Youd 1972). As such, change in lateral pressure in the free-field is shown in Figure 5.17 for the two cases of explored K_0. For the NL K_0 = 0.5 scenario, lateral pressure is seen to increase due to seismic excitation, approaching its vertical counterpart for the 4x shaking case. As expected, no such change takes place for the linear LS scenario.

5.4.4 Impact of Soil-Structure Interface

To investigate the significance of modeling the soil-structure interface, additional runs were conducted with the soil and structure fully bonded. Despite occurrence of some separation in the 4x shaking cases (Figure 5.13 and Figure 5.14), the fully bonded cases did not display any appreciable change in the computed earth pressures and accelerations for this fully embedded modeling scenario.

5.5 Discussion

In this section, considerations related to the following issues are discussed: i) sensitivity of the results to mesh refinement and input motion characteristics, ii) potential influence of modeling own-weight construction stages, and iii) response of the embedded structure using a simplified spring-dashpot models. For that purpose, additional simulations were conducted as discussed in the Appendix C. On this basis, the main outcomes may be summarized as:

1. .Further mesh refinement did not lead to appreciable changes in the reported acceleration response of the ground or the structure. As such, the characteristics reported above concerning acceleration response of the top of the structure in terms of reductions in amplitude and high frequency content (relative to the free field response), are not influenced by the employed mesh resolution. This was also noted when using other input ground motions as detailed in the Appendix.
2. Numerical simulation of construction stages did not appreciably influence the structure's acceleration response. However, this concern does affect the profile of earth pressure around the structure. In the conducted study, variation of the order of about 25 % in peak and/or residual values were observed, and closer scrutiny is warranted (based on actual construction staging scenarios when available).
3. Employing the computed motion at the base of the structure, the relatively simple rotational spring-dashpot values of Gazetas (1991) resulted in an acceptable match of the roof seismic response although the spectral acceleration within 2 - 4 Hz was not replicated. As such, effort towards further refinement, where motion of the free-field along the height of the structure is included such as the more recent studies of Tsigginos et al. (2008) and Assimaki and Gazetas (2009) should be explored to further improve the matching.

5.6 Summary and Conclusions

In order to highlight a number of salient response characteristics associated with SSI for a large embedded structure, a parametric study was undertaken. The employed modeling techniques and derived material properties were presented. The free-field response and that of the structure were examined using NL and LS formulations. For the cases studied, and employed numerical formulations, it was shown that NL and LS responses were similar, but some aspects of NL response were not captured by LS. Overall, the following conclusions may be drawn:

1. Consistent with previous findings, it is observed that NL and LS properties resulted in close estimates of peak acceleration, and soil stress and strain response for low levels of shaking. The difference between the two analysis methods was shown to become more significant as peak shear strains exceeded 0.1%. In particular, LS models significantly underestimated the high frequency content observed in the free-field acceleration.
2. Due to the relative rigidity of the structure compared to the surrounding soil, acceleration at the top of the structure (ground surface) was: i) much reduced when compared to free-field, becoming quite similar to that at the structure's base, and ii) relatively devoid of high frequency amplification, partially due to an averaging mechanism of the ground response along its embedment depth.
3. Lateral pressure near the toe of the structure was especially high for the NL case, possibly due to the increased soil confinement at this location, and the associated pressure-dependent increase in soil stiffness and strength.
4. For static own-weight soil state of stress around the normally consolidated scenario (e.g., Ko = 0.5 or so), seismic excitation might result in higher level of lateral confinement being

reached at the end of shaking. As the shaking acceleration increases in amplitude and/or duration, the static lateral stress magnitude may gradually approach its vertical counterpart.

5. When allowed, separation near ground surface at the soil-structure interface might occur. However, it was observed that this mechanism was of little consequence on the overall structural response for this particular geometric configuration.
6. Along the structure's base, the initial static vertical stress might become fully relieved locally during a strong shaking excursion. Potentially, some level of final permanent structural displacement might ensue, horizontally and vertically, as might be predicted by a NL modeling formulation.
7. Overall, 3D LS and NL analyses such as those conducted herein, require close attention in terms of all aspects involved in their numerical implementation (meshing and element-type details, soil modeling properties, and employed time integration algorithm). Familiarity with the involved salient response characteristics is advisable. In this regard, starting with simpler scenarios (e.g., such as 1D site response modeling), and gradually moving towards the desired 3D configuration will provide insights as to influence and significance of the various implemented mechanisms.

5.7 Acknowledgement

This research was partially funded by the US Nuclear Regulatory Commission with Dr. Thomas Weaver as the program Manager. Furthermore, this work used the Extreme Science and Engineering Discovery Environment (XSEDE) Stampede at Texas Advanced Computing Center (TACC) through allocation BCS170005. This chapter has been accepted for publication by Journal of Geotechnical and Geoenvironmental Engineering ASCE and titled as "Three-dimensional Seismic Response of a Large Embedded Structure and Induced Earth Pressure". The

dissertation/thesis author was the primary investigator and author of this paper. Professor Elgamal and Dr. Kim cooperated as co-authors to this journal paper.

Table 5.1 Soil material properties

Site Classification	Medium Dense Sand
Normalized SPT blow count $(N_1)_{60}$	15
Soil mass density ρ	2000 kg/m^3
[1]Shear Modulus G_{max}	$G_{max} = 4376.3(N_1)_{60}^{0.333}(\sigma_m)^{0.5}$ (units in kPa; Seed et al. 1986)
Shear Wave Velocity V_s	$V_s = \sqrt{G/\rho}$
[2]Friction Angle ϕ	35.2°
Shear Strength s	$s = \sigma_m \sin(\phi)$
Poisson's ratio ν	0.35

[1] $\sigma_m = (\sigma_v + 2\sigma_h)/3$, where σ_v and σ_h are the vertical and horizontal stresses respectively

[2] $\phi = \sqrt{15.4(N_1)_{60}} + 20°$ (Sabatini et al. 2002)

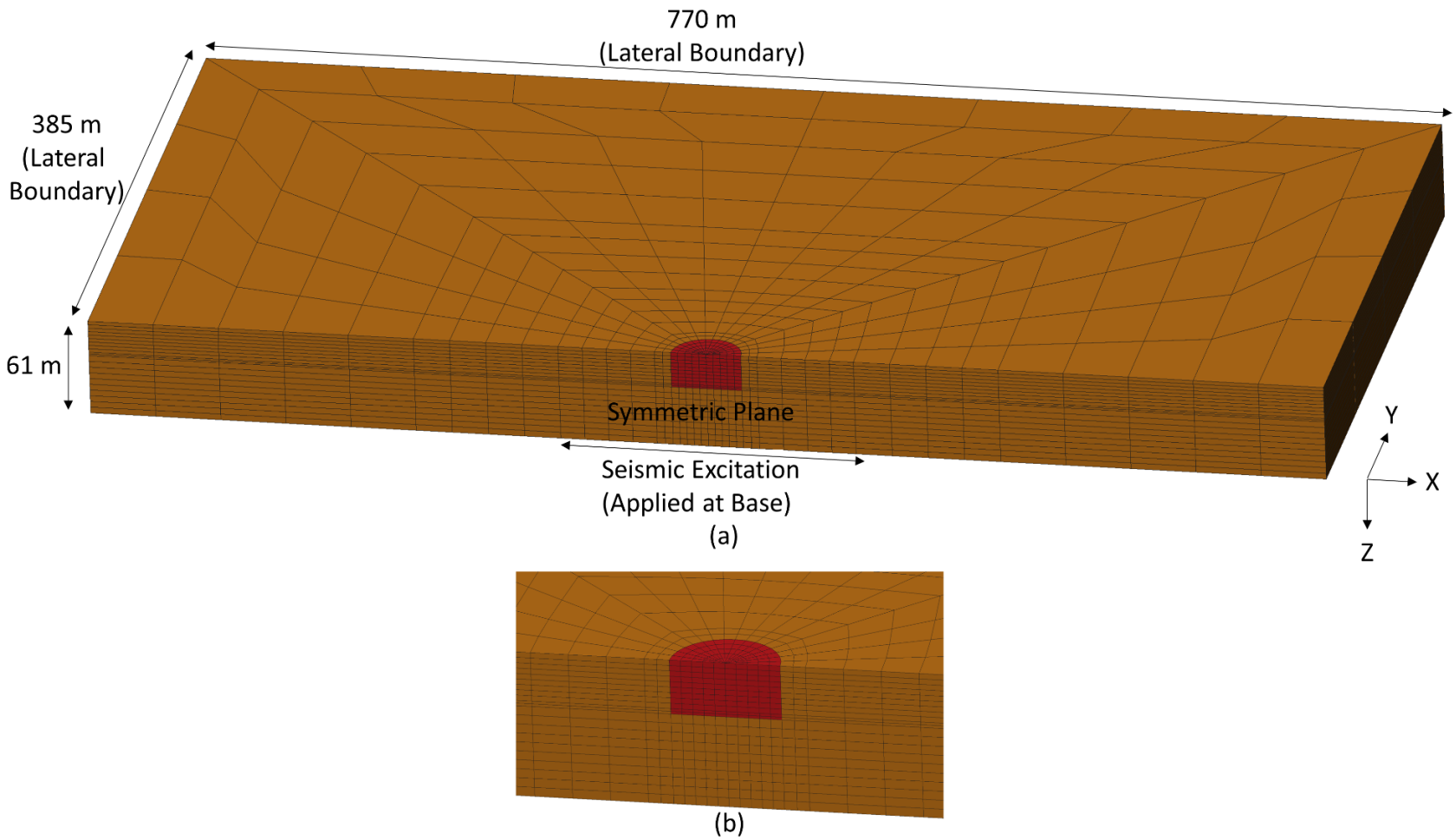

Figure 5.1 3D FE model with fully embedded cylindrical structure; (a) full model; (b) close-up view of structure

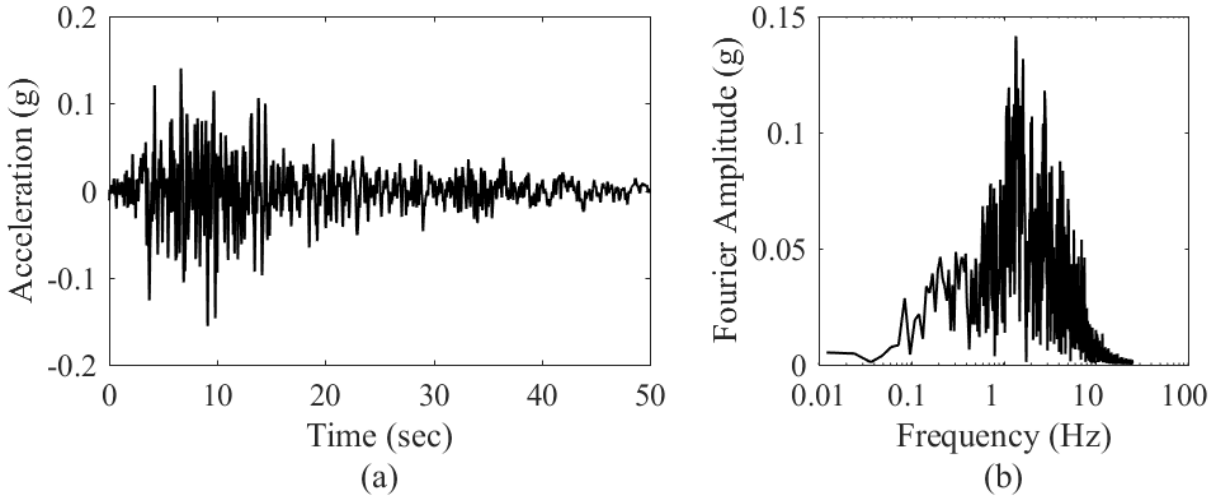

Figure 5.2 Earthquake input motion; (a) incident ground motion time history; (b) Fourier amplitude spectrum of the incident ground motion

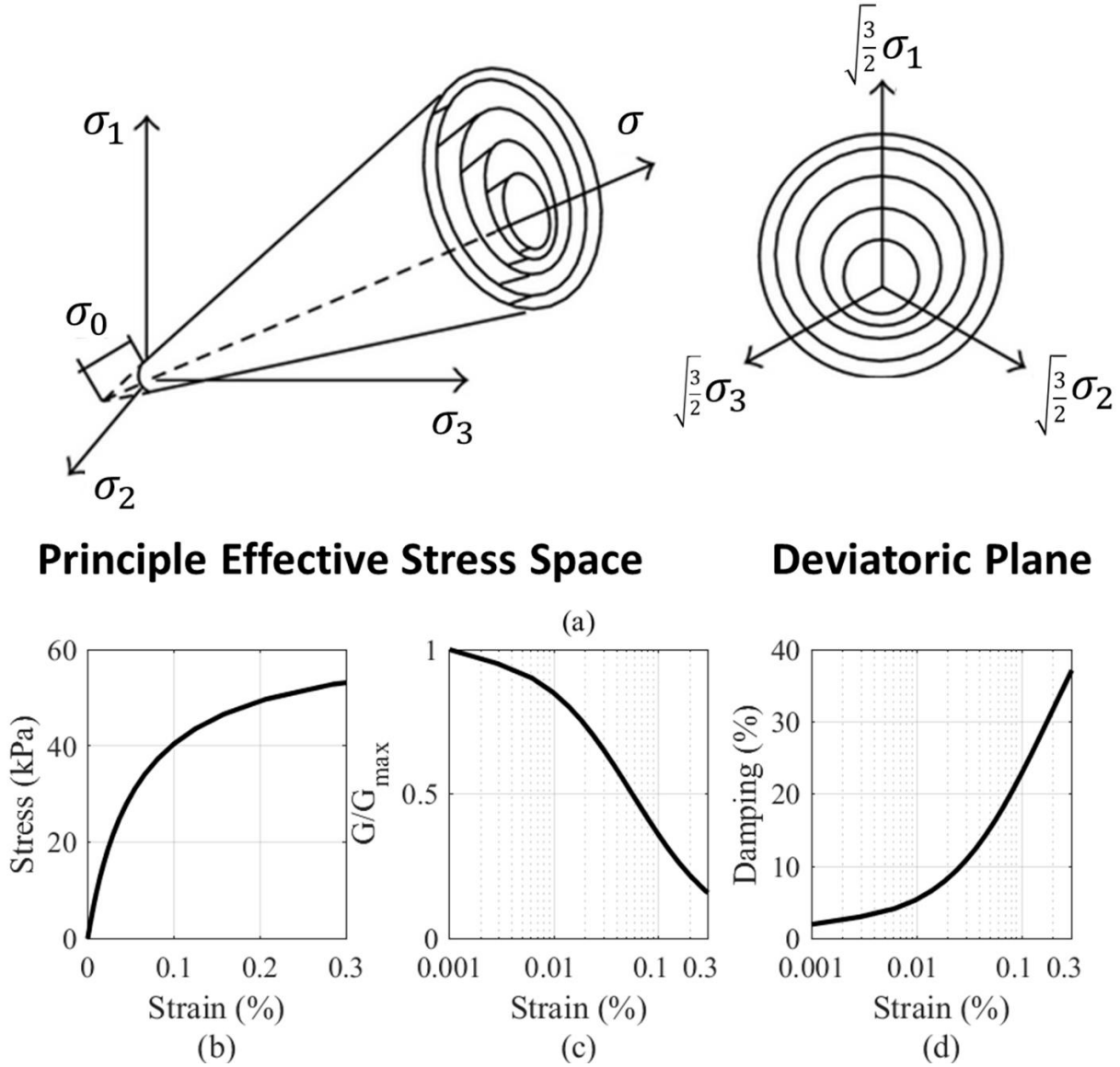

Figure 5.3 Numerical soil material properties (hyperbolic backbone curve; Konder and Zelasko 1963) at reference pressure of 1 atm: (a) Conical yield surfaces for granular soils in principal stress space and deviatoric plane (Yang et al. 2003), (b) shear stress versus shear strain; (c) modulus reduction curve (d) damping ratio versus strain

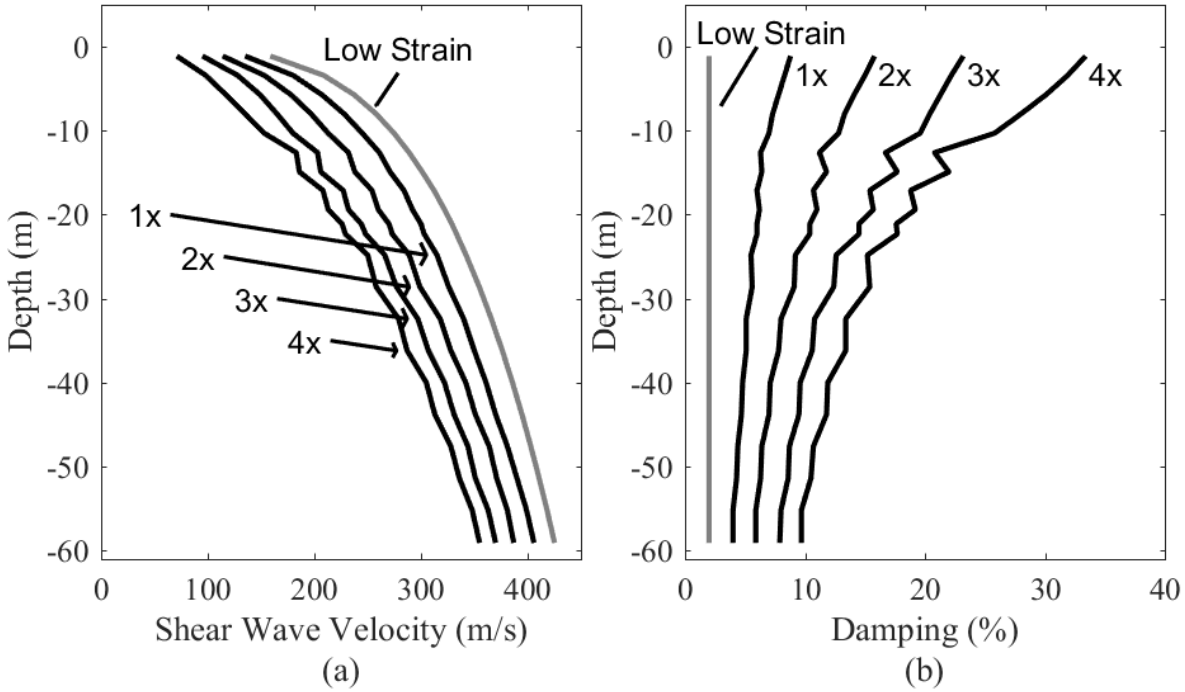

Figure 5.4 Equivalent linear (EL) properties as computed by Shake91 for the 4 input-motion scaling factors: (a) shear wave velocity; (b) damping ratio

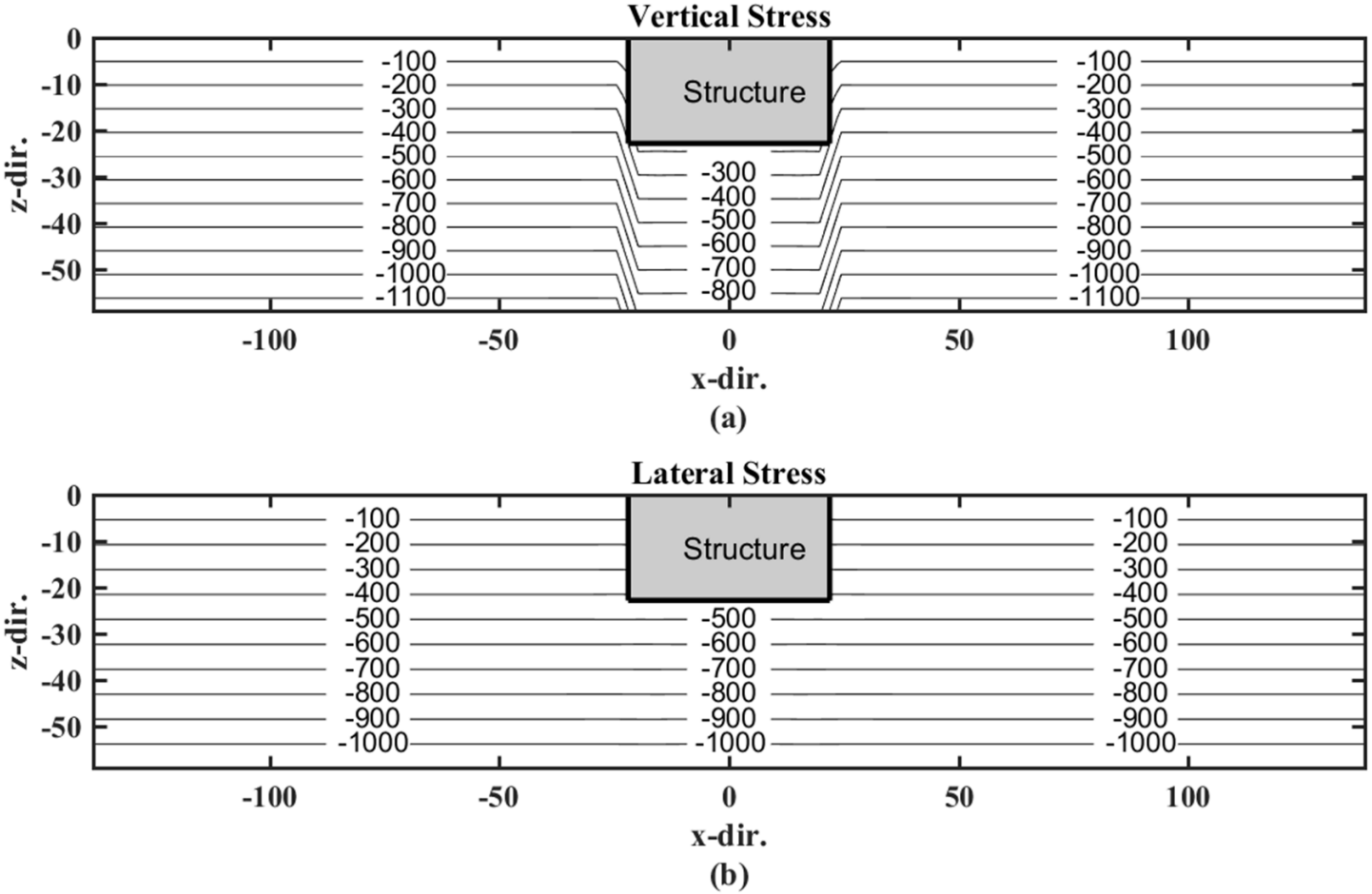

Figure 5.5 Static stress state (kPa) of soil with structure shown in grey with dimensions in meters: (a) vertical stress; (b) lateral stress

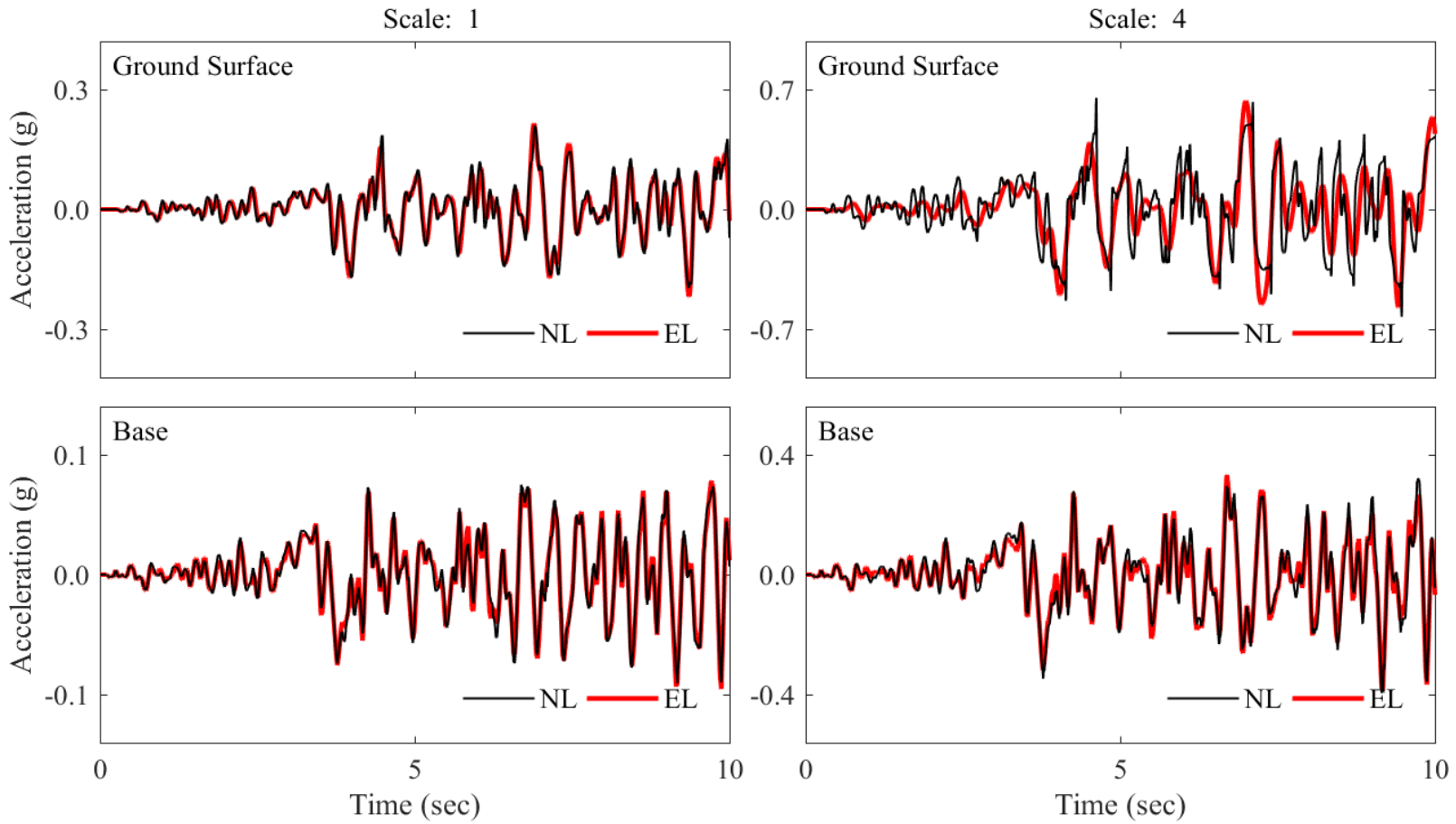

Figure 5.6 Acceleration time history at ground surface (0 m) and base of mesh (60.96 m) for nonlinear (NL) and equivalent linear (EL) site response analysis

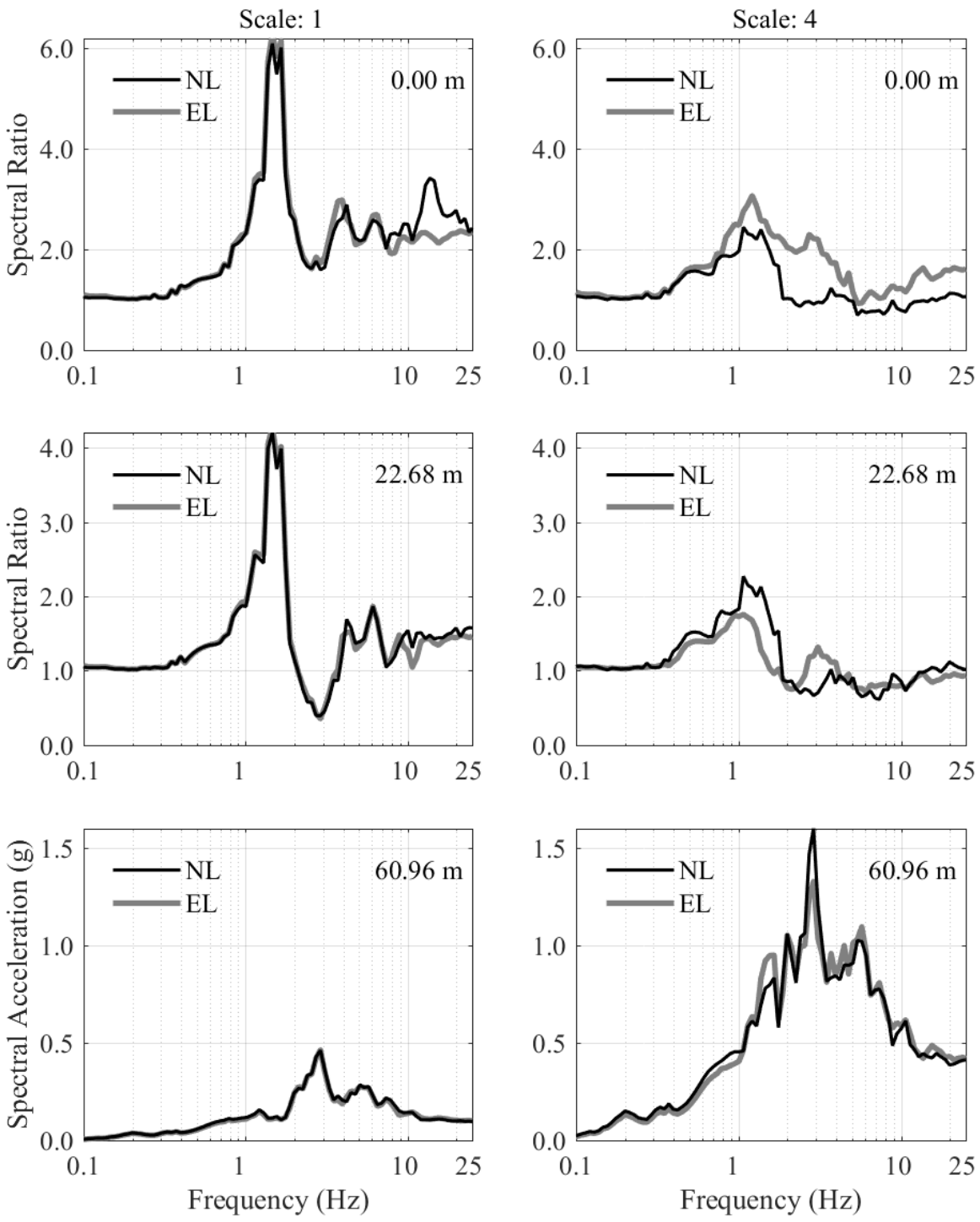

Figure 5.7 Response of free-field: ratio of spectral acceleration at ground surface (0 m), and base level of structure (22.68 m) to motion at base of mesh (60.96 m)

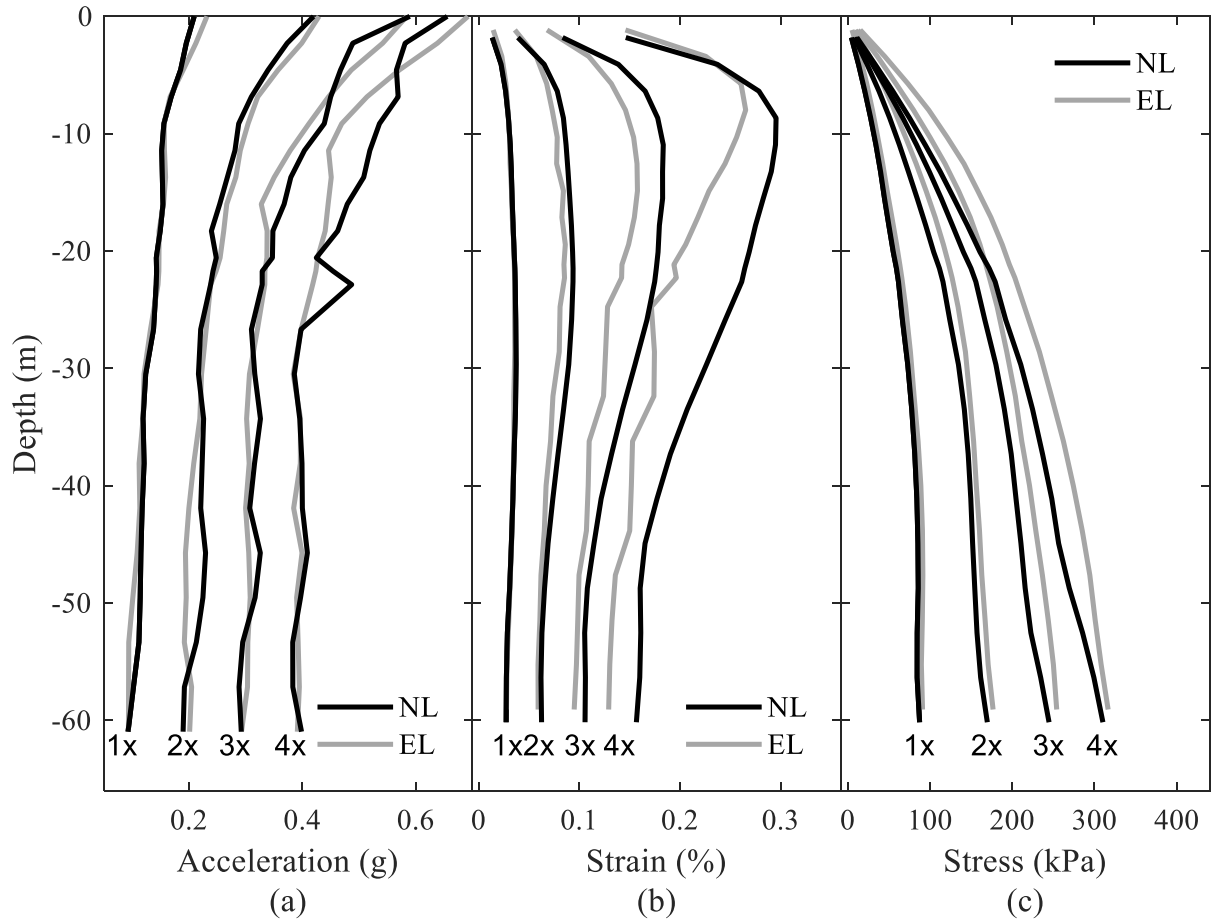

Figure 5.8 Peak free-field response profiles: (a) acceleration; (b) shear strain and (c) shear stress

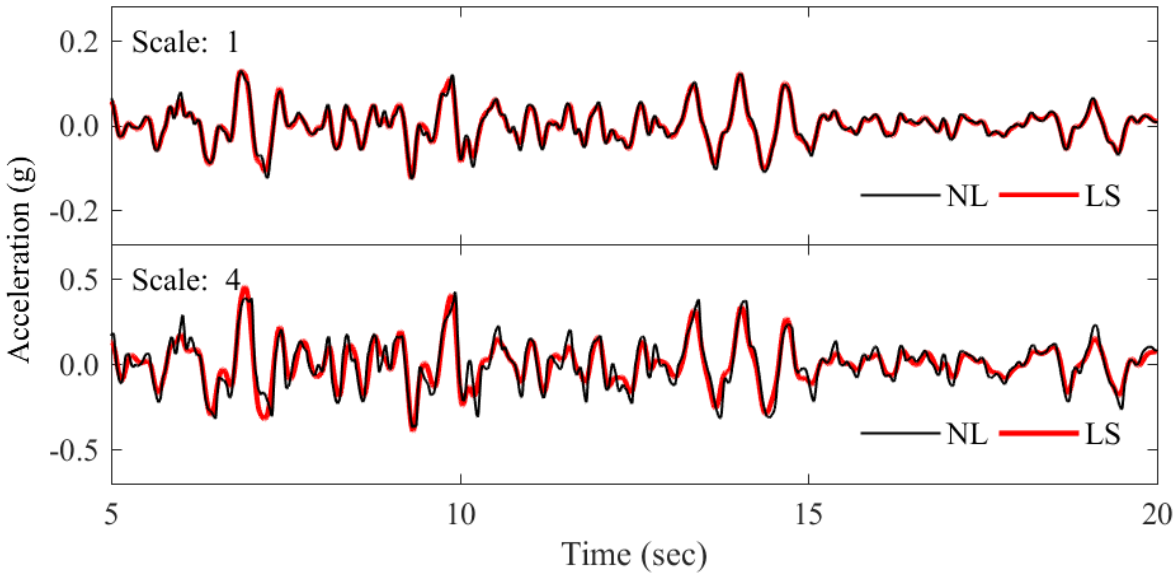

Figure 5.9 Nonlinear (NL) and linear soil properties (LS) acceleration time history at roof of structure

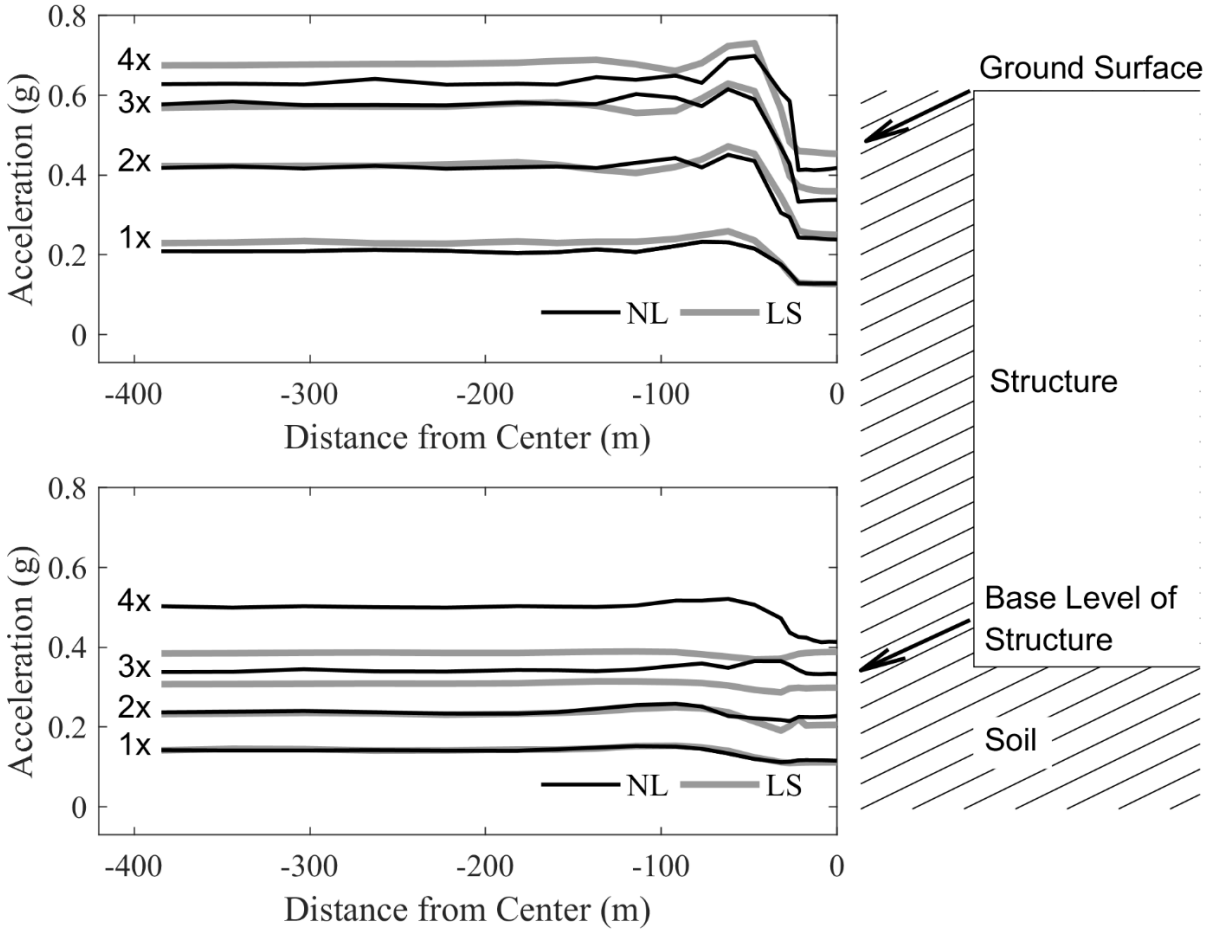

Figure 5.10 Peak acceleration along symmetry plane at: a) ground surface (0 m), and b) base of level of structure (22.68 m)

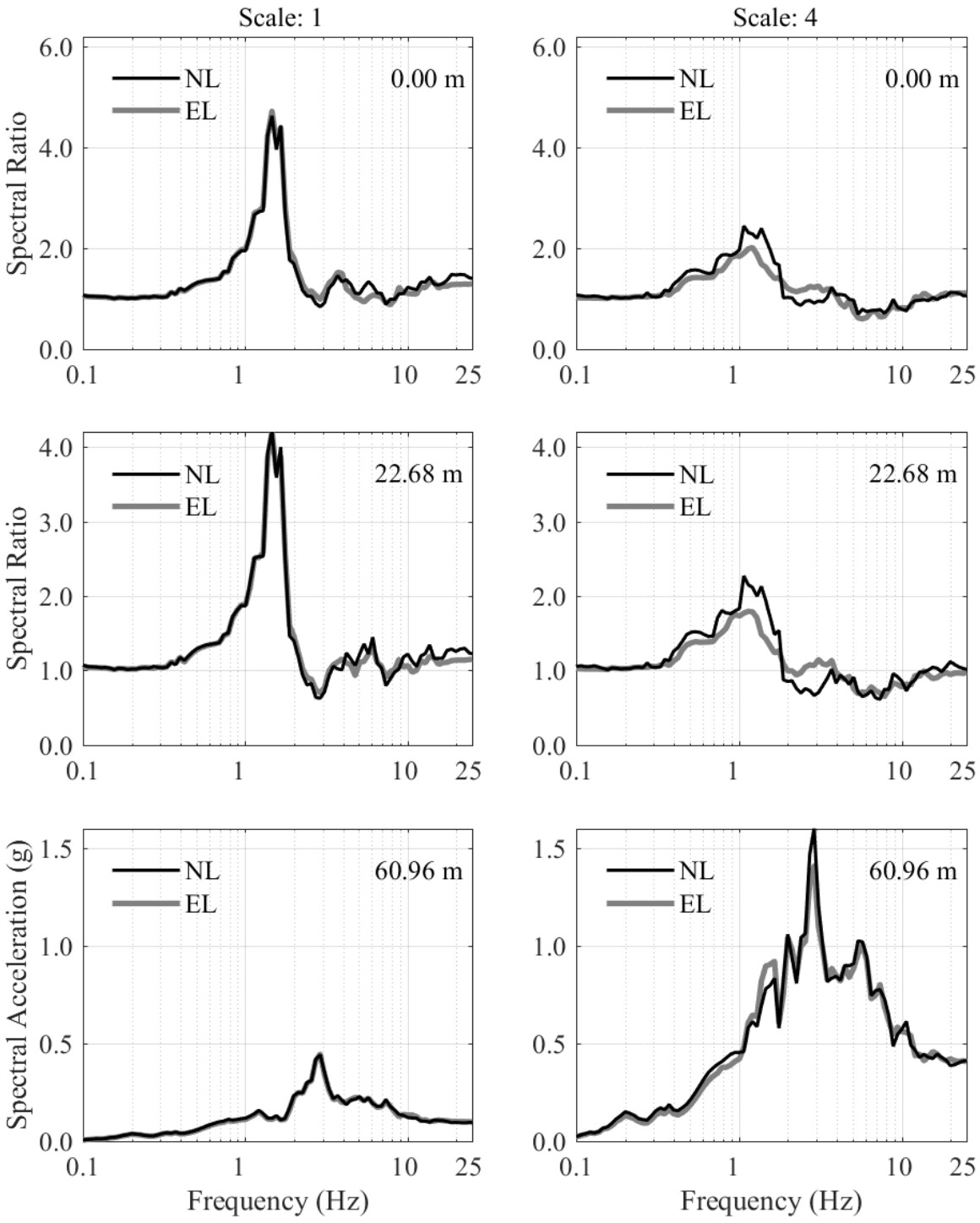

Figure 5.11 Response of structure: ratio of spectral acceleration at ground surface (0 m), and base level of structure (22.68 m) to motion at base of mesh at the structure

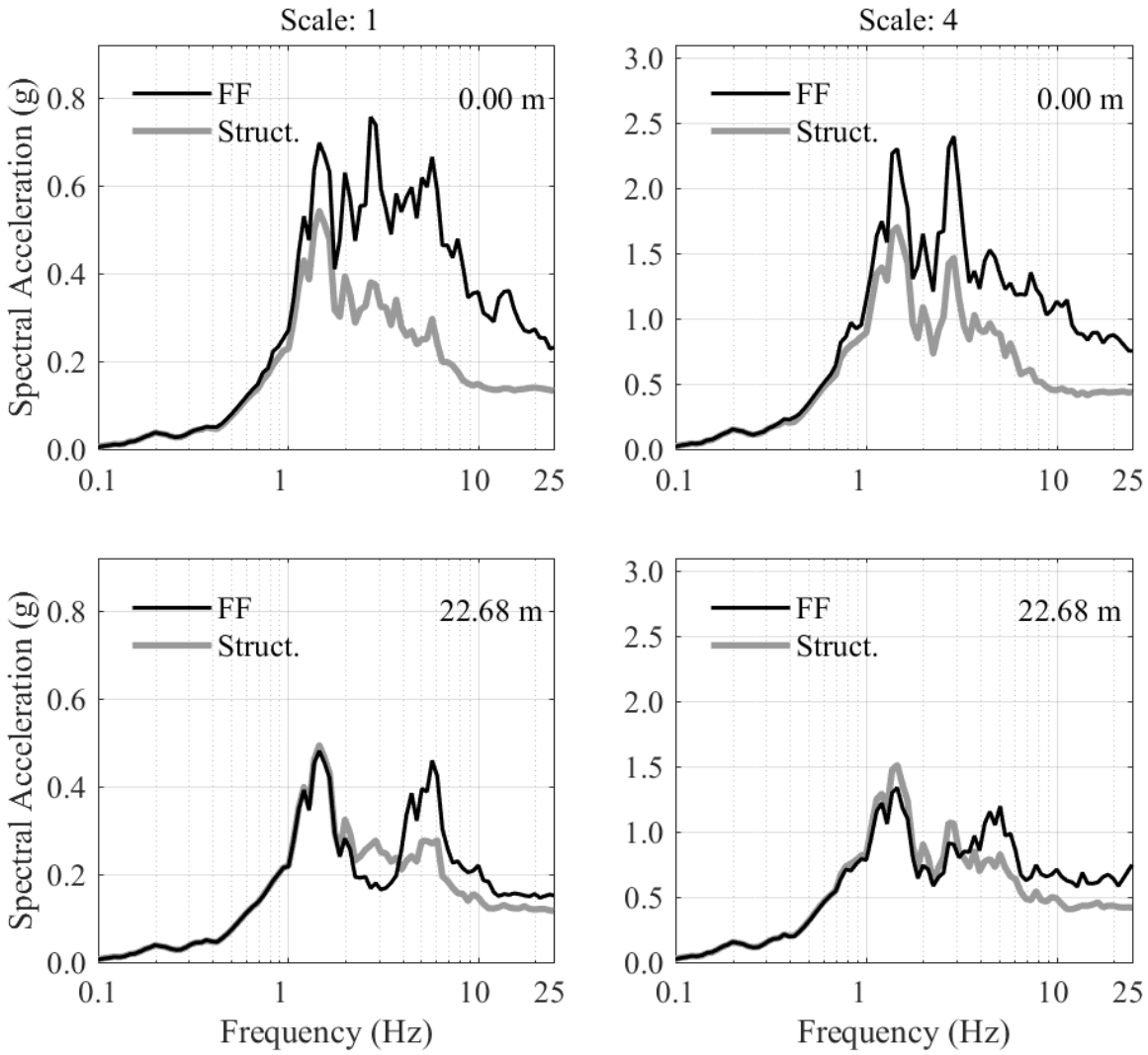

Figure 5.12 Free-field (FF) and structure (Struct.): nonlinear (NL) spectral acceleration at ground surface (0 m) and base level of structure (22.68 m) for scale factors of 1 and 4

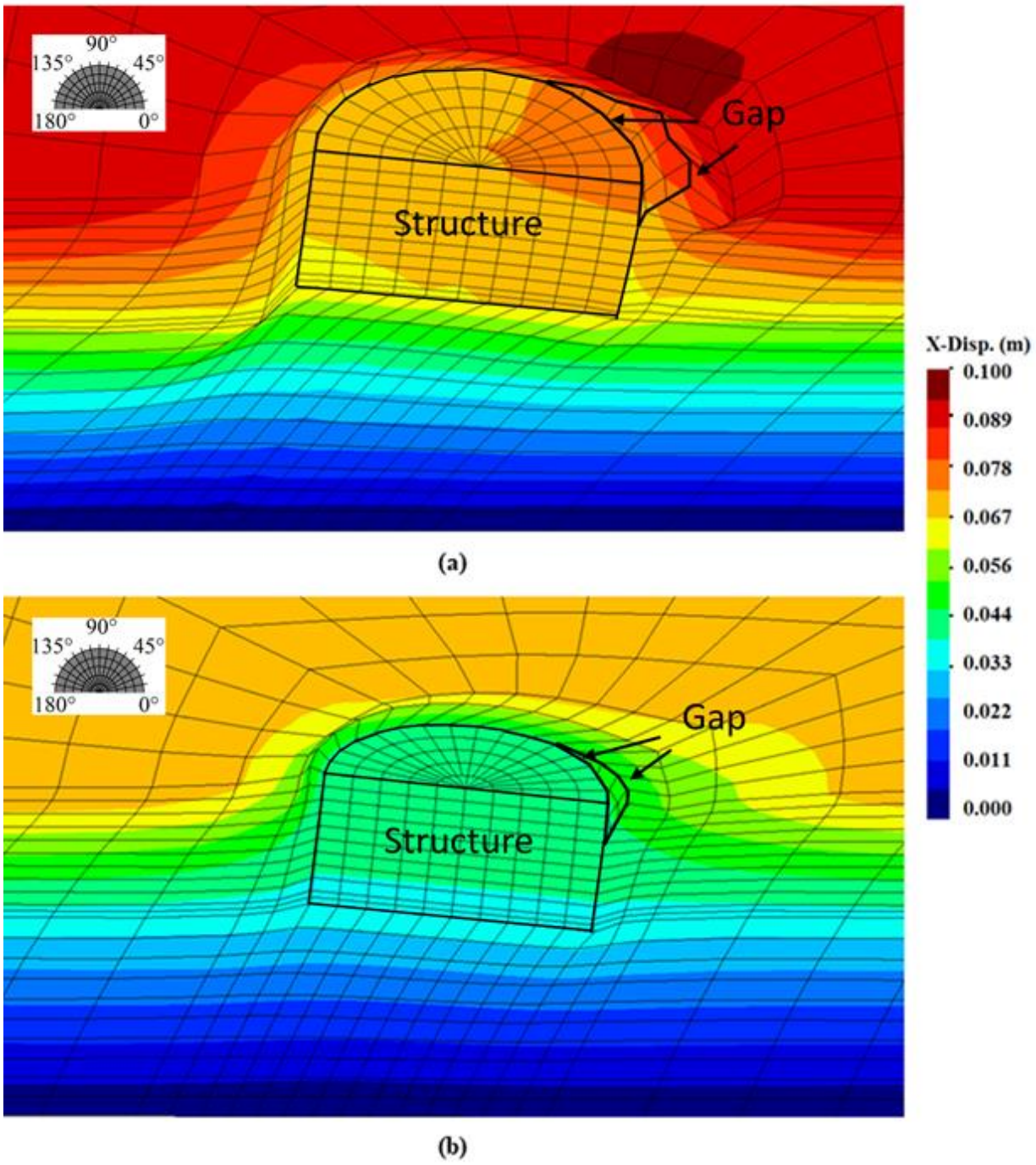

Figure 5.13 Deformed configuration at peak dynamic pressure using a scale factor of 4 with positive values indicating movement to the right for; (a) nonlinear (NL); (b) linear soil properties (LS)

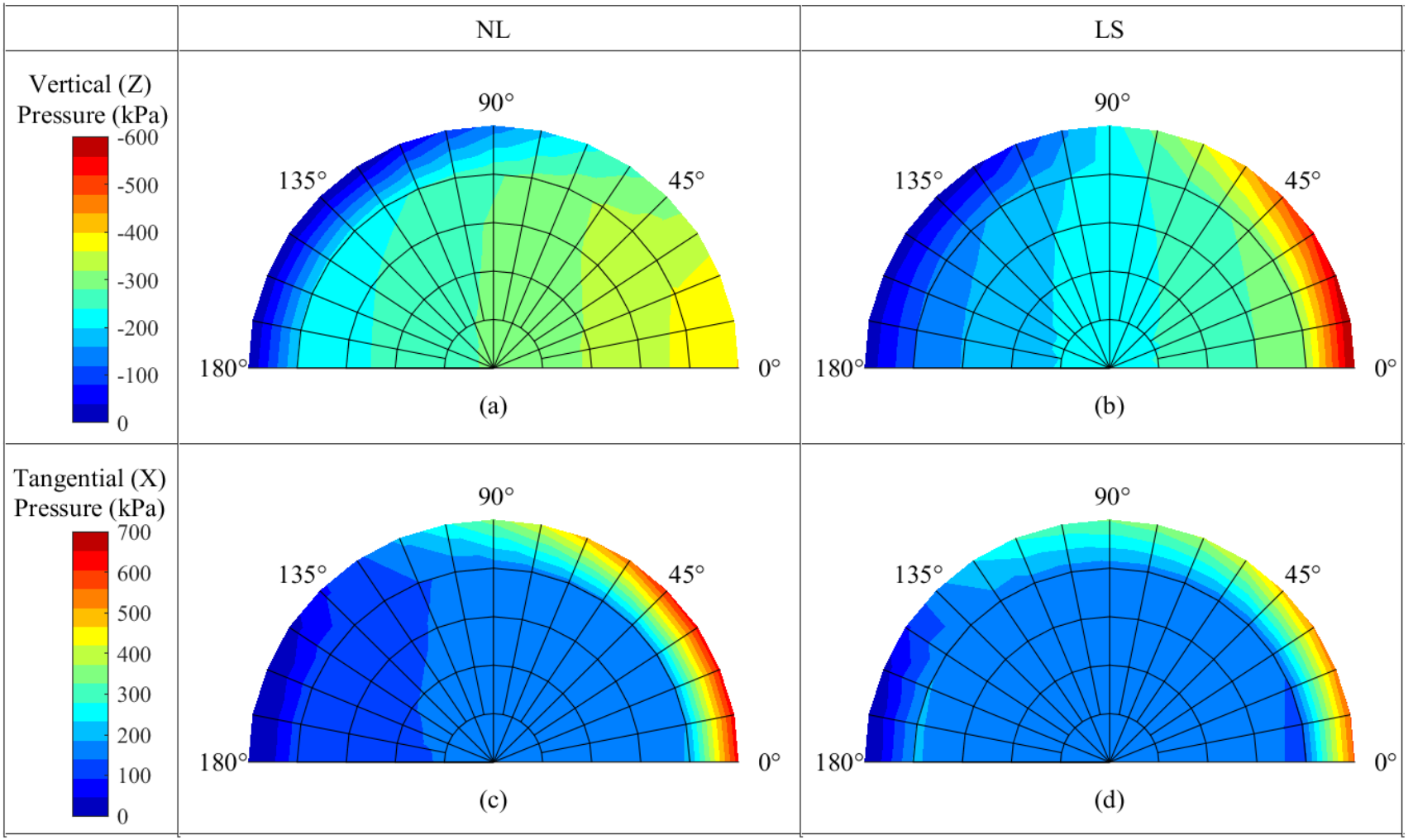

Figure 5.14 Pressure along base of structure at instant of peak dynamic pressure for the scale factor of 4; (a) vertical (Z) for NL; (b) vertical (Z) for LS; (c) tangential (X) for nonlinear (NL); (d) tangential (X) for linear soil properties (LS) (for reference, the initial static vertical stress is 224.26 kPa)

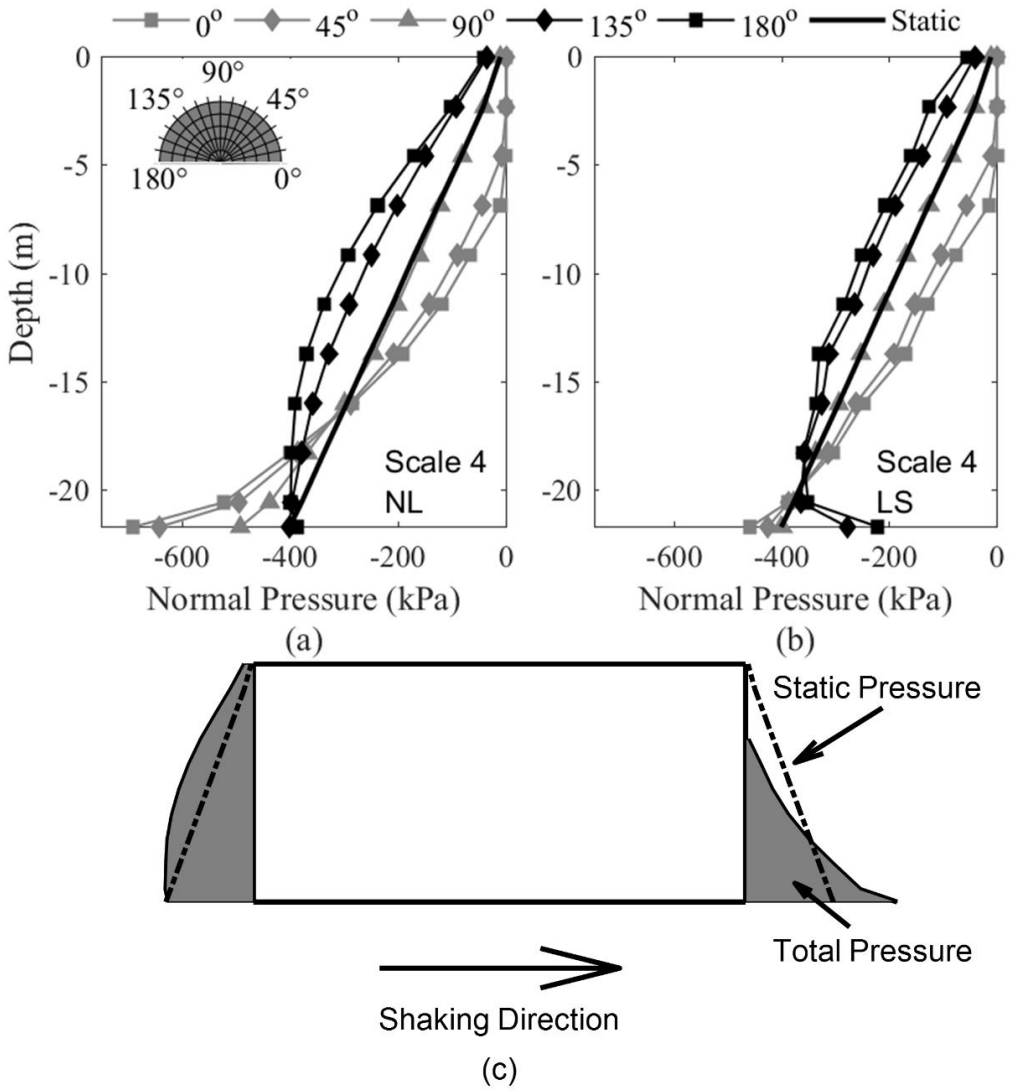

Figure 5.15 Normal pressure along the perimeter of the structure for motion scaled by 4; (a) nonlinear (NL); (b) linear soil properties (LS); (c) pressure distribution on structure at peak dynamic for nonlinear

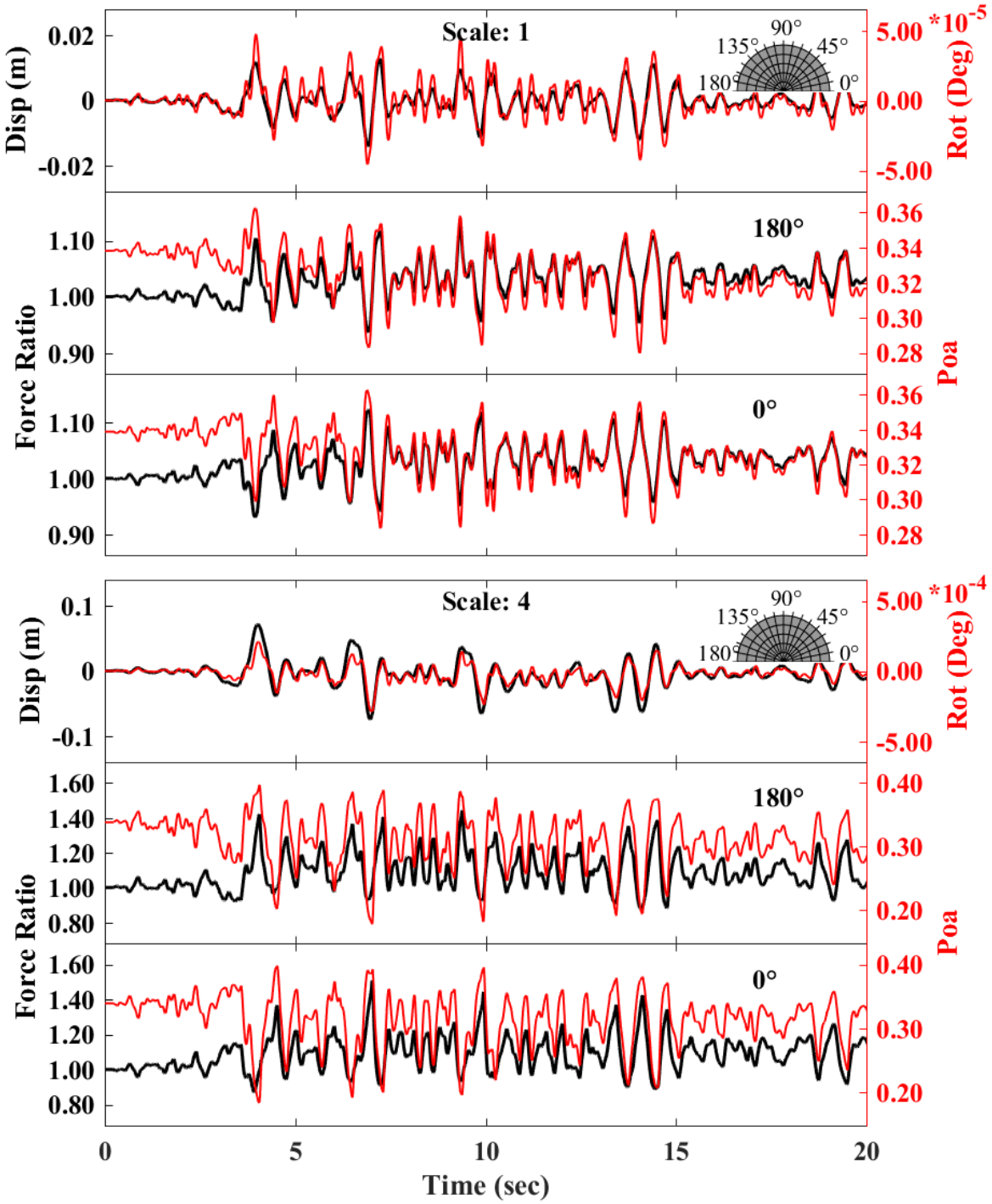

Figure 5.16 NL roof displacement and rotation of structure (positive in clockwise direction), ratio of resultant force to initial force, and force point of action (Poa) normalized by height (H=22.68 m) of structure for the input motions scaled by factors of 1 and 4

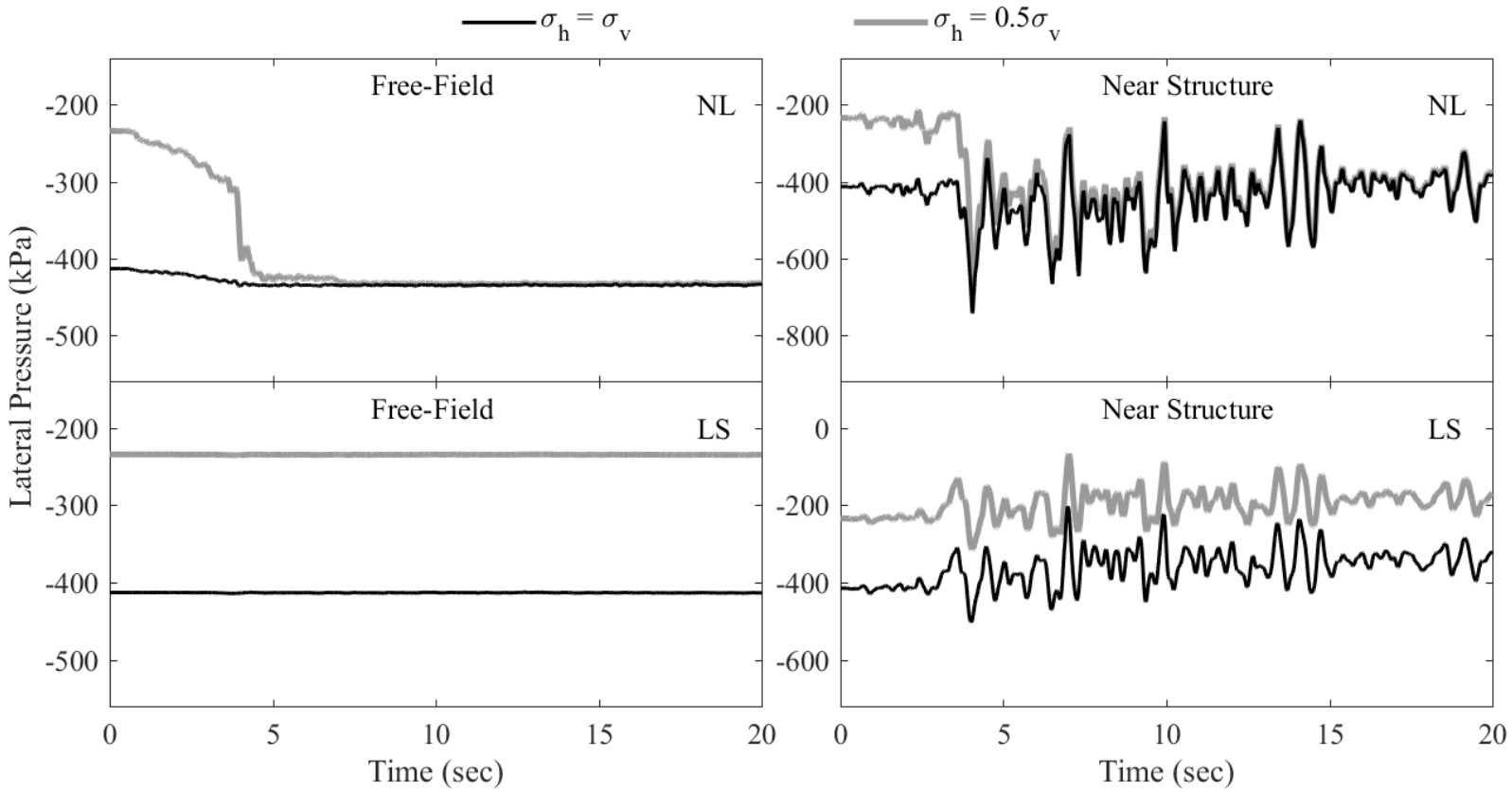

Figure 5.17 Lateral pressure time history of soil at free-field and near structure at a depth of 22.68 m using nonlinear (NL) and linear soil properties (LS)

Chapter 6

Recorded Seismic Response at the Higashi-dori, Aomori Test Site

6.1 Abstract

An opportunity to investigate the soil-structure interaction (SSI) mechanisms of large embedded structures is permitted by the availability of seismic data from an instrumented test site at Higashi-dori, Japan. The compiled data set includes the recorded response of two downhole arrays and scaled twin reactors. A study is reported herein to examine this data set and develop a representative computational model. In the following sections, the site and structural configuration are presented. The employed system identification techniques are outlined. The extracted site properties are shown to provide a reasonable match to the recorded data. Using these properties, a number of parametric computational studies are conducted to illustrate salient mechanisms associated with the seismic response of such large embedded structural systems.

6.2 Introduction

Motivated by many design considerations, several conceptual designs for advanced reactors have been proposed which would be partially or completely embedded below grade. The most popular type of nuclear power plants (NPP) are above ground or shallow embedment light water reactors (LWRs). There are little to no designs which are currently deeply embedded. Consequently, there is a need to explore the effects of soil structure interaction for these new types of NPP.

Of particular significance was the experimental and follow up analytical studies related to the large scale experiment at Higashi-dori (Xu et al. 2003; Xu et al. 2008) which were initiated to access the capabilities of current numerical models in predicting the response of deeply embedded NPP. This experiment sought to explore the usage of deeply embedded (50% of the structural height) advanced boiling water reactor (ABWR). The response of excavated and deeply embedded $1/10^{th}$ scaled models of nuclear reactor structures were evaluated in a number of different configurations. This experiment highlighted the need to consider the uncertainties in defining the soil properties and the impact that disturbed soil can have on the overall response. Furthermore, it was concluded that the uncertainties in the properties of back fill significantly compounded the difficulties in accurately capturing the response.

The following sections briefly describes the site and presents the data set that was made available. Subsequently, the employed system identification techniques used to extract the material properties are outlined. Thereafter, a comparison of the numerical results and recorded data was demonstrated to have a reasonable match. Using these properties, several parametric computational studies were conducted to highlight salient mechanisms associated with the seismic response of such large embedded structural systems.

6.3 Instrumentation at The Higashi-Dori Test Site

6.3.1 Test Site Configuration

Higashidōri, Aomori (Figure 6.1) was designated as a suitable location to conduct large-scaled testing and to investigate the seismic response of deeply embedded NPP structures. The test site was located in the northern part of Japan and experiences frequent seismic activity. From earlier site investigations, the soils have been identified to be representative of typical NPP sites and to be fairly uniform with horizontal layers across the site. The location was comprised primarily of both weathered-pyroclastic and pyroclastic rocks overlain by a 5-8 m layer of overburden (Xu et al. 2003).

For this project, three model-building configurations which included a reactor, twin reactor, and reactor-turbine were constructed at location A, B and D (Figure 6.3) respectively. Additionally, two free-field downhole arrays which will be referred to as downhole array A and downhole array B were instrumented with a number of sensors (Figure 6.3). Downhole array A was in between the three model-building configurations, while downhole array B was located in the far east. Both arrays were more than 300 meters apart from each building. Due to the availability of data, downhole array A, downhole array B and location B were the primary focus for this study.

6.3.2 Instrumentation at the Reactor and Turbine Buildings

The twin reactor setup (Figure 6.2) at location B (Figure 6.3) was comprised of two identical $1/10^{th}$ scaled models of a typical advanced boiling water reactor (ABWR) in Japan (Xu et al. 2008). As depicted in Figure 6.3, these structures were aligned in the North-South direction and will be referred to as BAS (south reactor) and BAN (north reactor). The reactors were three-

story reinforced concrete structures with dimensions of 8 m x 8 m in plan and a height of 10.5 m and weighing 660 metric tons each. The reactors were closely spaced with only 0.6 m of separation and embedded approximately 50% of their total height.

There were a number of acceleration and pressure sensors installed on each reactors as depicted in Figure 6.4 which illustrates the relative location for each sensor and corresponding floor. The provided data set included acceleration time histories recorded at the basemat (B), floor 1 (1F), floor 2 (2F) and roof (R) of the reactors in the N-S direction for each reactor. In addition to the accelerometers, several pressure sensors were installed on the walls of the reactors. These sensors were mounted 0.2 m and 3.55 m from the base of the reactor on the south and north wall of the BAS and BAN structures respectively (Figure 6.5). Through these sensors, we are able to investigate and evaluate the seismic response of deeply embedded structures due to seismic excitation and access the fidelity of the available seismic tools to replicate the recorded response.

6.3.3 Instrumentation at the Adjacent Geotechnical Arrays

The test site included two downhole arrays as indicated in Figure 3. Downhole array A was located in between the three test setup and was more than 300 m away from the buildings (Figure 6.3). Downhole array B was located towards the east of the test site (Figure 6.3). The two arrays included accelerometers at various depths which allows for the investigation of the seismic response of the soil as the waves propagates upwards. Four sensors are positioned at a depth of 1.5 m, 6.5 m, 13 m, and 34.3 m for downhole array A, while downhole array B included 5 sensors at a depth of 3 m, 6.8 m, 17.3 m, 27 m, and 52.75 m (Figure 6.6). The data set included acceleration time histories oriented in the N-S and E-W, and vertical direction for all the mentioned sensors with the exception of 6.5 m for Downhole Array A.

6.3.4 Recorded Earthquake Motion

During the ten-year span from 1989-1999, 27 earthquake events exceeding 10 gal were recorded at this test site. (Xu et al. 2003). Of the 27 earthquake events, only one event was recorded after the addition of the backfill and installation of the pressure sensors (Xu et al. 2003) which will be the primary focus of this study. For this event, the highest acceleration recorded at the downhole arrays was 13.6 gal. As a result of the fairly low maximum acceleration, little to no nonlinearity was to be expected. The recorded time histories were recorded with a time step of 0.005 seconds and was a little over 150 seconds long.

6.4 System Identification of Downhole Arrays

This section outlines the initial efforts to extract the material properties from the provided acceleration time histories from downhole array A and B. To achieve this, a 1D shear beam model was implemented in OpenSees to attempt to replicate the measured response of the soil column. To facilitate this effort, the software package (Gill et al. 1997) Sparse Nonlinear OPTimizer (SNOPT) was employed to determine the optimal parameters that minimizes the difference between the simulated and recorded response. For this study, the shear wave velocities (V_S) and damping ratios were adjusted by SNOPT until the best possible match was achieved. As a result of the low amplitude accelerations, nonlinear properties such as friction angle were not considered for optimization.

6.4.1 Downhole Site Seismic Response

Upon examining the acceleration response spectrum for downhole array B in the x-direction (N-S), it was evident that sensor 2 was clearly an outlier (Figure 6.9). In the low frequency range, the spectral acceleration was essentially the same for all sensors with the

exception of sensor 2. This suggests that the acceleration time history for sensor 2 should be scaled up to significantly improve the match in the low frequency range (Figure 6.10a). There did not appear to be any outliers for the recorded accelerations in the y-direction (E-W) of downhole B or either directions (Figure 6.10b) of downhole A (Figure 6.8). As such, no additional scaling was deemed necessary for any of the other sensors.

When examining the response spectrum at downhole array A and B, it was evident that there was little amplification until near ground surface in both lateral directions. Near ground surface, the response peaked around the same frequency (5.7 Hz) and reached a similar magnitude (0.07 g) in both lateral directions. Overall the spectral acceleration and PGA were fairly similar at the deeper depths. There was little amplification until near ground surface (depth of 1.5 m and 6.80 m for downhole array A and B respectively). Since the response did not change very much until near ground surface, sensors 1, and 3 for downhole array A, and 1, 2, and 3 for downhole array B were the primary focus for this study and were used for system identification of the soil properties. From the recorded acceleration time histories (Figure 6.7), it was observed that the majority of the seismic energy was within the 9 – 70 seconds time interval. To significantly reduce the computational time, only this time interval was used for the analysis.

6.4.2 Shear Beam Model

The 1D shear beam model implemented in OpenSees comprised of eighteen 8 node brick elements for downhole array A and fifteen for downhole array B. The shear beams were discretized into approximately 1 m high elements (Figure 6.11). The different colors in Figure 6.11, correspond to the different soil layers that were defined for this shear beam model. For downhole array A, the different soil properties were defined for the depths between 0 – 3 m, 3 – 5 m, 5 – 6.8 m and 6.8 – 17.3 m. The different layers were all assigned material properties according to what

would provide the optimal match between the simulated and recorded response as determined by SNOPT. Downhole array B, used a similar division except the last layer was defined to be at a depth of 6.8 – 13 m. The recorded motion from sensor 3 at each downhole was used as the input motion for their respective shear beam model. Due to the low amplitude of the motion, the analysis was linear. The Rayleigh damping formulation was used to account for the energy dissipation.

6.4.3 SNOPT

As discussed previously, SNOPT was utilized to help optimize the material properties of the shear beam model so that it may replicate the recorded response. This software package has been integrated into OpenSees and allows the user to specify which variables will be optimized to minimize the user defined objective function. To start the process, you will need to provide an initial guess for the variables that are to be optimized from which SNOPT will systemically evaluate how to best adjust the variables. It should be noted that the identified optimal solution is a local minimum and multiple starting points should be considered in an effort to locate the global minimum.

6.4.4 Objective Function

One of the most important aspect in utilizing SNOPT is defining a suitable objective function to capture the most important aspects of the response which in this case should be a good representation of how well the numerical model matches the recorded response. Multiple objective functions were considered for this study which included matching based on the acceleration response spectrum, transfer function of the Fourier spectrum, and the acceleration time histories. Of the implemented objective function, using the transfer function was the most successful. In the case of the acceleration response spectrum and time history there were many instances in which

the natural frequency was not matched very well. As mentioned previously, SNOPT identifies local minimums so many different start points should be considered.

The shear wave velocity for each individual soil layer and the Rayleigh damping coefficients were the material parameters to be optimized by SNOPT. The mass density was defined to be 2 Mg/m^3 throughout the soil column. Depending on the employed objective function, different aspects of the response was more readily captured. From the transfer function, the response exhibited clear and significant peaks at the natural frequency. Of particular interest was the first two natural modes which was the primary focus when defining suitable material parameters. In addition to obtaining a good match for the natural frequency, the damping parameters were also tuned such that the numerical model will amplify the acceleration time history in a similar manner as the recorded response.

6.4.5 Identified Site Properties

The final shear wave velocity and Rayleigh damping parameter identified for downhole array A can be found in Table 6.1 and Table 6.2. As shown in transfer functions (Figure 6.12 - Figure 6.13), the natural frequencies were consistent for both the x and y direction. When comparing the response as computed using the optimized material properties with the recorded response, it was observed that the natural frequencies were quite close. However, there was one small peak that was not present in the numerical model but was apparent in the transfer function between sensors 1 and 3. The peak at 12 Hz present in the transfer function between sensor 2 and 3.

When the material properties identified for downhole array A were applied to the shear beam model for downhole array B, it was found that the natural frequencies coincided with what was recorded. The natural frequency for this model was slightly higher than the case for downhole

array A due to the shorter height of the soil column and similar soil properties. Since there was a good match in the natural frequency at both downhole arrays, the selected shear wave velocity was believed to be suitable. Although it was found that the shear wave velocity was consistent for both arrays, the damping at downhole array A was found to be too low for downhole array B. Given the consistency in the shear wave velocities, an additional optimization was conducted using both arrays to identify a damping ratio that was best for downhole array A and B. From this process, it was determined that the damping that best matches both downhole arrays was around 1% at the natural frequency of the shear beam.

6.5 Soil-Structure Interaction

6.5.1 Recorded Response of Twin Reactors

When examining the response spectrum, it was concluded that the response for sensors at the same floors were similar and that the structure can be assumed to be fairly rigid. Consequently, only one acceleration time history at each floor was used to represent the response of the structure. As mentioned, the data set included the acceleration for the basemat, floor 1 (1F), 2 (2F) and roof for each reactor building.

Furthermore, there were four pressure time histories that were included. The pressure sensors were placed on the south and north wall of the BAS and BAN structure respectively (Figure 6.5). The names of these pressure sensors were BAS-SE-S1, BAS-SE-S4, BAN-SE-N3, and BAN-SE-S13 with the locations indicated in Figure 6.5. In addition to the sensors on the twin reactors, there are multiple sensors located in the soil around the structure which were referred to as S1, S2, and S3. Similar to the previous cases, the response spectrum for the sensors around the same depth were essentially identical and are grouped together for this study.

6.5.2 Soil-Structure Model

To follow up on the efforts to optimize the material properties using the 1D shear beam model, a 3D soil island was created using the identified parameters (Figure 6.18). This model was to be shaken in the x-direction (N-S) using the same motion from the 1D shear beam model. To capitalize on the symmetry of the model, a half mesh was used to significantly reduce the computational costs. The model was comprised primarily of 8 node brick elements with the above ground portion of the reactor represented using a lumped mass. The soil-structure interface was assumed to be in full contact due to the low intensity of the motion. The structure was represented using lumped masses and rigid links. The dimension and mass of the structure were based on the previously mentioned properties and was additionally considered rigid. The finite element mesh including the reactor is shown in Figure 6.18.

Similar to the NUREG reports (Xu et al. 2003; Xu et al. 2008), there seems to be a good agreement for the acceleration time histories. When examining the acceleration response spectrum for the roof and basemat (Figure 6.19 and Figure 6.20), it was observed that in general the peaks of the spectrum are at the same frequencies, but was overestimated. As depicted in Figure 6.21 - Figure 6.28 the pressure computed using OpenSees were higher than the recorded, especially at one particular frequency. From the NUREG 6957 report, it was shown that the numerical results were also much higher than recorded, but to not the same degree as observed with OpenSees. Overall the shape of the Fourier Spectrum (Figure 6.29 - Figure 6.32) was very similar despite the differing amplitudes.

6.5.3 Addition of Weak Soil Layer

After the inclusion of the twin reactor, the 3D model was further refined with the addition of a weak soil layer directly under the embedded structure. The weak soil layer was believed to be byproduct of the excavation activities. The reported thickness and shear wave velocity for this soil layer were 0.5 m and 150 m/s respectively, which was significantly weaker than the surrounding soil at similar depths. It was observed that this soil layer significantly reduced the stress near the base of the structure when compared to the previous iteration of the 3D FE model (Figure 6.33 - Figure 6.44). The presence of the weak layer did not seem to have much an effect on the pressure sensors at a much higher elevation as illustrated with sensor BAS-SE-S4, and BAN-SE-S4. The addition of the weak soil layer helped significantly improve the match for the sensors at the lower elevation.

6.5.4 Conclusions

The seismic response of the experiments conducted in Higashidōri, Aomori was investigated, in order to highlight a number of salient response characteristics associated with seismic excitation for large embedded structures, albeit for weak motions. The free-field response and reactor were examined using frequency and time domain techniques which were used to identify the material parameters. Overall, the following conclusions may be drawn:

1. The optimal material parameters as identified by SNOPT were able to replicate the response as recorded at the downhole arrays. However, the shear wave velocity was on average 25% higher than reported in the NUREG report.
2. Of the implemented objective functions, the transfer function was the most successful when trying to match the recorded response using SNOPT.

3. When applying the optimal soil properties to the larger 3D soil island, there was a fairly good match in the acceleration. The response spectrum appeared to peak at similar frequencies, although the finite element model overestimated the acceleration.
4. The pressure on the side of the structure was significantly overestimated by the finite element model. The shape of the Fourier Spectra looks similar for the simulated and recorded pressures.
5. It was observed that the addition of the weak soil layer significantly reduced the stress near the base of the structure and helped significantly improve the match for the sensors near the base.

6.5.5 Acknowledgement

This research was partially funded by the US Nuclear Regulatory Commission with Dr. Thomas Weaver as the program Manager.

Table 6.1 Comparison of shear wave velocity (m/s) at the Newfree Field as reported in the NUREG report and determined from the OpenSees analysis using SNOPT

Depth (m)	From Paper (Xu, et al. 2008)	SNOPT - FFT	Difference (%)	SNOPT - Time History	Difference (%)
0 - 2	140	117	-16.43	117	-16.43
2 - 5		210	50	210	50
5 - 6.8	210	286	36.19	286	36.19
6.8 - 17.3	430	517.23	20.29	449.19	12.95

Table 6.2 Rayleigh damping parameters determined from the OpenSees analysis using SNOPT

	From Paper (Xu, et al. 2008)	Damping (Rayleigh) - Fourier Transform		Damping (Rayleigh) - Time History	
Depth (m)	**Frequency Independent**	**am**	**ak**	**am**	**ak**
0- 5	5	0.08774	0.00015	0.0877	0.00012
> 5	2	0.08774	0.00015	0.0877	0.00012

Figure 6.1 Location of field test site in Japan (Xu et al. 2003)

Figure 6.2 NUPEC field test model of adjacent twin reactor buildings before placing of backfill soil (Xu et al. 2003)

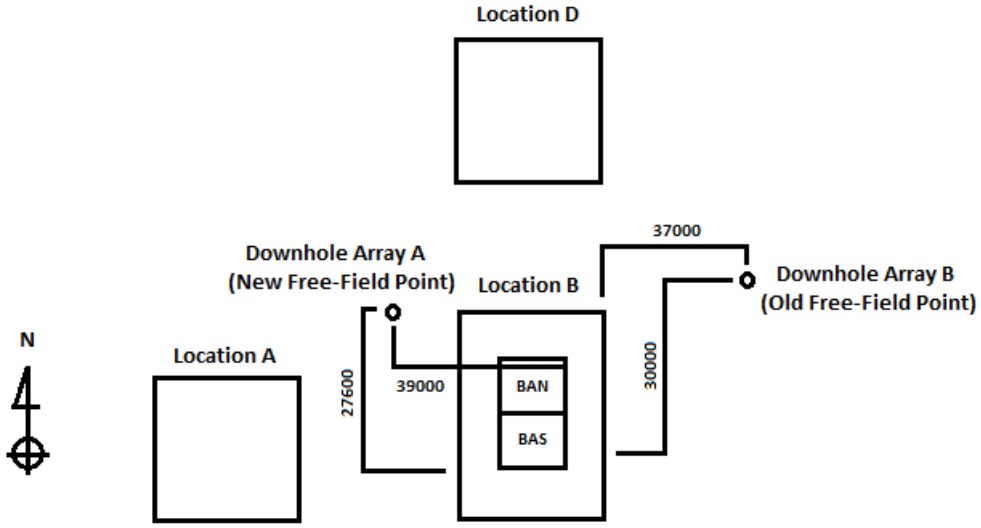

Figure 6.3 Plan view of test site (units in mm)

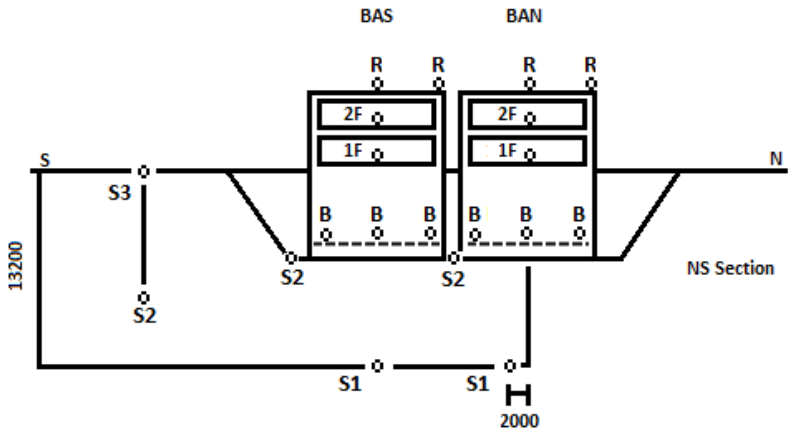

Figure 6.4 Locations of seismometer for twin configuration (BAN and BAS) which was embedded about 50% of its total height (10.5 m) [unit: mm] (Xu et al. 2008)

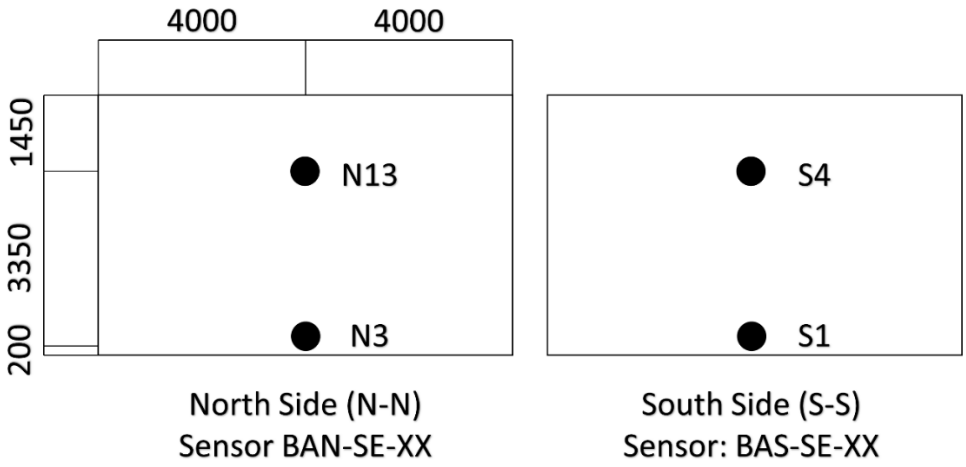

Figure 6.5 Locations of Pressure Sensors for the BAS and BAN Structures on Side Wall [unit: mm] (Xu et al. 2008)

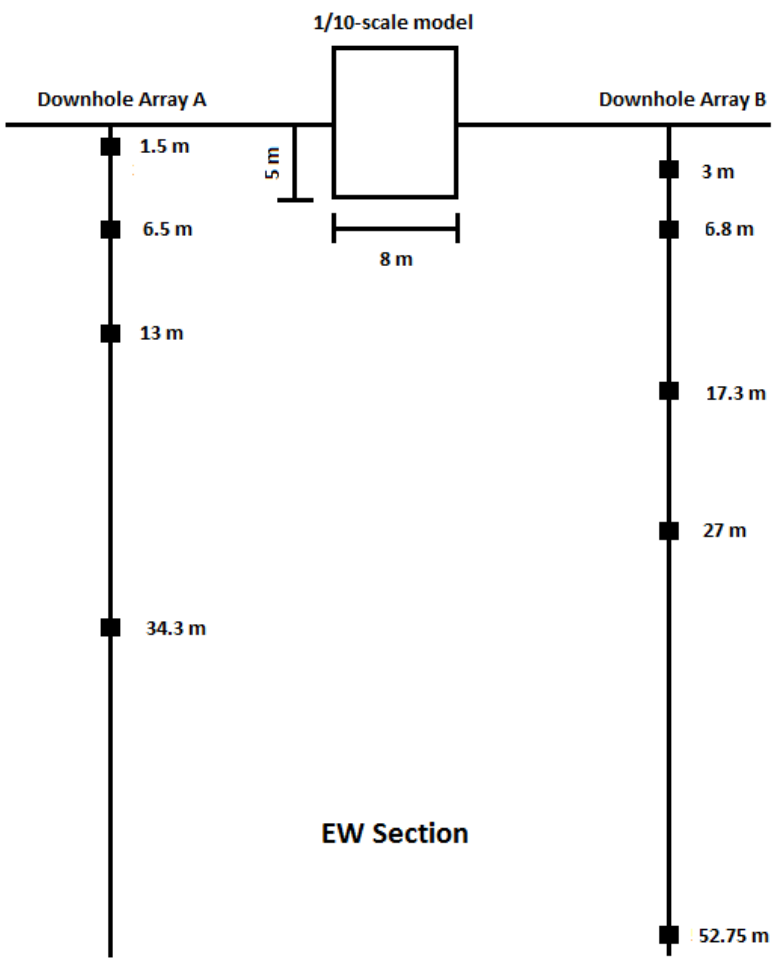

Figure 6.6 Layout of seismometer in Free-Field Downhole Arrays

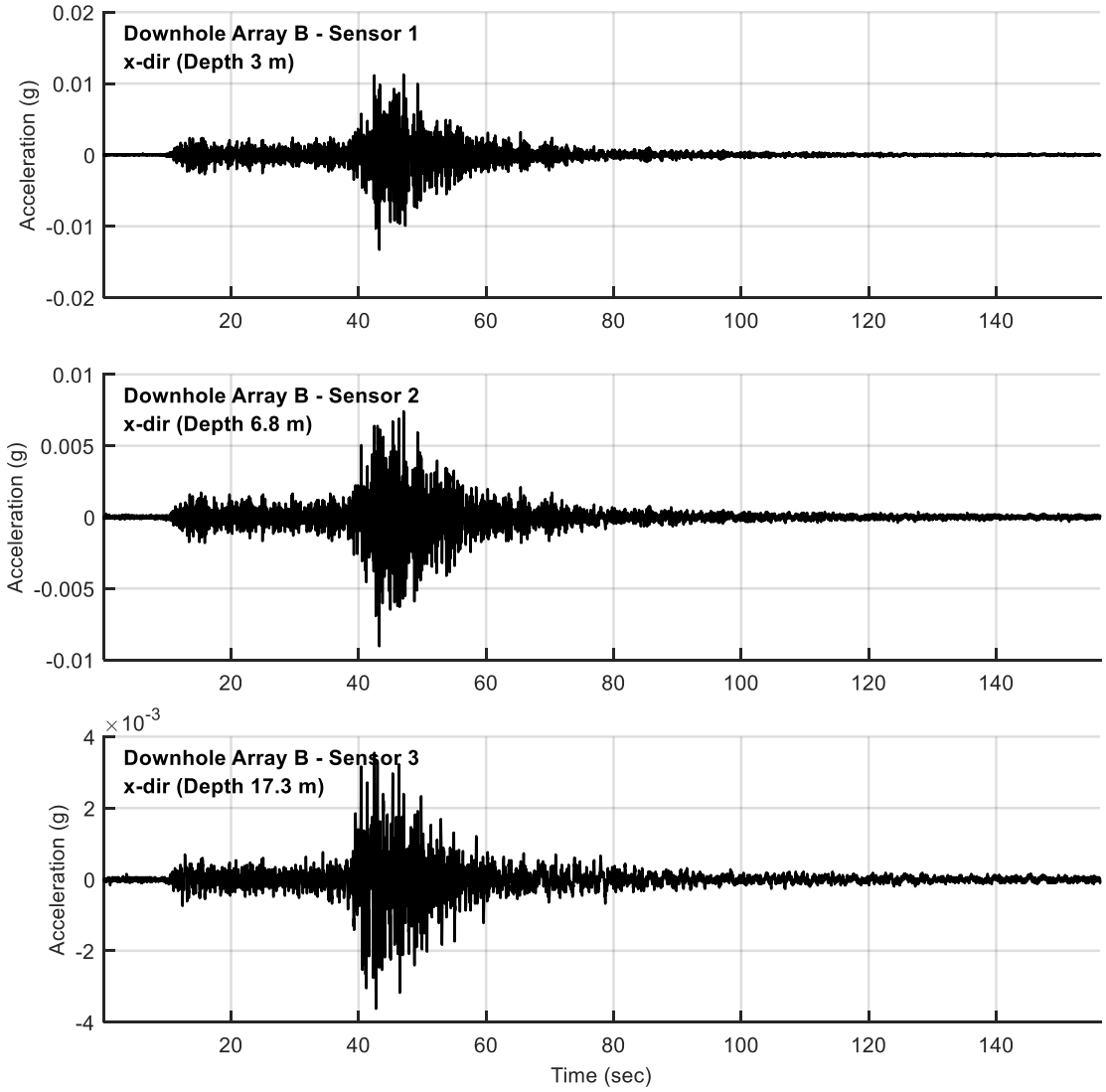

Figure 6.7 Acceleration time history at downhole array B in the x-direction (N-S)

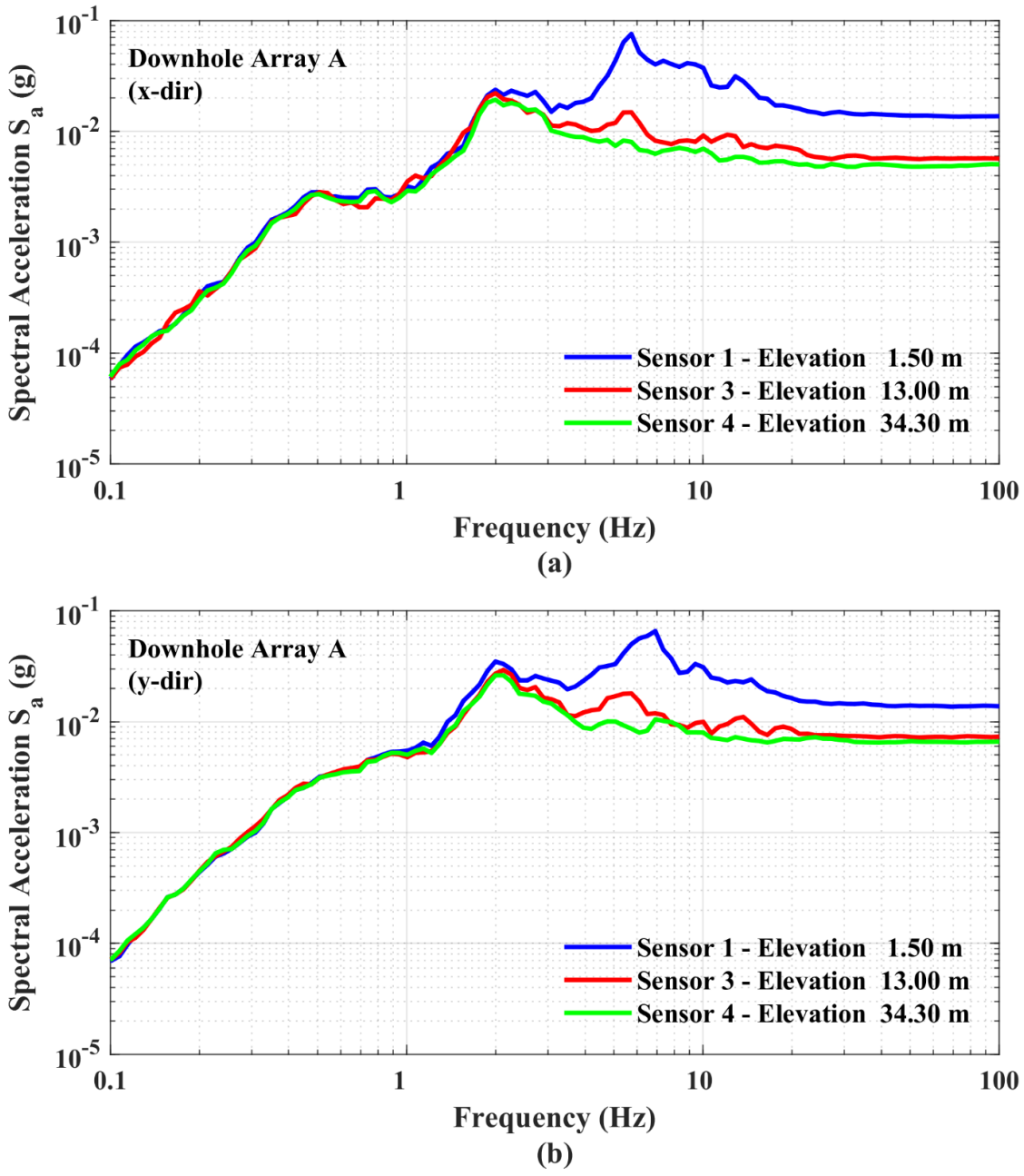

Figure 6.8 Acceleration response spectrum at downhole array A; a) x-direction (N-S); b) y-direction (E-W)

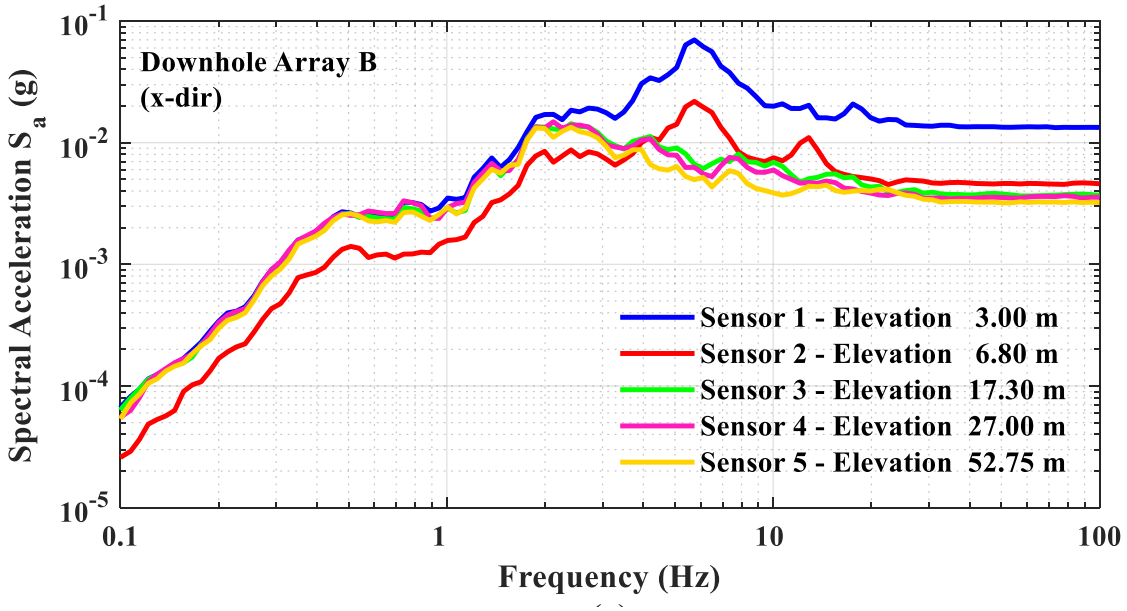

Figure 6.9 Acceleration response spectrum at downhole array B in x-direction (N-S) with no scaling

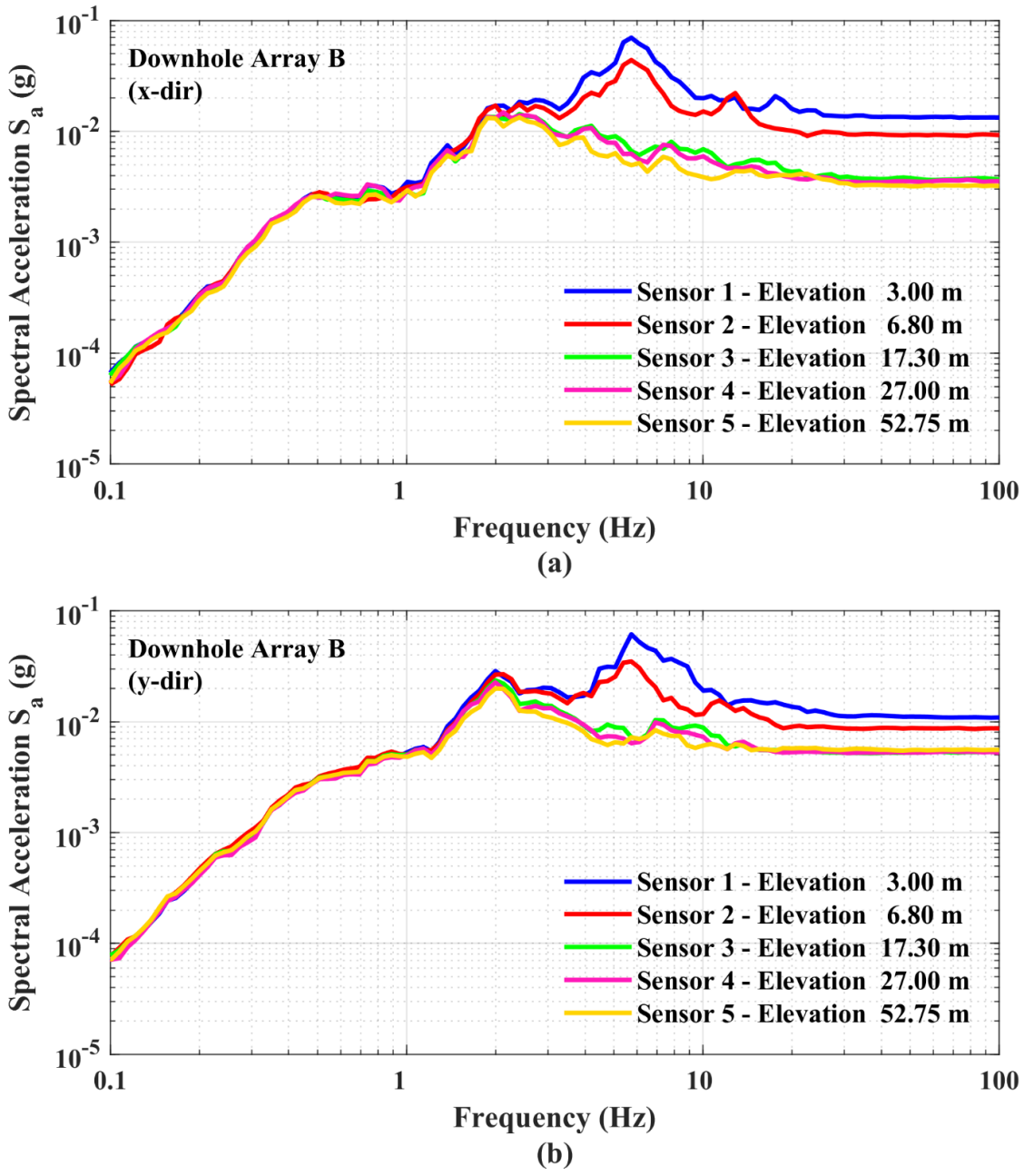

Figure 6.10 Acceleration response spectrum at downhole array B; a) x-direction (N-S); b) y-direction (E-W)

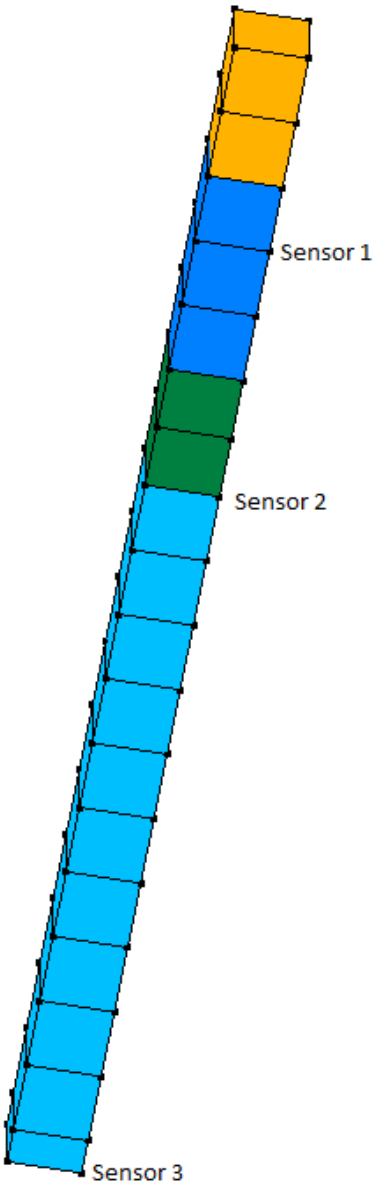

Figure 6.11 Mesh for the shear beam model for downhole array A (with a height of 17.3 m.)

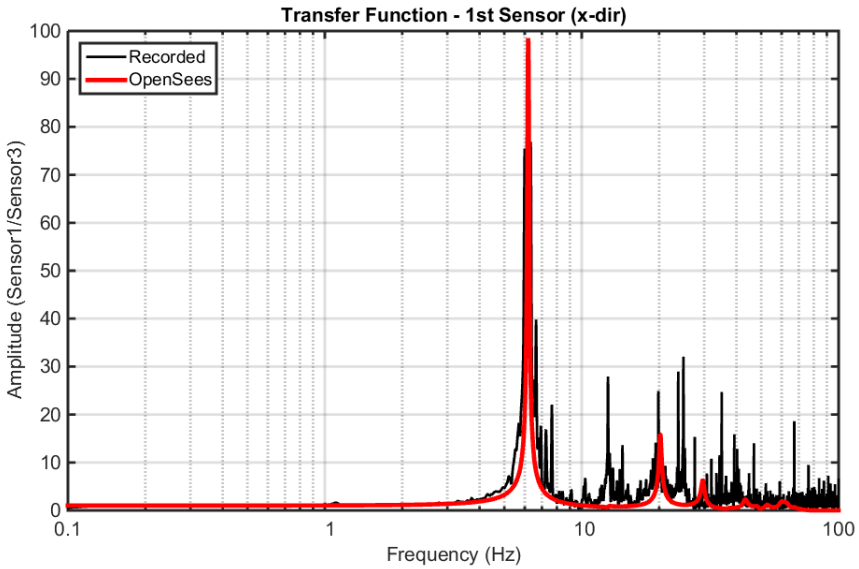

Figure 6.12 Comparison of transfer function using the Fourier spectrum of the acceleration time histories for the recorded response and OpenSees analysis (Sensor 1/Sensor 3) (x-direction, N-S)

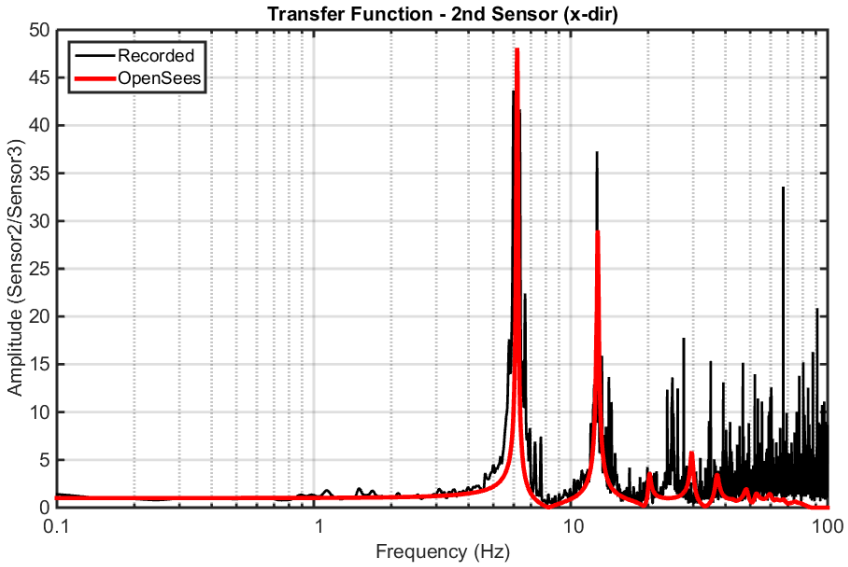

Figure 6.13 Comparison of transfer function using the Fourier spectrum of the acceleration time histories for the recorded response and OpenSees analysis (Sensor 2/Sensor 3) (x-direction, N-S)

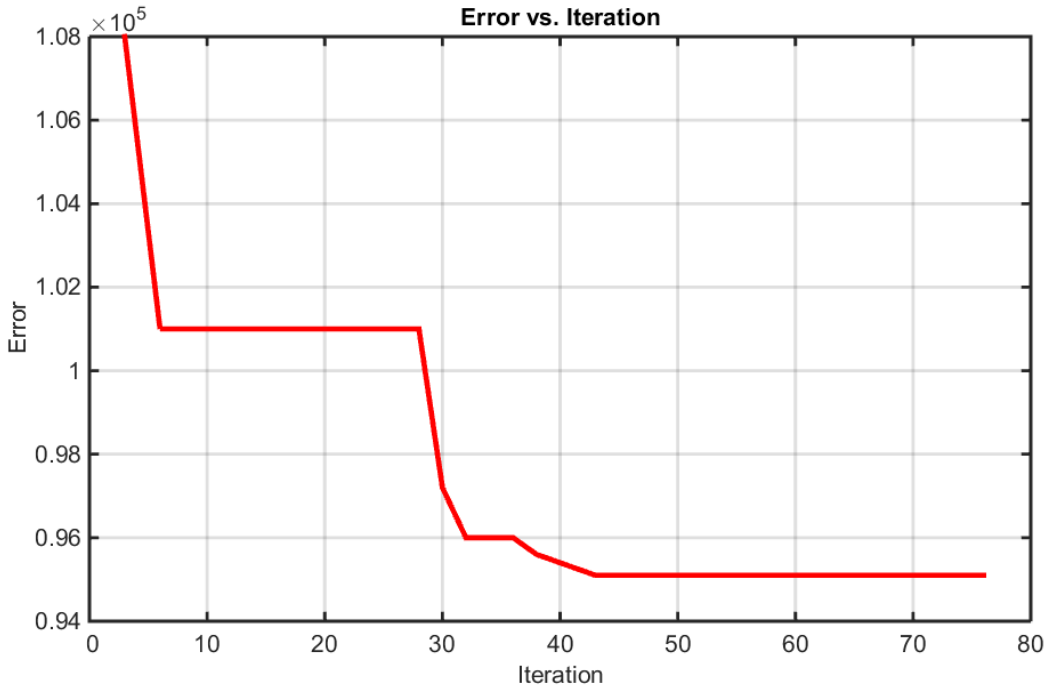

Figure 6.14 Plot of the error function (based on Fourier Transform)

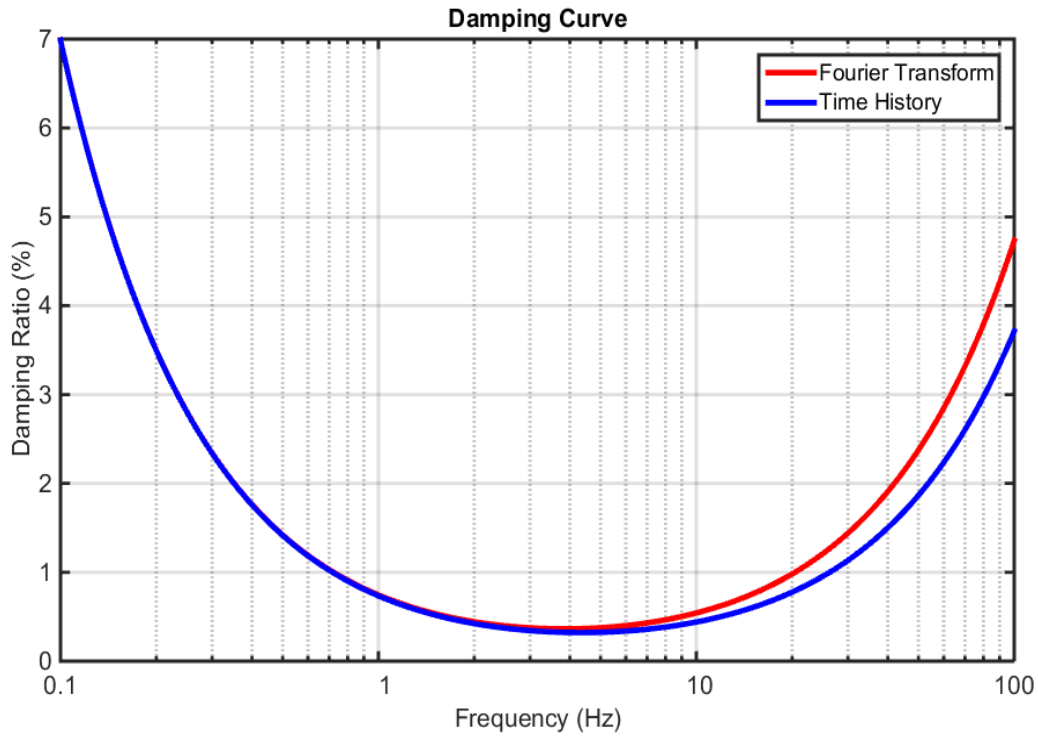

Figure 6.15 Damping curve as determined by SNOPT for different objective function

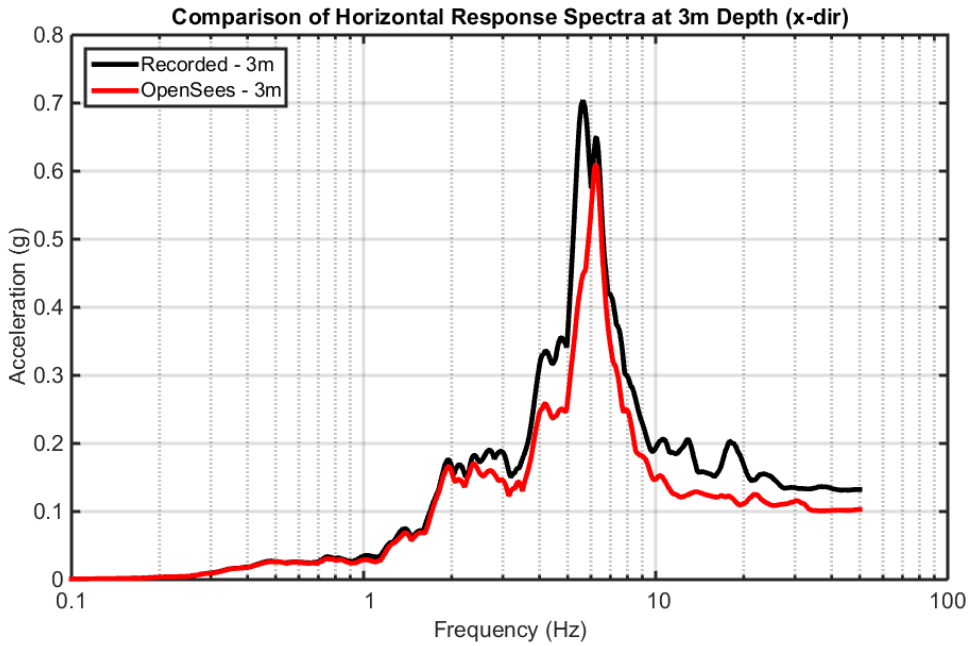

Figure 6.16 Comparison of the recorded and computed horizontal response Spectra at 3m depth in x-direction (N-S)

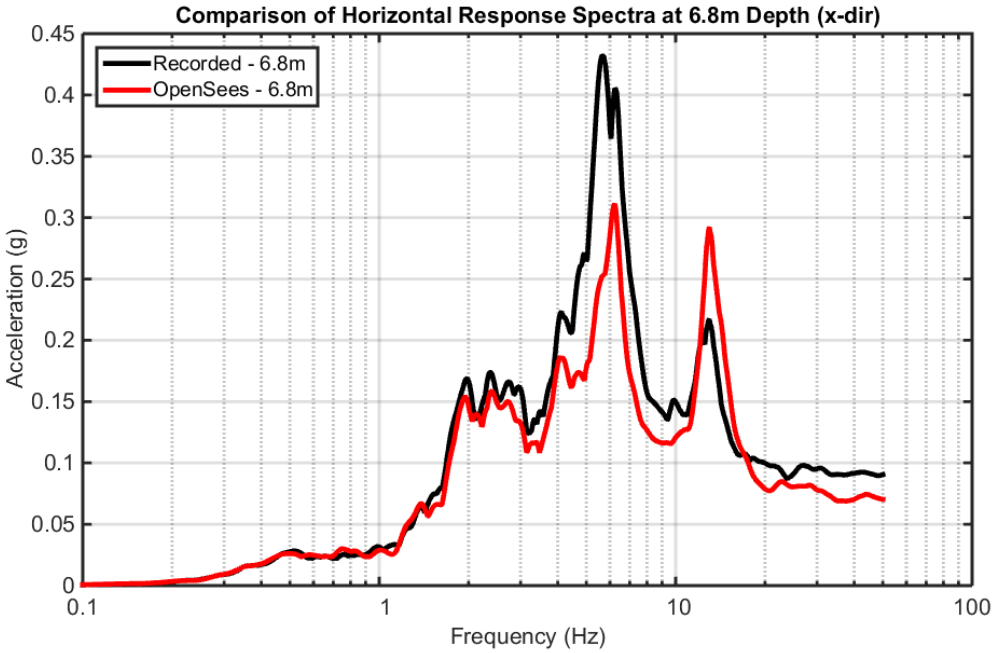

Figure 6.17 Comparison of the recorded and computed horizontal response spectra at 6.8m depth in x-direction (N-S)

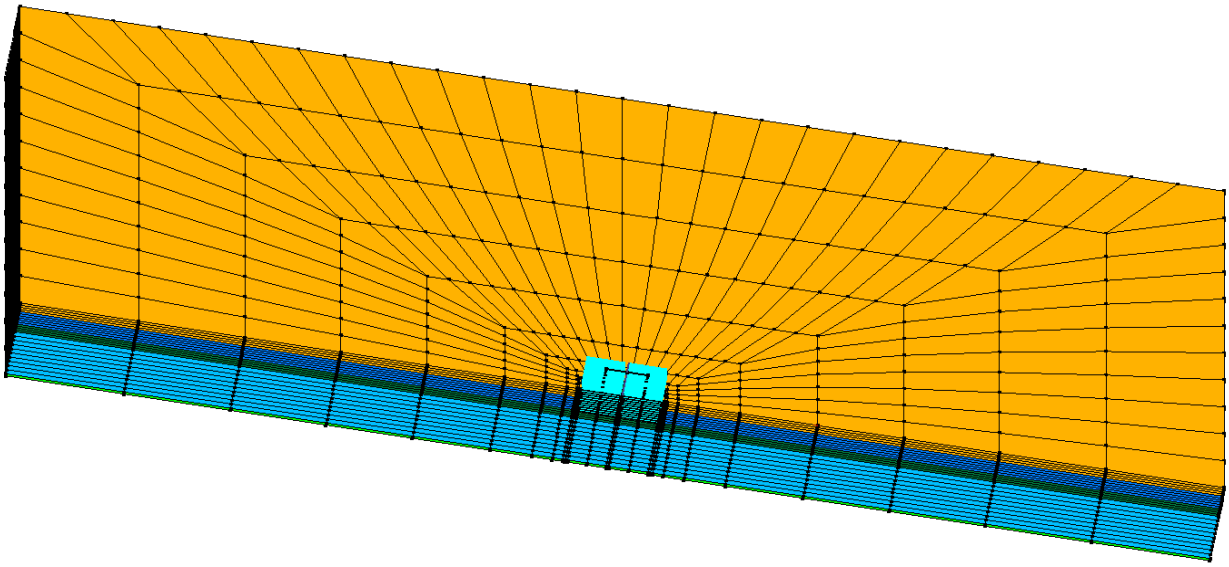

Figure 6.18 Finite element model with twin reactor structure

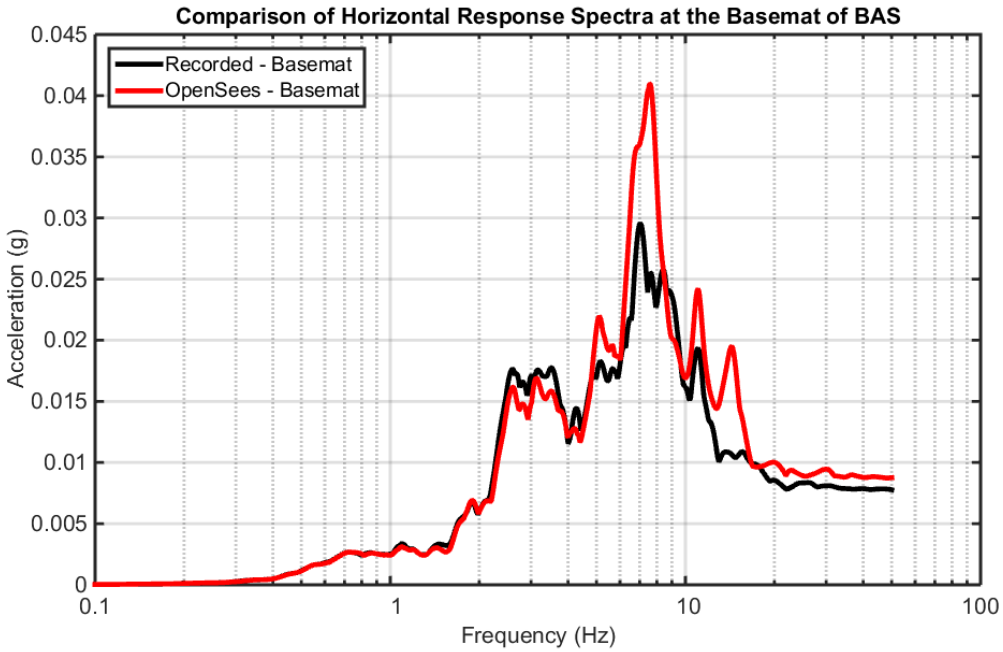

Figure 6.19 Response spectra at the Basemat center of the embedded twin reactor (BAS) in x-direction (N-S)

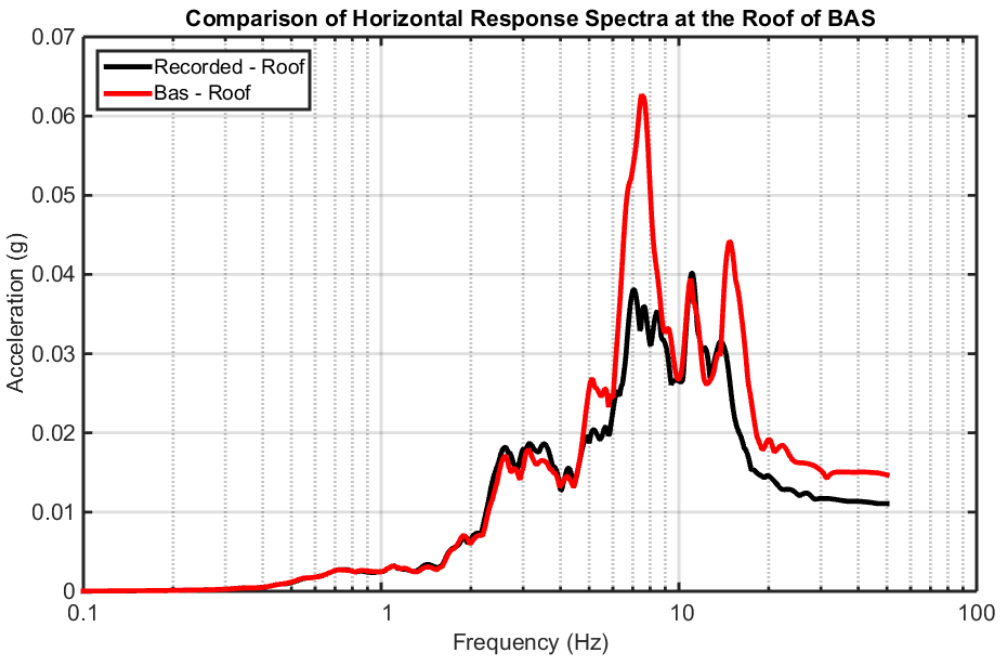

Figure 6.20 Response spectra at the roof center of the embedded twin reactor (BAS) in x-direction (N-S)

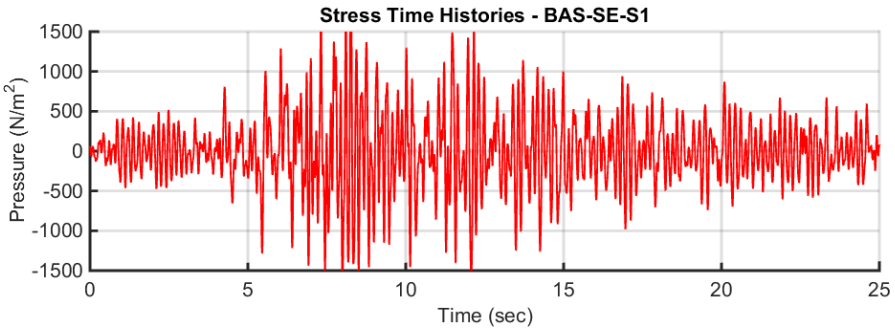

Figure 6.21 Computed Pressure Time History at the location of BAS-SE-S1 at a depth of 4.8 m

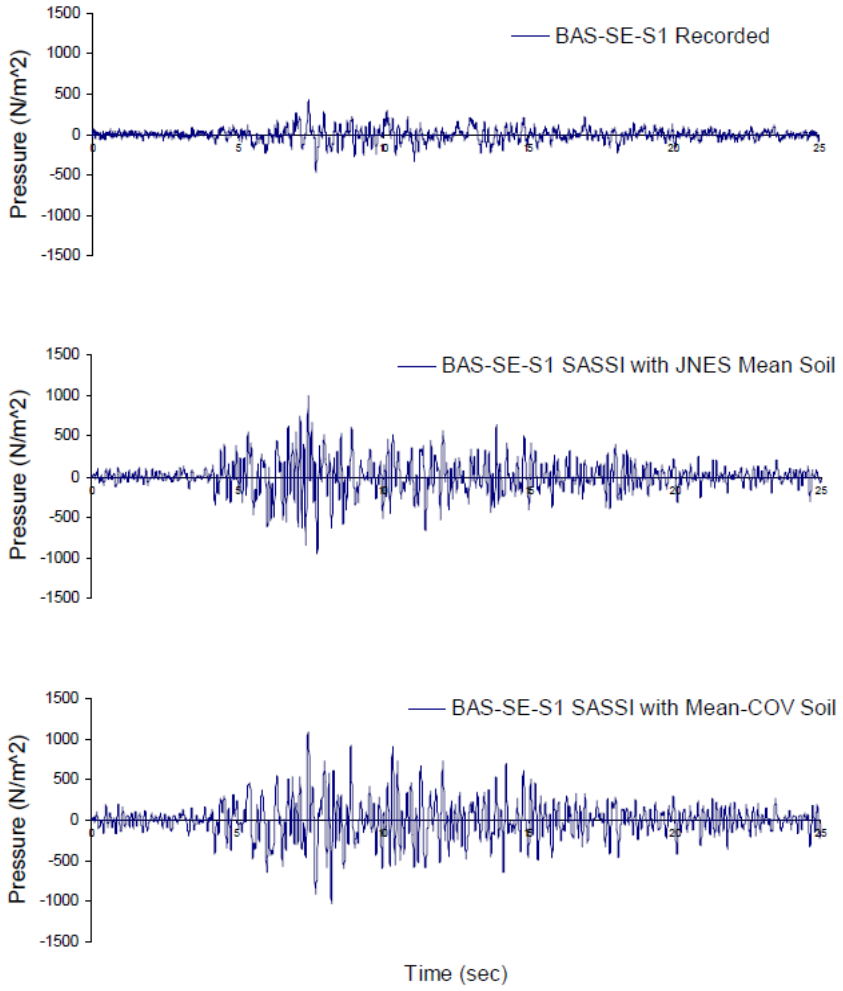

Figure 6.22 Comparison of seismic induced soil pressure at sensor BAS-SE-S1 (Xu et al. 2008)

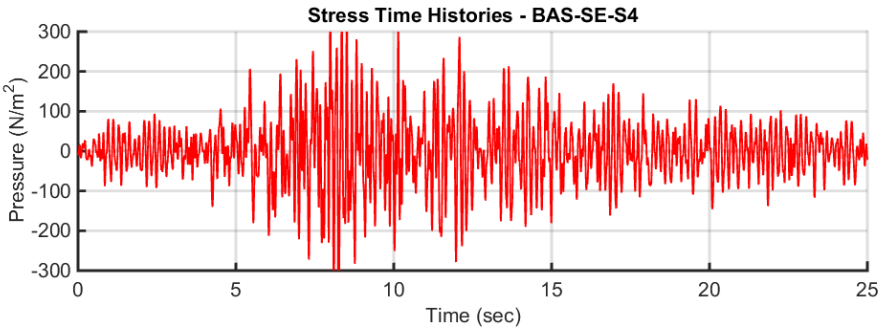

Figure 6.23 Computed pressure time history at the location of BAS-SE-S4 at a depth of 1.45 m

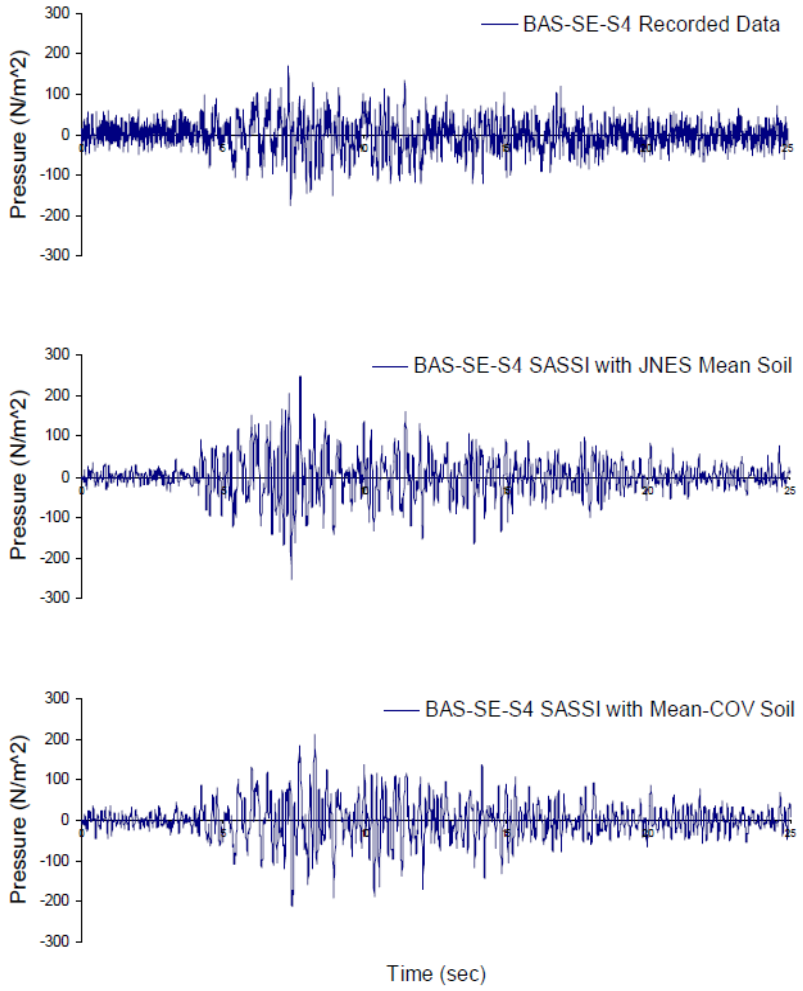

Figure 6.24 Comparison of seismic induced soil pressure at sensor BAS-SE-S4 at a depth of 1.45 m (Xu et al. 2008)

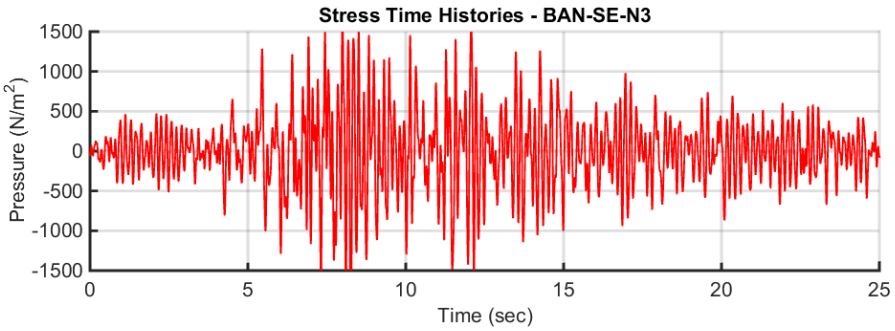

Figure 6.25 Computed pressure time history at the location of BAN-SE-N3 at a depth of 4.8 m

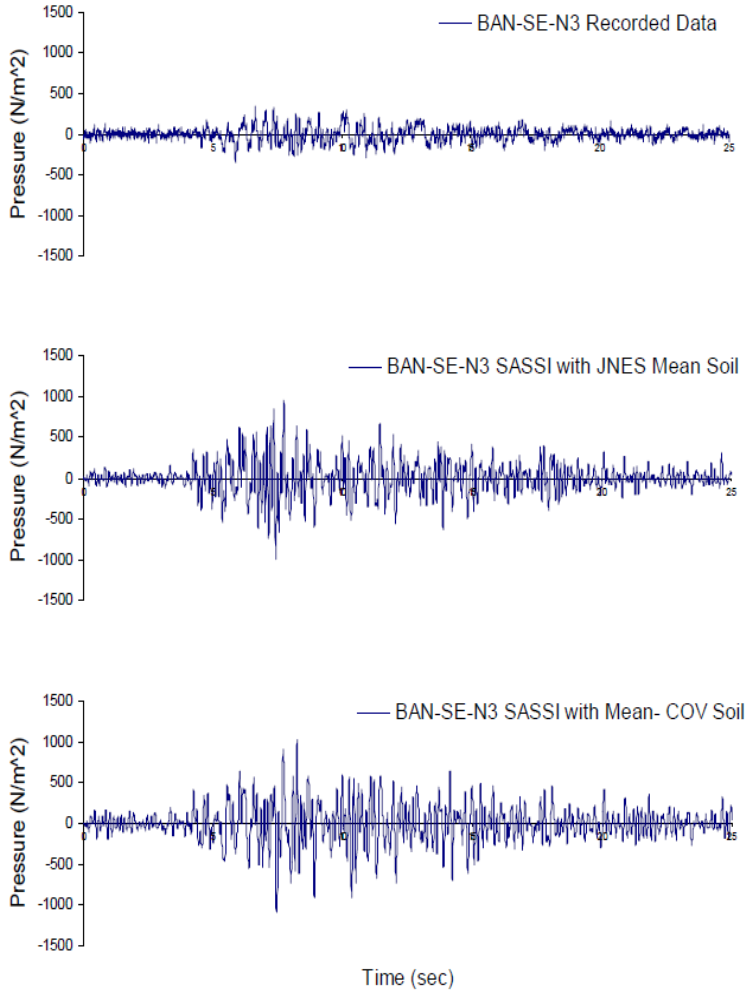

Figure 6.26 Comparison of seismic induced soil pressure at sensor BAN-SE-N3 at a depth of 4.8 m (Xu et al. 2008)

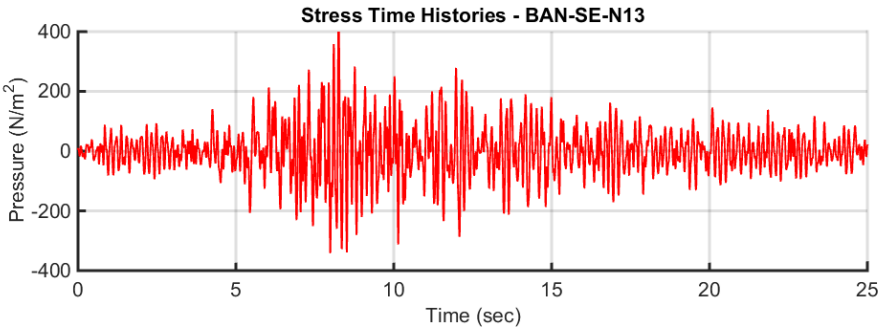

Figure 6.27 Computed pressure time history at the location of BAN-SE-N13 at a depth of 1.45 m

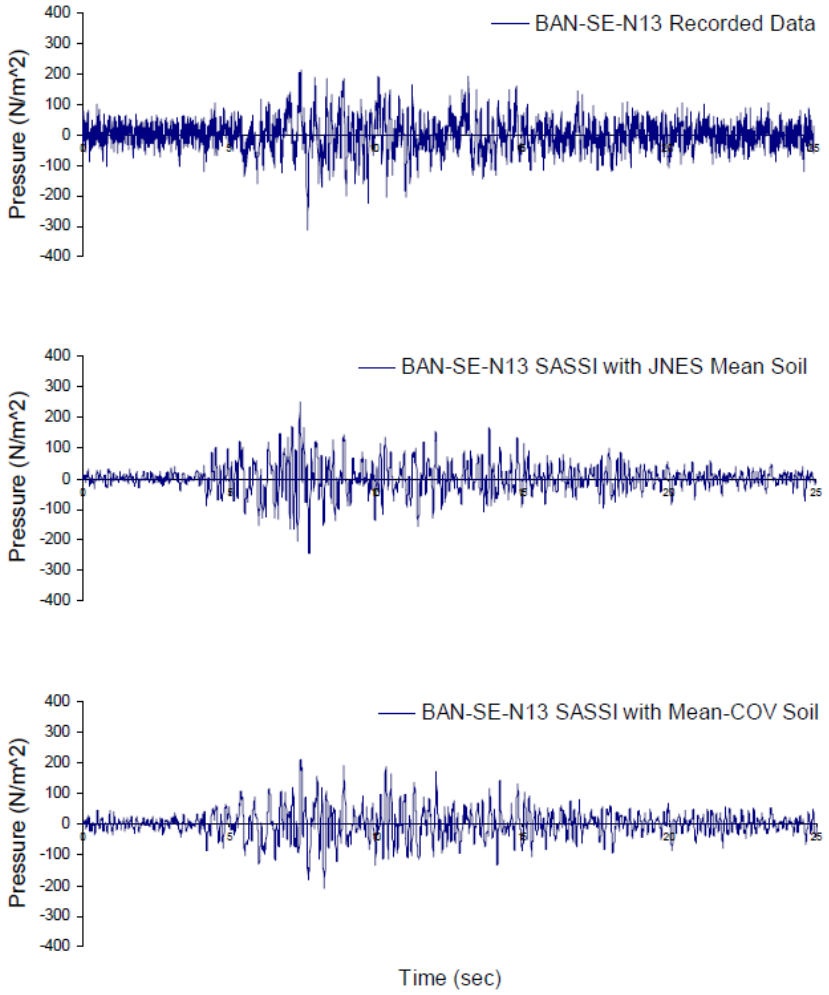

Figure 6.28 Comparison of seismic induced soil pressure at sensor BAN-SE-N13 at a depth of 1.45 m (Xu et al. 2008)

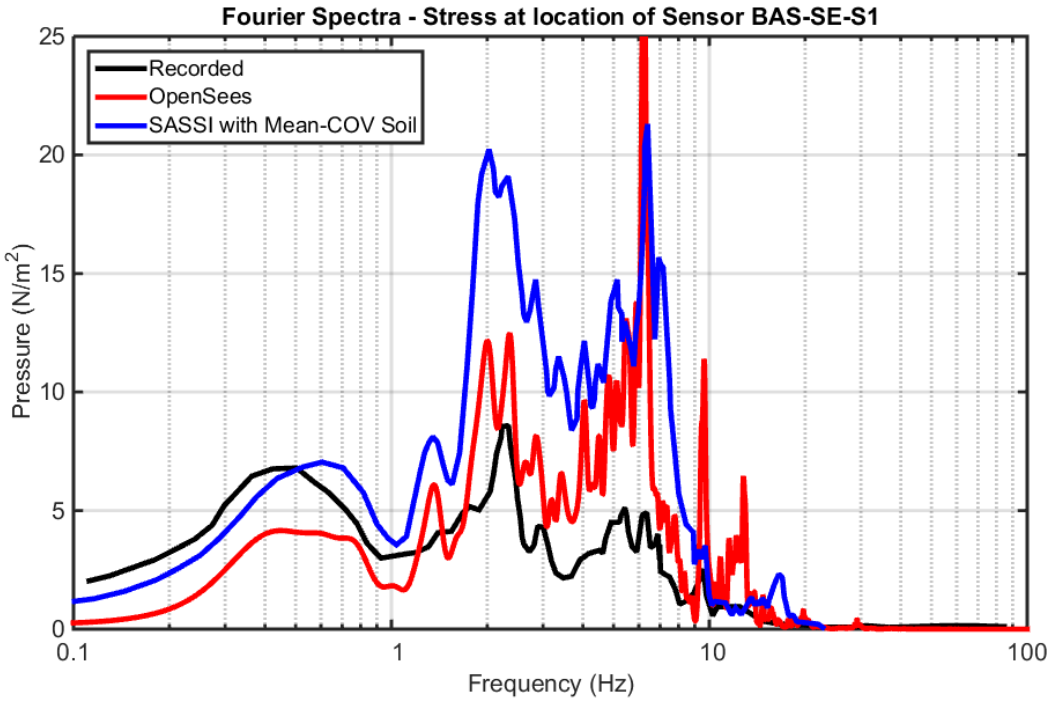

Figure 6.29 Comparison of the Fourier spectra at sensor BAS-SE-S1 at a depth of 4.8 m

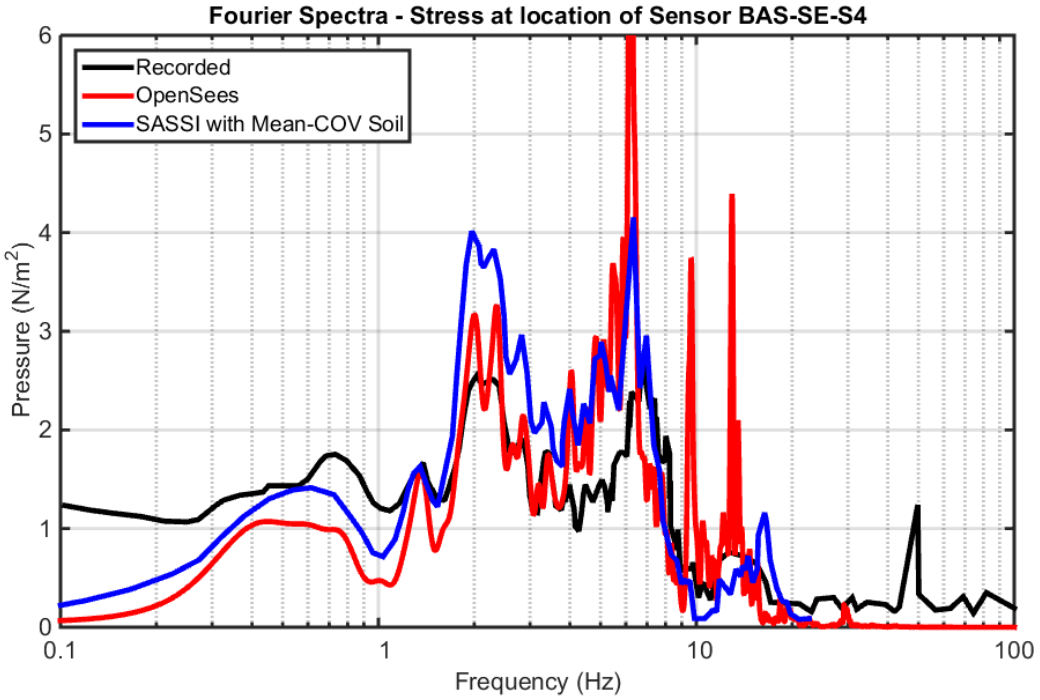

Figure 6.30 Comparison of the Fourier spectra at sensor BAS-SE-S4 at a depth of 1.45 m

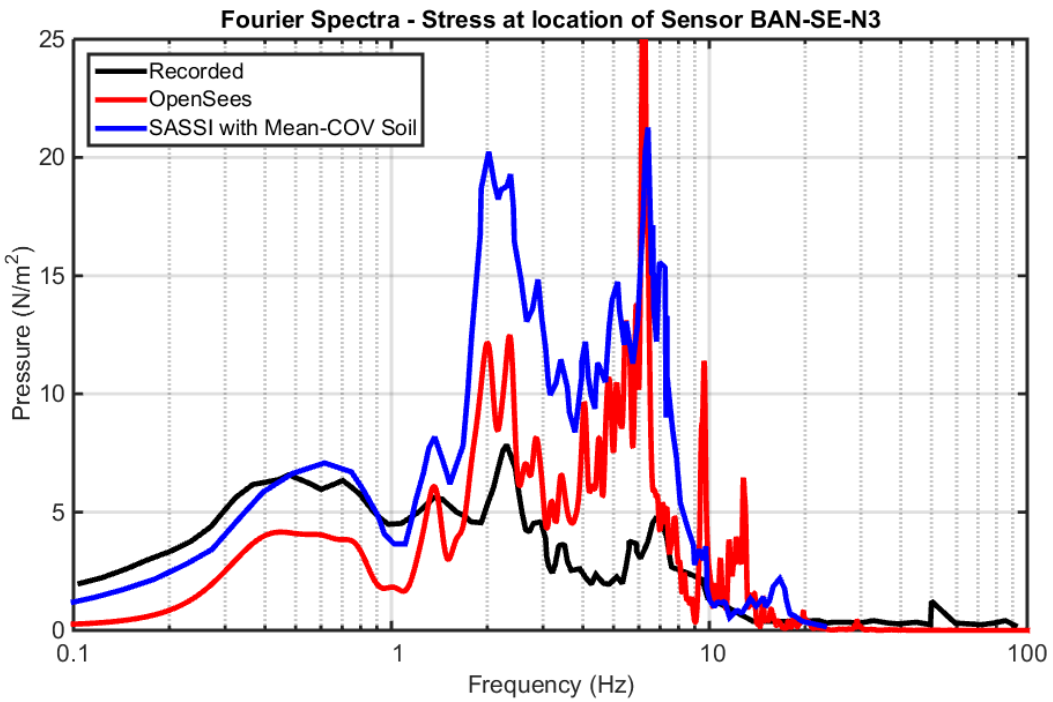

Figure 6.31 Comparison of the Fourier spectra at sensor BAN-SE-N3 at a depth of 4.8 m

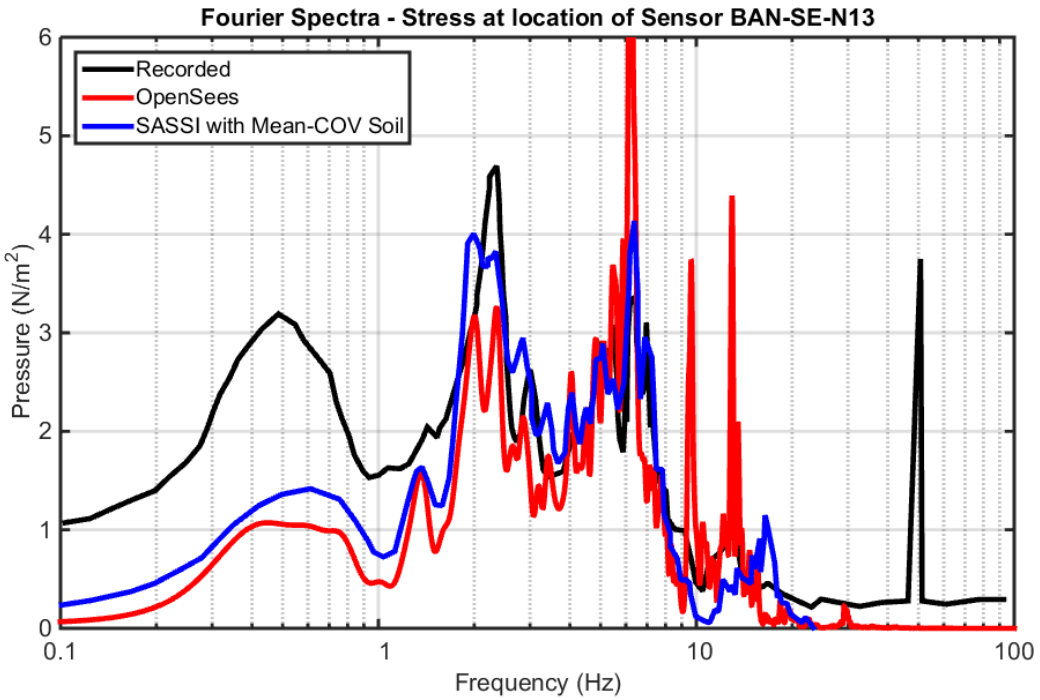

Figure 6.32 Comparison of the Fourier spectra at sensor BAN-SE-N13 at a depth of 1.45 m

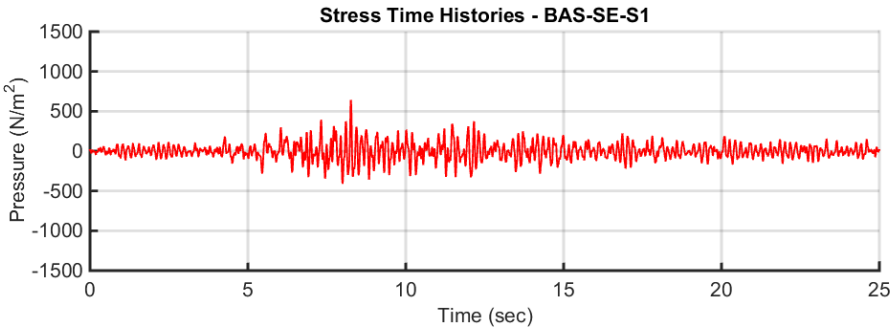

Figure 6.33 Computed pressure time history at the location of BAS-SE-S1 after addition of weak soil at a depth of 4.8 m

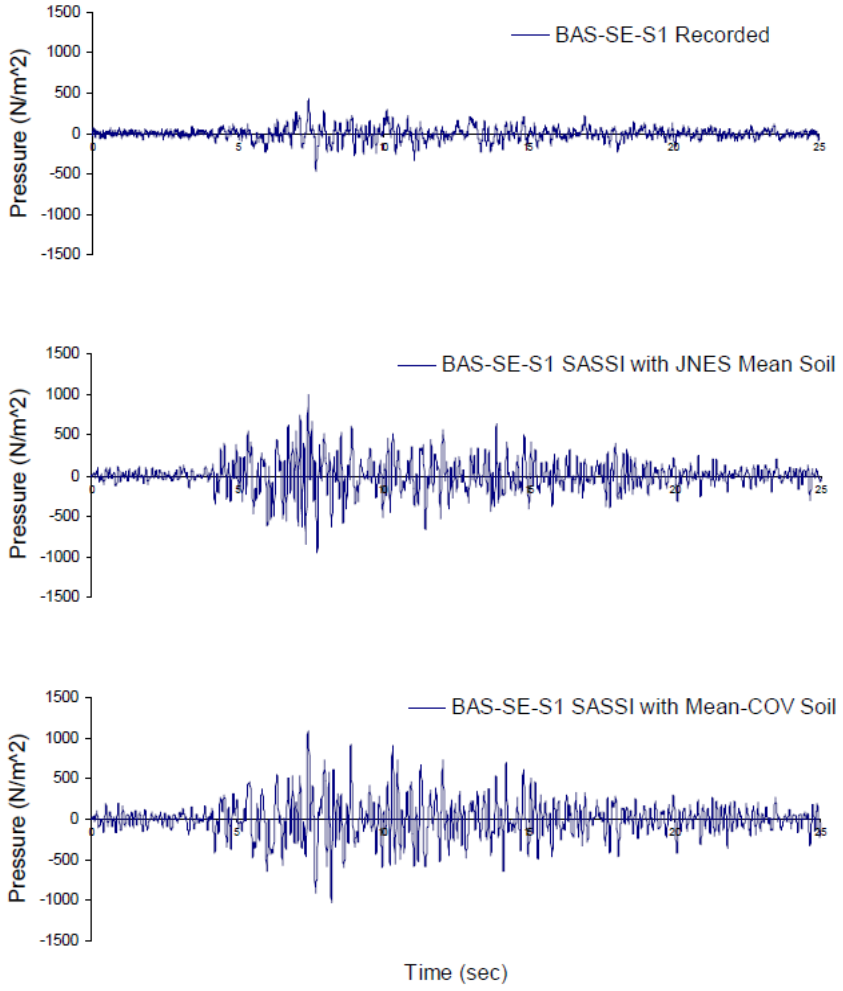

Figure 6.34 Comparison of seismic induced soil pressure at sensor BAS-SE-S1 at a depth of 4.8 m (Xu et al. 2008)

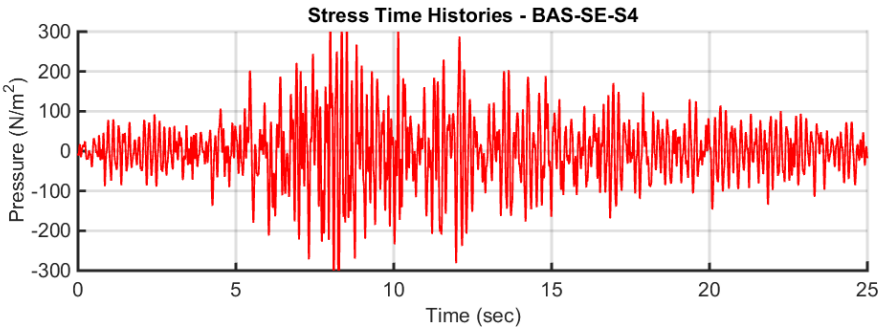

Figure 6.35 Computed Pressure Time History at the location of BAS-SE-S4 after addition of weak soil at a depth of 1.45 m

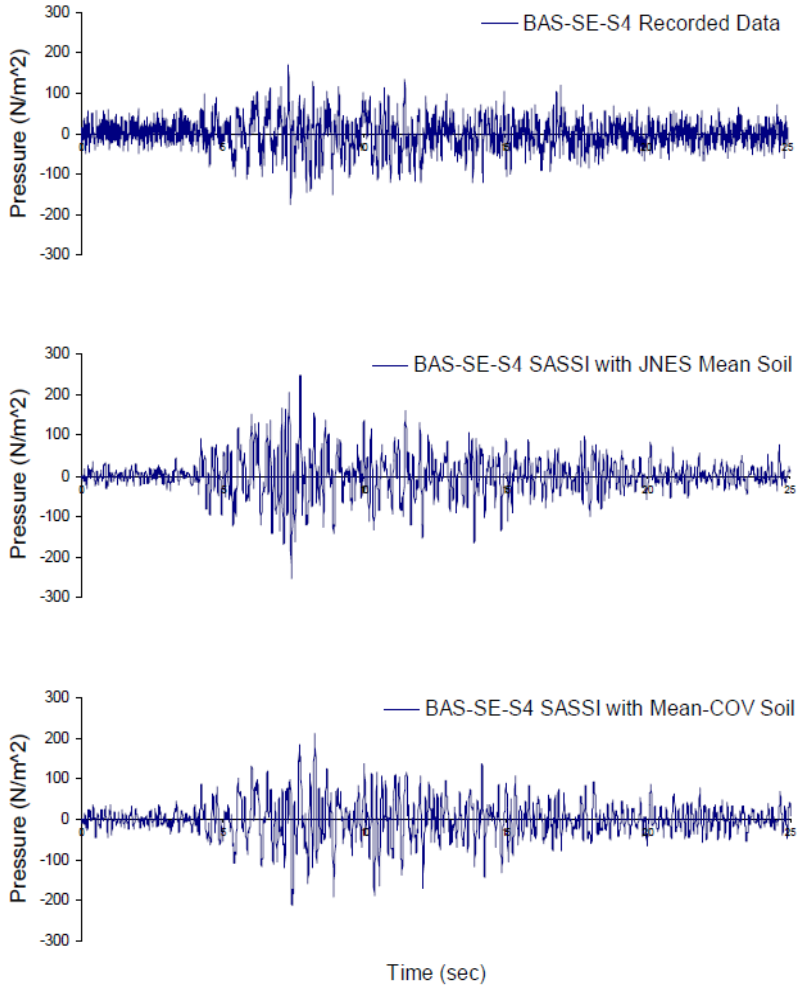

Figure 6.36 Comparison of seismic induced soil pressure at sensor BAS-SE-S4 at a depth of 1.45 m (Xu et al. 2008)

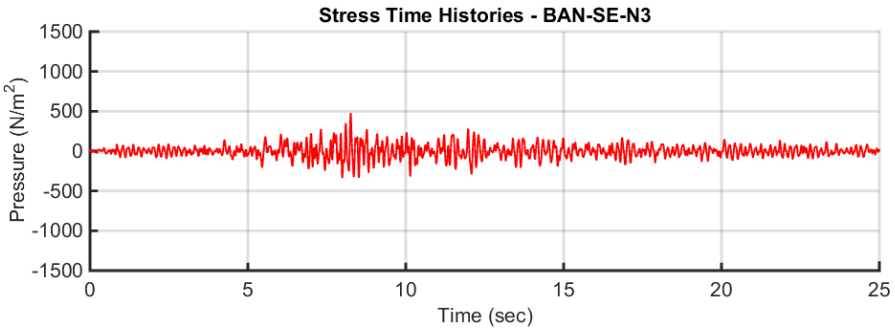

Figure 6.37 Computed pressure time history at the location of BAN-SE-N3 after addition of weak soil at a depth of 4.8 m

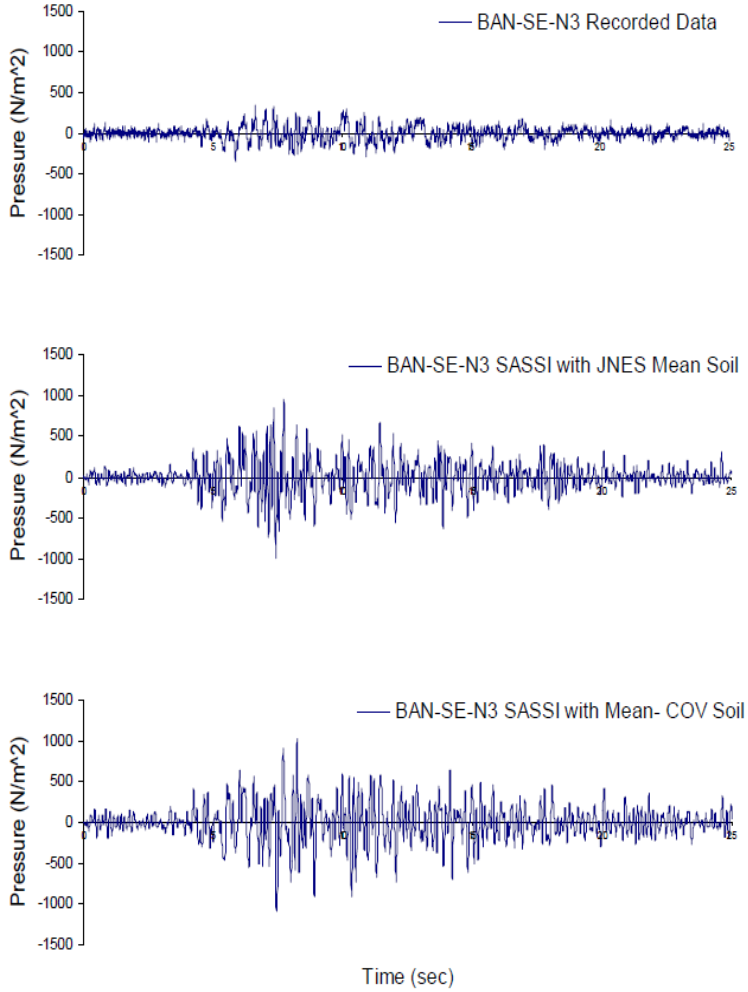

Figure 6.38 Comparison of seismic induced soil pressure at sensor BAN-SE-N3 at a depth of 4.8 m (Xu et al. 2008)

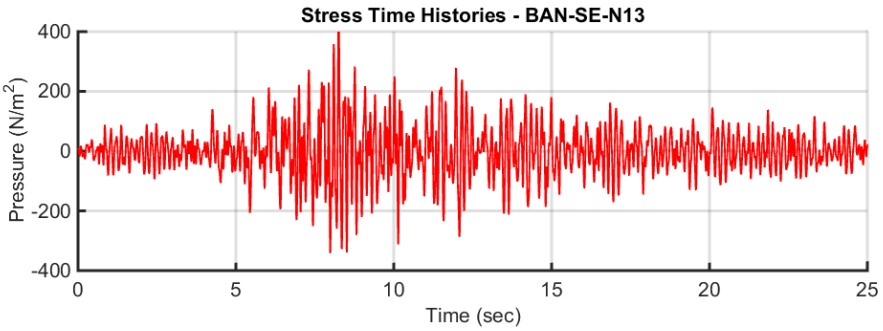

Figure 6.39 Computed pressure time history at the location of BAN-SE-N13 after addition of weak soil at a depth of 1.45 m

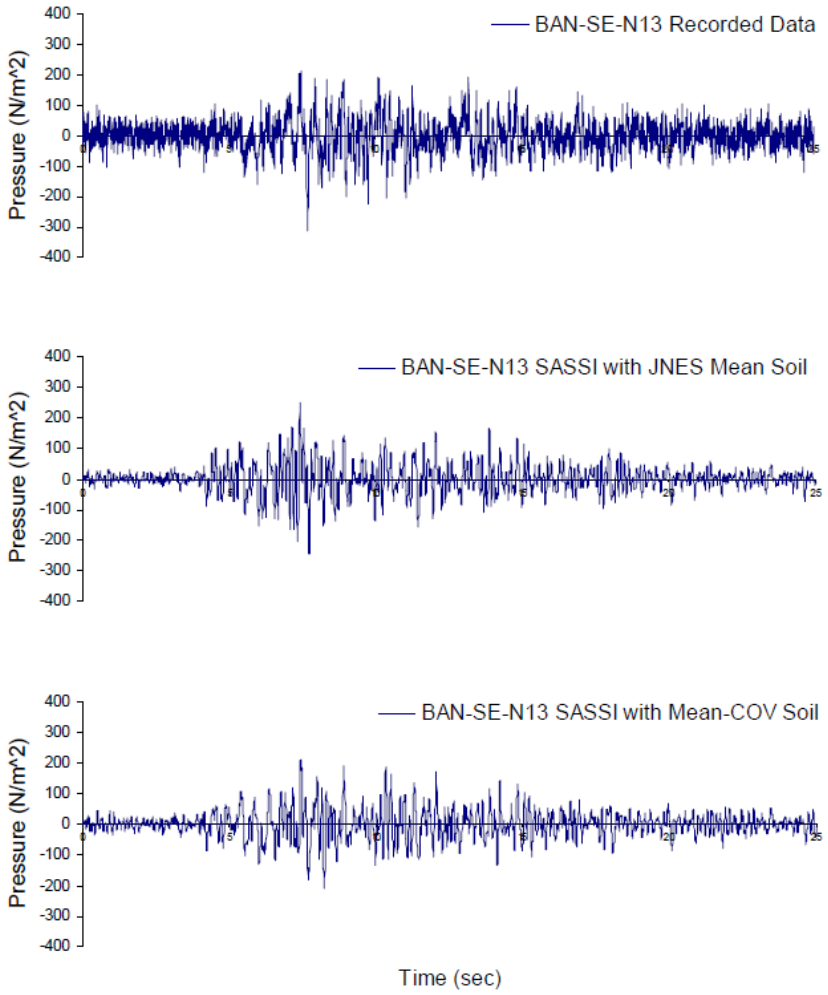

Figure 6.40 Comparison of seismic induced soil pressure at sensor BAN-SE-N13 at a depth of 1.45 m (Xu et al. 2008)

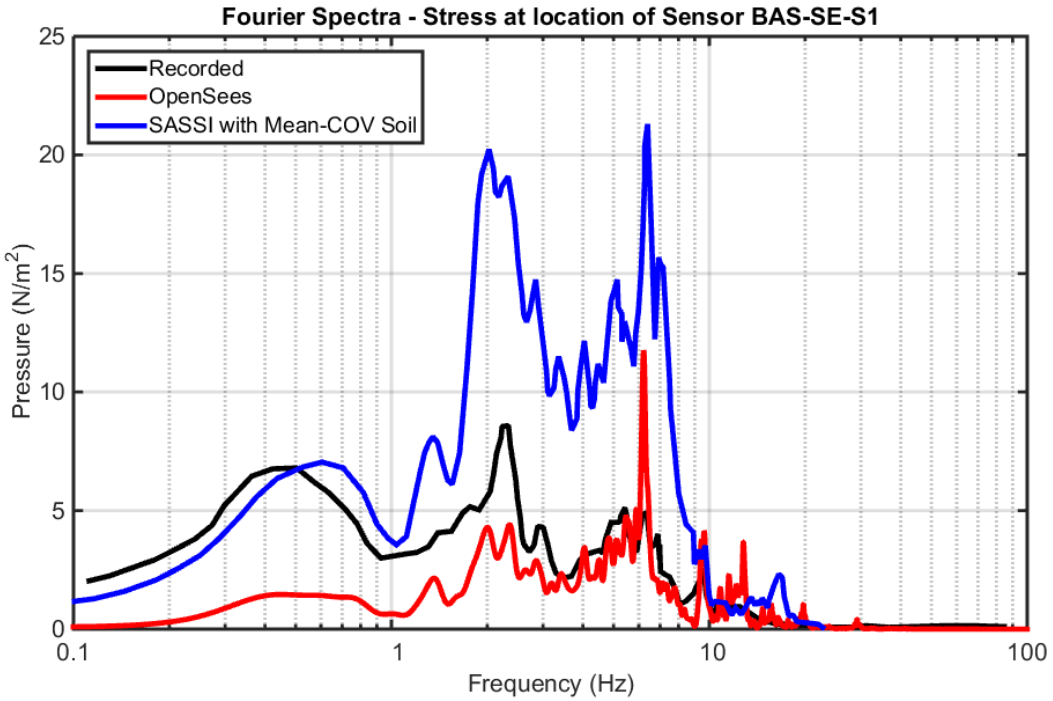

Figure 6.41 Comparison of the Fourier spectra at sensor BAS-SE-S1 after addition of weak soil at a depth of 4.8 m

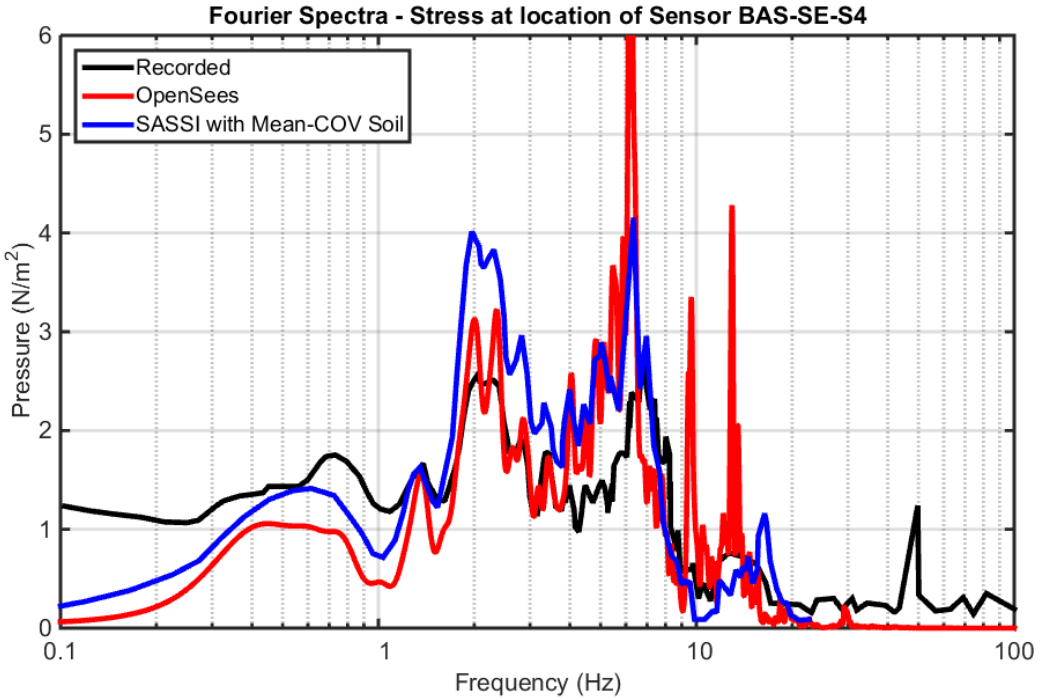

Figure 6.42 Comparison of the Fourier spectra at sensor BAS-SE-S4 after addition of weak soil at a depth of 1.45 m

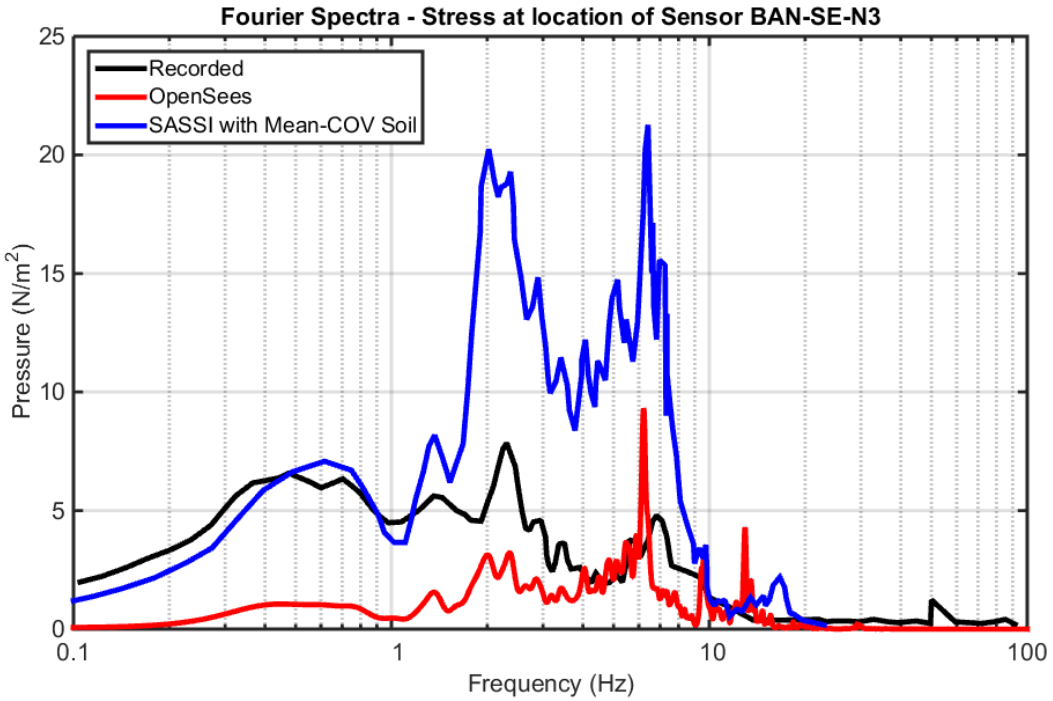

Figure 6.43 Comparison of the Fourier spectra at sensor BAN-SE-N3 after addition of weak soil at a depth of 4.8 m

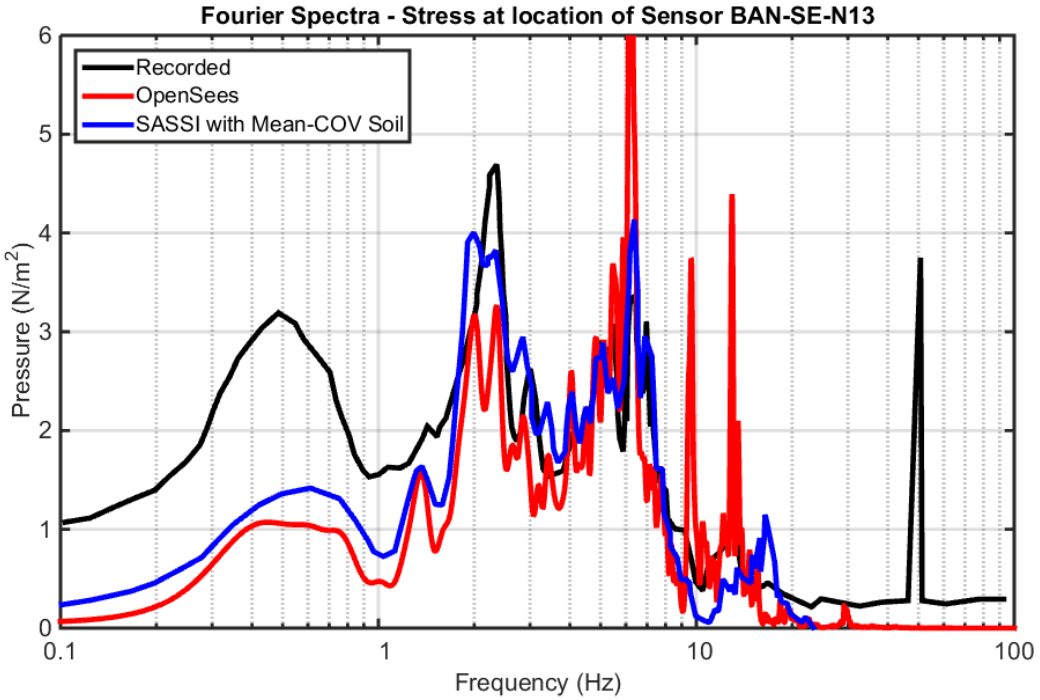

Figure 6.44 Comparison of the Fourier spectra at sensor BAN-SE-N13 after addition of weak soil at a depth of 1.45 m

Chapter 7

Recorded Seismic Response at the Fukushima Daiichi Nuclear Power Plant and Adjacent Downhole Arrays

7.1 Abstract

An opportunity to investigate seismic response and associated soil-structure interaction (SSI) mechanisms due to strong shaking was permitted by availability of data from the Fukushima Nuclear Power Plant (NPP). The magnitude 9.1 (M_w) Tōhoku earthquake was one of the most powerful recorded earthquakes to date and exceeded the design levels for a number of nuclear reactors. The data set includes recorded response of six boiling water reactors (BWR), and nearby ground downhole arrays at NPP site. The characteristics of seismic response at different depths within the ground can be inferred from the downhole records. Low amplitude as well as nonlinear response of the ground was evaluated using system identification techniques. During strong shaking, a clear and significant reduction in stiffness was observed within the upper soil strata. Of

special interest was the response of the most heavily instrumented BWR, Unit 6. Response at the base of Unit 6 was compared to that of the nearby downhole arrays. Amplification of motion along the height of Unit 6 was evaluated, revealing the primary role of rocking response. As such, the containment structure of Unit 6 behaved mainly as a rigid body and the amplification at the top of the reactor was primarily due to the observed rocking response.

7.2 Introduction

Data related to the seismic response of nuclear power plants (NPP) serves as an important source of information concerning the actual behavior of these large structures. Generally, such data have not been readily available, and the nuclear industry has been striving to generate related insights through alternatives such as large-scale experimentation. Over the last couple of decades, there have been a number of experiments seeking to investigate the seismic response of NPP structures with some of the most prominent including those at Lotung and Hualien (Luco and Wong 1990; Tang and Stepp 1990; de Barros and Luco 1995; Elgamal et al. 1995; Elgamal et al. 1996; Graves et al.1996; Ganev et al. 1997; Zeghal and Elgamal 2000; Luco and Francisco 2004; Luco and de Barros 2005). These experiments sought to evaluate the adequacy of soil-structure interaction (SSI) models and to develop related guidelines.

To ensure that there would be significant SSI effects in the Lotung experiment, a 1/4 scale model was constructed in the soft soils of Lotung (Tang and Stepp 1990). In general, it was concluded that the SSI models came reasonably close, and differences between the recorded and computed response were largely attributed to two factors, uncertainties in characterizing the ground properties and limitations in the SSI modeling techniques. Following the Lotung project, additional experiments were conducted in the highly seismic region of Hualien to complement the former study. Similar to Lotung, a 1/4 scale model was constructed, but in stiff soils (Graves et al.

1996). It was concluded that the numerical models matched fairly well with the recorded data. Great care was essential in modeling the boundary conditions and backfill material.

More recently, a large-scale experiment was conducted at Aomori, Japan (Xu et al. 2003; Xu et al. 2008; Clouteau et al. 2012) to investigate various aspects of soil-structure interaction. The project examined the response of both excavated and embedded $1/10^{th}$ scaled models of nuclear reactor structures and highlighted the need to consider uncertainties in soil properties. Due to the low level of shaking, the experiment was limited to assessment of essentially linear response. It was concluded that current finite element formulations achieved a level of success modeling the recorded weak motion response, and that further research was recommended for stronger seismic events where nonlinearity can be expected.

During the Tōhoku earthquake, instrumentation at the Fukushima Daiichi NPP recorded an invaluable data set (TEPCO 2011a) of seismic response due to strong shaking. This earthquake was one of the strongest recorded events to date and exceeded the design levels for a number of the nuclear reactors at the Fukushima Daiichi NPP (FNAIIC 2012). Soon thereafter, the external power supply was interrupted, impeding efforts to avert subsequent tsunami-induced damage. As such, specific structural damage if any due to seismic excitation was not possible to fully specify (FNAIIC 2012).

In this paper, seismic response of the instrumented nuclear reactors, and nearby geotechnical arrays (TEPCO 2011a) from the Tōhoku earthquake are investigated. The downhole arrays are examined using frequency and time domain techniques to characterize the ground properties in which the reactors are located. Thereafter, the response of the reactors, with a focus on the highly instrumented Unit 6, are discussed. As such, the salient seismic response characteristics of the site, and reactor are highlighted and analyzed.

7.3 Instrumentation at the Fukushima Daiichi Nuclear power plant

7.3.1 Nuclear Power Plant Configuration

The Fukushima Daiichi NPP (Figure 7.1) is located on a bluff off the eastern coast of Japan. Elevations at this region are referenced to the Onahama Port datum line (O.P.) and will be used throughout this paper (e.g., sea level is at +0 meters). The site (Figure 7.3) was originally +35 meters above sea level but was lowered to +10 meters for the construction of the NPP (Amano 2015). Excavation was done for a number of reasons including reducing the operational costs of pumping seawater and constructing the reactors on the equivalent of solid bedrock (Amano 2015). At the time of construction, it was believed that the constructed sea wall was more than sufficient to mitigate the risk of flooding despite the significantly lower elevation.

The NPP consisted of 6 boiling water reactors (BWR). Construction of the first reactor (Unit 1) started in 1967. The last reactor (Unit 6) was added many years later in 1979 (IAEA 2018). As depicted in Figure 7.1, the reactors were placed into two separate groups. Unit 1 – 4 were adjacent to one another on the south side of the NPP, while Unit 5 – 6 were on the north side. The reactors were all approximately 60 m high and embedded about 12 m (~20% of the total height) into the ground. Accompanying each reactor was a turbine building which was significantly shorter. The reactors and turbine buildings were all aligned in the east-west direction. In addition to these instrumented structures, there were two nearby downhole arrays south of Unit 1 – 4 and north of Unit 5 – 6 which will be referred to as the south array and north array respectively (Figure 7.1 – Figure 7.3).

Since the time of construction, the safety guidelines have long become outdated, and the NPP required a seismic risk reevaluation. The area was initially considered to have minimal

seismic activity and the demand was evaluated at a peak ground acceleration of 0.265 g (FNAIIC 2012). After more seismic data became readily available, it was concluded that the demand should be doubled (Table 7.1) and improvements were necessary to satisfy the updated guidelines (FNAIIC 2012). Despite the revised regulations, the Tōhoku earthquake clearly exceeded the design levels at a number of the reactors (Table 7.1).

7.3.2 Instrumentation at the Reactor and Turbine Buildings

At the Fukushima Daiichi NPP, all six units were instrumented with accelerometers at the basement of the reactors. Of the six reactors, Unit 6 was the most heavily instrumented and included additional sensors that were not present in Units 1 – 5. The floor and elevation view of Unit 6 are depicted in Figure 7.2 along with the label and location of eleven sensors (Figure 7.2) that were installed on the various floors of Unit 6 including the basement (+1.0 m), second floor (+19.0 m), sixth floor (+51.5 m) and roof (+65.5 m). Many of the floors included multiple sensors and recorded data in the East-West (E-W), North-South (N-S) and Up-Down (U-D) directions. Through these sensors, a unique opportunity was made available to investigate the seismic response of these large embedded structures due to strong shaking, and to document the response throughout the height of the reactor (TEPCO 2011a).

7.3.3 Instrumentation at the adjacent geotechnical arrays

There were two nearby geotechnical arrays approximately 1500 meters apart, south and north of the Fukushima Daiichi NPP (Figure 7.1 and Figure 7.3). The south array was on the bluff (ground surface at +34.9 m) which was the original height of the site prior to excavation (Figure 7.3). The north array was located in the excavated region (ground surface at +14.2 m), closer to the elevation at which the reactors were constructed. At the site, sandy loams were found near the

ground surface of the bluff (+20 to +35 m) with a combination of sandstone and mudstone underneath. The excavated region was lowered to the depth of the mudstone. Fills, sands, and gravels can be found near the ground surface of the excavated region.

Each array consisted of five sensors which were placed at 2 meters below ground surface, and at an elevation of -5, -100, -200, and -300 meters. The reported shear/pressure wave velocity profiles (TEPCO 2011a) for each downhole array are shown in Figure 7.4. In the upper 20 meters, the shear wave velocity (V_S) ranged from 430 – 460 m/s with a thin weak layer interbedded (120 – 280 m/s). Underneath, V_s increased to 460 – 610 m/s at an elevation of -20 – -100 meters and reached 780 m/s at -300 meters. Based on the measured stiffness, the calculated Poisson's ratio (ν) ranged from 0.42 to 0.49.

7.3.4 Recorded earthquake ground motions

The Fukushima Daiichi NPP is located in a seismically active region in Japan. In 1978, the Miyagi earthquake with a PGA of 0.125 g struck the NPP but no damage was detected (Brady 1980). Following this, one of the most powerful seismic events, the Tōhoku earthquake devastated Japan on March 11, 2011. The epicentral distance was approximately 180 kilometers away from Fukushima NPP. The resulting demand exceeded the design levels by as much as 20% for Units 2, 3, and 5 at the Fukushima Daiichi nuclear power plant (Table 7.1). The earthquake was reported to have a magnitude M_w = 9.1 with a duration in excess of 2 minutes (USGS 2018).

The recorded acceleration time histories at the south and north downhole arrays are shown in Figure 7.5 and Figure 7.6. At both arrays, there was minimal amplification until near ground surface where peak acceleration exceeded that of the underlying station by a factor of 2 or more. At the south array for instance, maximum acceleration at the elevation of -5.0 m was about 0.36 g

and 0.25 g, increasing to 0.61 g and 0.47 g near ground surface for the E-W and N-S direction respectively.

The corresponding spectral accelerations are shown in Figure 7.7. From the spectral acceleration (Figure 7.7), it was observed that a broad range of frequencies between 2 Hz and 8 Hz were significantly amplified at both arrays, which is to be expected due to the expected nonlinearity of the soil. Furthermore, an additional low frequency peak was apparent for the E-W direction but not in the N-S.

7.4 Pattern recognition based on the earthquake records

The recorded acceleration time histories (Figure 7.5 and Figure 7.6) at the south and north downhole arrays allow for an assessment of the site properties. These properties were evaluated using both time and frequency domain analysis techniques as discussed below.

7.4.1 South Array

By examining the Fourier spectral ratios of the two uppermost sensors (+32.9 m and -5.0 m) at the south array, the natural frequencies can be identified. The low-strain properties can be estimated from the relatively weaker portion of the record. At the south array there are three identifiable peaks for the E-W and N-S directions (Figure 7.8) which are around 2.6 Hz, 6.6 Hz and 11 Hz As to be expected, the higher resonances tended to have less amplification when compared to the first and are at frequencies close to what one would result from shear beam site amplification response. When considering such a shear beam with a height of 39.9 m (from +34.9 m to -5.0 m including the 2 meters above the first sensor) and natural frequency of 2.6 Hz, the corresponding average V_S is around 415 m/s ($f = V_s/4H$) which is comparable to the V_S as determined from the in-situ investigation (average V_S of 432 m/s).

When the fundamental frequency of the transfer function is displayed with respect to time (Figure 7.9), change in stiffness of the topmost soil stratum can be evaluated. As shown, the frequency at the end of shaking (> 200 seconds) is similar to what was identified at the beginning. During the interval of stronger shaking, the peak frequency was observed to decrease to as low as 2.3 Hz. This degradation corresponds to as much as a 20% reduction in the low-strain shear modulus (G). Furthermore, the observed nonlinearity appeared to be fairly consistent for both orthogonal directions and followed a similar trend. Similar to the first mode, the higher natural frequencies, decreased significantly during the portion of strong shaking, returning to the initial value near the end of shaking. When examining the response at deeper depths (i.e., below the -5.0 m sensor), there was no observable nonlinearity, due to the much lower acceleration amplitudes (Figure 7.5 and Figure 7.6) and stiffer soils.

7.4.2 North Array

At the north array, soil height (H) between the uppermost two sensor (+14.2 m and -5.0 m) is 19.2 m. Within this zone, average V_s is 412 m/s based on in-site investigations (TEPCO 2011a). Upon examining the change in fundamental frequency of the uppermost sensors transfer function (Figure 7.10), it can be seen that the fundamental frequency initially starts near 7 Hz, quickly drops, and gradually rebounds back, but only reaches a lower value of about 5.4 Hz. The frequency at the end of the record (5.4 Hz) appears to be a more reasonable estimate for the fundamental resonance ($f = V_s/4H$), resulting in a V_s of about 415 m/s, which is in close agreement with its documented counterpart. As such, the initial 7 Hz estimate requires further scrutiny, with potential influence of aging effects or other factors related to the wave propagation patterns in the vicinity of this location.

Between 100 and 150 seconds, the seismic event increased in intensity and the soil stiffness was reduced considerably. As shown, the frequency decreased by a quarter of its' initial value and was consistent in both orthogonal lateral directions, which corresponds to a reduction of about 50% of the initial *G*. The reduced frequency during the strong shaking phase appeared to be in close agreement with the amplified frequency in the response spectrum (Figure 7.7). After about 200 seconds, the soil essentially regained most of its initial stiffness. Similar to the southern array, the deeper layers (i.e., below the -5.0 m sensor) exhibited no perceptible nonlinearity.

7.4.3 Comparison of downhole array responses

Overall the two downhole arrays exhibited fairly similar behavior despite the difference in elevation. At both locations there appeared to be little to no amplification until near ground surface. Deeper in the ground, peak accelerations were comparable for sensors between the elevations of -5 m and -300 m. Both downhole arrays exhibited significant nonlinearity at ground surface. Furthermore, the observed stiffness reduction was consistent in both orthogonal directions for the two arrays and was most prevalent during the strongest portion of the shaking event.

7.4.4 Identification of downhole array nonlinear site properties

In addition to the above efforts to extract the soil properties using time and frequency domain techniques, a 1D shear beam model was implemented in the open source finite element (FE) framework OpenSees (Mazzoni et al. 2006), to simulate the seismic response of the downhole arrays. To aid in this effort, Δ-DOGS (Beyhaghi et al. 2016) was utilized to identify the optimal set of material properties that would best replicate the recorded response. This software package is a derivative-free optimization algorithm which seeks to identify the global minimum of the objective function (Figure 7.12) by continuously adjusting the input soil modeling parameters. In

this analysis, the objective function was specified to be sum of squares of the difference in the recorded and computed ground surface spectral acceleration.

The shear beam model utilized the PressureDependMultiYield (PDMY) material model (Yang et al. 2003) to simulate the nonlinear soil response. The soil model defines the backbone curve using the initial shear modulus (G_{max}) specified at a user-defined reference pressure (1 atm) and the reference strain γ_r:

$$\tau = \frac{G_{max}\gamma}{1 + \frac{\gamma}{\gamma_r}} \tag{2}$$

The shear modulus increases based on the confinement with a pressure dependence coefficient of 0.5. The mass density was defined to be 2 Mg/m^3.

Prior to conducting the finite element simulations, the low strain properties were identified based on the predominant frequency at low-strain. As mentioned previously, the predominant frequencies for the south and north array were 5.4 Hz and 2.7 Hz. Based on these frequencies, the reference V_S (at a confinement of 1 atm) was defined to be 338 m/s and 310 m/s respectively at the south and north downhole arrays respectively.

With the low-strain stiffness of the shear beam defined, Δ-DOGS seeks to optimize the viscous damping and the reference strain γ_r (which defines the corresponding modulus reduction curve). For that purpose, Δ-DOGS controls viscous damping values at two selected frequencies within the range of amplification as observed from the ground surface response spectra (Figure 7.7). On this basis, at the north array, the damping was specified at 3 Hz and 5 Hz, while at the south it was specified at 2.5 Hz and 6.5 Hz.

Figure 7.13 compares the simulated response using the optimal material properties against the recorded response. In general, there was a good match in the frequency of the response although

the peak for the north array in the E-W direction appears to be slightly shifted. It was found that the modulus reduction curve as determined by Δ-DOGS was comparable to that of EPRI for a similar depth at the south and north arrays (Figure 7.14).

When examining the objective function with respect to the different combinations of viscous damping and γ_r (Figure 7.15), it was found that there was a narrow band that produced a similar match when compared to the optimal set of material properties. As to be expected when hysteresis damping decreases (by increasing γ_r), a higher Rayleigh viscous damping is necessary to compensate.

7.5 Basement response of the reactor structures and nearby ground

In addition to the downhole arrays, accelerometers were located in the basement of each reactor structures. From the horizontal motion response spectra (Figure 7.16), it can be observed that:

1. In general, basement responses bear significant similarity to those of the downhole array at similar depth (i.e., -5.0 m) as shown in Figure 7.7. Overall shape of the basement spectra appears to more closely match the ground response in their vicinity, with units 1-4 being closer to the south array and units 5-6 closer to the north array.
2. In the E-W direction, units 2, 3 and 5 exhibited larger peaks in the range of 3-4 Hz, exceeding the response of the other units by as much as 50 % or so.
3. In the E-W direction, peak basement accelerations varied in a fairly wide range of about 0.35 g – 0.55 g.
4. In the N-S direction, peak basement acceleration also varied in the wide range of about 0.3 g – 0.45 g. Furthermore, Units 1 and 5 appear to display significant peaks in the relatively

high frequency range of 10-20 Hz. To a certain extent, this high frequency also appears in the downhole array data (Figure 7.7), and is filtered out in the Unit 1-4, and 6 responses.

5. In the vertical direction, spectral acceleration at the basement were comparable across all the reactors (Figure 7.17). The response exhibited a primary peak at a frequency band of 2.5 to 5.0 Hz with the magnitude ranging from 0.7 g to 1.0 g. Furthermore, vertical acceleration in the range of 10-20 Hz reached as much as 0.55 g.

Anomalies in the above reported responses might be attributable to various considerations, including: i) dynamic characteristics of each individual NPP unit, ii) location of each structure at the site, with the units in two clusters including middle and corner configurations (Figure 7.3), and iv) variability of the ground motion at the site, and the associated overall SSI effects (Figure 7.3). At this point, the reported response serves to highlight the range of observed variability at the base of these closely spaced structures. Further scrutiny of this recorded response may be facilitated by availability of additional information as relates to the above-mentioned considerations.

7.5.1 Seismic Response of Unit 6 Reactor Structure

The following section is focused on the reactor-core building (Figure 7.2) from the basement (+1.0 m) to the 6th floor (+51.5 m). As mentioned above, Unit 6 basement acceleration was similar to that of the nearby north array -5.0 m as depicted in the time histories of Figure 7.18. From the acceleration spectra ( ), it may be observed that the frequency content of the reactor and downhole array response is comparable up to about 6 Hz, with peak values around 1.6 Hz. At higher frequencies, Unit 6 basement response is significantly reduced when compared to that of the downhole array for both the E-W and N-S directions. Such reduction in high frequency was

actually noted in the basement response of the other reactors and might be partially attributed to averaging effects (Yamahara 1970, Scanlan 1976, Luco and Wong 1986, Luco and Mita 1987).

In addition to the basement, Unit 6 included additional sensors on other floors and was the most heavily instrumented of the reactors (Figure 7.2). Upon examining these records (Figure 7.18), it is observed that the maximum basement acceleration was amplified from 0.44 g and 0.30 g to 0.50 g and 0.59 g at the 6th floor in the E-W and N-S directions respectively. As indicated from the FFT transfer function of 6th floor and basement lateral acceleration (Figure 7.20), the response around 3 Hz was considerably amplified by the reactor. As shown in Figure 7.20, peak resonance tended to appear at a slightly lower frequency as the shaking amplitudes increased during this seismic event. This amplification was observed in both lateral directions, prominently in the higher 6th floor response.

Furthermore, it was observed that lateral acceleration for sensors on the same floor were quite similar for both E-W and N-S directions (**Error! Reference source not found.**), an expected outcome due to the overall rigidity of the structure. On the other hand, vertical acceleration of sensors on the same floor were noticeably different (), indicating presence of a rocking response mechanism (Yim et al. 1980, Luco and Wong 1986, Bolisetti and Whittaker 2011). To further explore this mechanism, rotation of the structure was calculated using vertical response of sensors on the same floor, as well as lateral response of sensors on different floors. For that purpose, rotation is obtained by subtracting the particular vertical or horizontal responses being considered and dividing by the spacing between them.

The resulting rotation, shown in the orientation defined in the plane of sensors P3-P5 (Figure 7.2), was found to be consistent as calculated via the recorded vertical and horizontal motions (Figure 7.23 -). As such, the structure undergoes rocking, while behaving in large part as

a rigid body. From the FFT of this rotational response (Figure 7.26), it is observed that much of the amplification is around 3 Hz, coinciding with the identified reactor-basement resonance of Figure 7.20.

On the basis of this identified rocking response, lateral acceleration for each floor can be computed simply by using the recorded basement lateral motion and rotation. This response, assuming a rigid body idealization, is displayed in Figure 7.26 which compares the computed and recorded acceleration at the 2^{nd} and 6^{th} floors. Similarity in this response affirms that the amplification observed at the higher floors was due in large part to rocking, highlighting the fairly rigid configuration of this reactor building.

7.6 Discussion and conclusions

An initial effort is made to investigate the recorded response of the Fukushima Daiichi Nuclear Power Plant, in order to identify the salient characteristics associated with strong shaking at this site. Overall, the following conclusions may be drawn:

1. North and South Downhole Arrays
    i. In general, the time and frequency domain identified low-amplitude shear wave velocity V_s estimates were consistent with those from the earlier reported in-situ investigation data.
    ii. There was significant nonlinear response near ground surface which resulted in a maxim reduction of the order of 20% and 50% in the low-amplitude shear modulus for the south and north downhole arrays respectively. From the sensors at greater depths (> -5 m elevation), nonlinear response was not as readily perceptible.

iii. Significant amplification in ground acceleration was mainly in the zone between downhole sensors closest to ground surface.

iv. In addition to the fundamental, the south array demonstrated two additional higher site shear response resonances.

2. Basement Response of the Reactors

   i. A noticeable level of variability was observed in peak basement lateral acceleration of the 6 units, potentially due to considerations such as geometric layout of the structures, their individual dynamic characteristics, and the involved SSI and wave propagation mechanisms. Closer scrutiny may be facilitated by further availability of related information.

   ii. In general, basement motions were similar to their closest downhole sensor accelerations. A main difference was the significant reduction in high frequency content in the basement records (for frequency greater than about 6 Hz).

3. Reactor Unit 6

   i. The difference in the vertical acceleration at the same floor indicated presence of a rocking response.

   ii. The rotation computed using lateral motions was found to be consistent with that from the vertical motions, demonstrating the high rigidity of the structure.

   iii. As such, amplification of acceleration at the higher elevation was mainly due to rocking

   iv. In this seismic event, peak acceleration at the top was nearly double the values recorded at the basement level.

7.7 Acknowledgement

This research was partially funded by the US Nuclear Regulatory Commission with Dr. Thomas Weaver as the program Manager. This chapter has been submitted for publication to Soil Dynamics and Earthquake Engineering and titled as “Recorded Seismic Response at the Fukushima Daiichi Nuclear Power Plant and Adjacent Downhole Arrays”. The dissertation/thesis author was the primary investigator and author of this paper. Professor Elgamal and Professor Bewley cooperated as co-authors to this journal paper.

Table 7.1 Observed data from the Tōhoku earthquake and design PGA for the Fukushima Nuclear Power Plants (TEPCO 2011b)

NPP		Recorded PGA			Design PGA		
		N-S	E-W	U-D	N-S	E-W	U-D
Fukushima Daiichi	Unit 1	0.47	0.46	0.26	0.50	0.50	0.42
	Unit 2	0.35	0.56	0.31	0.45	0.45	0.43
	Unit 3	0.33	0.52	0.24	0.46	0.45	0.44
	Unit 4	0.29	0.33	0.20	0.46	0.45	0.43
	Unit 5	0.32	0.56	0.26	0.46	0.46	0.44
	Unit 6	0.30	0.45	0.25	0.45	0.46	0.42
Fukushima Daini	Unit 1	0.26	0.23	0.31	0.44	0.44	0.52
	Unit 2	0.25	0.20	0.24	0.44	0.44	0.51
	Unit 3	0.28	0.22	0.21	0.44	0.44	0.51
	Unit 4	0.21	0.21	0.29	0.42	0.42	0.51

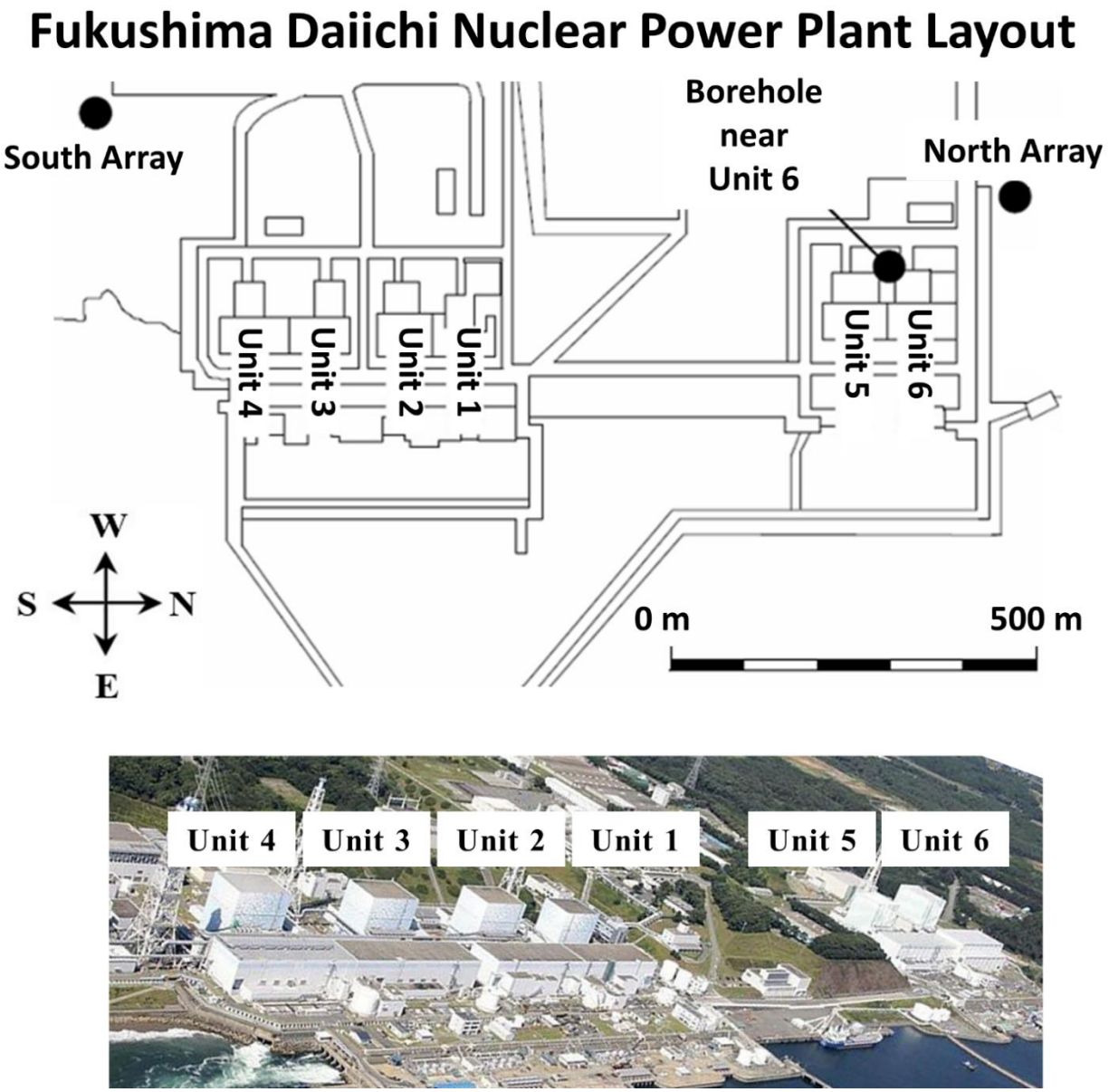

Figure 7.1 Plan view of Fukushima Daiichi Nuclear Power Plant. (adapted from TEPCO 2011a; AP Photo/Yomiuri Shimbun, Masamine Kawaguchi)

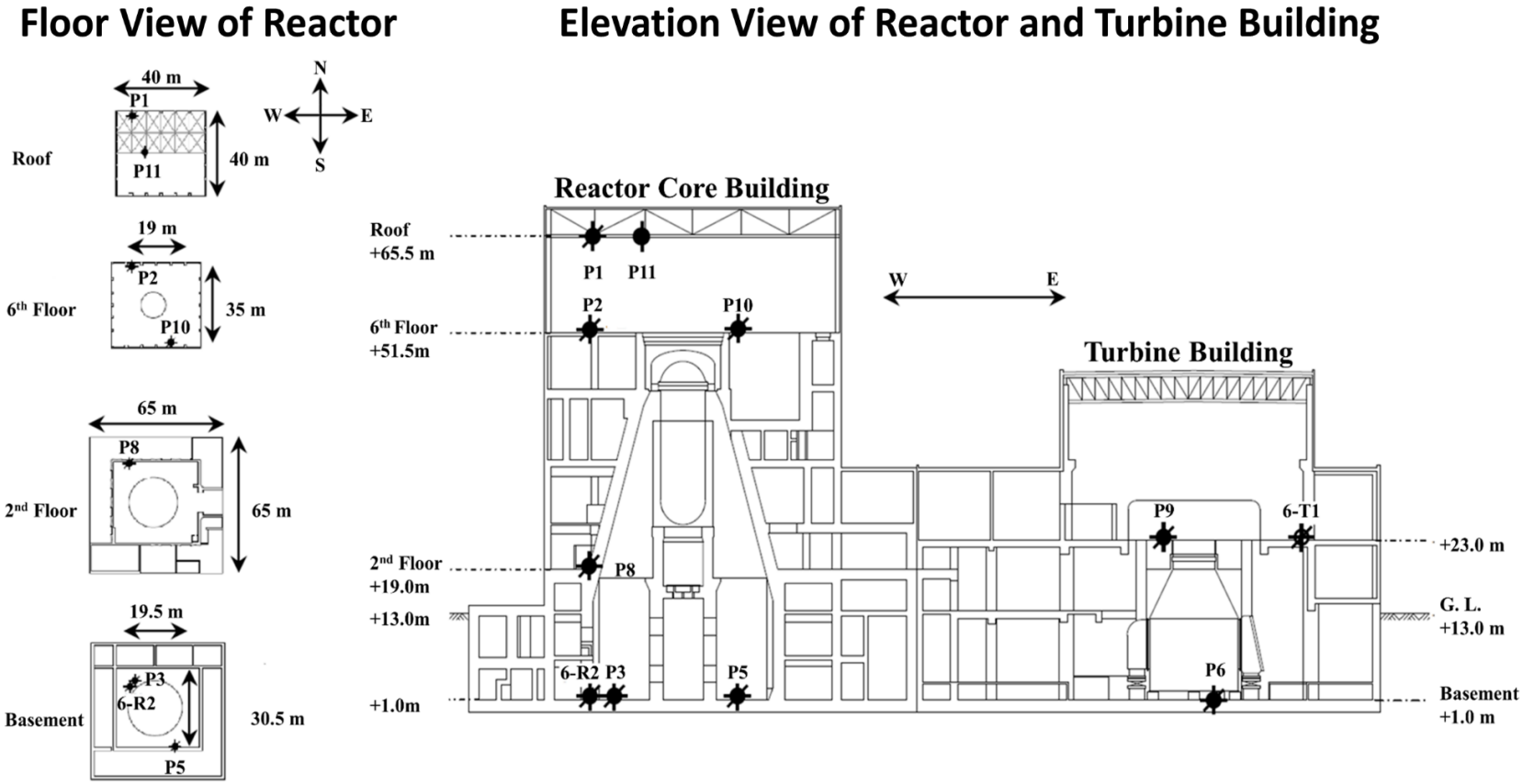

Figure 7.2 Layout of sensors deployed on Unit 6. (adapted from TEPCO 2011a)

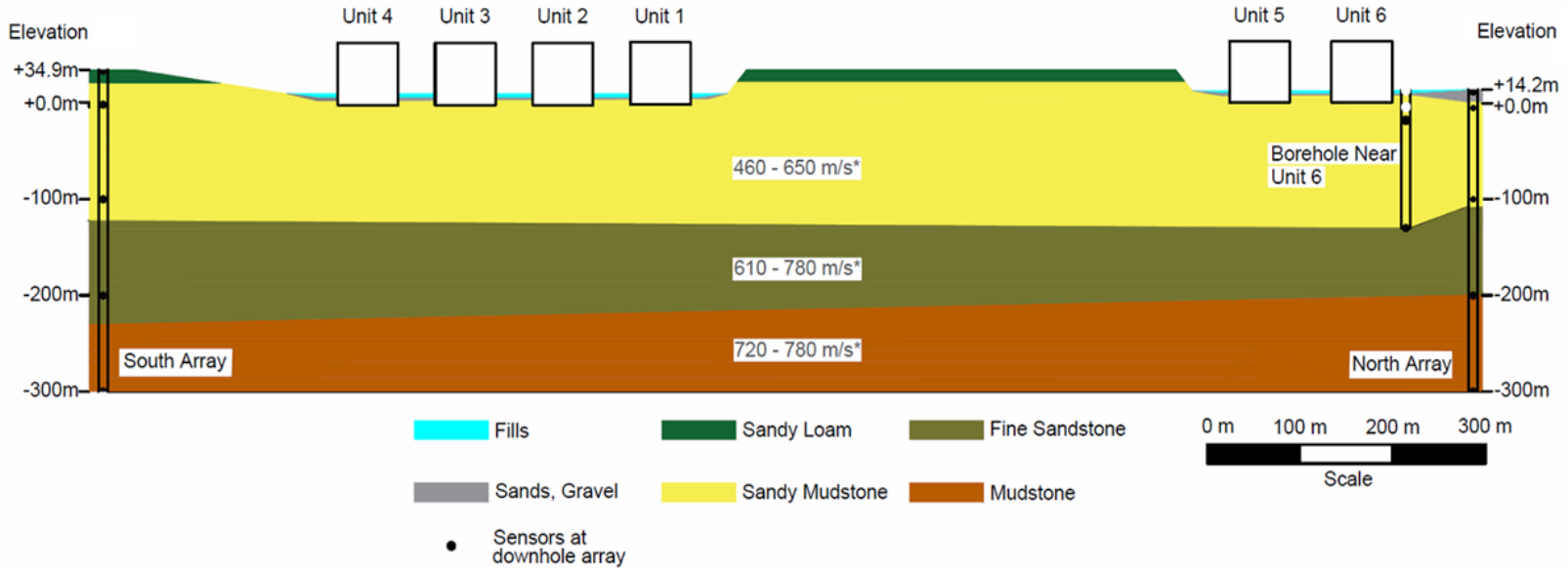

Figure 7.3 Soil profile at the Fukushima Daiichi Nuclear Power Plant (NPP) based on data from the downhole data (after TEPCO 2011a) with sea level at +0 meters
* Shear wave velocity increases with depth

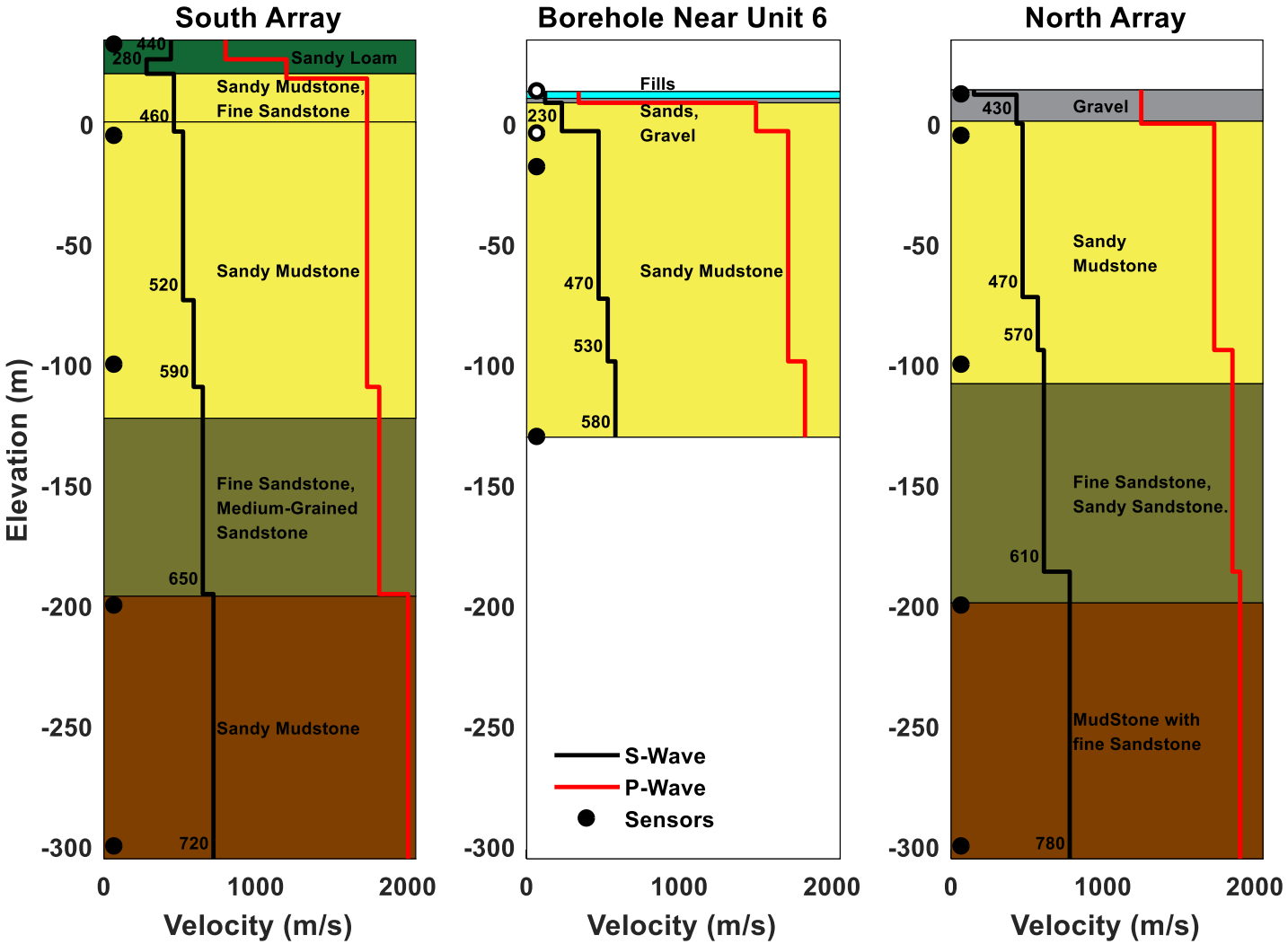

Figure 7.4 Soil profiles at the Fukushima Daiichi NPP site as documented by Japan Association for Earthquake Engineering (adapted from TEPCO 2011a)

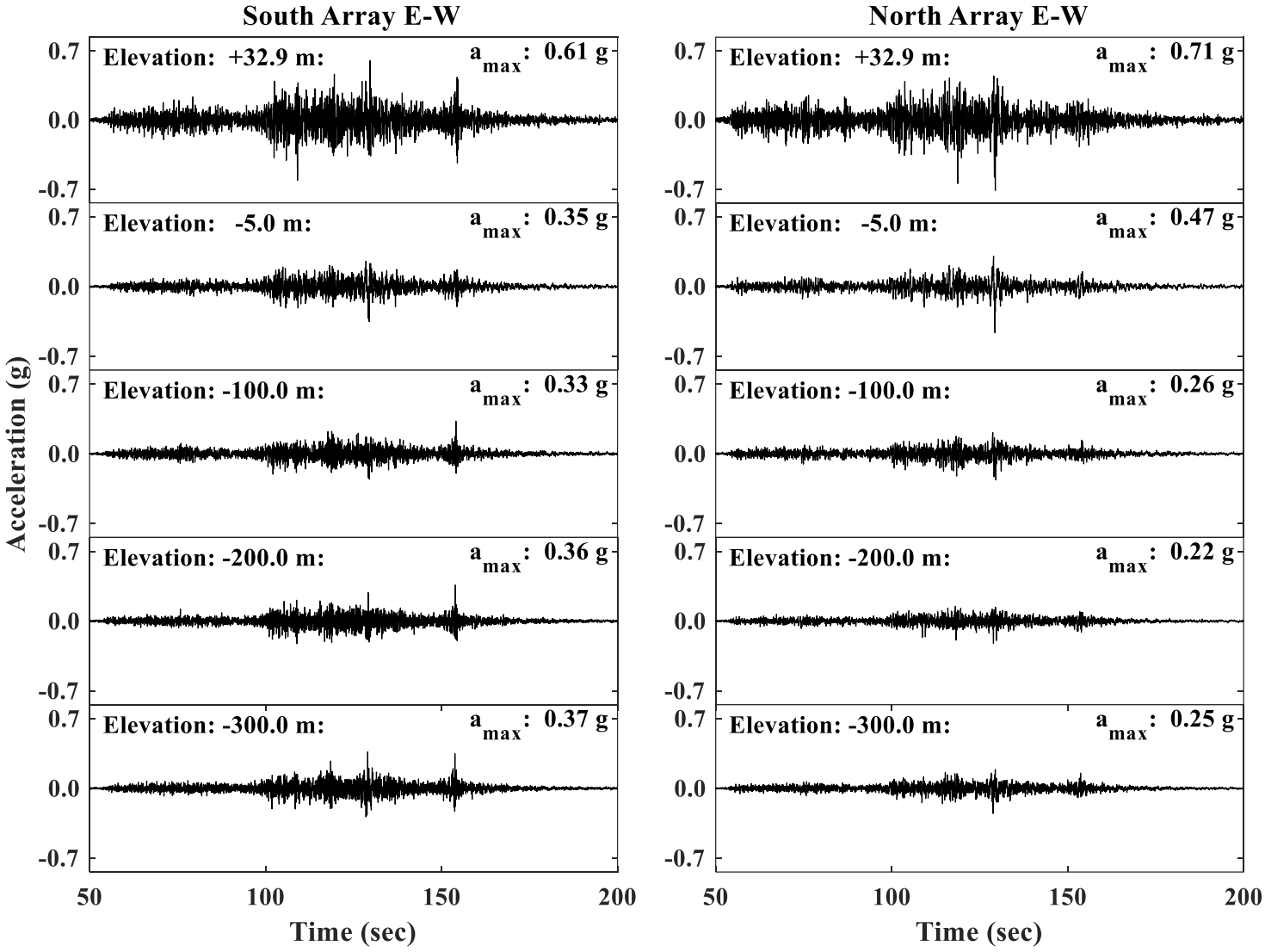

Figure 7.5 E-W Acceleration time history at the south and north downhole arrays

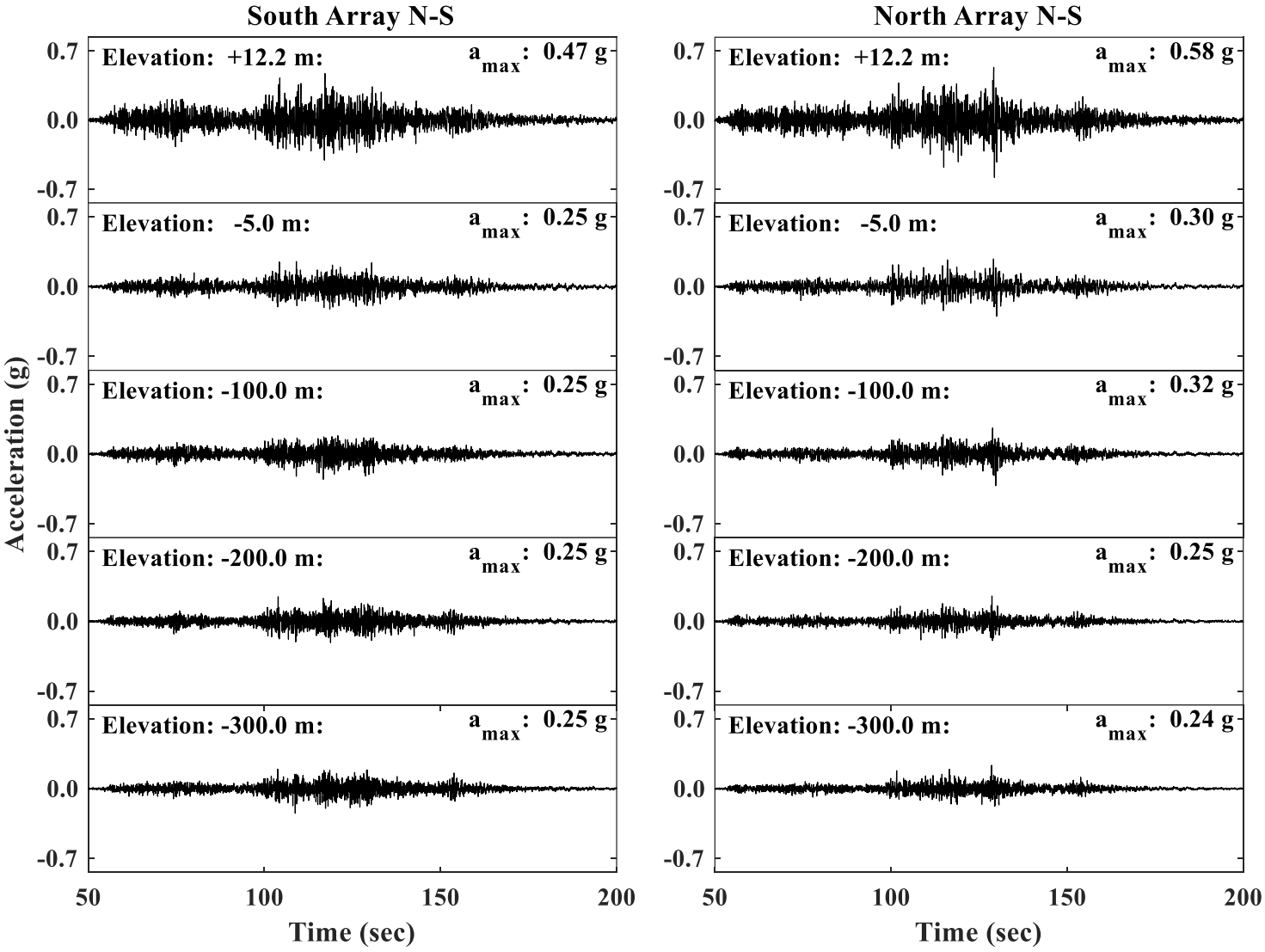

Figure 7.6 N-S Acceleration time history at the south and north downhole arrays

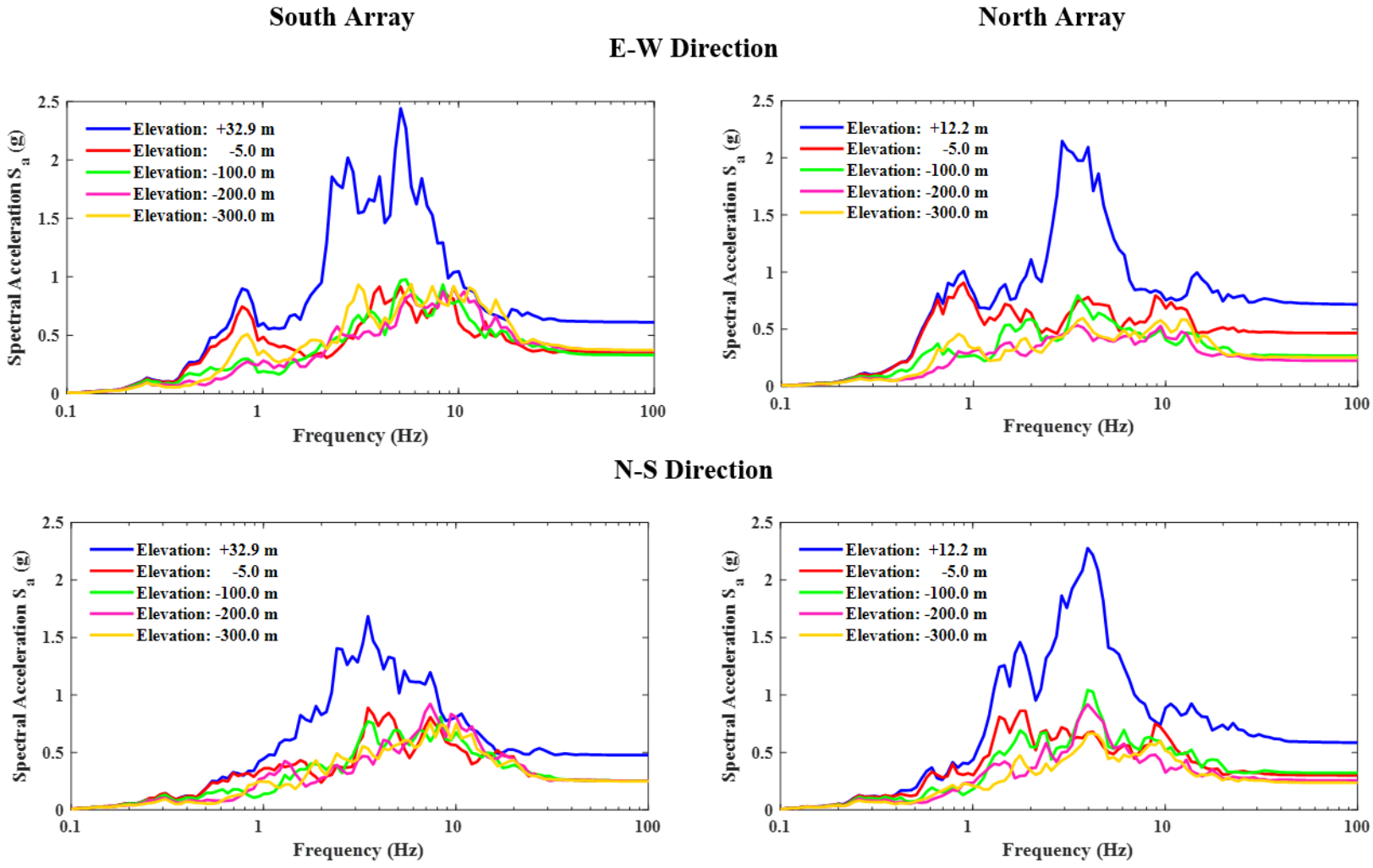

Figure 7.7 Acceleration response spectra (5% damping) for south and north downhole arrays

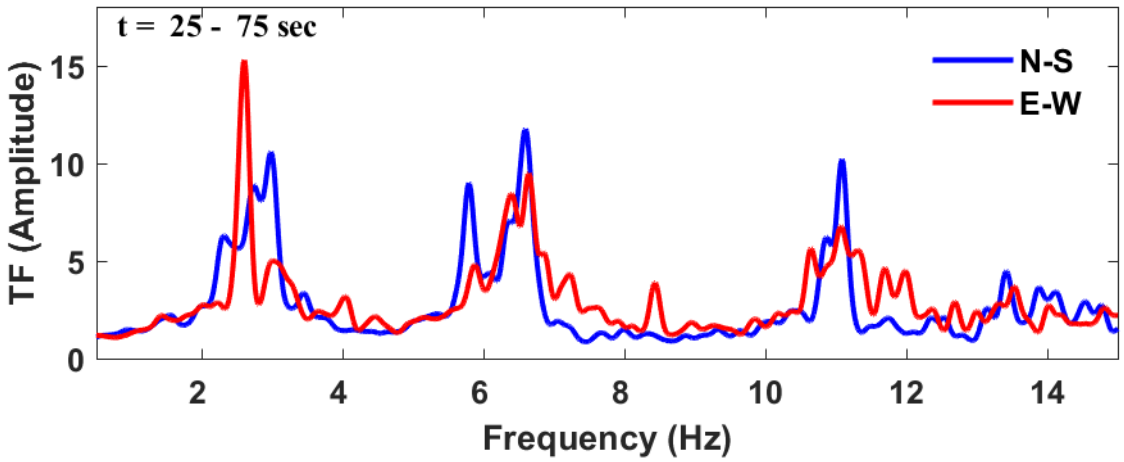

Figure 7.8 South array +32.9 m to -5.0 m acceleration transfer function amplitude (25 sec – 75 sec)

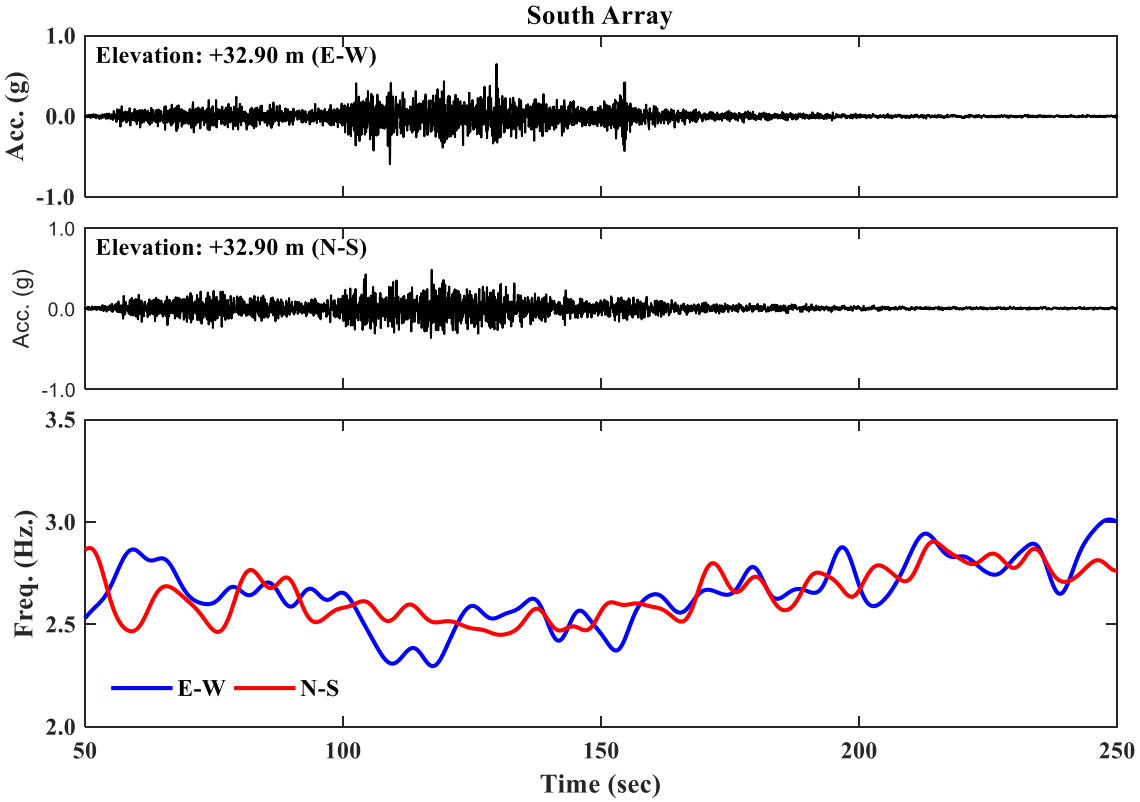

Figure 7.9 South array ground surface accelerations and the corresponding +32.9 m to -5.0 m smoothed transfer function peak frequency variation during the Tōhoku earthquake

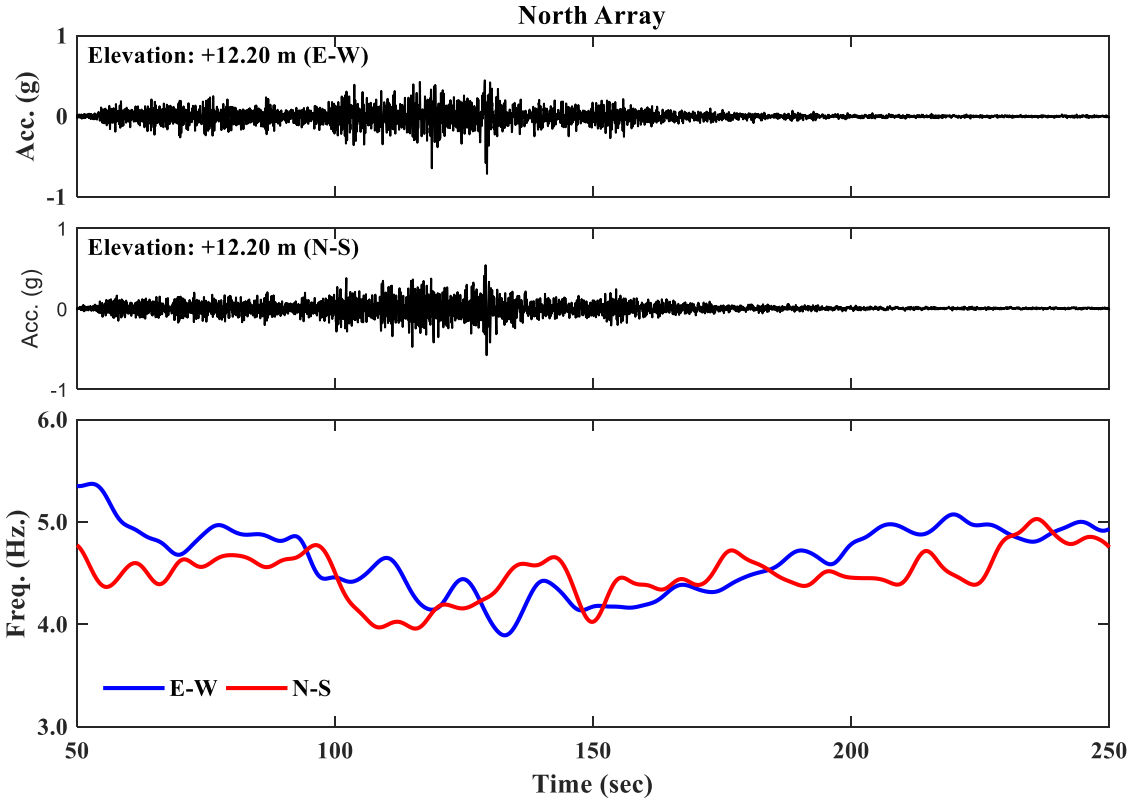

Figure 7.10 North array ground surface accelerations and the corresponding +12.2 m to -5.0 m smoothed transfer function peak frequency variation during the Tōhoku earthquake

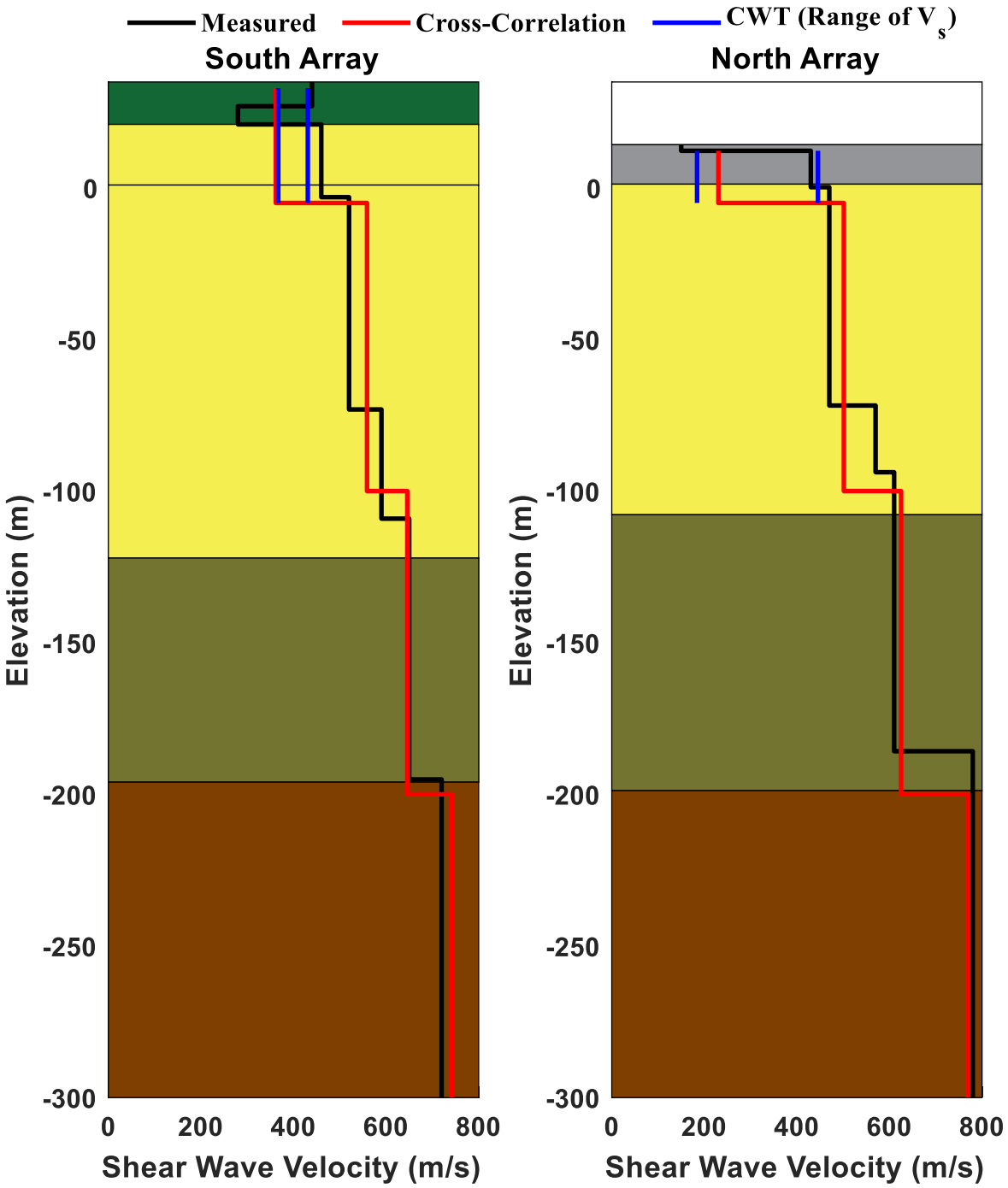

Figure 7.11 Shear wave velocity profile as computed from cross correlation and determined from the continuous wavelet function (CWT)

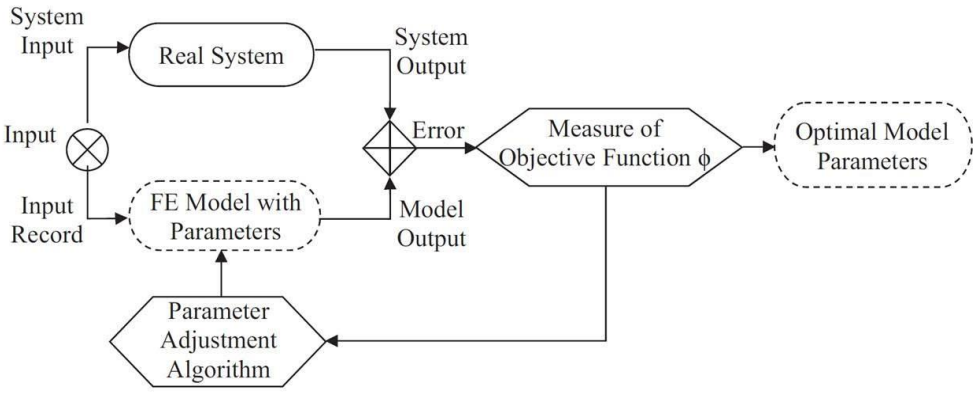

Figure 7.12 Block diagram illustrating the optimization procedure framework

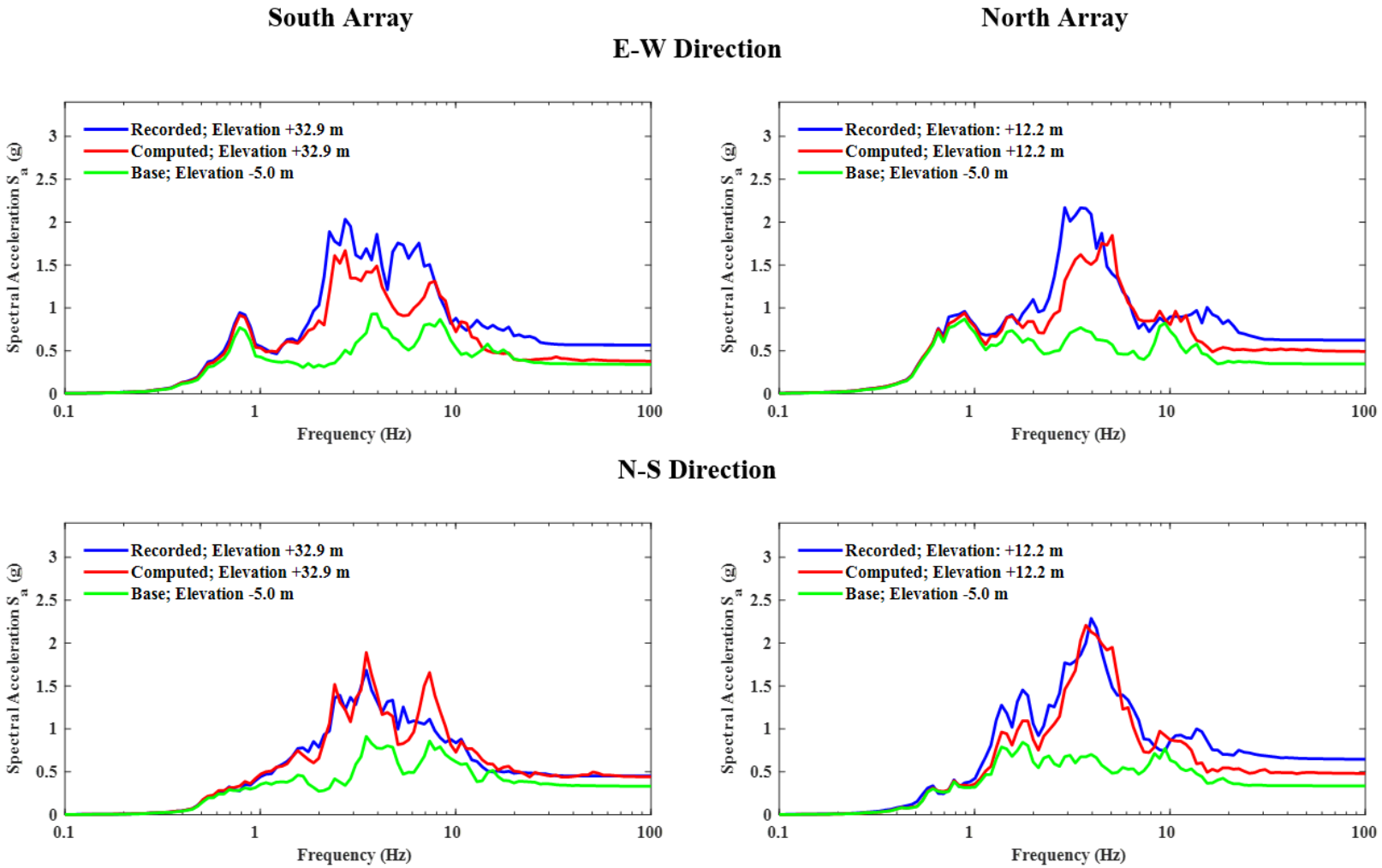

Figure 7.13 Computed response spectra (5% damping) using the optimal material parameters as identified by Δ-DOGS for the south and north array in the E-W and N-S direction

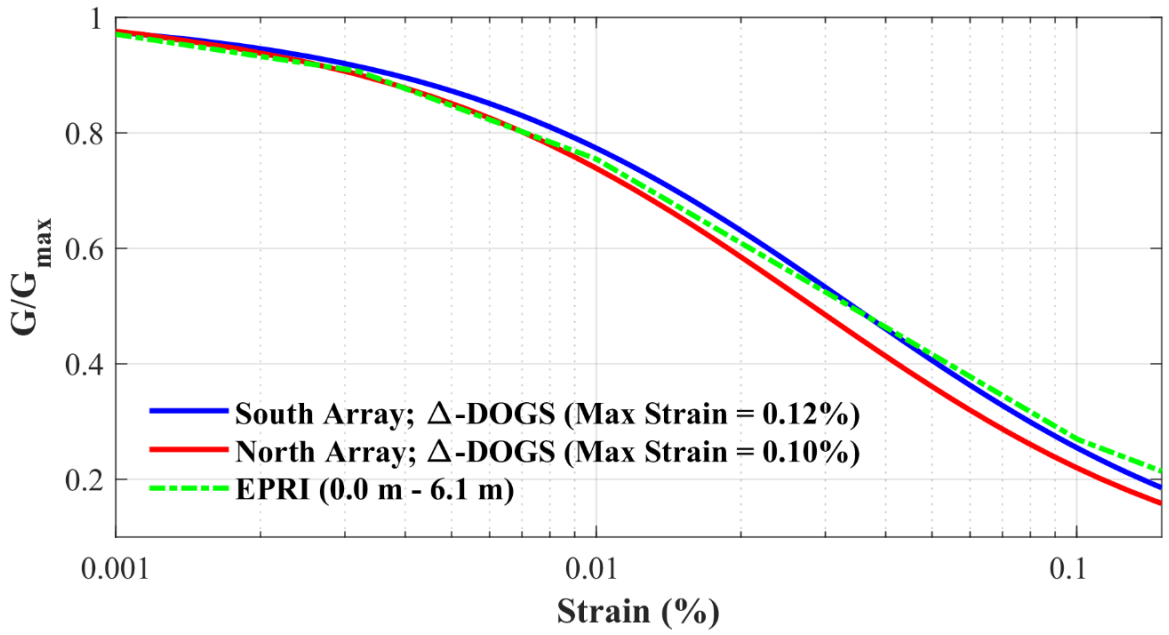

Figure 7.14 Modulus reduction curves for the south and north array as determined by Δ-DOGS

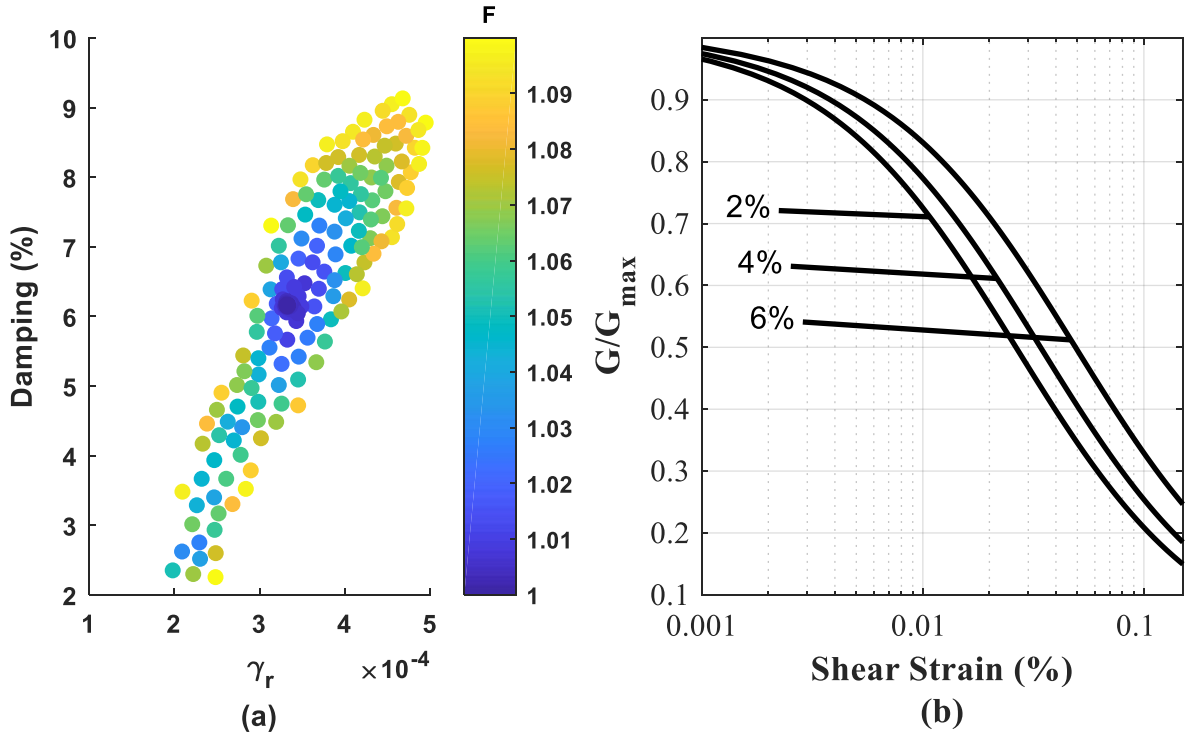

Figure 7.15 South array optimization; (a) Normalized objective function (F) for various combinations of viscous damping and γ_r; (b) Modulus reduction curve for 2%, 4% and 6% viscous damping

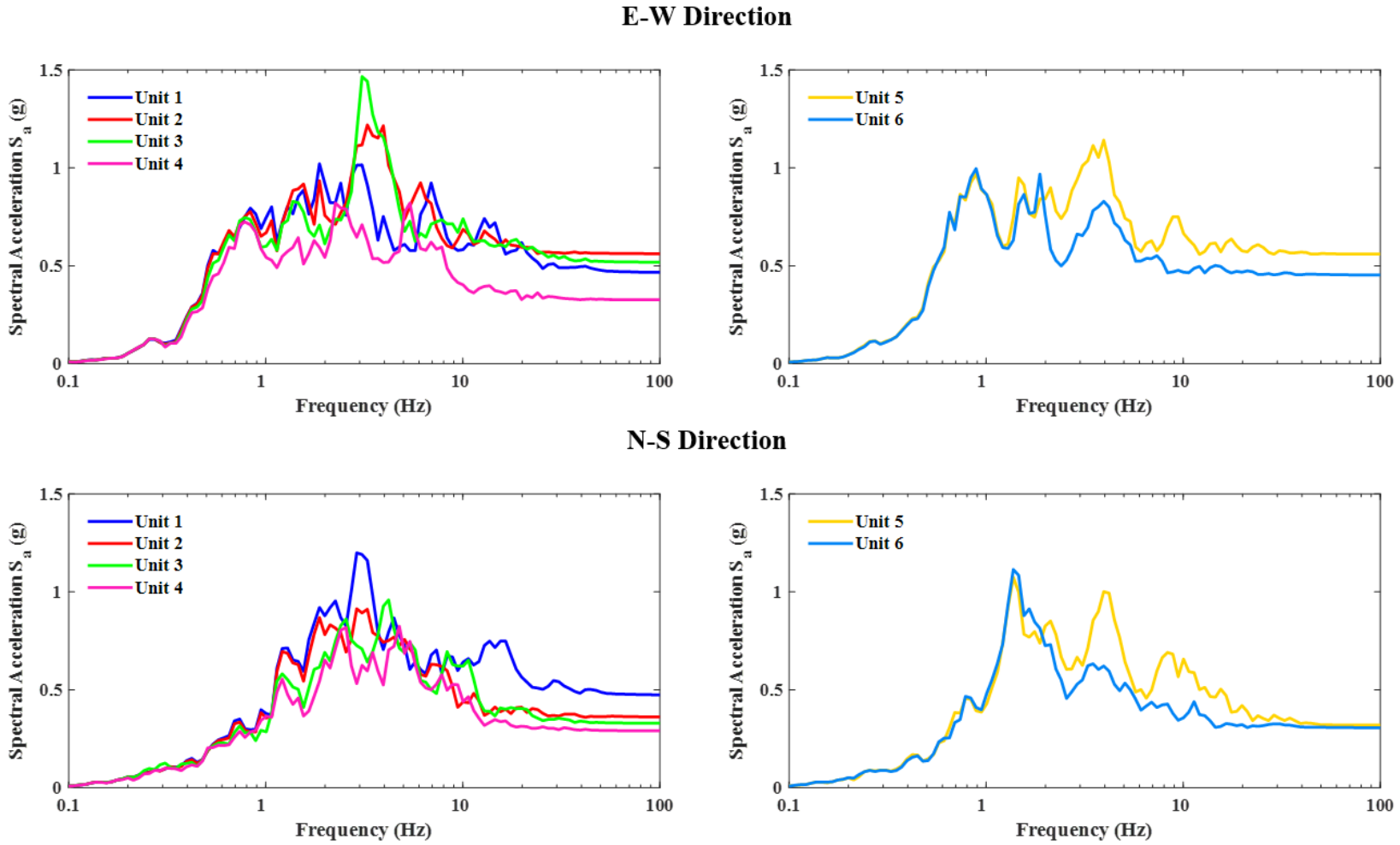

Figure 7.16 Response spectra (5% damping) for basement of six reactors at Fukushima Daiichi Nuclear Power Plant in the E-W and N-S direction

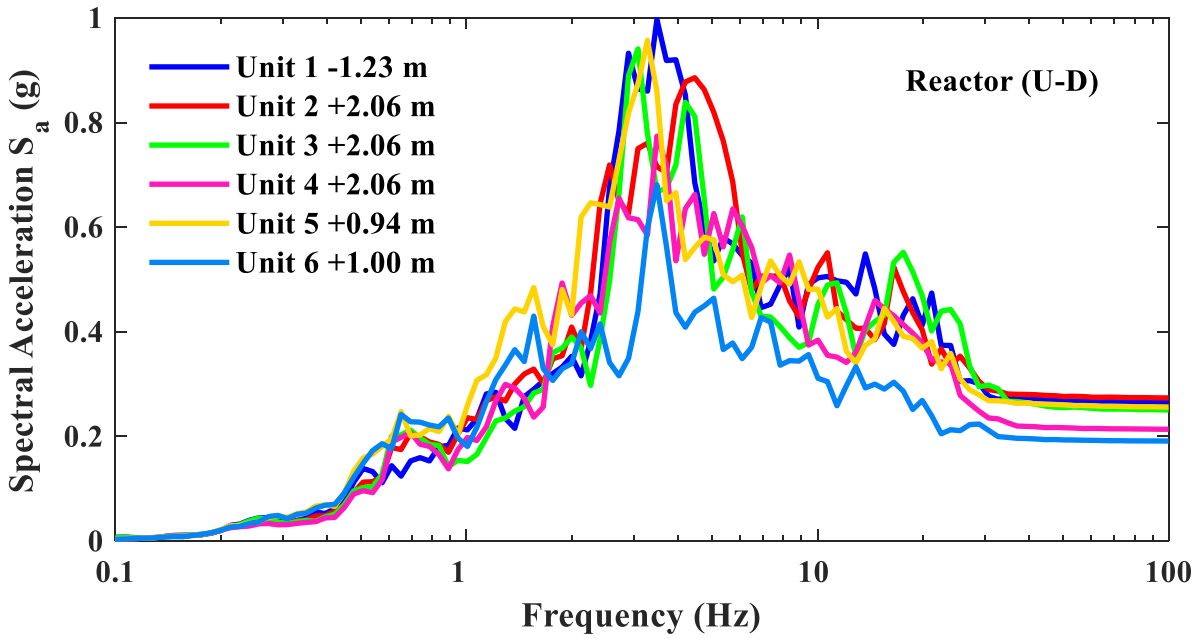

Figure 7.17 Response spectrum of the basement of the six reactors at Fukushima Daiichi Nuclear Power Plant in the U-D direction

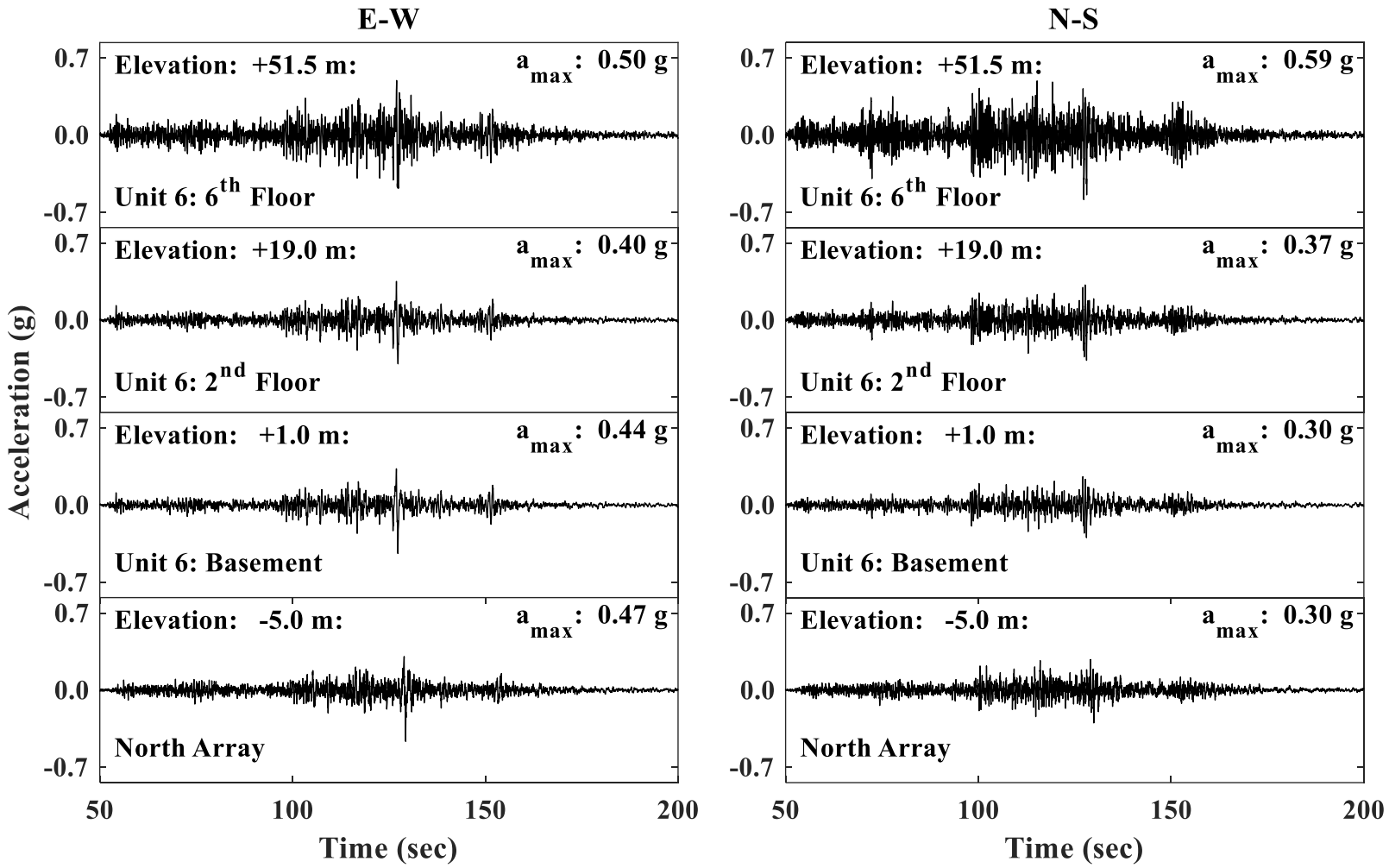

Figure 7.18 Recorded acceleration of Unit 6 and nearby north array at -5.0 m

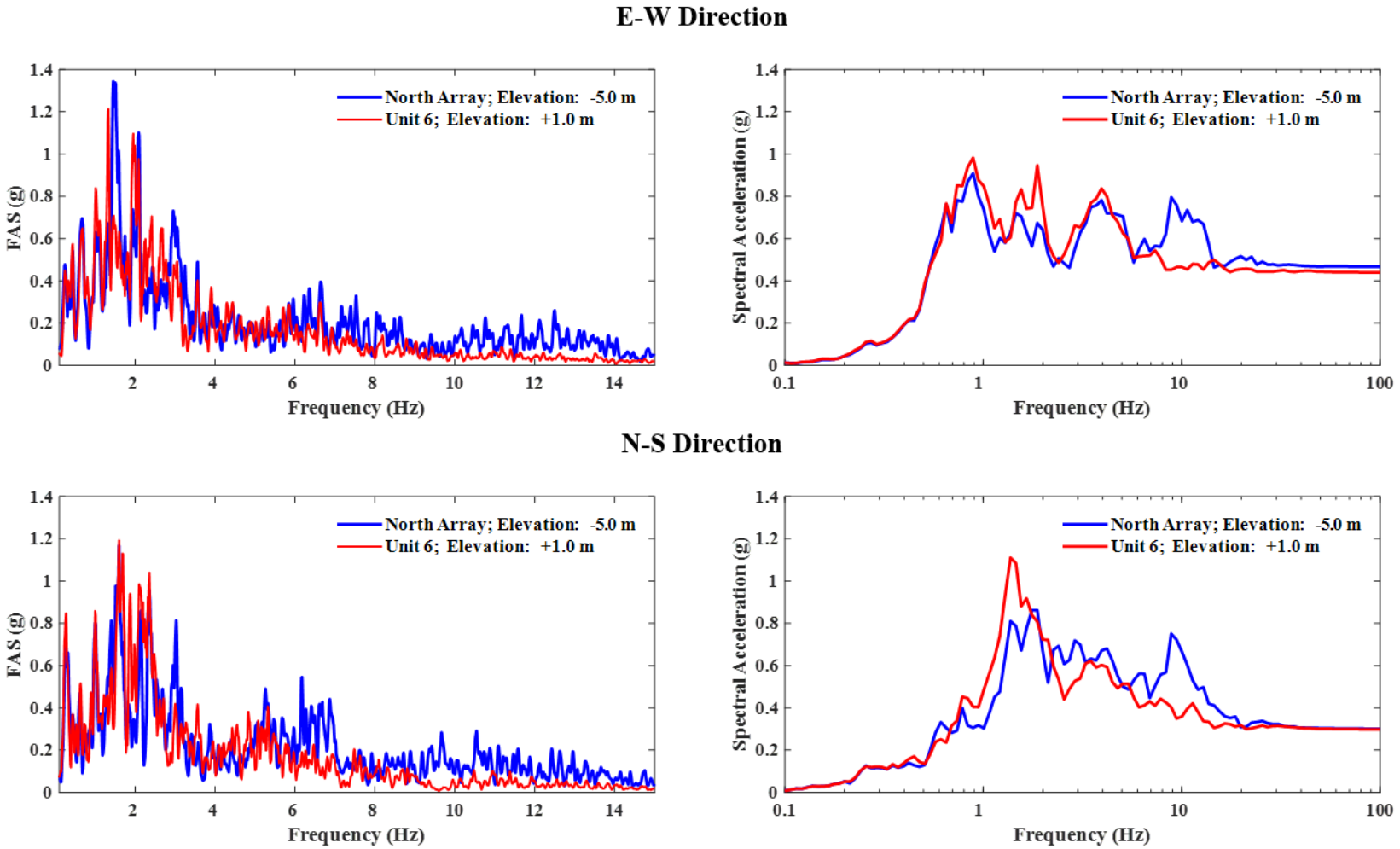

Figure 7.19 Unit 6 and north array Fourier Amplitude spectra and spectral acceleration

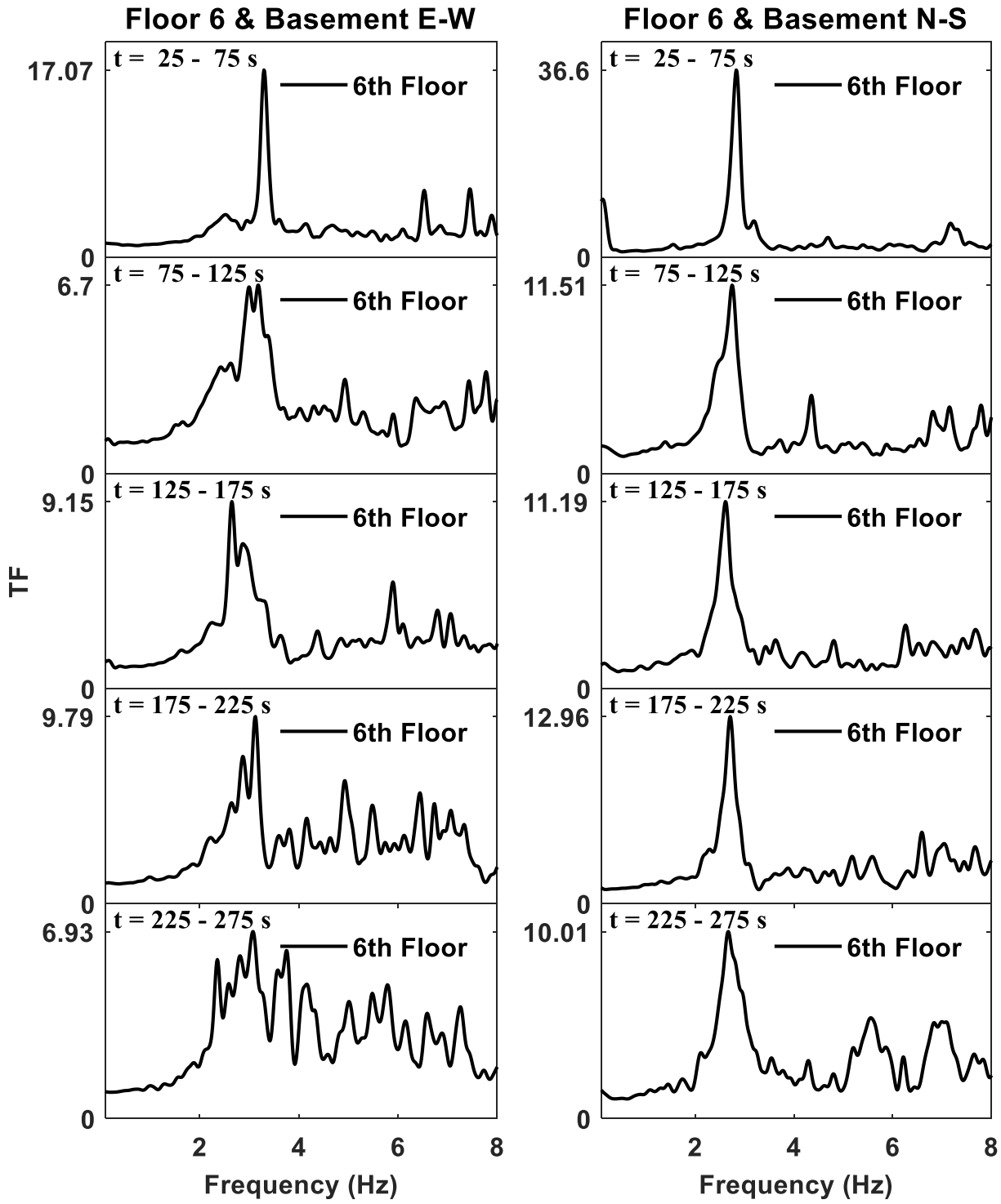

Figure 7.20 Unit 6 transfer function of Fast Fourier Transform of the acceleration at 6th floor (P2; +51.5 m) and basement (P3; +1.0 m)

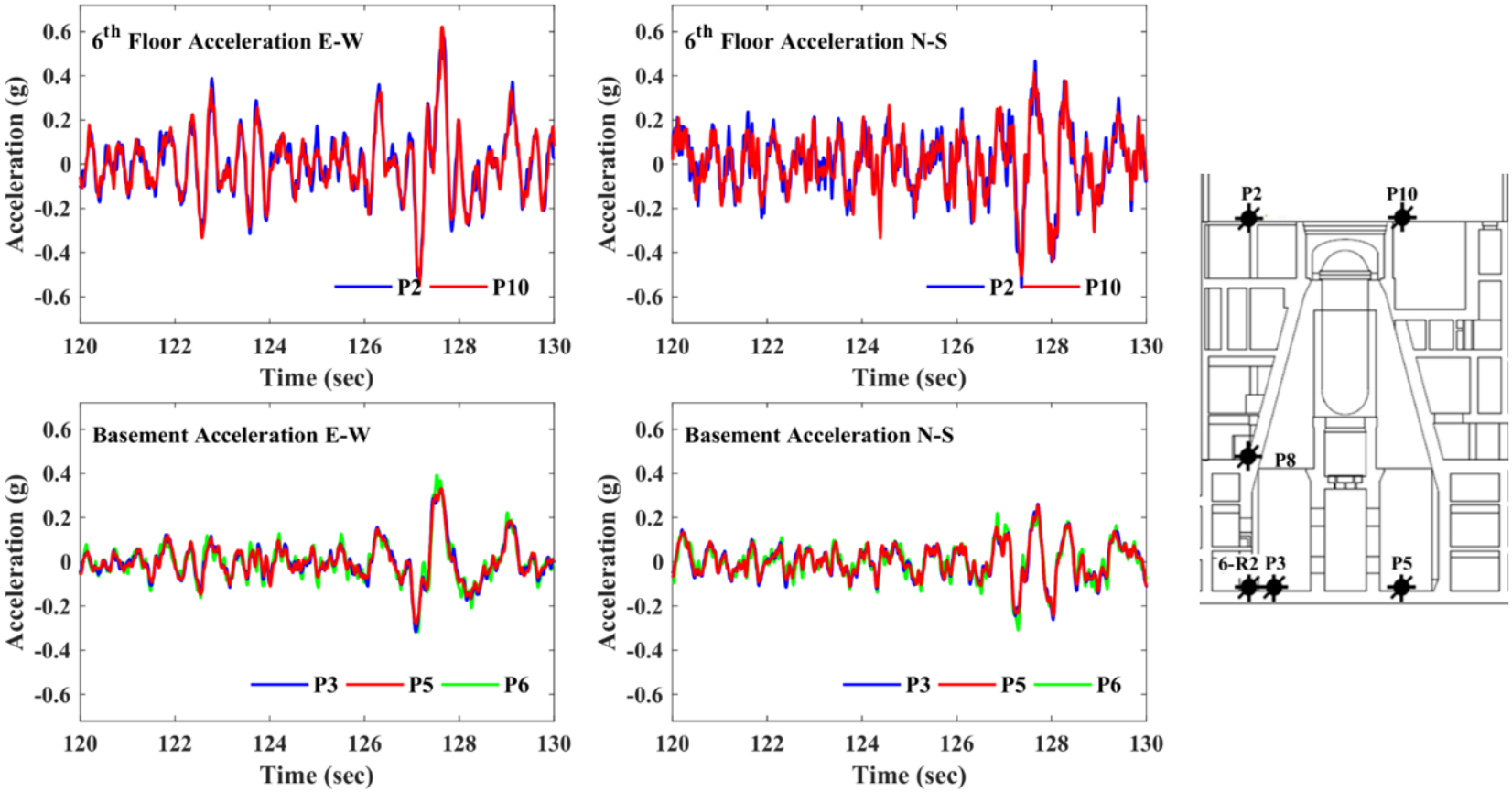

Figure 7.21 Unit 6 recorded lateral acceleration at the 6th floor and basement

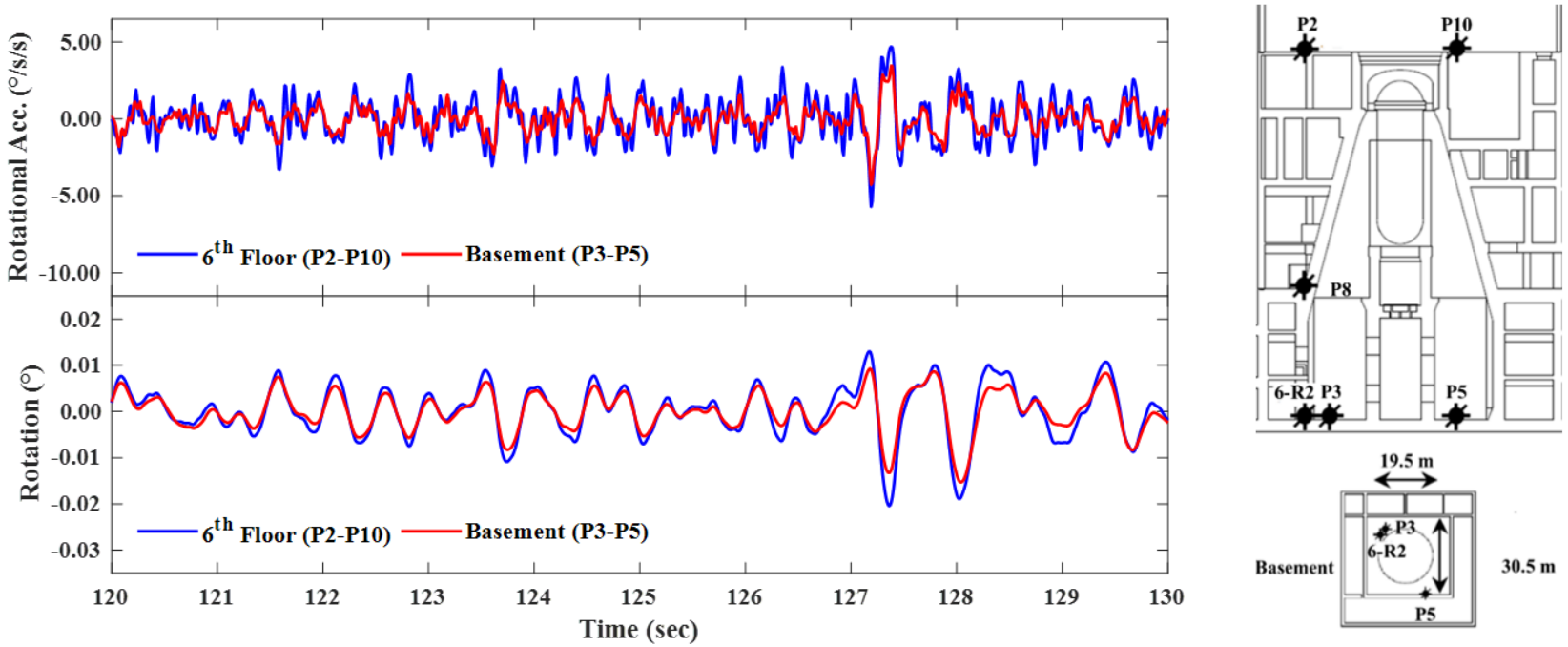

Figure 7.22 Unit 6 vertical acceleration at the 6th floor and at the basement

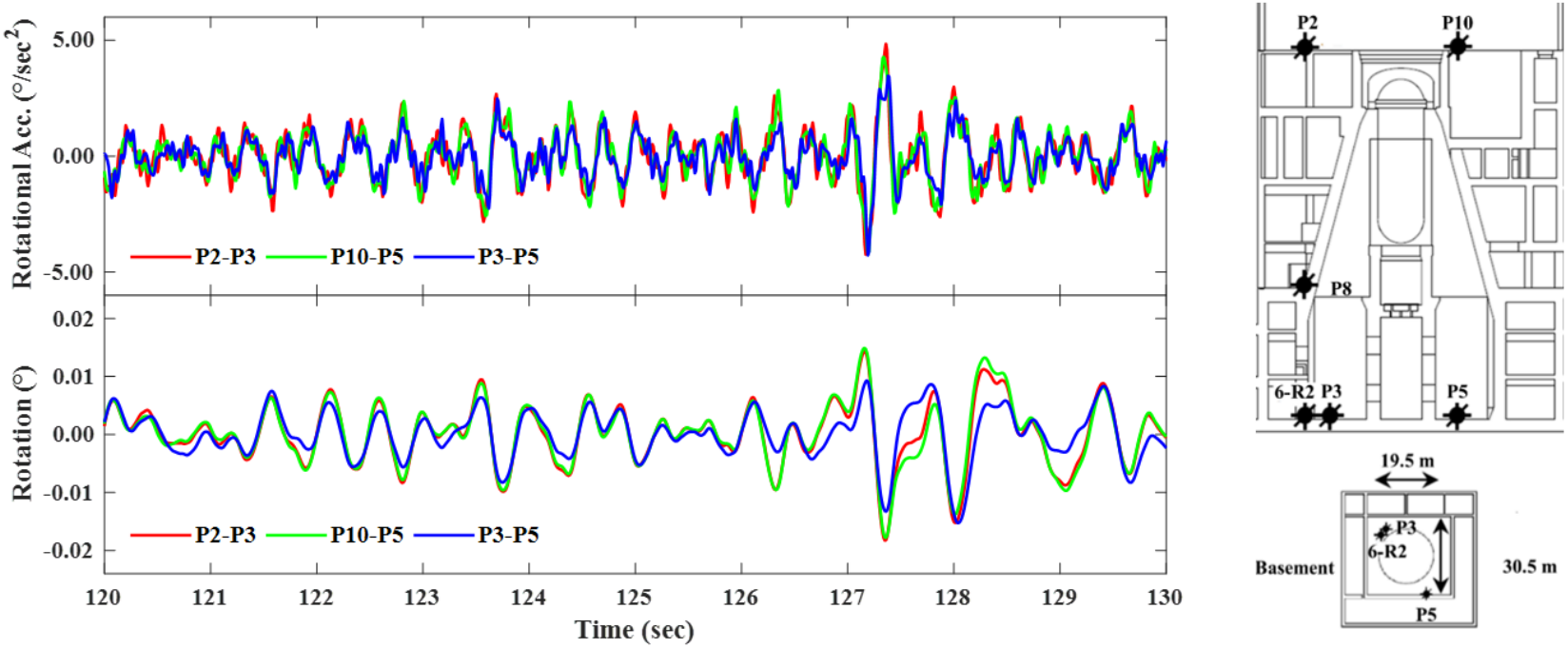

Figure 7.23 Unit 6 rotational acceleration and displacement of the 6th floor and basement computed using vertical acceleration

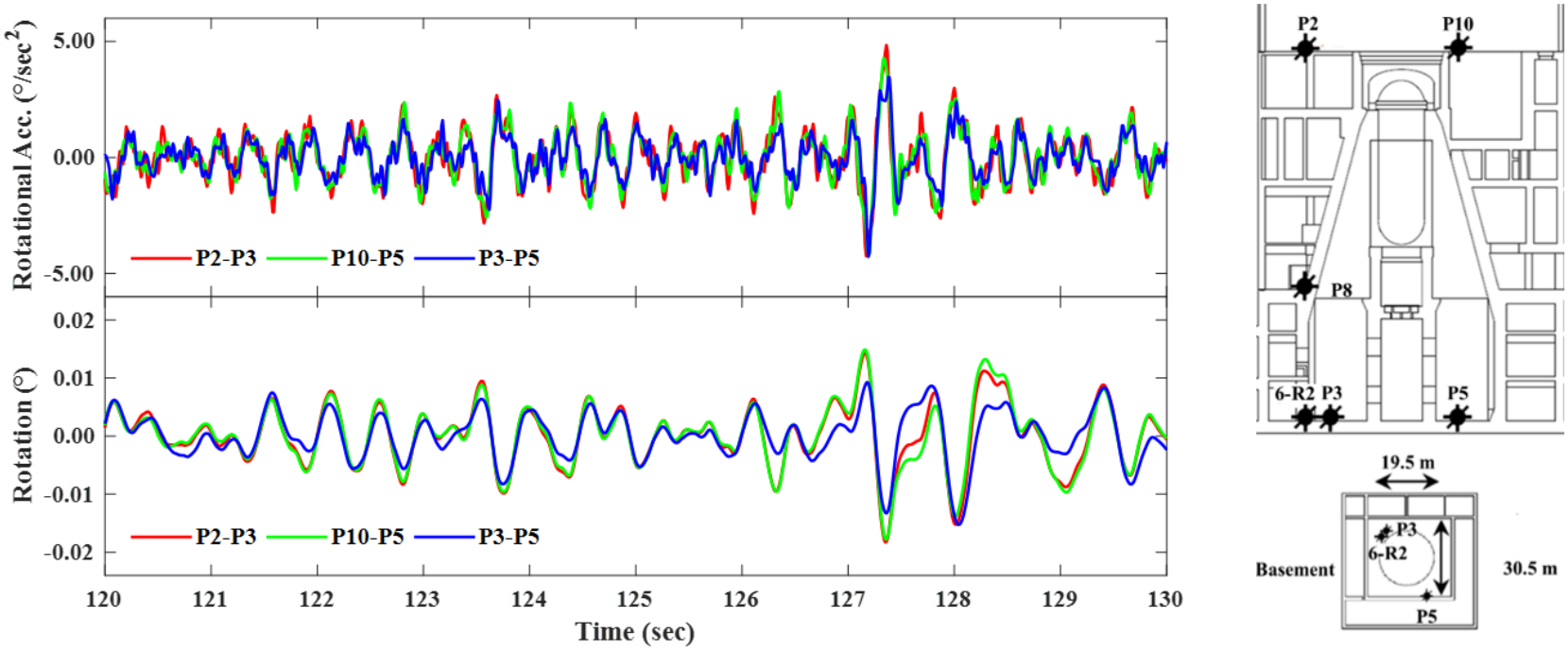

Figure 7.24 Unit 6 rotational acceleration of the wall structure displayed in the P3-P5 plane

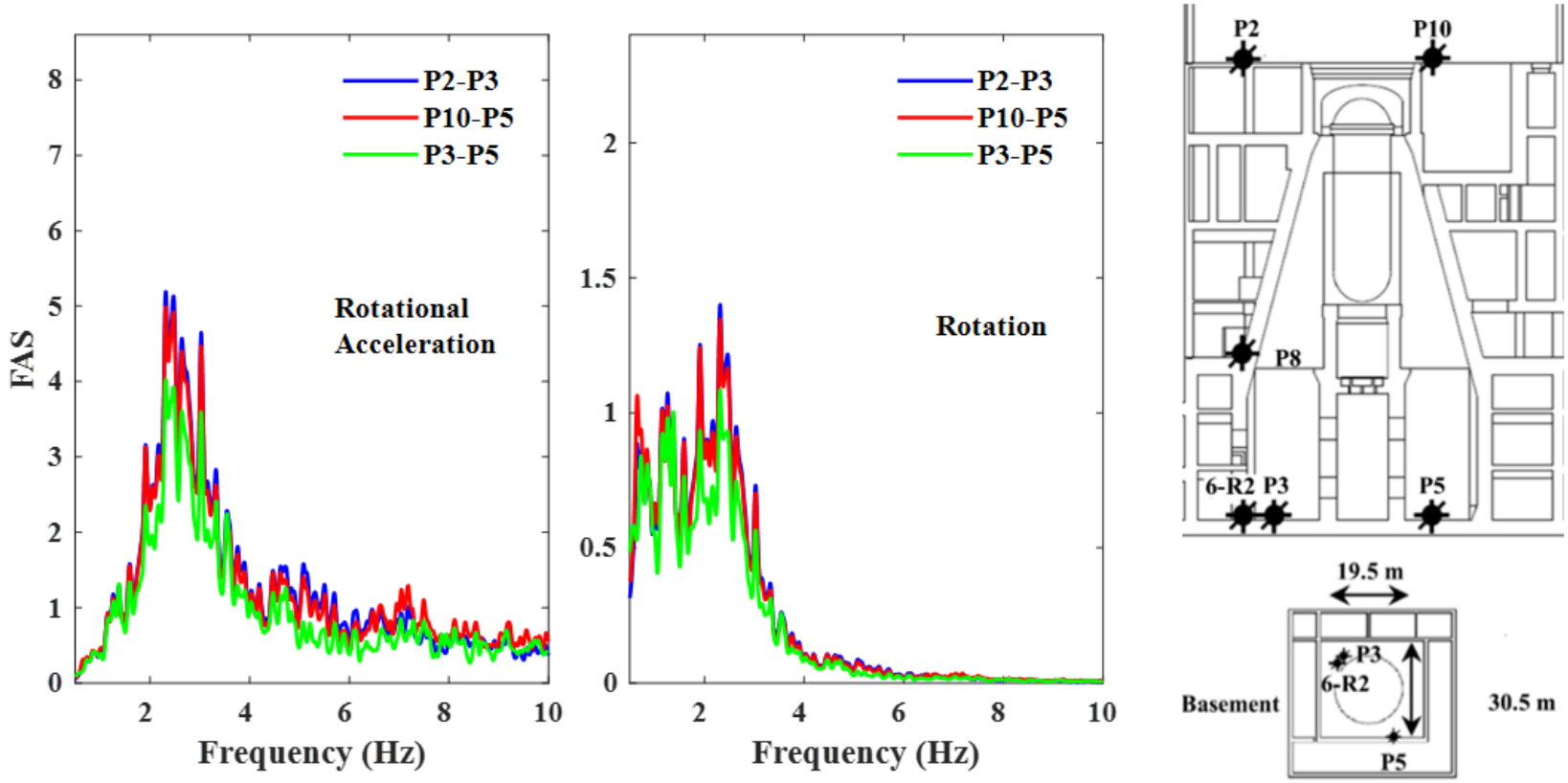

Figure 7.25 Unit 6 fourier amplitude spectrum of the rotational acceleration in the P3-P5 plane

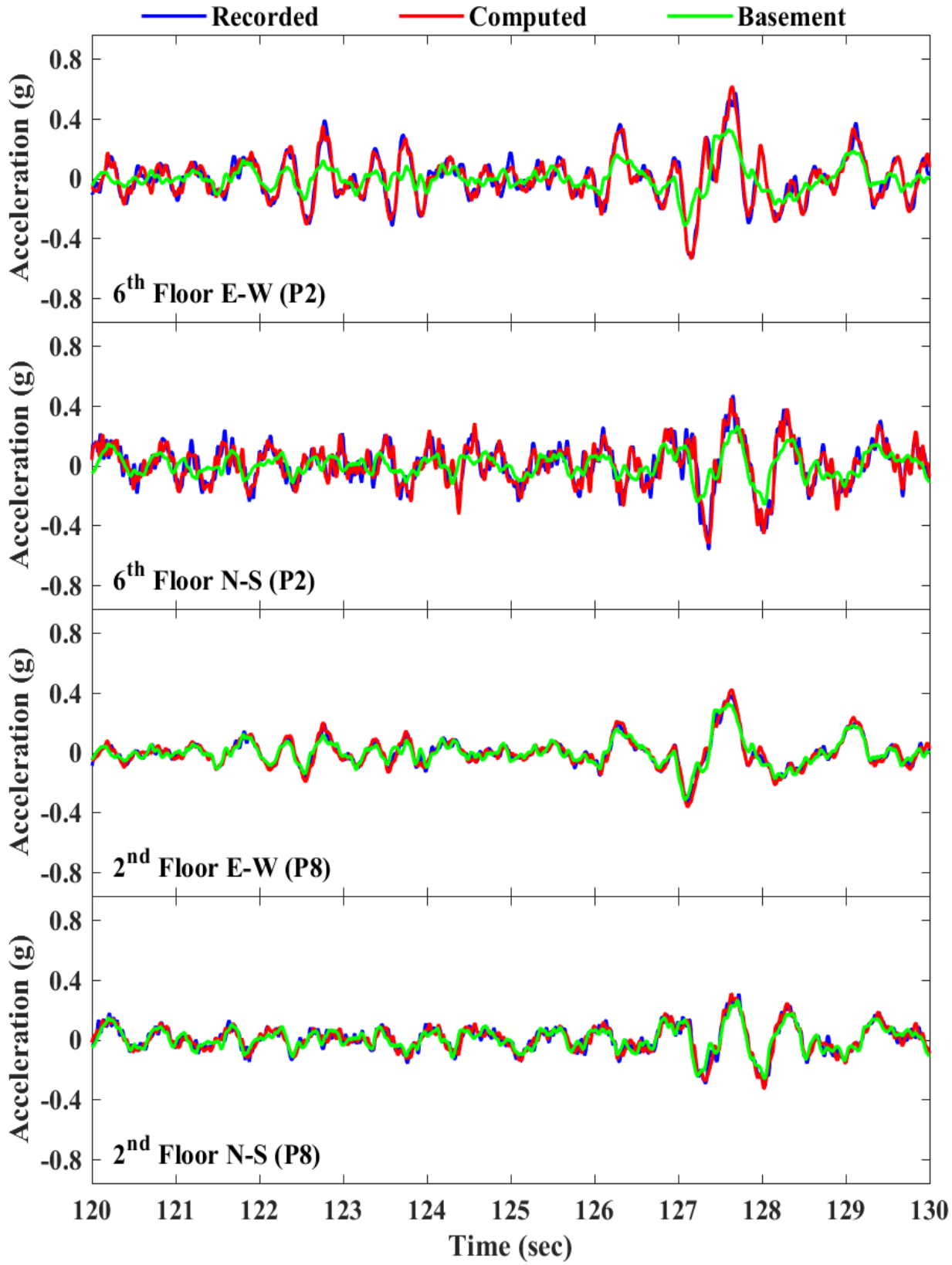

Figure 7.26 Unit 6 lateral acceleration at the 2nd and 6th floors

Chapter 8

Summary and Conclusion

8.1 Summary

For large relatively stiff structures, soil structure interaction (SSI) plays a major role in dictating the overall seismic response. In light of recent strong seismic excitation affecting such structures, three-dimensional response as well as nonlinear soil behavior are among the areas of increased interest. As such, a series of numerical studies were conducted to shed more light on the involved SSI mechanisms.

Furthermore, the contributions detailed in this report were primarily motivated by availability of data from the Aomori field tests and the Fukushima Nuclear Power Plant. Prior to discussing the findings derived from these data sets, a literature review examining current methodology was presented. Building on the introductory material, the primary focus of this report lies in the parametric study of a fully embedded structure and discussion of the unique data sets from Aomori and Fukushima which allowed for the investigation of seismic response of large embedded structures. These data sets included both the response at free-field and nuclear reactors due to weak and strong shaking from which we can evaluate current analytical and numerical

methods. The low level shaking from the Aomori field tests served as a useful benchmark due to the essentially linear response. Of particular significance was the data from the Fukushima earthquake which exceeded the design basis. Equivalent linear codes such as SASSI are widely used to perform soil-structure interaction analysis and have been shown to be of significant value for low to moderate levels of earthquake excitation. However, in the aftermath of recent events such as that of the Fukushima Daiichi nuclear power plant incident, beyond-design basis earthquake excitation has been a concern of growing importance. With increasing demands, nonlinearity due to the soil and soil-structure interface is expected to play a larger role, mechanisms that the equivalent linear approach would face additional challenges in capturing. The three main focus of this thesis can be broken down into:

1. Parametric Study of Large Embedded Structure Seismic Response
2. Modeling of Large Embedded Structure due to Weak Seismic Activity
3. Modeling of Large Embedded Structure due to Strong Seismic Activity

8.1.1 Parametric Study of Large Embedded Structure (Chapter 5)

In order to highlight a number of salient response characteristics associated with soil structure interaction for a large embedded structure, a parametric study was undertaken. The free-field response and that of the structure were examined using nonlinear and linear soil formulations. For the cases studied, and employed numerical formulations, it was shown that nonlinear and linear soil responses were similar, but some aspects of nonlinear response were not captured by linear soil. Overall, the following conclusions were drawn:

1. Consistent with previous findings, it is observed that nonlinear and linear soil properties resulted in close estimates of peak acceleration, and soil stress and strain response for low

levels of shaking. The difference between the two analysis methods was shown to become more significant as peak shear strains exceeded 0.1%. In particular, linear models significantly underestimated the high frequency content observed in the free-field acceleration.

2. Due to the relative rigidity of the structure compared to the surrounding soil, acceleration at the top of the structure (ground surface) was: i) much reduced when compared to free-field, becoming quite similar to that at the structure's base, and ii) relatively devoid of high frequency amplification, partially due to an averaging mechanism of the ground response along its embedment depth.
3. Lateral pressure near the toe of the structure was especially high for the nonlinear case, possibly due to the increased soil confinement at this location, and the associated pressure-dependent increase in soil stiffness and strength.
4. For static own-weight soil state of stress around the normally consolidated scenario (e.g., Ko = 0.5 or so), seismic excitation might result in higher level of lateral confinement being reached at the end of shaking. As the shaking acceleration increases in amplitude and/or duration, the static lateral stress magnitude may gradually approach its vertical counterpart.
5. When allowed, separation near ground surface at the soil-structure interface might occur. However, it was observed this mechanism was of little consequence on the overall structural response for this geometric configuration.
6. Along the structure's base, the initial static vertical stress might become fully relieved locally during a strong shaking excursion. Potentially, some level of final permanent structural displacement might ensue, horizontally and vertically, as might be predicated by a nonlinear modeling formulation.

8.1.2 Modeling of Large Embedded Structure due to Weak Seismic Activity (Chapter 6)

The seismic response of the experiments conducted in Higashidōri, Aomori was investigated, in order to highlight a number of salient response characteristics associated with seismic excitation for large embedded structures, albeit for weak motions. The free-field response and reactor were examined using frequency and time domain techniques which were used to identify the material parameters. Overall, the following conclusions were drawn:

1. The optimal material parameters as identified by SNOPT were able to replicate the response as recorded at the downhole arrays. However, the shear wave velocity was on average 25% higher than reported in the NUREG report.
2. Of the implemented objective functions, the transfer function was the most successful when trying to match the recorded response using SNOPT.
3. When applying the optimal soil properties to the larger 3D soil island, there was a fairly good match in the acceleration. The response spectrum appeared to peak at similar frequencies, although the finite element model overestimated the acceleration.
4. The pressure on the side of the structure was significantly overestimated by the finite element model. The shape of the Fourier Spectra looks similar for the simulated and recorded pressures.
5. It was observed that the addition of the weak soil layer significantly reduced the stress near the base of the structure

8.1.3 Modeling of Large Embedded Structure due to Strong Seismic Activity (Chapter 8)

The seismic response of the Fukushima Daiichi Nuclear Power Plant was a unique opportunity to investigate seismic response characteristics associated with strong shaking for large

embedded structures. The free-field response and reactor were examined using frequency and time domain techniques which revealed significant nonlinear response. The implications of the potential for such strong shaking needs to be accounted for in the design of important structures such as nuclear power plant. Overall, the following conclusions were drawn:

1. North and South Downhole Arrays
    i. In general, the time and frequency domain identified low-amplitude shear wave velocity V_s estimates were consistent with those from the earlier reported in-situ investigation data.
    ii. There was significant nonlinear response near ground surface which resulted in a maxim reduction of the order of 20% and 50% in the low-amplitude shear modulus for the south and north downhole arrays respectively. From the sensors at greater depths (> -5 m elevation), nonlinear response was not as readily perceptible.
    iii. Significant amplification in ground acceleration was mainly in the zone between downhole sensors closest to ground surface.
    iv. In addition to the fundamental, the south array demonstrated two additional higher site shear response resonances.
2. Basement Response of the Reactors
    i. A noticeable level of variability was observed in peak basement lateral acceleration of the 6 units, potentially due to considerations such as geometric layout of the structures, their individual dynamic characteristics, and the involved SSI and wave propagation mechanisms. Closer scrutiny may be facilitated by further availability of related information.

ii. In general, basement motions were similar to their closest downhole sensor accelerations. A main difference was the significant reduction in high frequency content in the basement records (for frequency greater than about 6 Hz).

3. Reactor Unit 6

i. The difference in the vertical acceleration at the same floor indicated presence of a rocking response.

ii. The rotation computed using lateral motions was found to be consistent with that from the vertical motions, demonstrating the high rigidity of the structure.

iii. As such, amplification of acceleration at the higher elevation was mainly due to rocking

iv. In this seismic event, peak acceleration at the top was nearly double the values recorded at the basement level.

8.2 Concluding Remarks

Overall, this research has set a stage for enhancement of our computational capabilities based on the currently available recorded data and simulation tools. On this basis, further parametric studies will aid in launching nonlinear numerical analysis as a main tool for conducting seismic response assessments.

References

Amano, Y. (2015). The Fukushima Daiichi Accident: Report by the Director General. *International Atomic Energy Agency, Vienna, Austria, Report No. GC (59)/14. http://www-pub. iaea. org/MTCD/Publications/PDF/Pub1710-ReportByTheDG-Web. pdf*.

Assimaki, D., & Gazetas, G. (2009). A simplified model for lateral response of large diameter caisson foundations—Linear elastic formulation. *Soil Dynamics and Earthquake Engineering*, *29*(2), 268-291.

Baltaji, O., Numanoglu, O. A., Veeraraghavan, S., Hashash, Y. M., Coleman, J. L., & Bolisetti, C. (2017). Non-linear Time Domain Site Response and Soil Structure Analyses for Nuclear Facilities using MASTODON. *Proceedings of 24th international conference on structural mechanics in reactor technology.* Busan, Korea.

Bathe, K. J. (2007). Conserving energy and momentum in nonlinear dynamics: a simple implicit time integration scheme. *Computers & structures*, *85*(7), 437-445.

Beyhaghi, P., Cavaglieri, D., & Bewley, T. (2016). Delaunay-based derivative-free optimization via global surrogates, part I: linear constraints. *Journal of Global Optimization, 66*(3), 331-382.

Bhaumik, L., & Raychowdhury, P. (2013). Seismic response analysis of a nuclear reactor structure considering nonlinear soil-structure interaction. *Nuclear Engineering and Design, 265*, 1078-1090.

Bielak, J., Loukakis, K., Hisada, Y., & Yoshimura, C. (2003). Domain reduction method for three-dimensional earthquake modeling in localized regions, Part I: Theory. *Bulletin of the Seismological Society of America, 93*(2), 817-824.

Bolisetti, C., & Whittaker, A. S. (2011). Seismic structure–soil–structure interaction in nuclear power plant structures. *Transactions, SMiRT, 21*, 6-11.

Bolisetti, C., & Whittaker, A. S. (2015). *Site Response, Soil-Structure Interaction and Structure-Soil-Structure Interaction for Performance Assessment of Buildings and Nuclear Structures.* MCEER-15-0002, Multidisciplinary Center for Earthquake Engineering Research (MCEER), University at Buffalo, NY.

Bolisetti, C., Whittaker, A. S., & Coleman, J. L. (2018). Linear and nonlinear soil-structure interaction analysis of buildings and safety-related nuclear structures. *Soil Dynamics and Earthquake Engineering, 107*, 218-233.

Bolisetti, C., Whittaker, A. S., Mason, H. B., Almufti, I., & Willford, M. (2014). Equivalent linear and nonlinear site response analysis for design and risk assessment of safety-related nuclear structures. *Nuclear Engineering and Design, 275*, 107-121.

Brady, A. G. (1980). *An investigation of the Miyagi-ken-oki, Japan, earthquake of June 12, 1978.* US Dept. of Commerce, National Bureau of Standards.

Brinkgreve, R., Swolfs, W., & Engin, E. (2011). *PLAXIS 2D Reference manual. Delft University of Technology and PLAXIS bv The Netherlands.*

BSSC. (2004). *NEHRP Recommended Provisions for Seismic Regulations for New Buildings and Other Structures, 2003 Edition, Report Nos. FEMA 450-1*. Washington, D.C: Federal Emergency Management Agency.

Clouteau, D., Broc, D., Devesa, G., Guyonvarh, V., & Massin, P. (2012). Calculation methods of Structure–Soil–Structure Interaction (3SI) for embedded buildings: Application to NUPEC tests. *Soil Dynamics and Earthquake Engineering, 32*(1), 129-142.

Coleman, J. L., Bolisetti, C., & Whittaker, A. S. (2016). Time-domain soil-structure interaction analysis of nuclear facilities. *Nuclear Engineering and Design, 298*, 264-270.

de Barros, F. C., & Luco, J. E. (1995). Identification of foundation impedance functions and soil properties from vibration tests of the Hualien containment model. *Soil Dynamics and Earthquake Engineering, 14*(4), 229-248.

Elgamal, A.-W., Zeghal, M., Parra, E., Gunturi, R., Tang, H., & Stepp, J. (1996). Identification and modeling of earthquake ground response—I. Site amplification. *Soil Dynamics and Earthquake Engineering, 15*(8), 499-522.

Elgamal, A.-W., Zeghal, M., Tang, H., & Stepp, J. (1995). Lotung downhole array. I: Evaluation of site dynamic properties. *Journal of Geotechnical Engineering, 121*(4), 350-362.

EPRI. (1993). *Guidelines for Determining Design Ground Motions.*

Fukushima Nuclear Accident Independent Investigation Commission (FNAIIC). (2012). *The official report of the fukushima nuclear accident independent investigation commission: Executive summary.* National Diet of Japan.

Ganev, T., Yamazaki, F., Katayama, T., & Ueshima, T. (1997). Soil-structure interaction analysis of the Hualien containment model. *Soil Dynamics and Earthquake Engineering, 16*(7-8), 459-470.

Gazetas, G. (1991). Formulas and charts for impedances of surface and embedded foundations. *Journal of geotechnical engineering, 117*(9), 1363-1381.

Geomatrix Consultants Inc. (1991). *Ground Motion Following Selection of SRS Design Basis.* WSRC Report AA20210s, Prepared for Westinghouse Savannah River Site.

Geotechnical Engineers Inc. (GEI). (1983). *Evaluation of Dynamic Soil Properties for F-Area Sand Filter Structures.* Report Prepared for E.I. Dupont de Nemours &Co.

Gill, P. E., Murray, W., & Michael, S. A. (1997). *SNOPT: An SQP Algorithm for Largescale Constrained Optimization.*

Graves, H. L. (2004). Hualien large-scale seismic test, International Workshop for Site Selection, Installation, and Operation of Geotechnical Strong-Motion Arrays, Cosmos. UCLA.

Graves, H. L., Tang, H. T., & Liao, Y. C. (1996). Large-scale seismic test program at Hualien Taiwan. *Nuclear engineering and design, 163*(3), 323-332.

Hagiwara, T., & Kitada, Y. (2005). A test to evaluate non-linear soil structure interaction. *Proceedings of the 18th international conference on structural mechanics in reactor technology.* Bejing, China.

Hashash, Y. M., Musgrove, M. I., Harmon, J. A., Groholski, D. R., Phillips, C. A., & Park, D. (2015). *DEEPSOIL 6.1, User Manual.*

Houston, S. L. (1985). Thermo Mechanical Behavior of Seafloor Sediments . *ASCE*, 1249-1293.

Idriss, I. M., & Sun, J. I. (1993). *User's manual for SHAKE91: a computer program for conducting equivalent linear seismic response analyses of horizontally layered soil deposits.* Center for Geotechnical Modeling, Department of Civil and Environmental Engineering, University of California Press, Davis.

International Atomic Energy Agency (IAEA). (2018, December 10). Retrieved from Power Reactor Information System: https://pris.iaea.org/PRIS/CountryStatistics/CountryDetails.aspx?current=JP

International Atomic Energy Agency (IAEA). (2018). Retrieved from Power Reactor Information System: https://pris.iaea.org/PRIS/CountryStatistics/CountryDetails.aspx?current=JP

Ishibashi, I., & FANG, Y.-S. (1987). Dynamic earth pressures with different wall movement modes. *Soils and Foundations, 27*(4), 11-22.

Ishihara, K. (1996). *Soil behaviour in earthquake geotechnics.* Oxford Science Publication, 120.

Ishii, T., Arai, M., & Tsuchida, H. (1960). Lateral Earth Pressures in an Earthquake . *Second world conference on Earthquake Engineering.* Tokyo, Japan.

Kammerer, A., & Jeremic, B. (2013). THE NRC ESSI SIMULATOR PROGRAM, CURRENT STATUS. *Proceedings of the 22nd international conference on structural mechanics in reactor technology.* San Francisco, California.

Konder, R. L., & Zelasko, J. S. (1963). A hyperbolic stress-strain formulation for sands. *Proceedings of the 2nd Pan American Conference on Soil Mechanics and Foundation Engineering*, (pp. 289–324). Brazil.

Koyanagi, T., Kikuchi, R., Kanechika, M., & Suzuki, A. (2009). Simulation analysis of reactor buildings on Niigataken Chuetsu-oki earthquake at Kashiwazaki-Kariwa Nuclear Power Plant. *Transactions of the 20th International Conference on Structural Mechanics in Reactor Technology.* Espoo, Finland.

Kurokawa, K. (2013). Fukushima nuclear accident independent investigation commission by the National Diet of Japan. *Nippon Genshiryoku Gakkai-Shi, 55*(3), 146-151.

Lambe, T. W., & Whitman, R. V. (1969). *Soil mechanics.* New York: Wiley.

Li, J., Lu, J., Kim, K., Elgamal, A. W., Park, E. H., Musgrove, M., . . . Rathje, E. (2016). *Earth Pressures on Deep Foundation Walls During Seismic Events. Technical Report, U.S. Nuclear Regulatory Commission.*

LS-DYNA. (2012). *Keyword User's Manual, Volume I, August 2012, Version 971 R6.1.0.* Livermore Software Technology Corporation (LSTC).

LSTC. (2001). *LS-DYNA User's Manual, vols. 1 & 2, Version 960.* Livermore Software Technology Corp.

Luco, J. E., & de Barrros, F. C. (2005). Identification of structural and soil properties from vibration tests of the Hualien containment model. *Earthquake engineering & structural dynamics, 34*(1), 21-48.

Luco, J. E., & Francisco, C. P. (2004). Assessment of predictions of the response of the Hualien containment model during forced vibration tests. *Soil Dynamics and Earthquake Engineering, 24*(12), 1013-1035.

Luco, J. E., & Mita, A. (1987). Response of circular foundation to spatially random ground motion. *Journal of engineering mechanics, 113*(1), 1-15.

Luco, J. E., & Wong, H. L. (1990). Forced vibration of Lotung containment model: theory and observations. *Journal of Engineering Mechanics, 116*(4), 845-861.

Luco, J., & Wong, H. (1986). Response of a rigid foundation to a spatially random ground motion. *Earthquake Engineering & Structural Dynamics, 14*(6), 891-908.

Lysmer, J., & Kuhlemeyer, R. L. (1969). Finite dynamic model for infinite media. *Journal of the Engineering Mechanics Division, 95*(4), 859-878.

Lysmer, J., Ostadan, F., & Chin, C. (1999). *SASSI2000–Theoretical Manual.* Geotechnical Engineering Division, Civil Engineering Department, University of California, Berkeley.

Lysmer, J., Tabatabaie-Raissi, M., Tajirian, F., Vahdani, S., & Ostadan, F. (1981). *SASSI: A system for analysis of soil-structure interaction.* UCB/GT/81-02, University of California, Berkeley.

Manie, J. (2014). *User's Manual–Release 9.5. Delft, Netherlands.*

Matsuo, H. (1941). Experimental study on the distribution of earth pressure acting on a vertical wall during earthquakes. *J. of the Japan Society of Civil Engrg, 27*(2).

Matsuo, H. (1960). Lateral earth pressure and stability of quay walls during earthquakes. *Proc. of 2nd WCEE, 1*, pp. 165-183.

Mazzoni, S., McKenna, F., Scott, M. H., & Fenves, G. L. (2006). Open system for earthquake engineering simulation: User command language manual. Pacific Earthquake Engineering Research Center University of California, Berkeley, OpenSees version 2.0 users manual. Retrieved from http://opensees.berkeley.edu/OpenSees/manuals/usermanual/index.html

Meyerhof, G. (1956). Penetration tests and bearing capacity of cohesionless soils. *Journal of the Soil Mechanics and Foundations Division, 82*(1), 1-19.

Mock, E., & Cheng, L. (2011). Full-scale shake table test of retaining walls with and without sound wall. *Univ. of California, Davis, CA.*

Mononobe, N. (1929). On determination of earth pressure during earthquake. *9*, pp. 177-185. Proc. World Engineering Congress.

Mylonakis, G., Kloukinas, P., & Papantonopoulos, C. (2007). An alternative to the Mononobe–Okabe equations for seismic earth pressures. *Soil Dynamics and Earthquake Engineering, 27*(10), 957-969.

Numanoglu, O. A., Hashash, Y. M., Cerna-Diaz, A., Olson, S. M., Bhaumik, L., Rutherford, C. J., & Weaver, T. (2017). Nonlinear 3-D Modeling of Dense Sand and the Simulation of a Soil-Structure System under Multi-Directional Loading. *Geotechnical Frontiers 2017*, 379-388.

Ortiz, L. A., Scott, R., & Lee, J. (1983). Dynamic centrifuge testing of a cantilever retaining wall. *Earthquake Engineering & Structural Dynamics, 11*(2), 251-268.

Ostadan, F., Deng, N., & Kennedy, R. (2005). Soil-structure interaction analysis including ground motion incoherency effects. *Transactions of the 18th International Conference on Structural Mechanics in Reactor Technology.* Beijing, China.

Psarropoulos, P. N., Klonaris, G., & Gazetas, G. (2005). Seismic earth pressures on rigid and flexible retaining walls. *Int. J. Soil Dyn. Earthquake Eng., 25*, 795–809.

Sabatini, P. J., Bachus, R. C., Mayne, P. W., Schneider, J. A., & Zettler, T. E. (2002). *Geotechnical engineering circular no. 5: evaluation of soil and rock properties.* (No. FHWA-IF-02-034).

Saxena, N., & Paul, D. K. (2012). Effects of embedment including slip and separation on seismic SSI response of a nuclear reactor building. *Nuclear Engineering and Design, 247*, 23-33.

Scanlan, R. (1976). Seismic wave effects on soil-structure interaction. *Earthquake Engineering & Structural Dynamics, 4*(4), 379-388.

Schnabel, P. B., Lysmer, J., & Seed, H. B. (1972). Shake. *A Computer Program for Earthquake Response Analysis of Horizontally Layered Sites, College of Engineering, University of Berkeley, CA. Rep., No. EERC*, 72-12.

Seed, H. B., & Idriss, I. M. (1973). Soil-structure interaction of massive embedded structures during earthquakes. *In Proc. 5th Wld Conf. Earthq. Engng.* Rome, Italy.

Seed, H. B., Wong, R. T., Idriss, I. M., & Tokimatsu, K. (1986). Moduli and damping factors for dynamic analyses of cohesionless soils. *Journal of Geotechnical Engineering, 112*(11), 1016-1032.

Sherif MA, F. Y. (1984). Dynamic earth pressure on walls rotating about top. *Soils and Foundations, 24*(4), 109–17.

Sinha, S. K., Feng, Y., Yang, H., Wang, H., & Jeremic, B. (2017). 3-D Non-linear Modeling and Its Effects in Earthquake Soil-Structure Interaction. *Proceedings of 24th international conference on structural mechanics in reactor technology.* Busan, Korea.

Sitar, N., Mikola, R., & Candia, G. (2012). Seismically induced lateral earth pressures on retaining structures and basement walls. Keynote Lecture, Geotechnical Engineering State of the Art and Practice, Keynote Lectures from GeoCongress 2012, GSP 226,.

Solberg, J. M., Hossain, Q., & Mseis, G. (2016). Nonlinear Time-Domain Soil-Structure Interaction Analysis of Embedded Reactor Structures Subjected to Earthquake Loads. *Nuclear Engineering and Design, 304*, 100-124.

Subramanian, K. P. (2005). Soil structure interaction model and variability of parameters in seismic analysis of nuclear island connected building. *Proceedings of the 18th international conference on structural mechanics in reactor technology.* Beijing, China.

Suzuki, T., Matsumoto, K., Nakamura, N., Kosaka, K., & Kinoshita, T. (2013). A study on influence of ground condition and surrounding building for seismic response of nuclear power plant building. *Proceedings of 22nd international conference on structural mechanics in reactor technology.* San Francisco, California.

Tabatabaie, M., Sumodobila, B., Wong, C., & Oswald, J. (2009). The Effect of Foundation Embedment on Seismic SSI Response of EPRTM Nuclear Island Structures. *Proceedings of the 20th International Conference on Structural Mechanics in Reactor Technology*. Espoo, Finland.

Tang, H. T., Tang, Y. K., & Stepp, J. C. (1990). Lotung large-scale seismic experiment and soil-structure interaction method validation. *Nuclear engineering and design, 123*(2-3), 397-412.

TEPCO. (2011a). Fukushima Data Set CD-ROM. Tokyo, Japan.

TEPCO. (2011b). *The record of the earthquake intensity observed at Fukushima Daiichi Nuclear Power Station and Fukushima Daini Nuclear Power Station (Interim Report)*. Retrieved from http://www.tepco.co.jp/en/press/corp-com/release/11040103-e.html

Tsigginos, C., Gerolymos, N., Assimaki, D., & Gazetas, G. (2008). Seismic response of bridge pier on rigid caisson foundation in soil stratum. *Earthquake Engineering and Engineering Vibration, 7*(1), 33.

USGS. (2018, December 10). *M 9.1 - near the east coast of Honshu, Japan*. Retrieved from USGS: https://earthquake.usgs.gov/earthquakes/eventpage/official20110311054624120_30/executive#executive

Veletsos, A. S., & Younan, A. H. (1997). Dynamic response of cantilever retaining walls. *Journal of Geotechnical and Geoenvironmental Engineering, 123*(2), 161-172.

Veletsos, A. S., Parikh, V. H., & Younan, A. H. (1995). Dynamic response of a pair of walls retaining a viscoelastic solid. *John Wiley and Sons, Ltd,*, pp 1567-1589.

Veletsos, A., & Younan, A. (1994b). Dynamic Modeling and Response of Soil-Wall Systems. *Journal of Geotechnical Engineering, 120*(12), 2155-2179.

Wang, H., Yang, H., Sinha, S. K., Luo, C., & Jeremic, B. (2017). 3-D Non-linear Earthquake Soil-Structure Interaction Modeling of Embedded Small Modular Reactor (SMR). *Proceedings of 24th international conference on structural mechanics in reactor technology.* Busan, Korea.

Watanabe, K. M. (2003). Behaviors of Several Types of Model Retaining Walls Subjected to Irregular Excitation. *Japanese Geotechnical Society, Soils and Foundations, 5*, 13-27.

Watanabe, K., Koseki, J., & Tateyama, M. (2011). Seismic Earth Pressure Exerted on Retaining Walls Under a Large Seismic Load. *Japanese Geotechnical Society, Soils and Foundations, 51*(3), 379-394.

Wilson, P. (2009). *Large Scale Passive Force-Displacement and Dynamic Earth Pressure Experiments and Simulations." Ph.D. Dissertation, Structural Engineering, UC San Diego. (https://escholarship.org/uc/item/16g547dp).*

Xu, J., Costantino, C., & Hofmayer, C. (2003). *Collaborative Study of NUPEC Seismic Field Test Data for NPP Structures.* Washington, DC: U.S. Nuclear Regulatory Commission.

Xu, J., Miller, C., Costantino, C., & Hofmayer, C. (2006). *Assessment of Seismic Analysis Methodologies for Deeply Embedded Nuclear Power Plant Structures.* NUREG/CR-6896, U.S. Nuclear Regulatory Commission.

Xu, J., Nie, J., Costantino, C., & Hofmayer, C. (2008). *Correlation Analysis of JNES Seismic Wall Pressure Data for ABWR Model Structures.* NUREG/CR-6957, U.S. Nuclear Regulatory Commission.

Yamahara, H. (1970). Ground motions during earthquakes and the input loss of earthquake power to an excitation of buildings. *Soils and foundations, 10*(2), 145-161.

Yang, Z., Elgamal, A., & Parra, E. (2003). Computational model for cyclic mobility and associated shear deformation. *Journal of Geotechnical and Geoenvironmental Engineering, 129*(12), 1119-1127.

Yang, Z., Lu, J., & Elgamal, A. (2008). OpenSees Soil Models and Solid-Fluid Fully Coupled Elements. *User's Manual. Ver, 1*.

Yim, C. S., Chopra, A. K., & Penzien, J. (1980). Rocking response of rigid blocks to earthquakes. *Earthquake Engineering & Structural Dynamics, 8*(6), 565-587.

Yoshida, N., Kobayashi, S., Suetomi, I., & Miura, K. (2002). Equivalent linear method considering frequency dependent characteristics of stiffness and damping. *Soil Dynamics and Earthquake Engineering, 22*(3), 205-222.

Youd, T. L. (1972). Compaction of sands by repeated shear straining. *Journal of Soil Mechanics & Foundations Div, 98*(sm7).

Zeghal, M., & Elgamal, A.-W. (2000). Site response and vertical seismic arrays. *Progress in structural Engineering and Materials, 2*(1), 92-101.

Appendix A

Linear Results (1D Site Response)

A.1 DEEPSOIL (Frequency Independent), OpenSees (Rayleigh Damping) and PLAXIS (Rayleigh Damping)

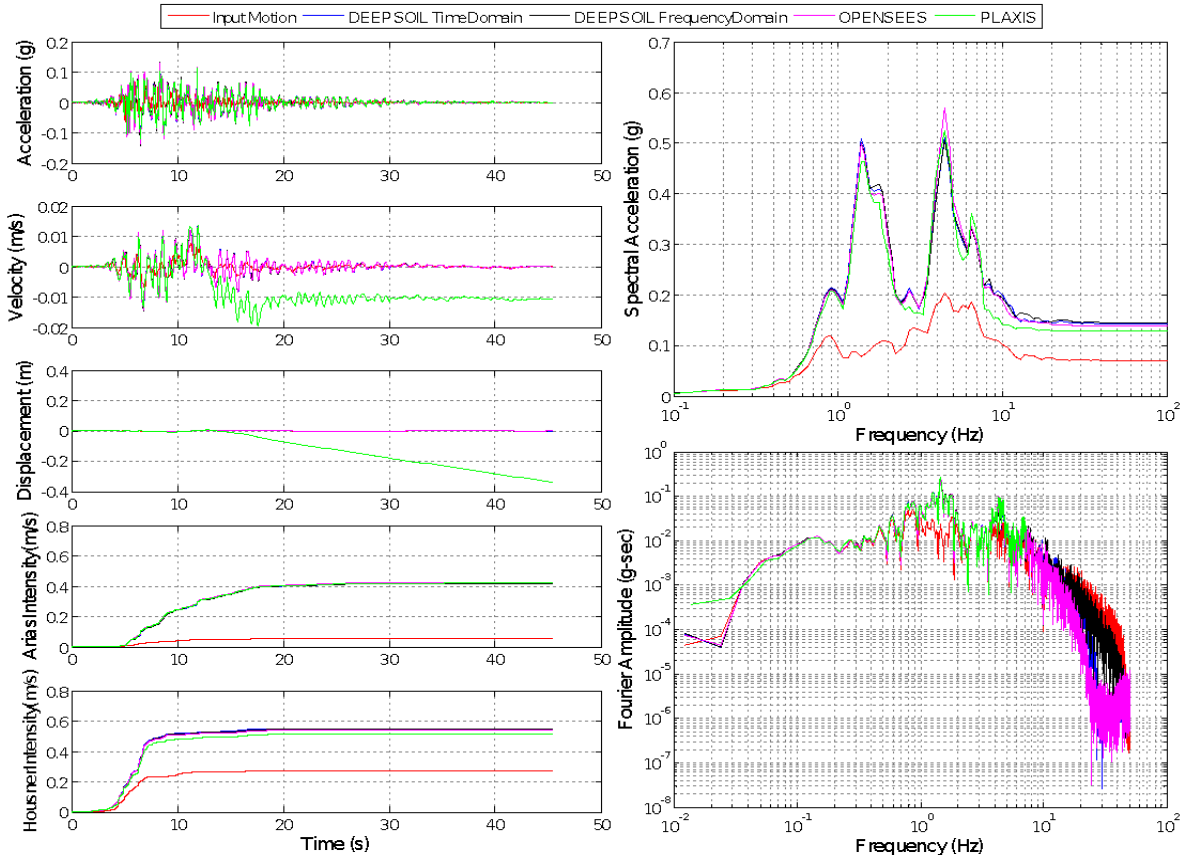

Figure A.1 Comparison of Linear Site Response Results for NGA_no_1787_HE000

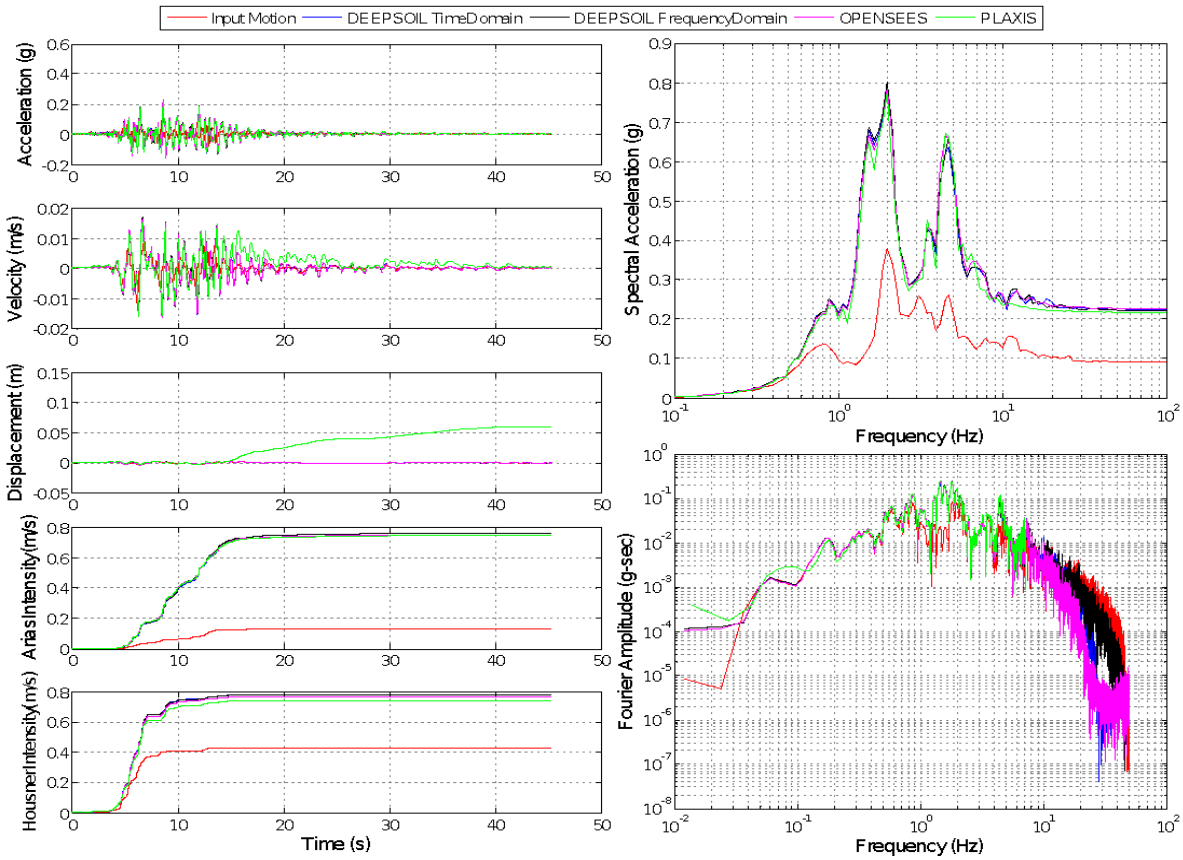

Figure A.2 Comparison of Linear Site Response Results for NGA_no_1787_HE090

A.2 OpenSees and Diana

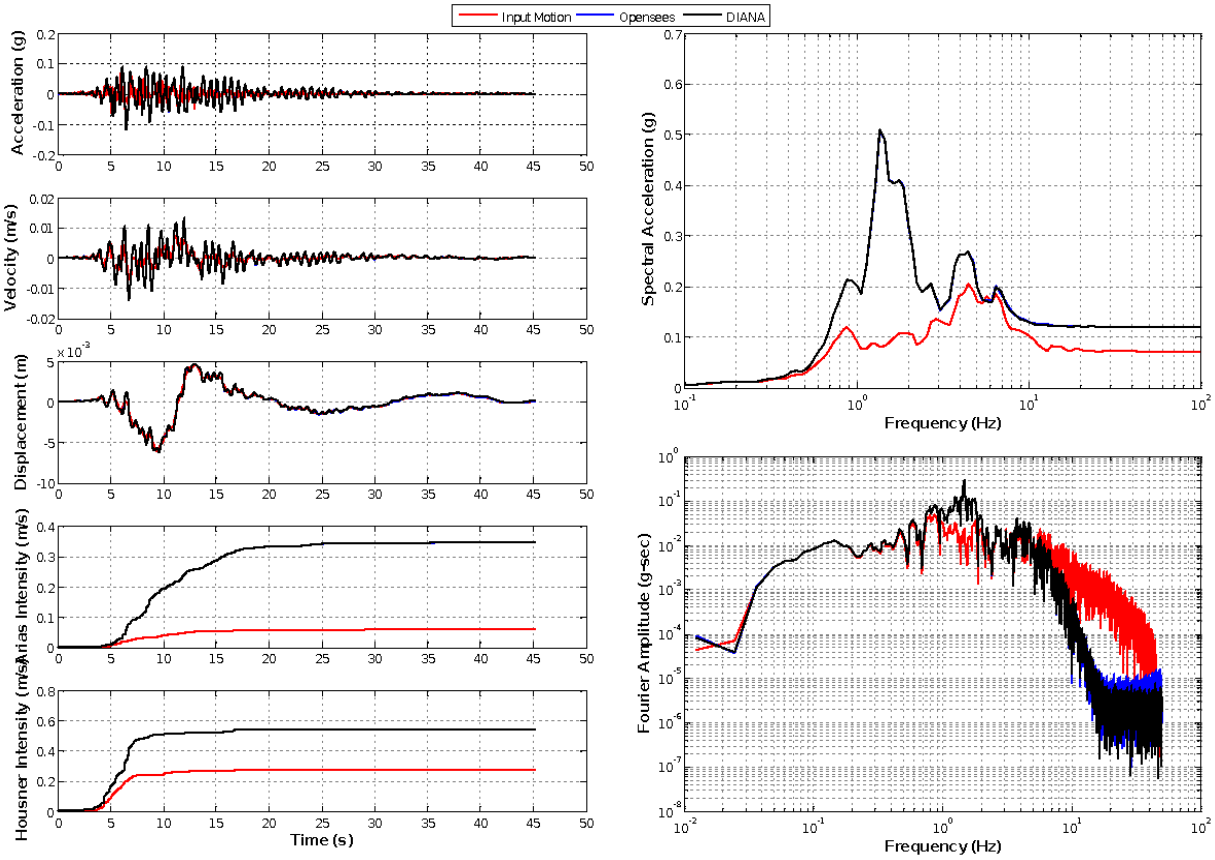

Figure A.3 Comparison of Linear Site Response Results for NGA_no_1787_HEC000 Using Stiffness Proportional Damping

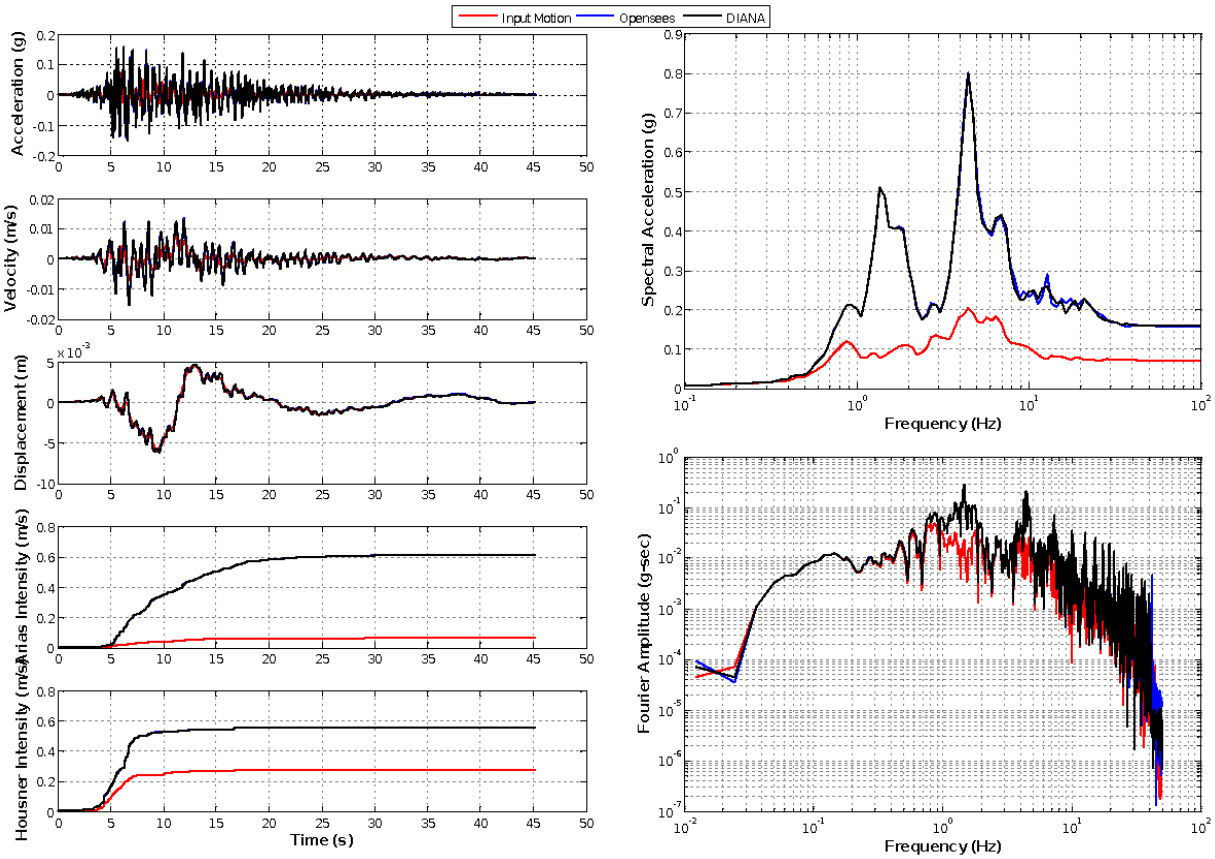

Figure A.4 Comparison of Linear Site Response Results for NGA_no_1787_HEC000 Using Mass Proportional Damping

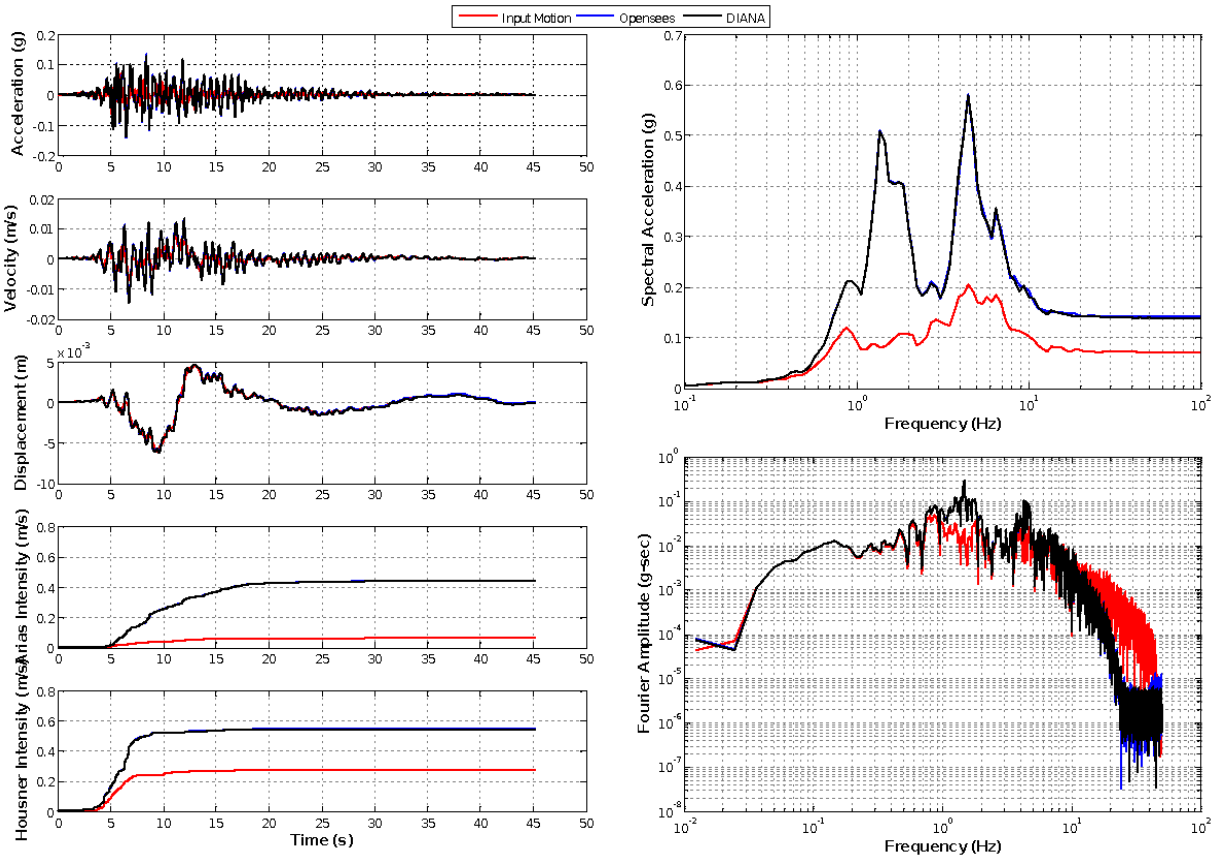

Figure A.5 Comparison of Linear Site Response Results for NGA_no_1787_HEC000 Using Both Mass and Stiffness Proportional Damping

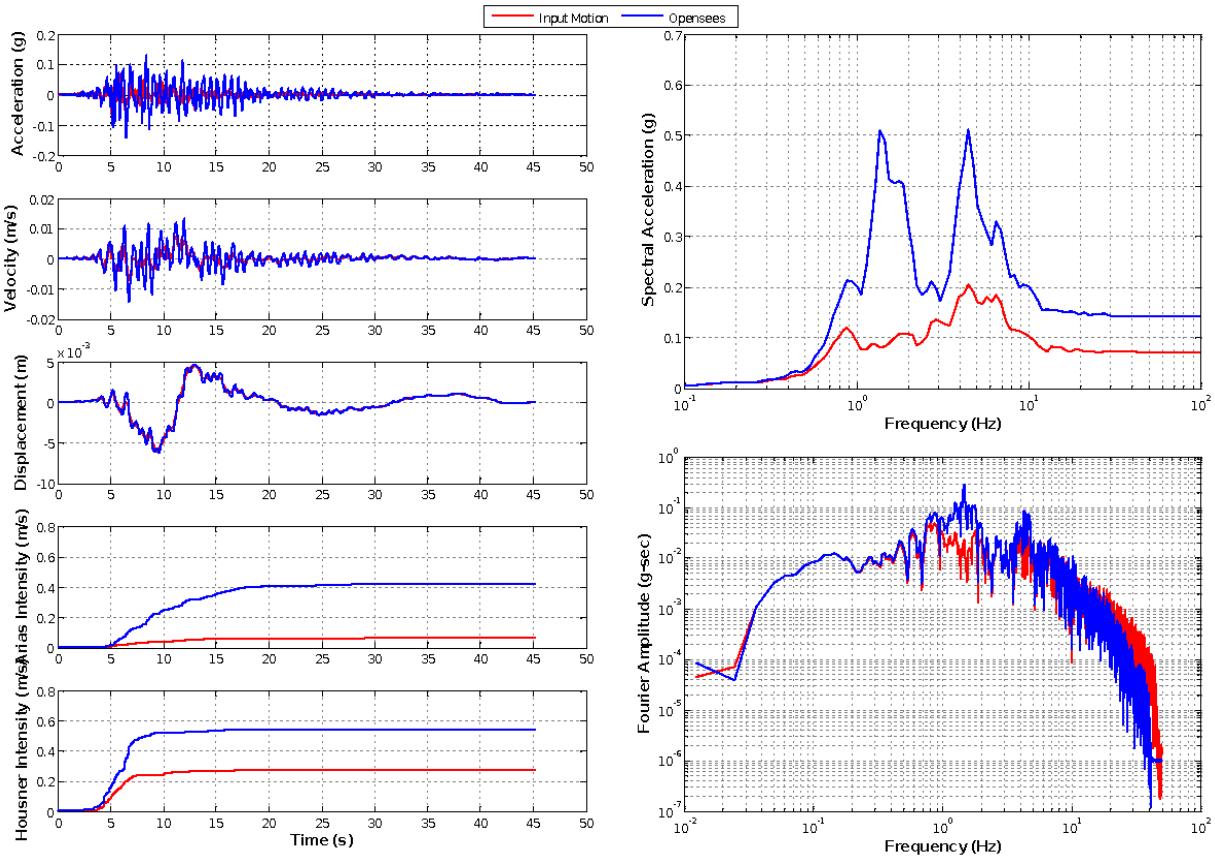

Figure A.6 Comparison of Linear Site Response Results for NGA_no_1787_HEC000 using Luco Damping (Luco 2008)

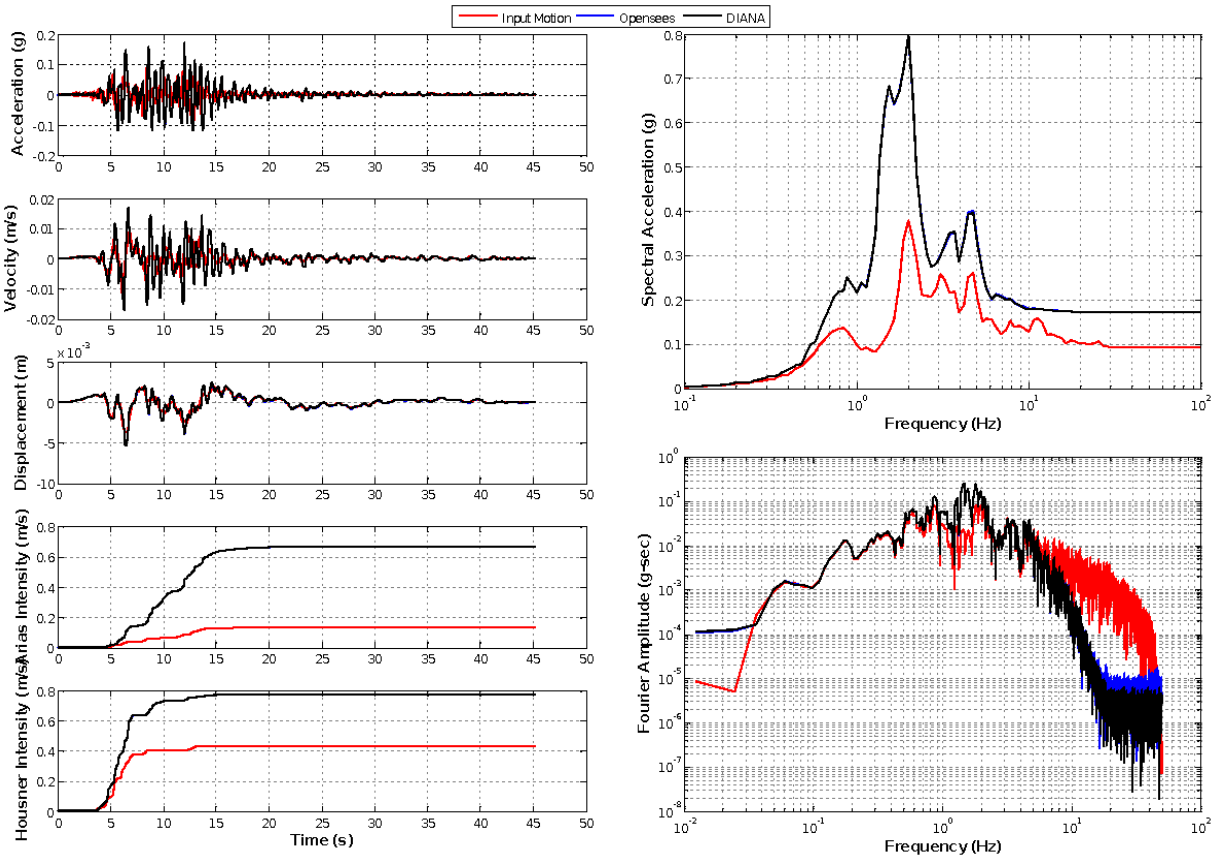

Figure A.7 Comparison of Linear Site Response Results for NGA_no_1787_HEC090 using Stiffness Proportional Damping

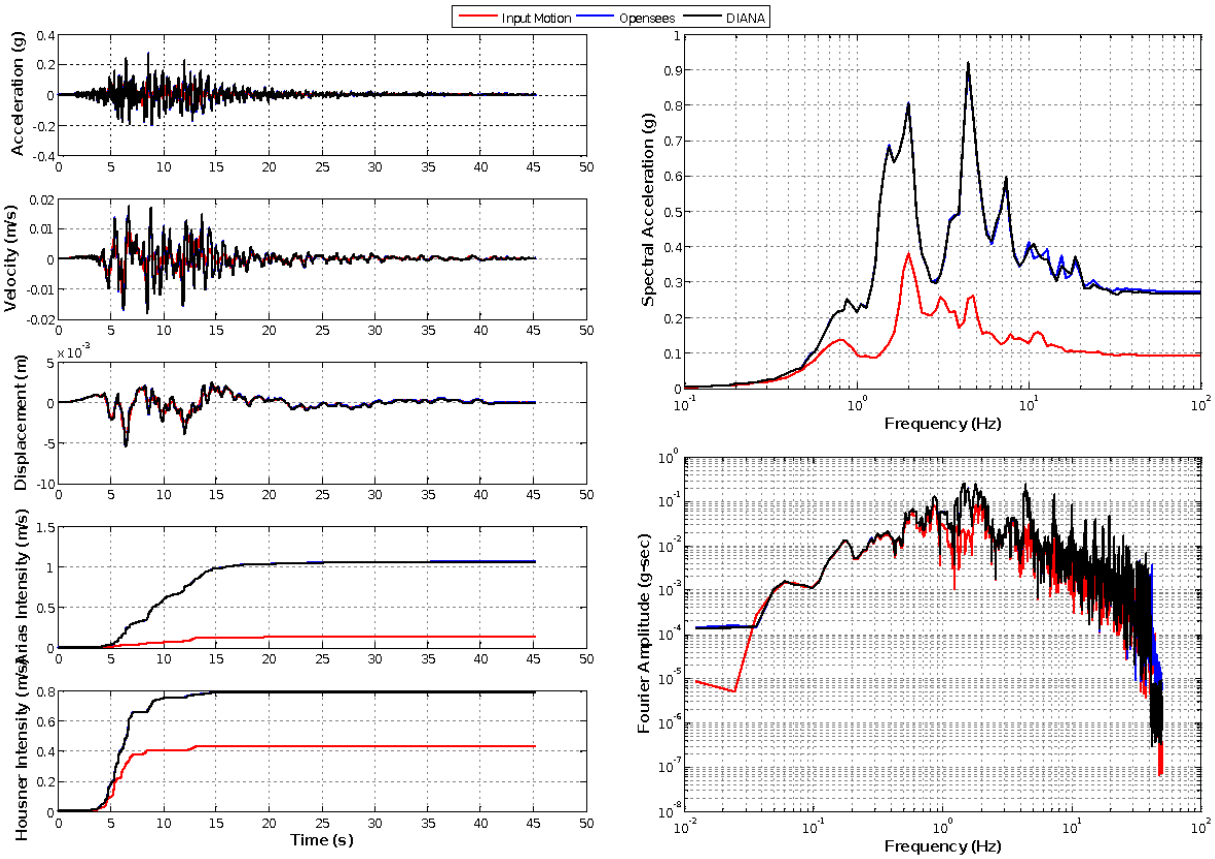

Figure A.8 Comparison of Linear Site Response Results for NGA_no_1787_HEC090 using Mass Proportional Damping

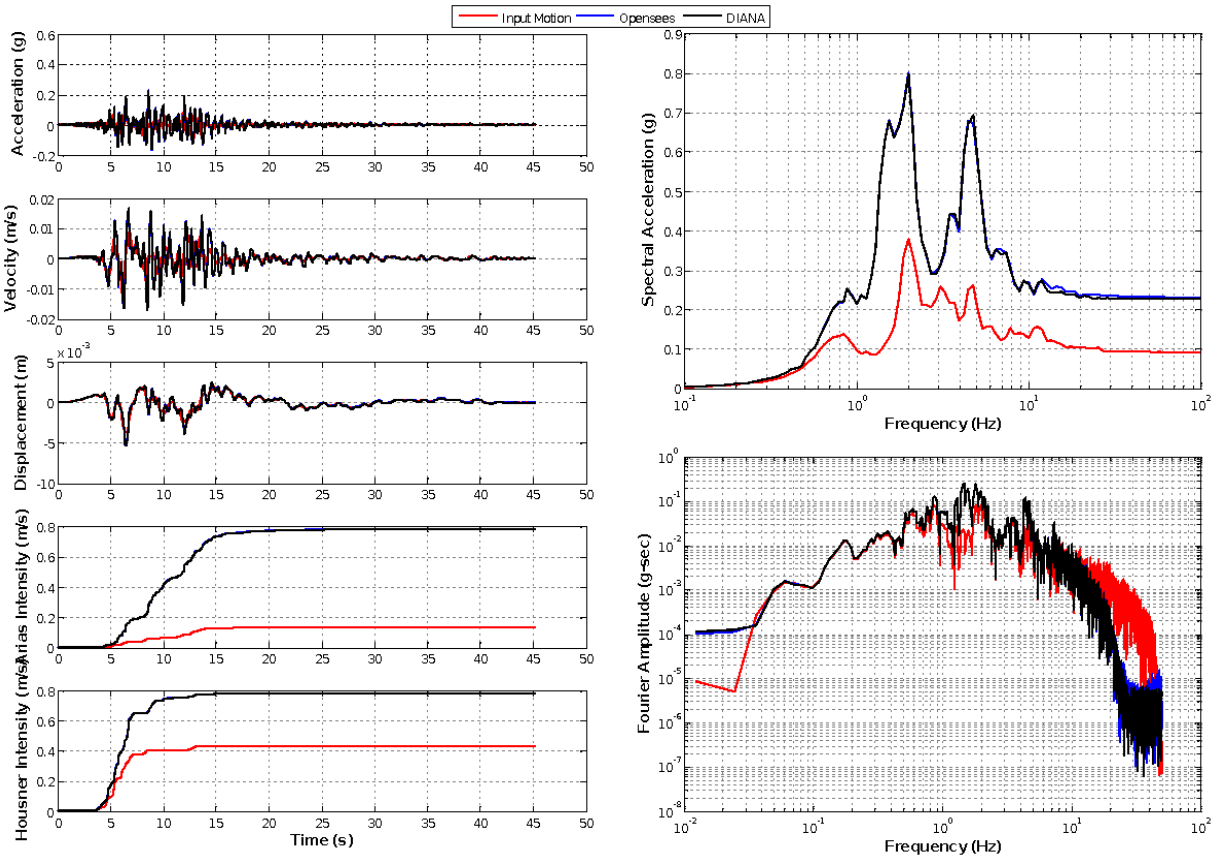

Figure A.9 Comparison of Linear Site Response Results for NGA_no_1787_HEC090 Using Both Mass and Stiffness Proportional Damping

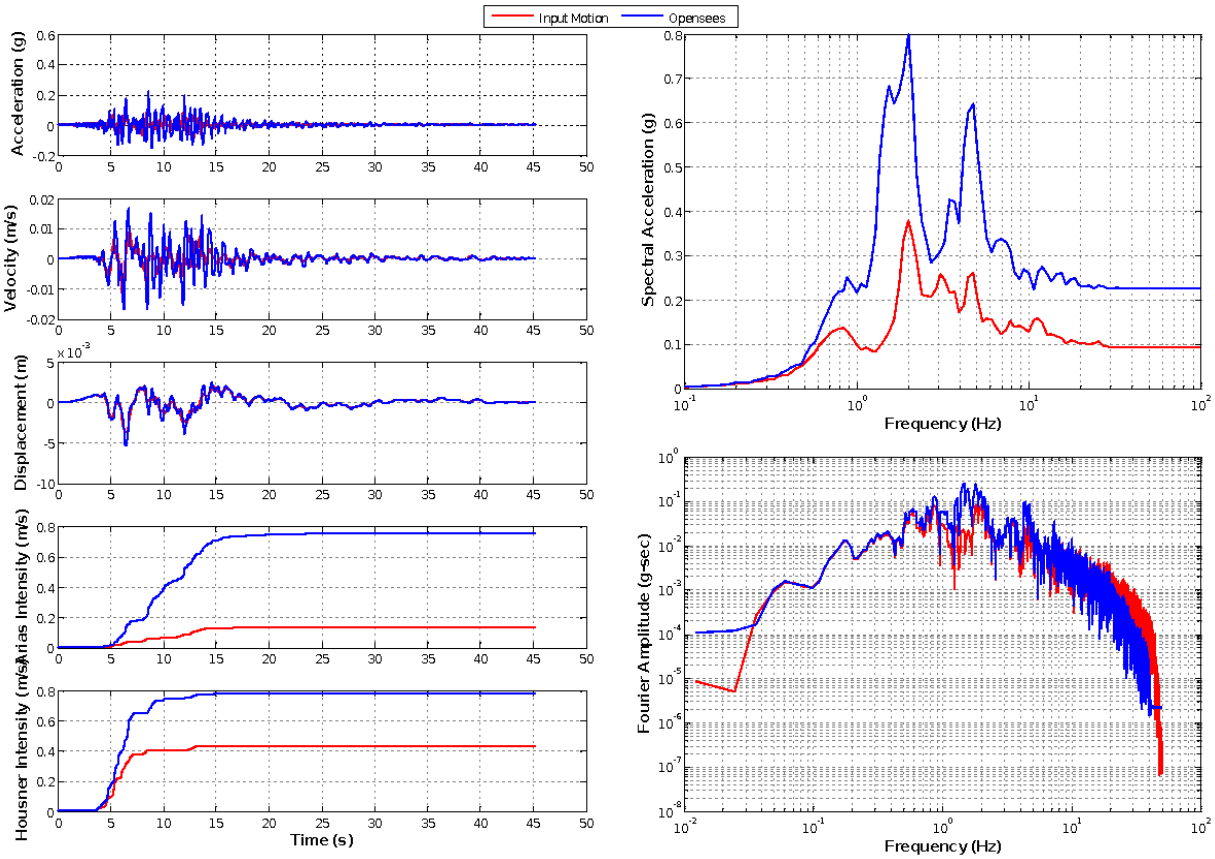

Figure A.10 Comparison of Linear Site Response Results for NGA_no_1787_HEC090 Using Luco Damping (Luco 2008)

A.3 LS Dyna

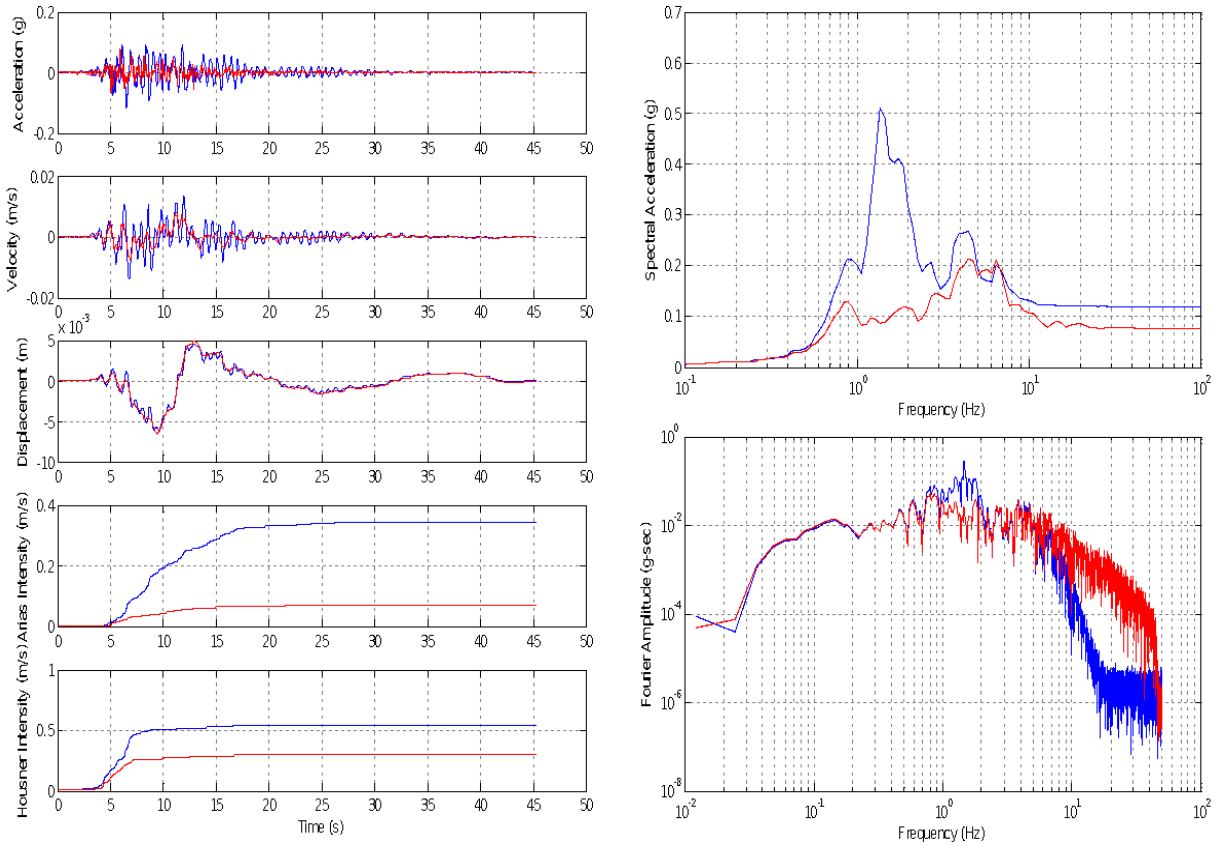

Figure A.11 Comparison of Linear Site Response Results for NGA_no_1787_HEC000 Using Stiffness Proportional Damping

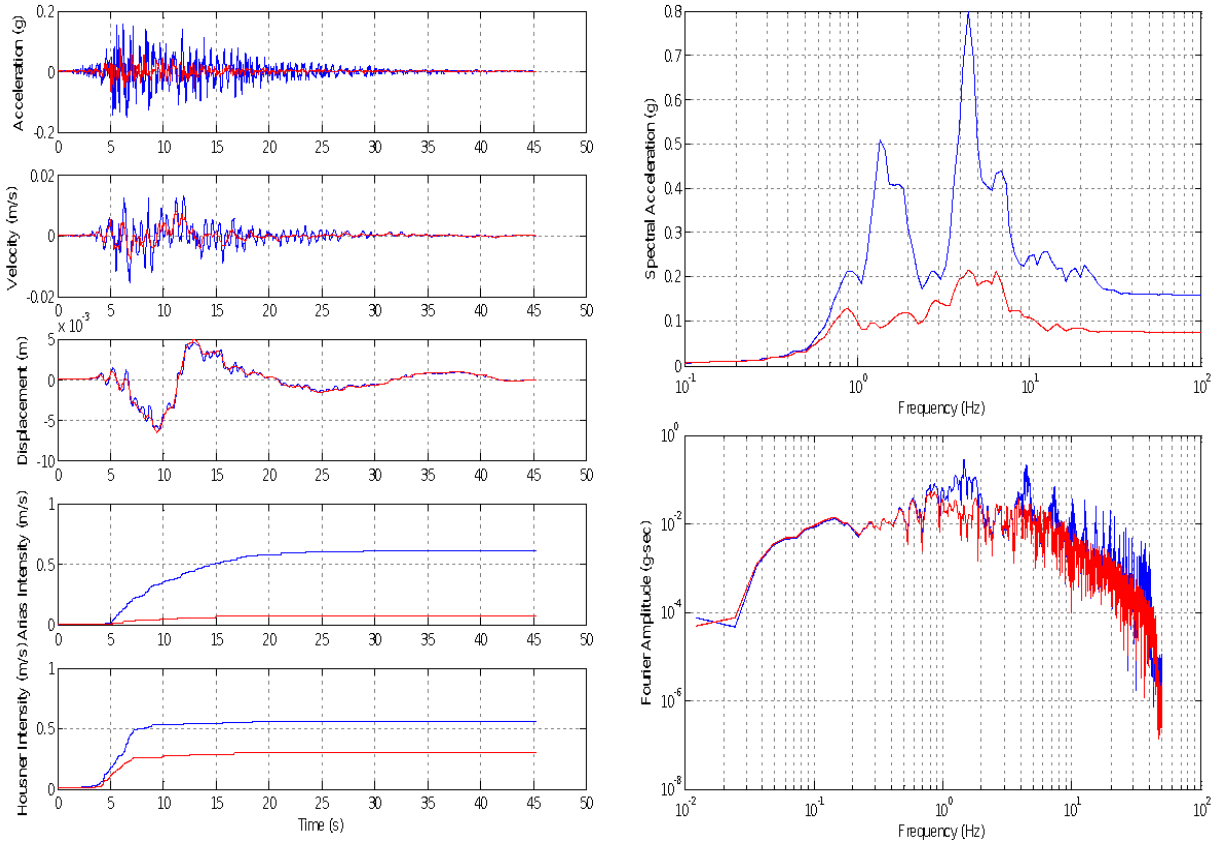

Figure A.12 Comparison of Linear Site Response Results for NGA_no_1787_HEC000 Using Mass Proportional Damping

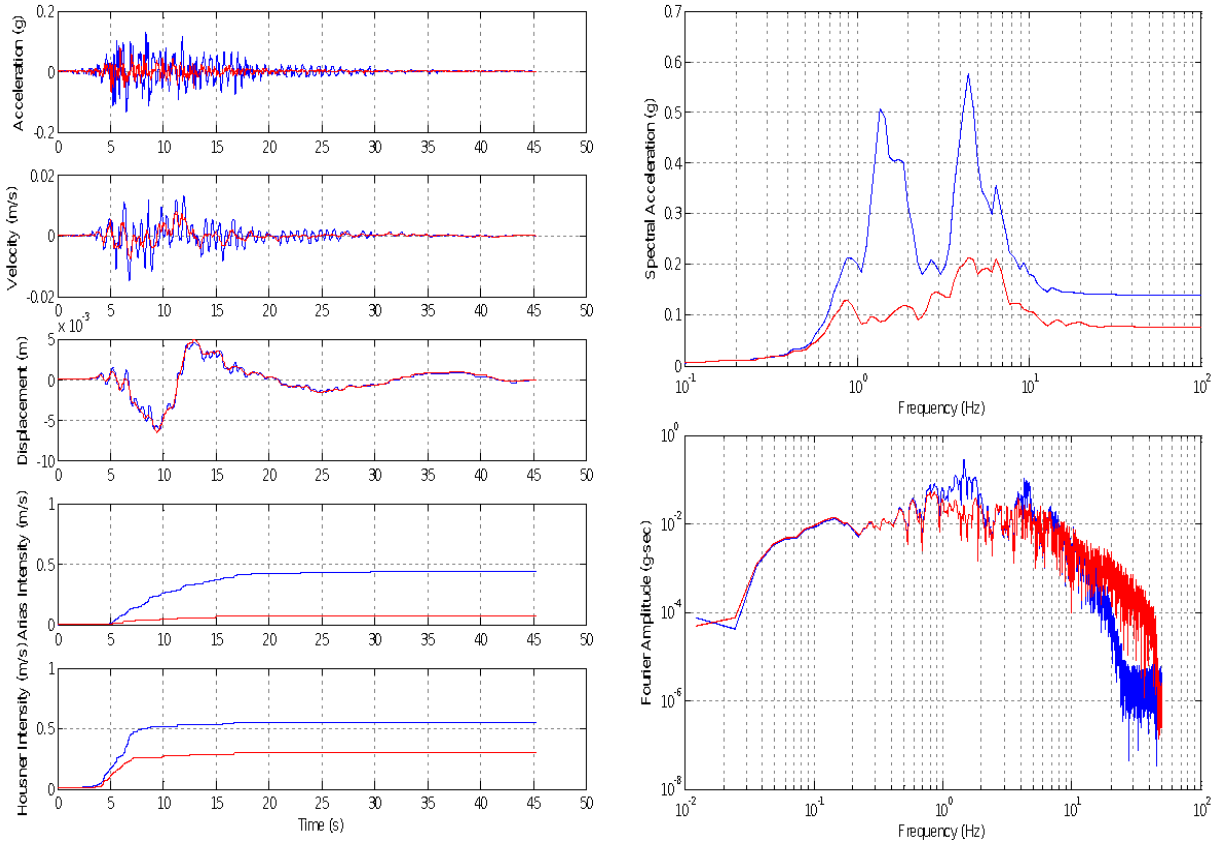

Figure A.13 Comparison of Linear Site Response Results for NGA_no_1787_HEC000 Using Both Mass and Stiffness Proportional Damping

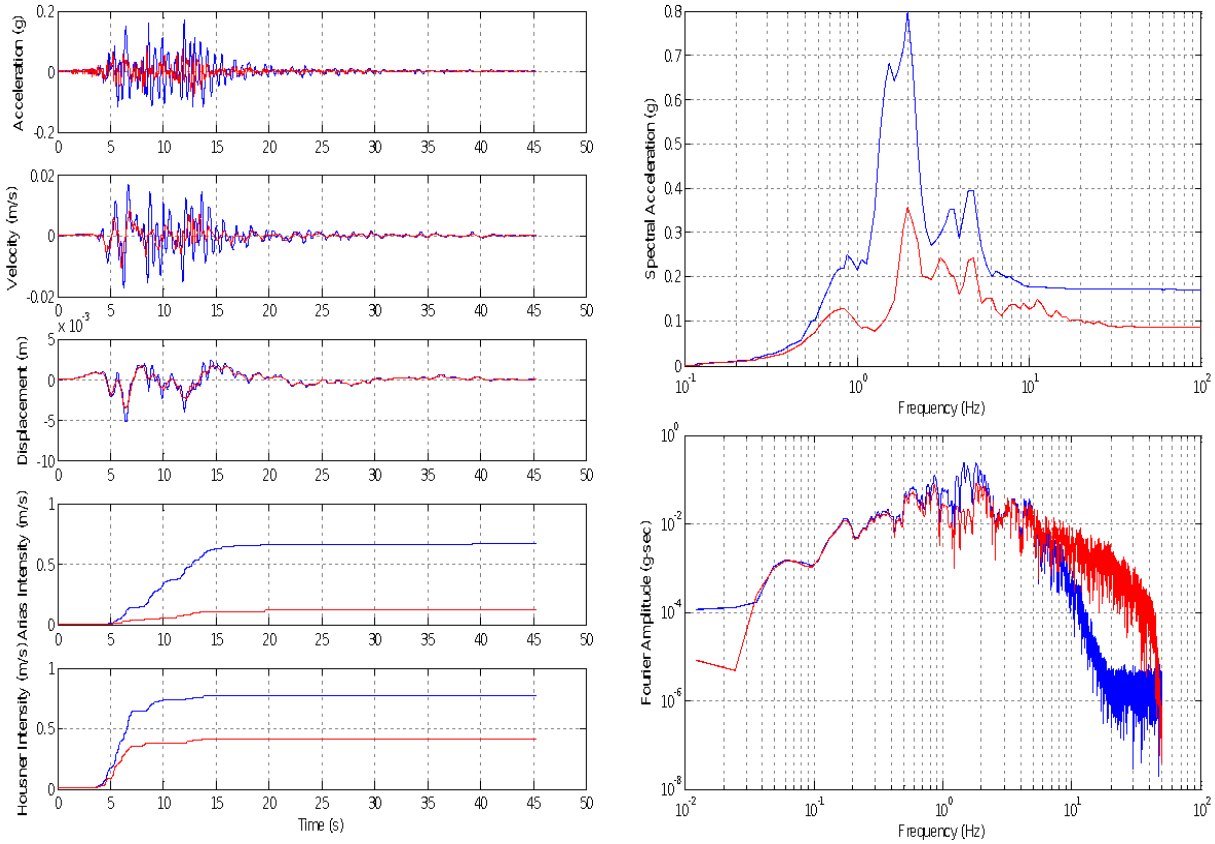

Figure A.14 Comparison of Linear Site Response Results for NGA_no_1787_HEC090 Using Stiffness Proportional Damping

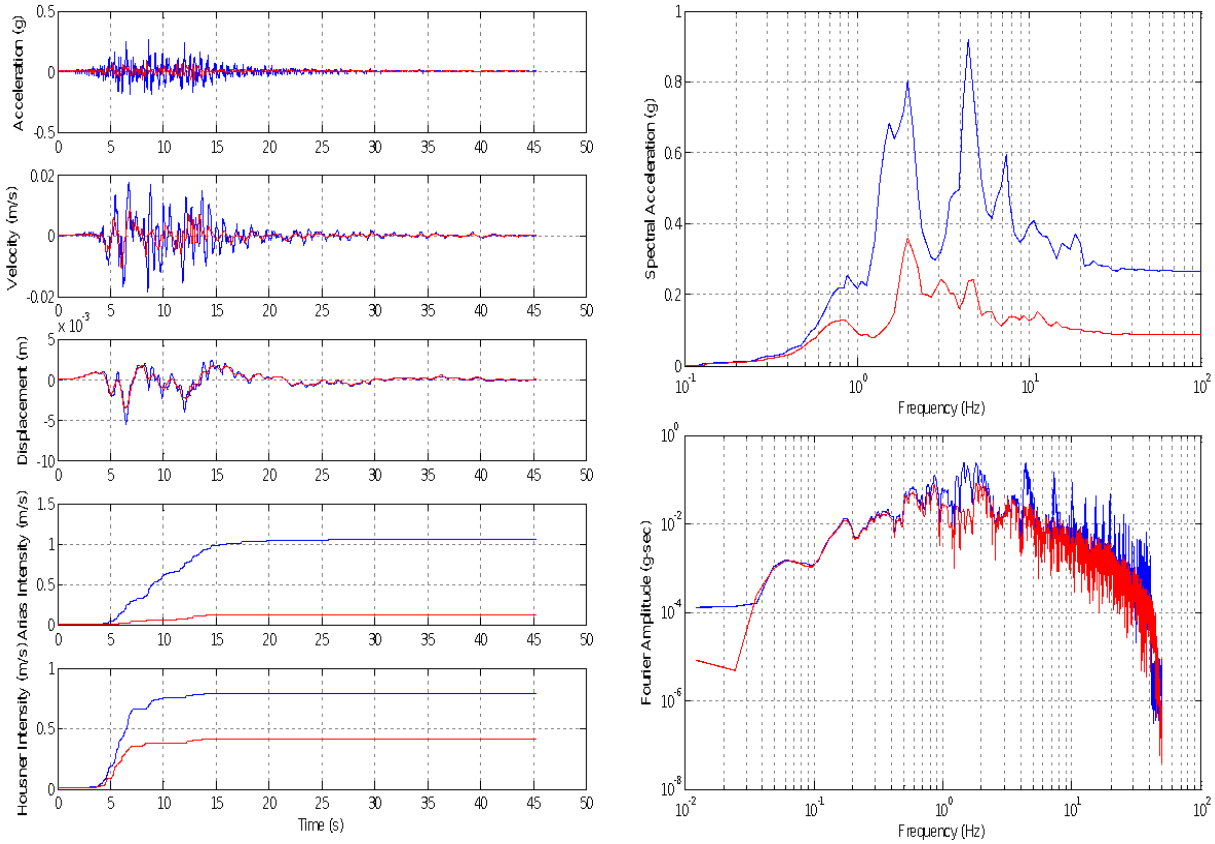

Figure A.15 Comparison of Linear Site Response Results for NGA_no_1787_HEC090 Using Mass Proportional Damping

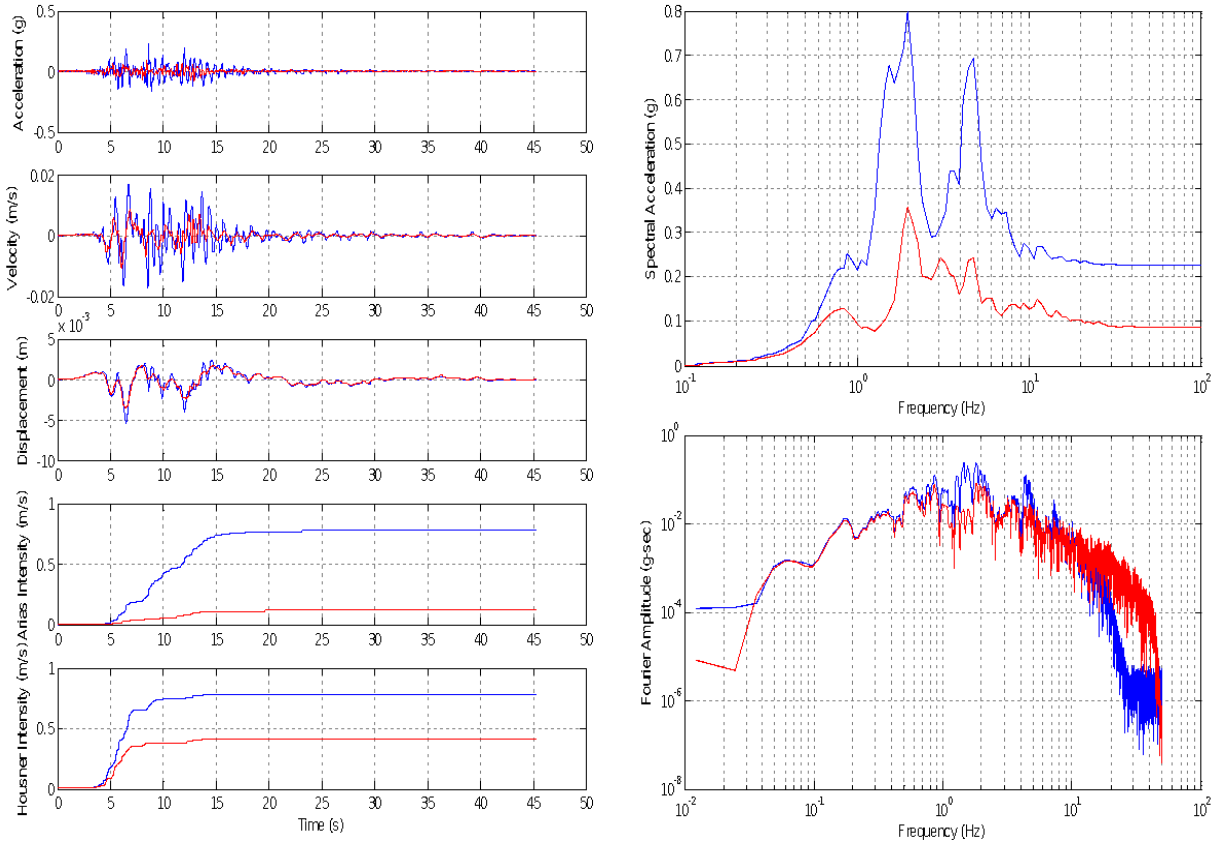

Figure A.16 Comparison of Linear Site Response Results for NGA_no_1787_HEC090 Using Both Mass and Stiffness Proportional Damping

Appendix B

Nonlinear Results (1D Site Response)

B.1 DEEPSOIL (Frequency Independent) and OpenSees (Rayleigh Damping)

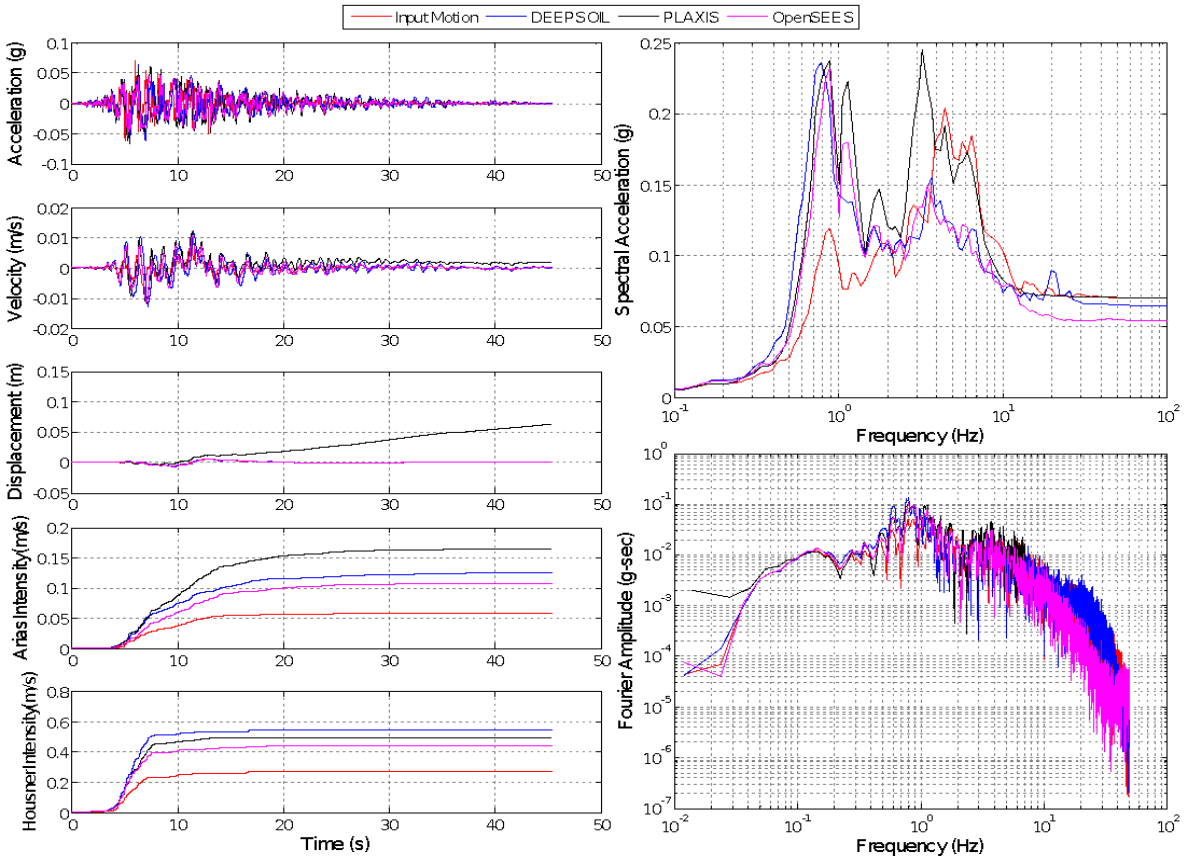

Figure B.1 Comparison of Non-linear Site Response Results for NGA_no_1787_HE000

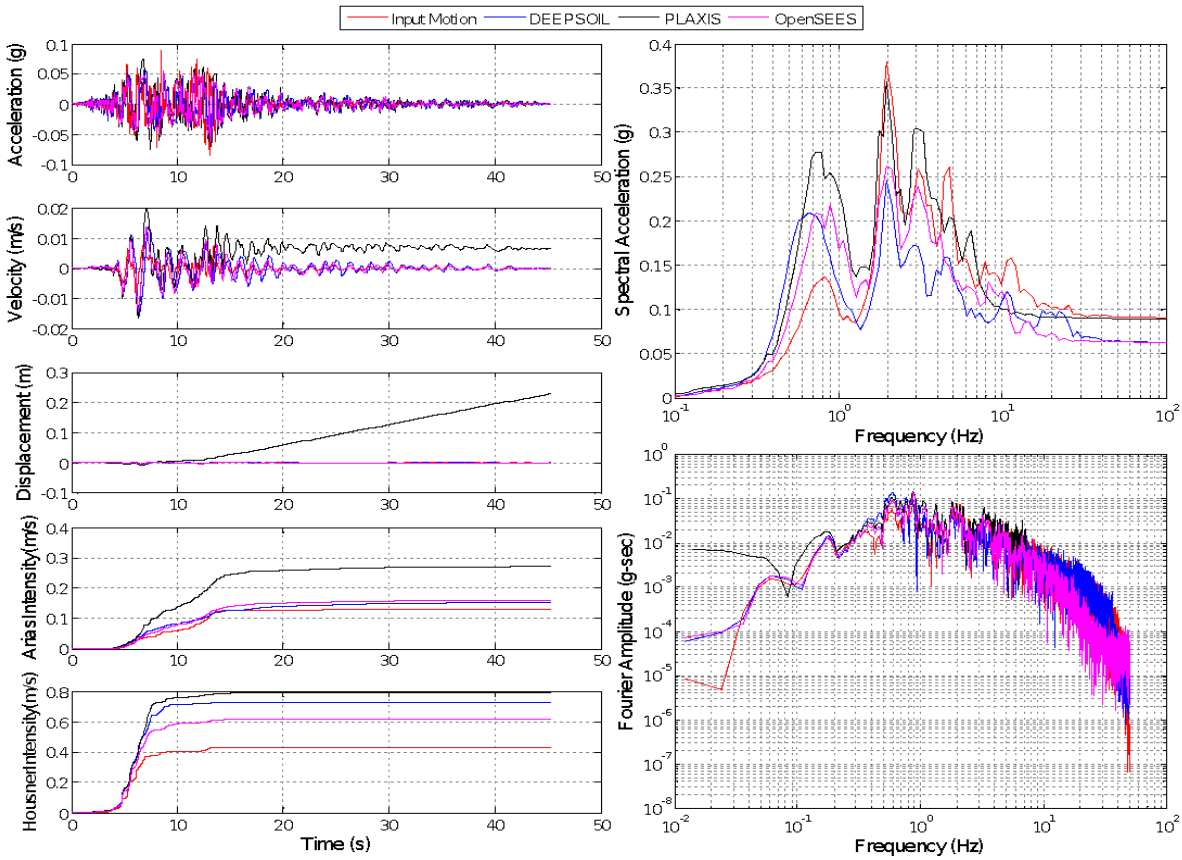

Figure B.2 Comparison of Non-linear Site Response Results for NGA_no_1787_HE090

B.2 Response due to Other Input Motions

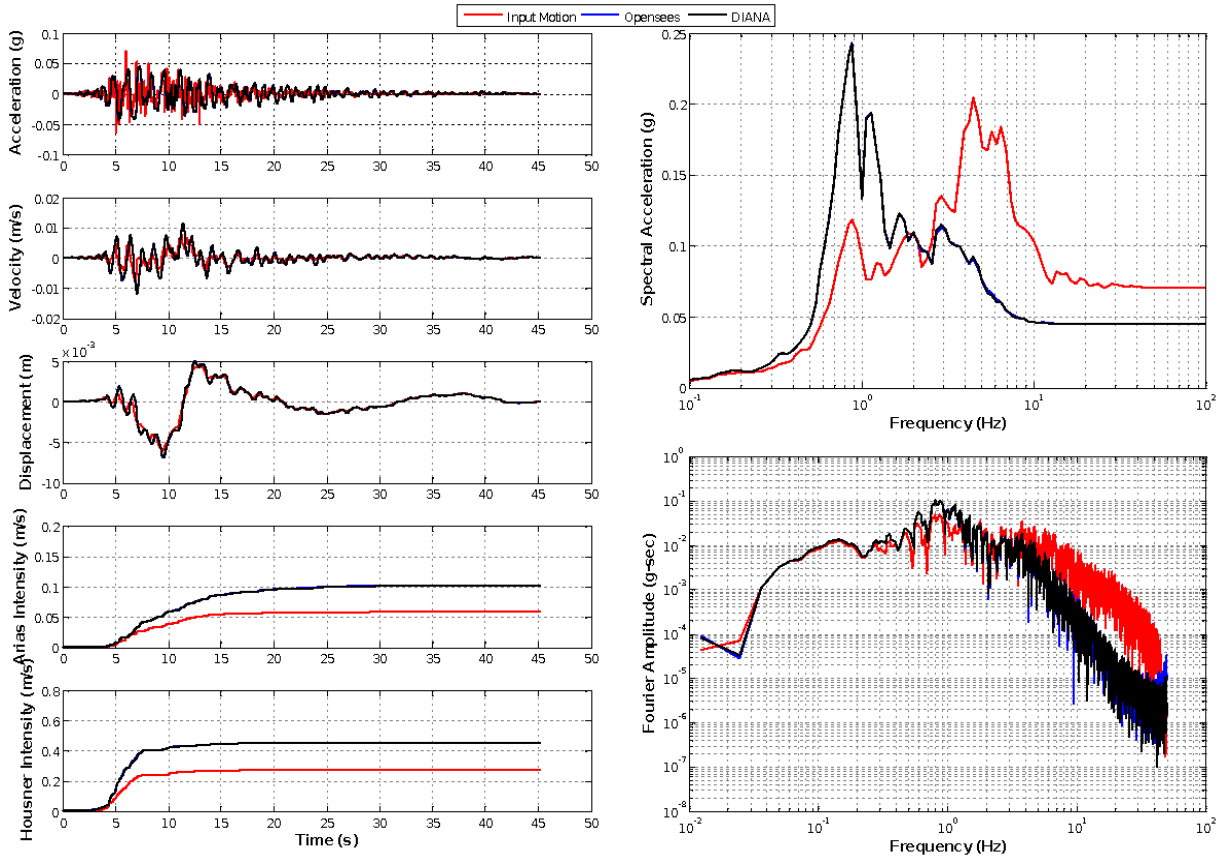

Figure B.3 Comparison of nonlinear site response results for NGA_no_1787_HEC000 Using stiffness proportional damping

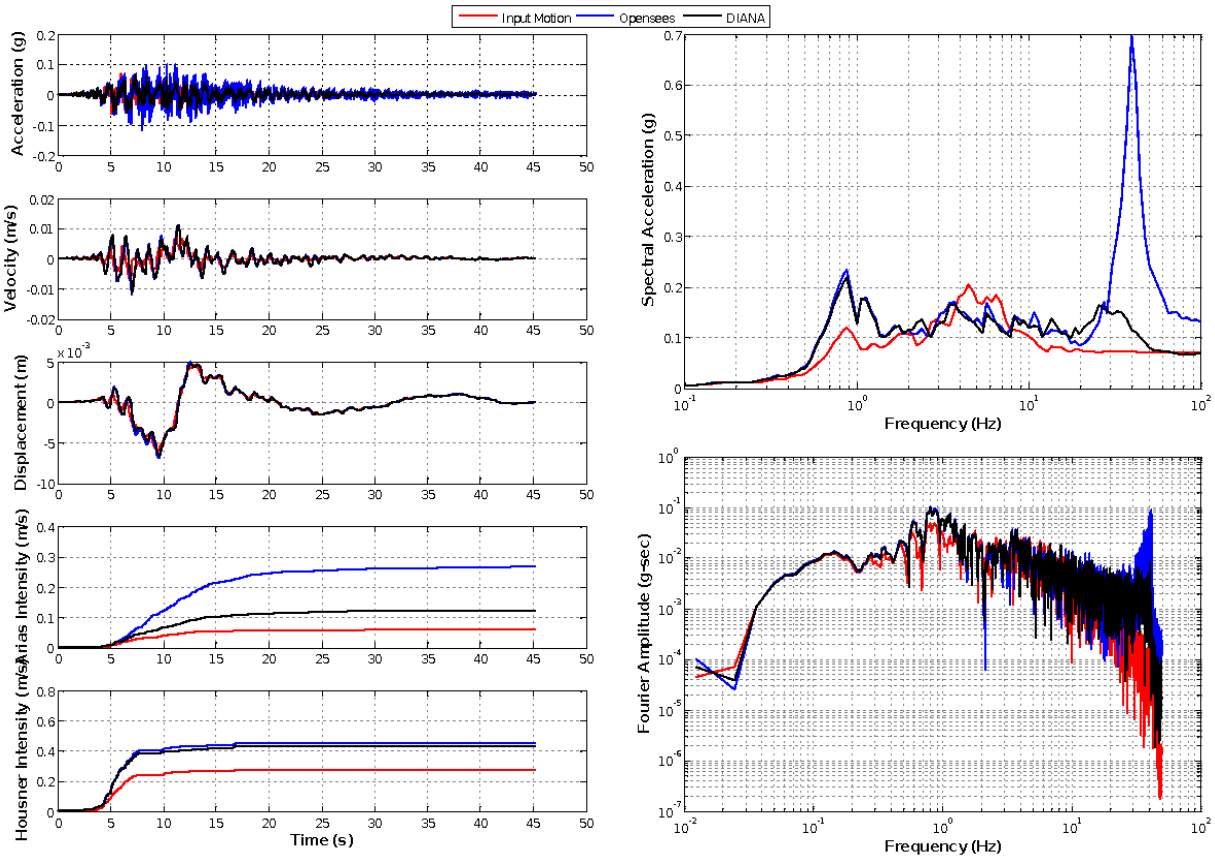

Figure B.4 Comparison of nonlinear site response results for NGA_no_1787_HEC000 Using Mass Proportional Damping

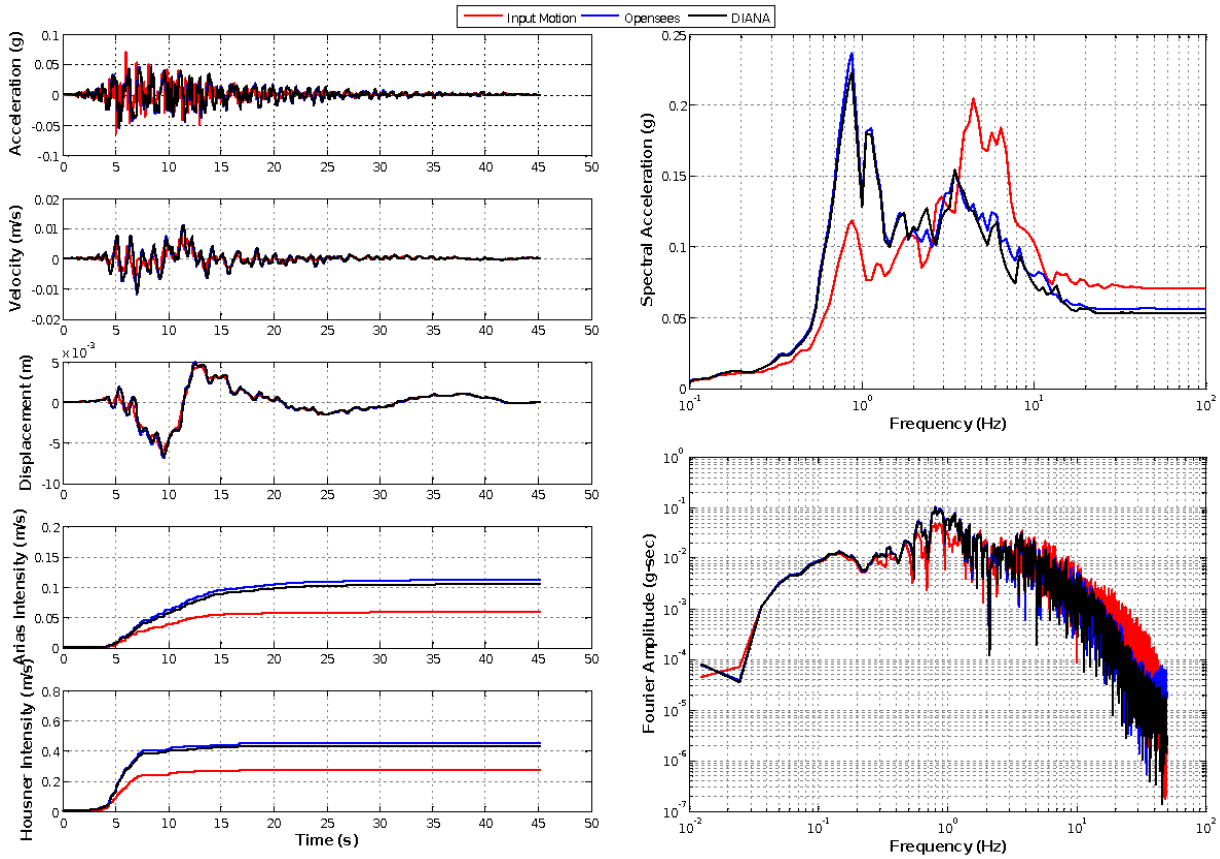

Figure B.5 Comparison of nonlinear site response results for NGA_no_1787_HEC000 using both Mass and Stiffness Proportional Damping

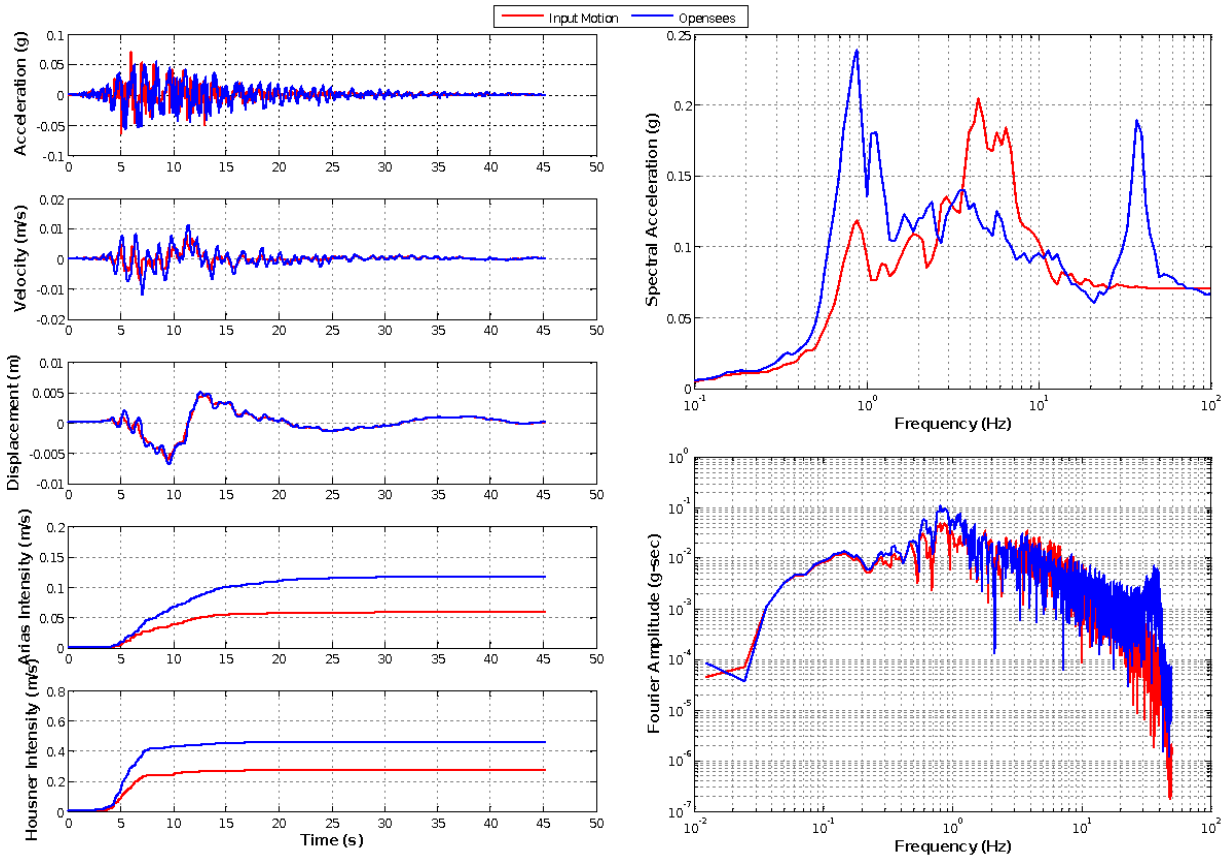

Figure B.6 Comparison of nonlinear site response results for NGA_no_1787_HEC000 using Luco Damping (Luco 2008)

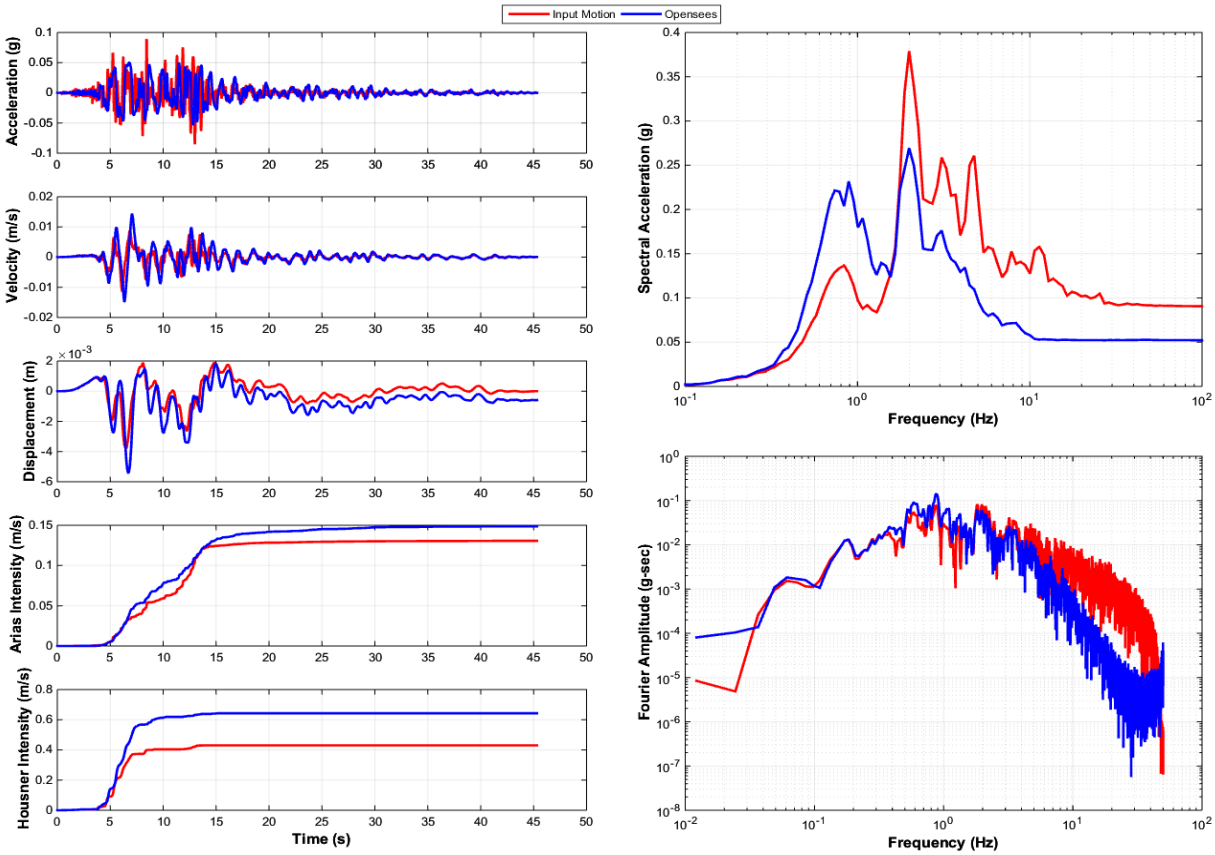

Figure B.7 Comparison of nonlinear site response results for NGA_no_1787_HEC090 using stiffness proportional damping

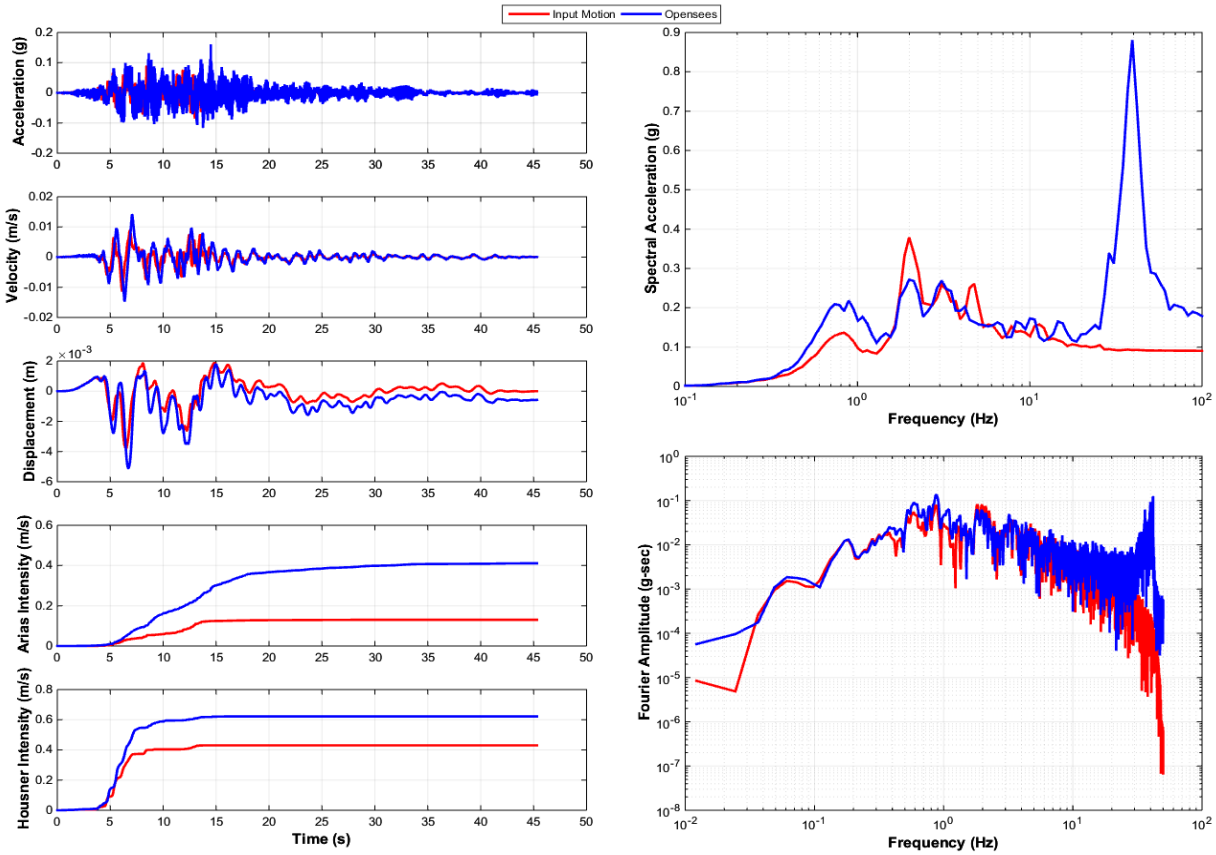

Figure B.8 Comparison of nonlinear site response results for NGA_no_1787_HEC090 using mass proportional damping

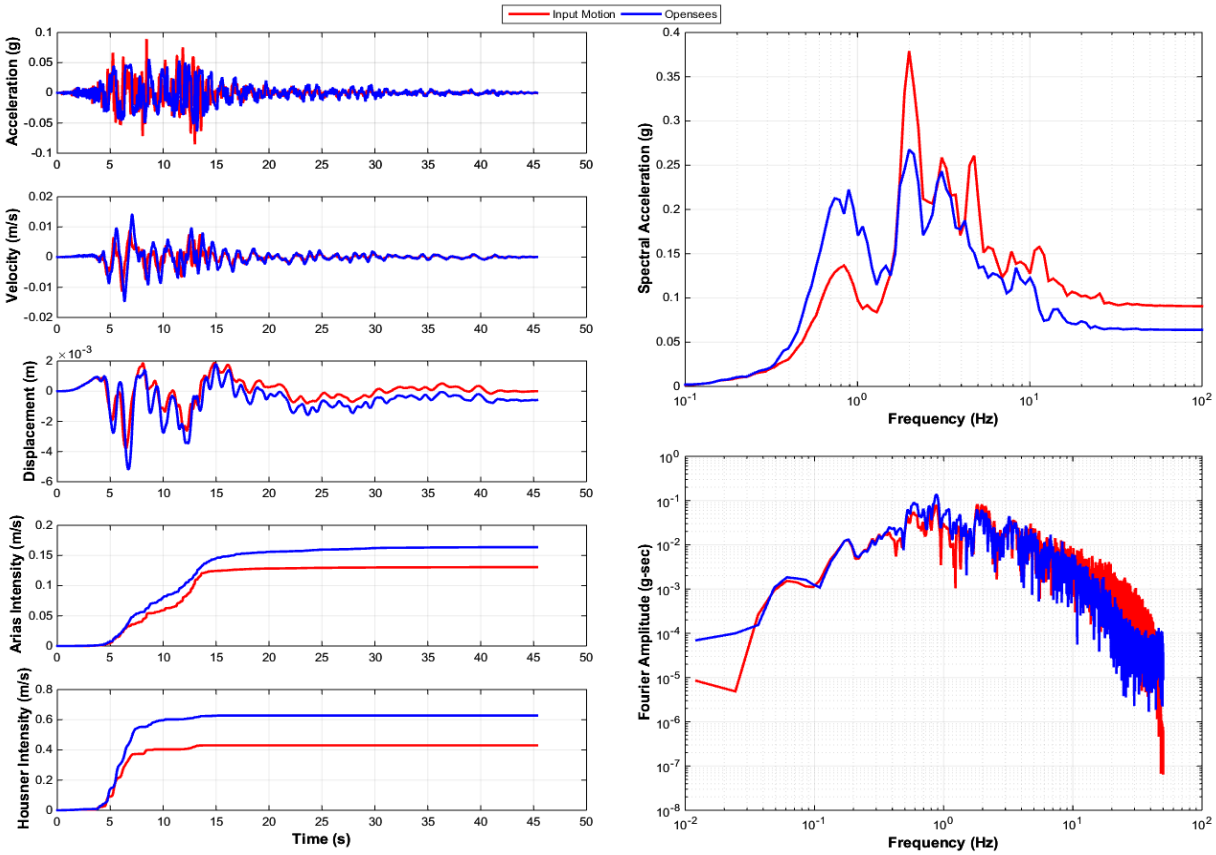

Figure B.9 Comparison of nonlinear site response results for NGA_no_1787_HEC090 using both mass and stiffness proportional damping

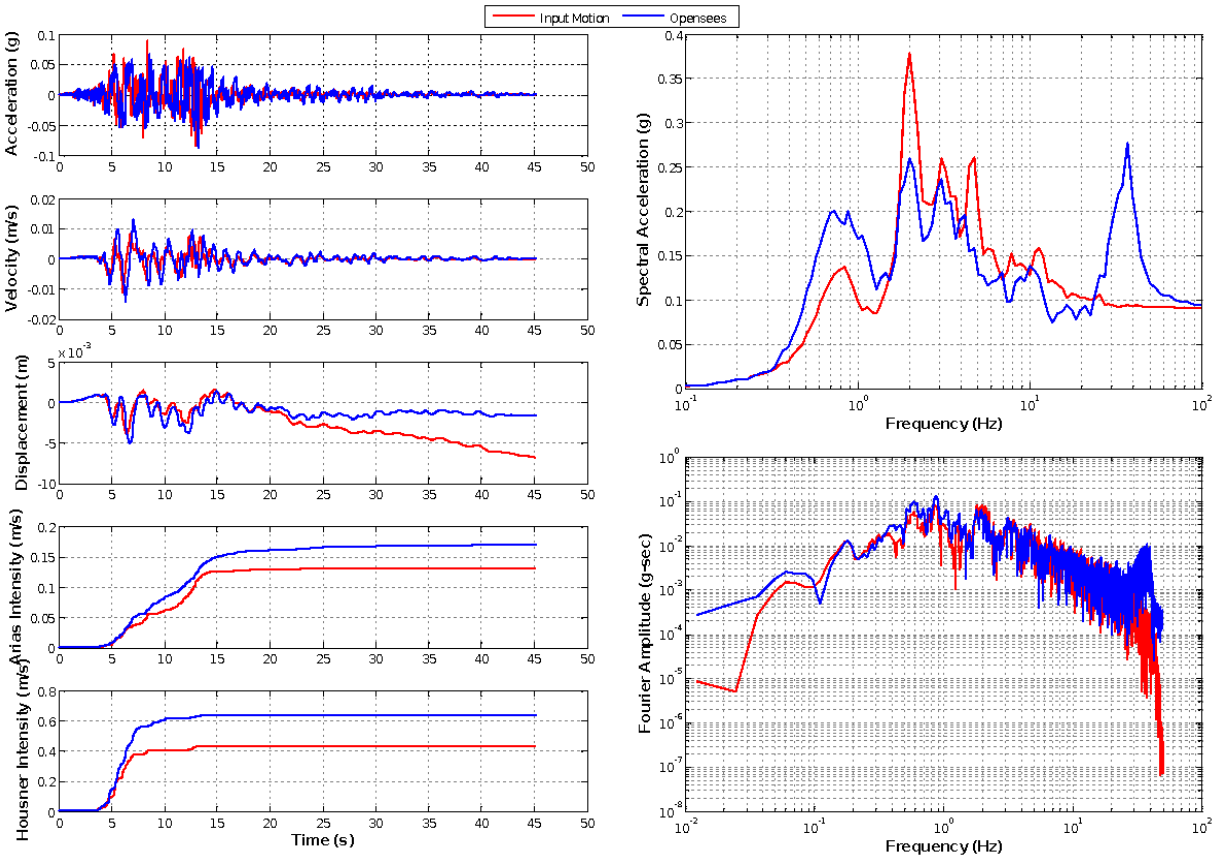

Figure B.10 Comparison of nonlinear site response results for NGA_no_1787_HEC090 using Luco damping (Luco 2008)

Appendix C

Additional Parametric Studies for Fully Embedded Structure

In exploring the FE response characteristics, a series of additional 2D plane strain OpenSees simulations were conducted. In this 2D environment, the related insights can be gleaned in a more efficient manner, as the simulations only require a fraction of the computational effort needed in 3D.

C.1 Mesh Refinement

Two different levels of refinement were addressed as illustrated in Figure C.1. The first model had the same level of refinement as that of the 3D mesh with increasing lateral spacing moving away from the structure, while the second model was significantly more refined. Upon comparing the responses, it was observed that the higher refinement had marginal impact on the overall response of the structure. As shown in Figure C.1**,** the acceleration of the structure was virtually identical for the two cases. There were minimal differences in the high frequency response but overall it appears that the original mesh was adequate for the purposes of this study. Away from the structure, free-field response was virtually identical and additional mesh refinement was unnecessary.

C.2 Response due to Other Input Motions

Additional input motions were employed to assess applicability of the main conclusions of this study, under a broader range of seismic excitation scenarios. For that purpose, input motions with a wide frequency range were selected (Figure C.2). From this study (Figure C.2), it was observed that similar to the 3D reported outcome, in all cases there was: i) a significant reduction in the high frequency response of the structure when compared to the free-field, and ii) at the top of the structure, acceleration remained similar to that at the base.

C.3 Simulation of Staged Construction

To investigate the influence of the-imposed uniform horizontal state of stress, an additional OpenSees FE analysis was conducted. A simple idealization of staged construction was explored, where gravity analysis was imposed in four phases (Figure C.3): i) free-field scenario (purple color elements), ii) removal of loads due to excavation in order to place the structure, iii) addition of structure (blue color elements), and iv) placement of fill around the structure (yellow color elements).

In the first step, gravity was activated for all ground elements. Subsequently, the yellow and blue elements were removed to simulate excavation. Afterwards, the blue elements were added and assigned properties for the structure. Finally, the fill zones around the structure were activated using the same properties as the original ground. The resulting stress state (Figure C.3) in close vicinity to the structure is somewhat different from that of earlier employed smooth state of stress. At about 100 meters away from the structure, the stresses gradually converge to what would be expected in the free-field.

As shown in Figure C.3, the two different gravity-imposed stress states had a relatively minor impact on the dynamic response of the structure. Away from the structure, free-field

responses were virtually the same. The high frequency response for the staged construction scenario was marginally reduced when compared to that of the uniform stress state.

Adjacent to the structure, differences in initial stress state due to the gravity application procedure had an impact on the dynamic lateral pressure exerted on the structure (Figure C.4). In this regard, the initial stress state depends on the procedure by which gravity is applied. However, the dynamic portion of the stress remained somewhat similar between the two cases.

C.4 Simple Spring-Dashpot model

In this section, motion of the structure at the ground surface was estimated, using the FE computed motion at its base. The structure was modeled by elastic beam column elements with the same mass and stiffness properties of the 3D FE model. The rotational spring-dashpot model of Gazetas (1991) was included at the base (Table 2), and motion at the base level of the structure (22.86 m) was applied as the input excitation.

Upon comparing the response spectra (Figure C.5), it can be seen that there is a reasonable level of overall agreement. Spectral acceleration amplification of the FE model in the 2 - 4 Hz range was not equally matched by this relatively simple spring-dashpot model. With this promising simplified modeling response, it is likely that more elaborate spring-dashpot efforts (e.g., Tsigginos et al. 2008, Assimaki and Gazetas 2009) will result in closer matching. For that purpose, calibration is needed over the expected nonlinear range of ground-structure response.

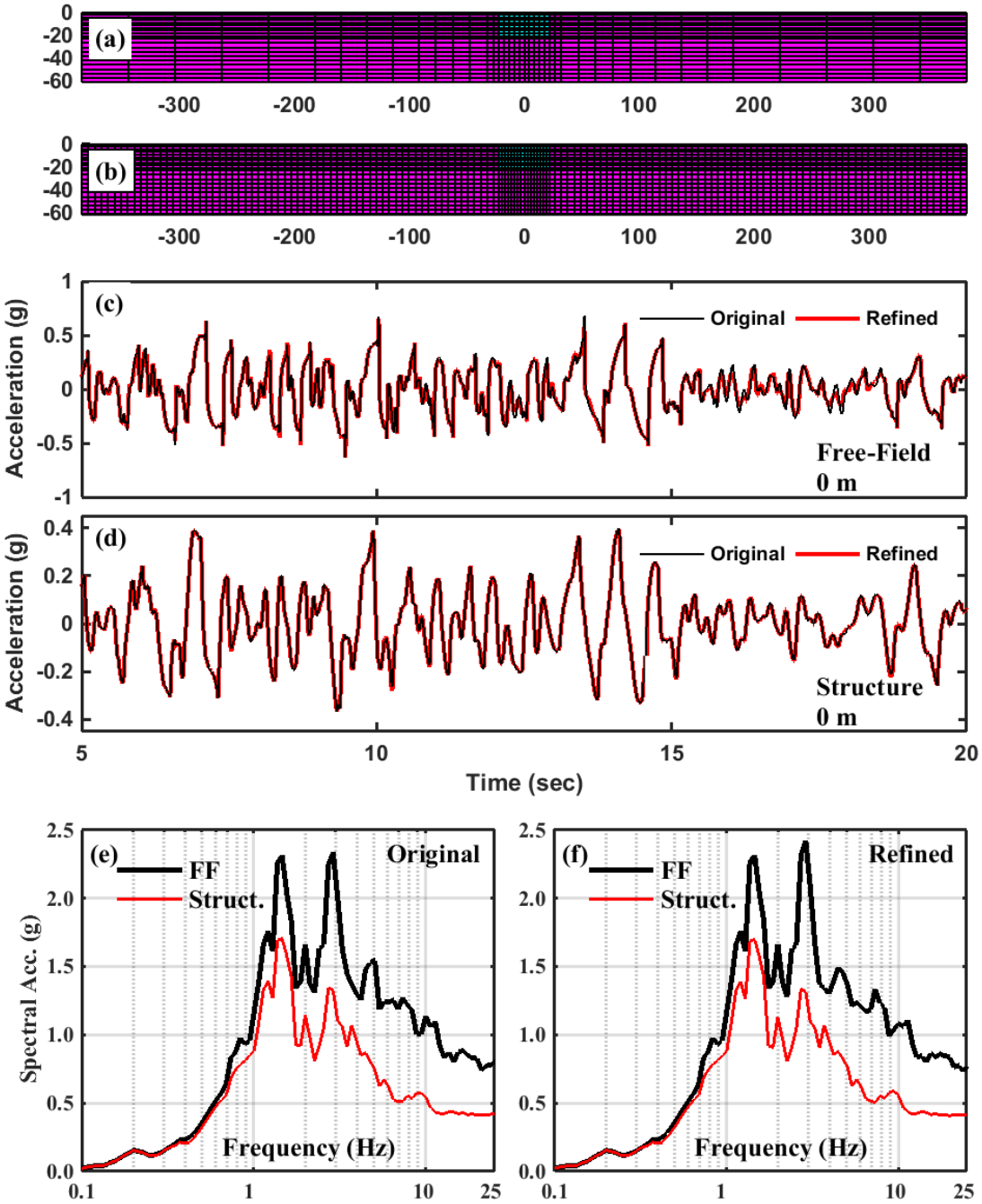

Figure C.1 (a) 2D finite element mesh with original level of refinement; (b) 2D finite element mesh with higher refinement; (c) acceleration at a depth of 0 m for free-field; (d) acceleration at a depth of 0 m for structure; (e) spectral acceleration using original mesh at free-field (FF) and structure (Struct.); (f) spectral acceleration using more refined mesh at free-field (FF) and structure (Struct.)

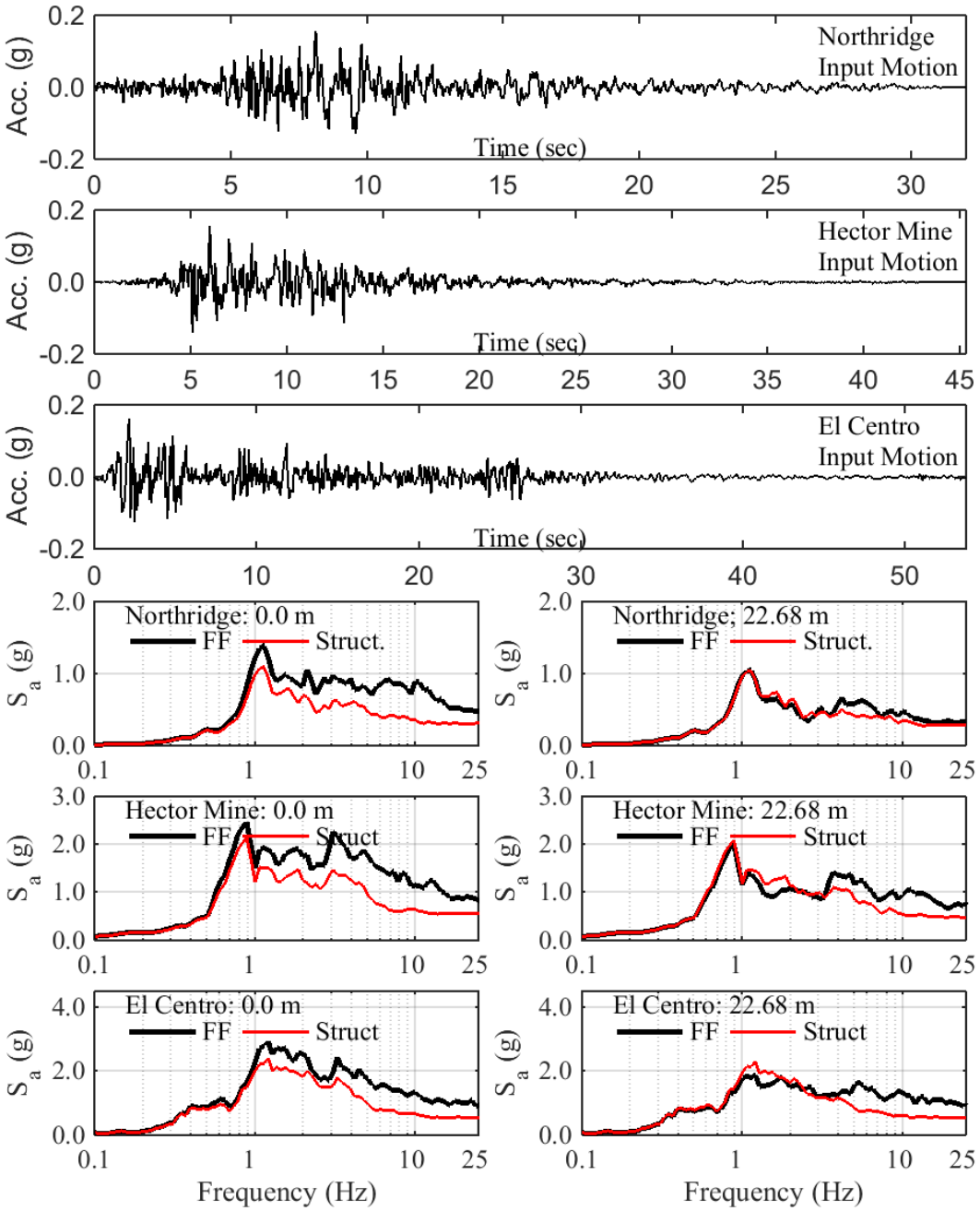

Figure C.2 Base input motion and response spectrum at ground surface (0.0 m) and base level of the structure (22.68 m) due to the Northridge Earthquake (1/17/94, 12:31, LEONA VALLEY #3, 000 CDMG STATION 24307), Hector Mine Earthquake (OCT 16, 1999 02:47, HEC, 000 and El Centro 1940 Earthquake (Component SOOE) at free-field (FF) and structure (Struct)

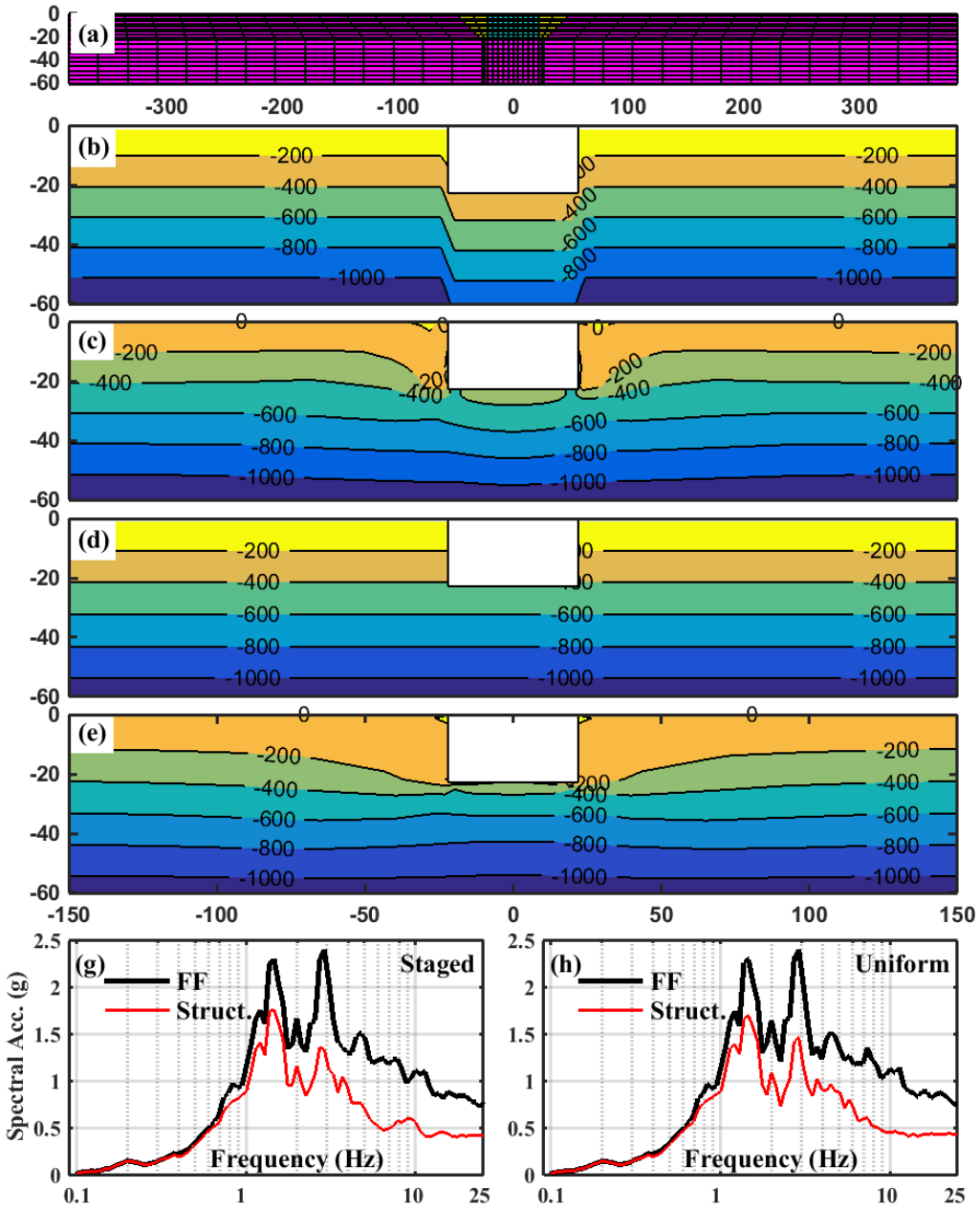

Figure C.3 (a) FE model (units in m) for staged construction including soil (purple), fill (yellow) and the structure (blue); and final stress states (kPa) (b) vertical for uniform stress state; c) vertical for staged construction; (d) lateral for uniform stress state; (e) lateral for staged construction; (g) spectral acceleration for the free-field and structure (at ground surface) for uniform stress state due to Taft motion; (h) spectral acceleration for the free-field and (at ground surface) for staged construction due to Taft motion

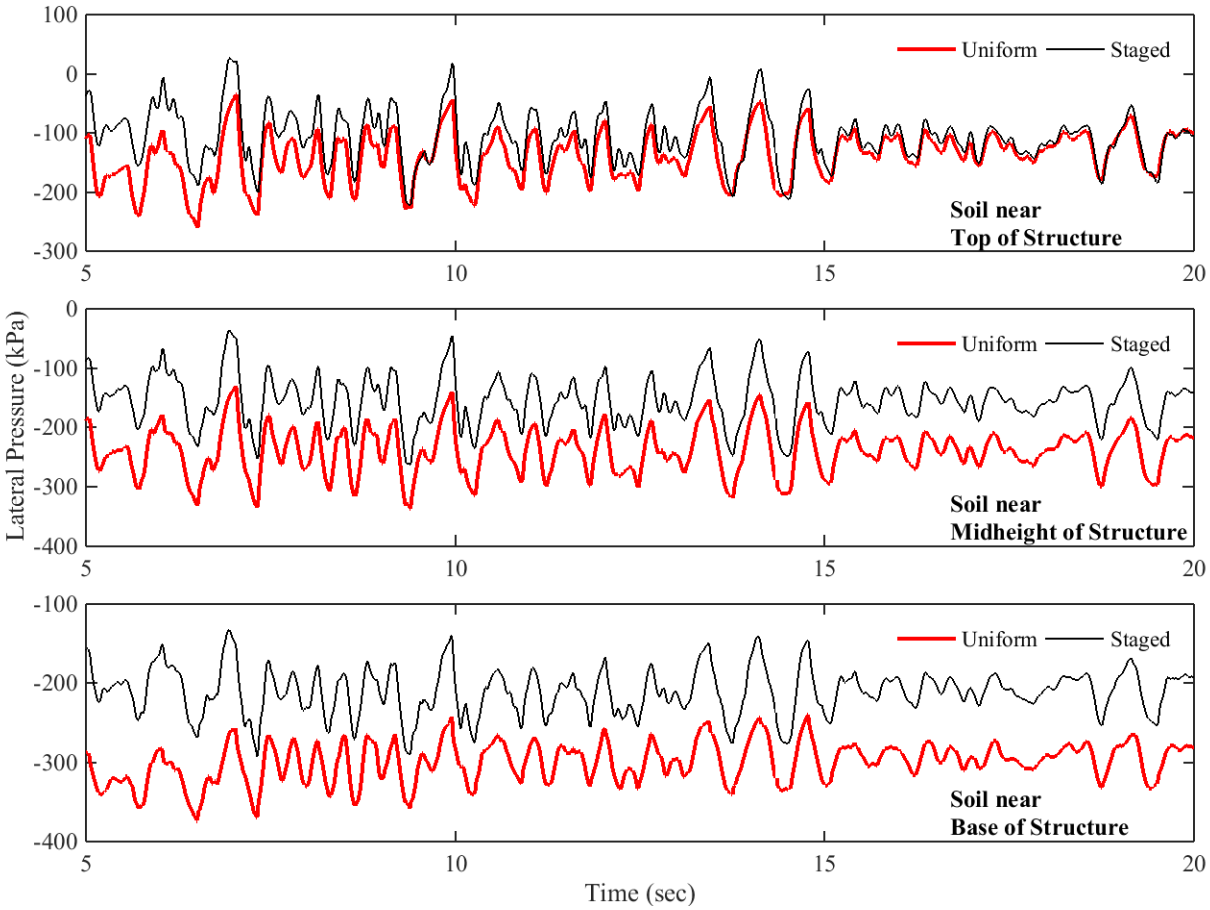

Figure C.4 Soil pressures adjacent to structure using uniform stress state and staged construction due to Taft motion

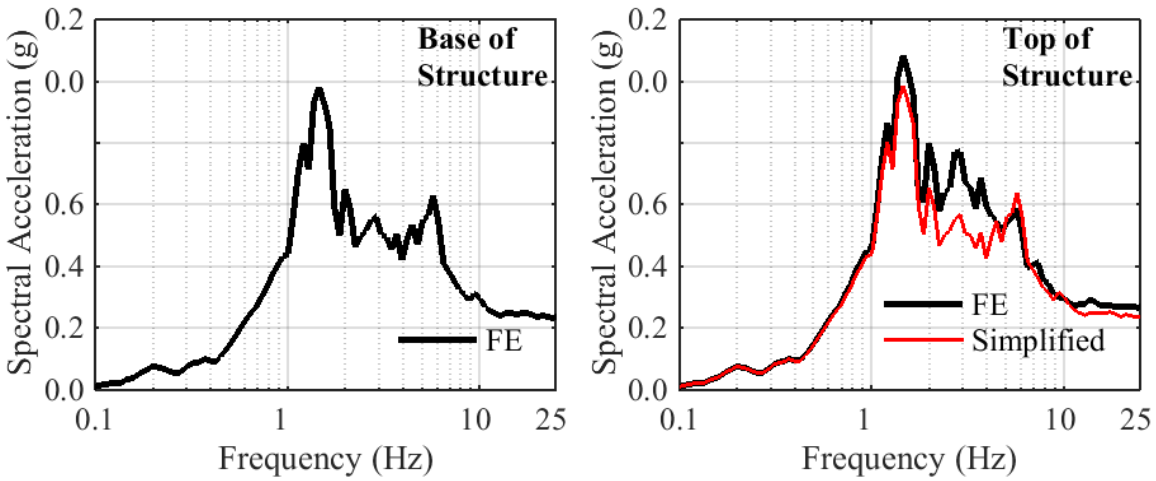

Figure C.5 Spectral acceleration at base and top levels of the structure for FE model and spring-dashpot model (Gazetas 1991)

C.5 Density of Structure

To explore the impact that the mass of the embedded structure has on the seismic response, additional simulations were conducted with the density ranging from 25% to 300% the density of the soil. All other properties were the same as the fully embedded structure discussed in Chapter 5. As illustrated from the acceleration (Figure C.7) and displacement time histories (Figure C.8), the structure tended to lag behind the free-field. However, as the density of the structure was increased, the lag (Figure C.8 - Figure C.9) in between the structure and free-field diminished. As the lag dwindled, the spectral acceleration (Figure C.10) for the structure approached the free-field and was most prominent around the primary peak (1 – 2 Hz). However, similar to the cases observed for the fully embedded structure (Chapter 5), the high frequency response was still greatly diminished.

At the instance of peak dynamic pressure, it was observed that as the density of the structure was increased, the relative displacement (Figure C.11) between the structure and free-field was reduced (in particular at the top of the structure). The resulting force exerted on the structure was

at its maximum (160% of the static stress) when the density of the structure was at its minimum (25% of the soil density). As the relative displacement and lag was diminished, there was a noticeable decrease in the resultant force on the structure (Figure C.12 - Figure C.14) up to around 200% of the soil density where the resultant force starts to increase (Figure C.15),.

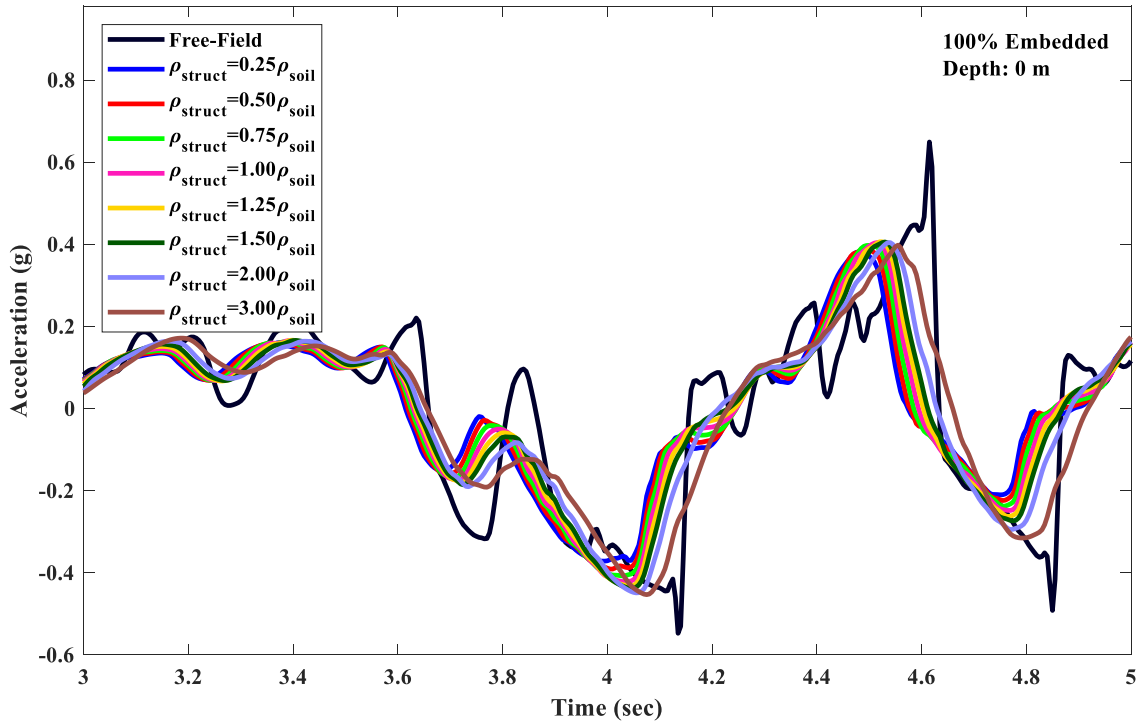

Figure C.6 Acceleration time history for 100% embedded structure at ground surface (0m)

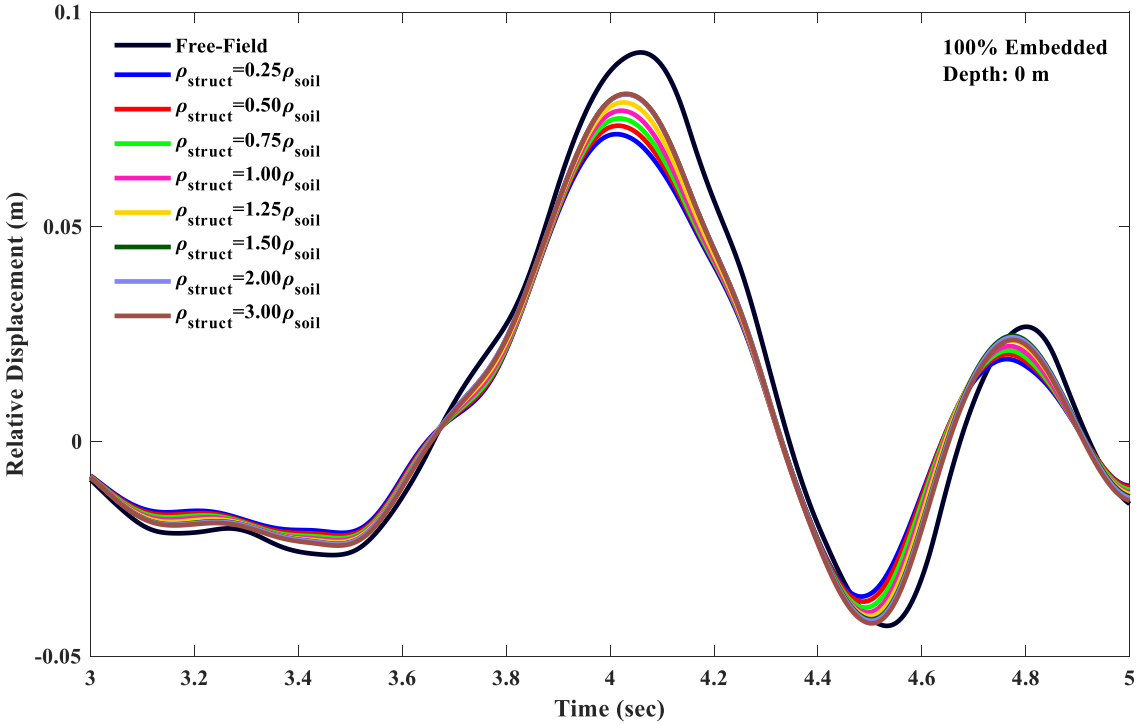

Figure C.7 Relative displacement time history for 100% embedded structure at ground surface (0m)

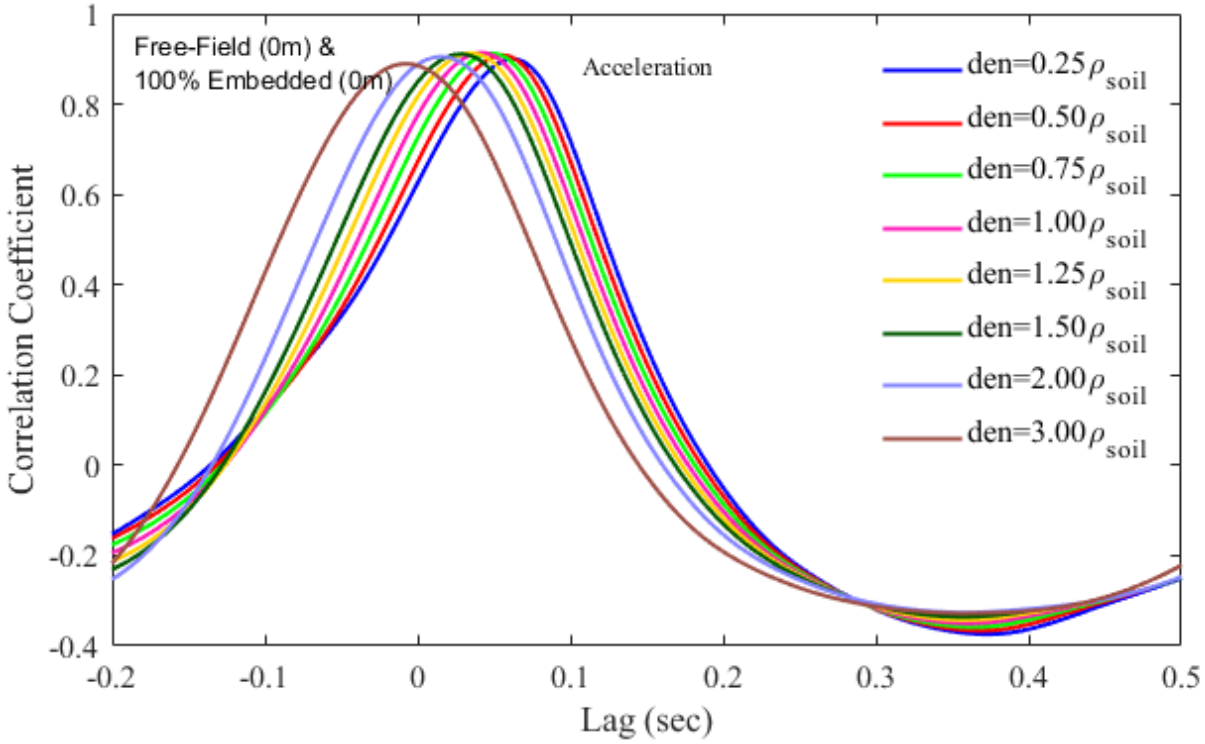

Figure C.8 Cross Correlation of acceleration of free-field and structure at ground surface (0m)

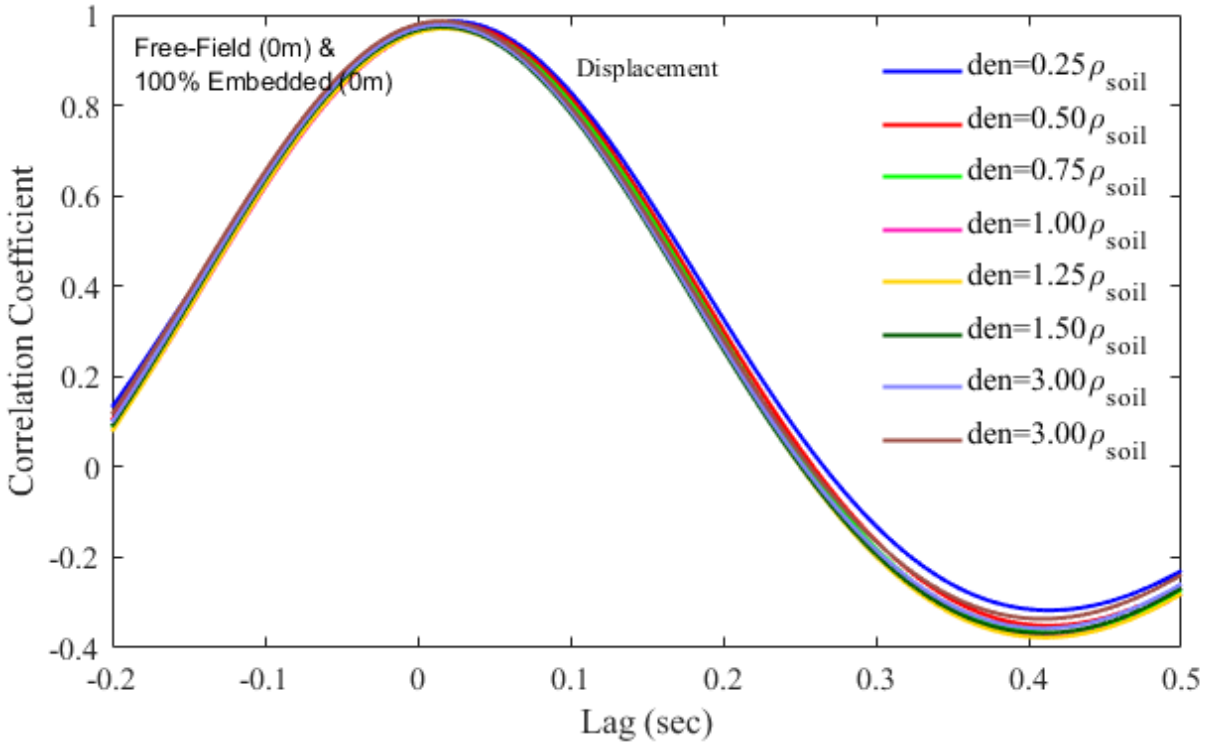

Figure C.9 Cross Correlation of displacement of free-field and structure at ground surface (0m)

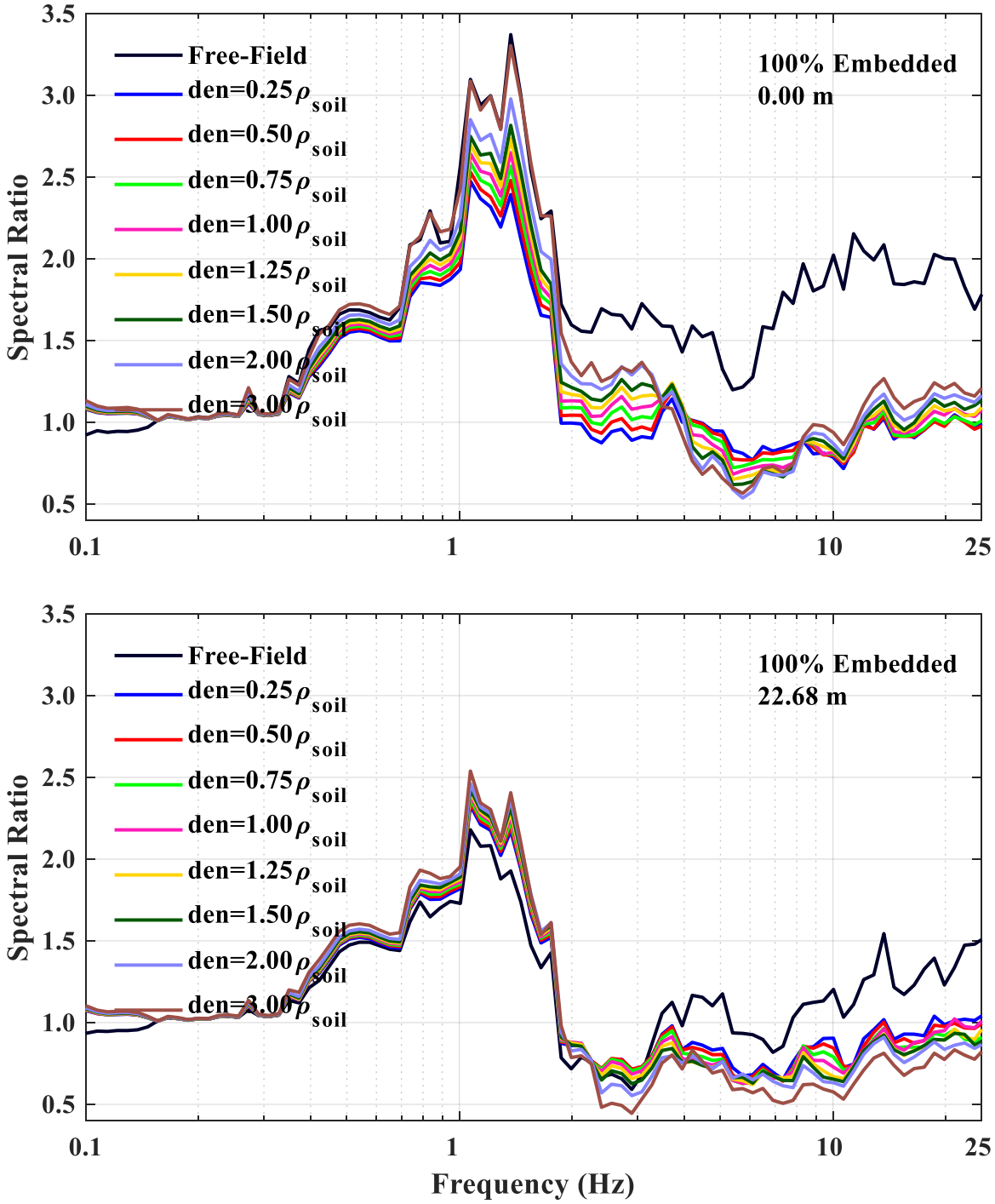

Figure C.10 Ratio of spectral acceleration at ground surface (0 m), and base level of structure (22.68 m) to motion at base of mesh at the structure fir 100% embedded structure

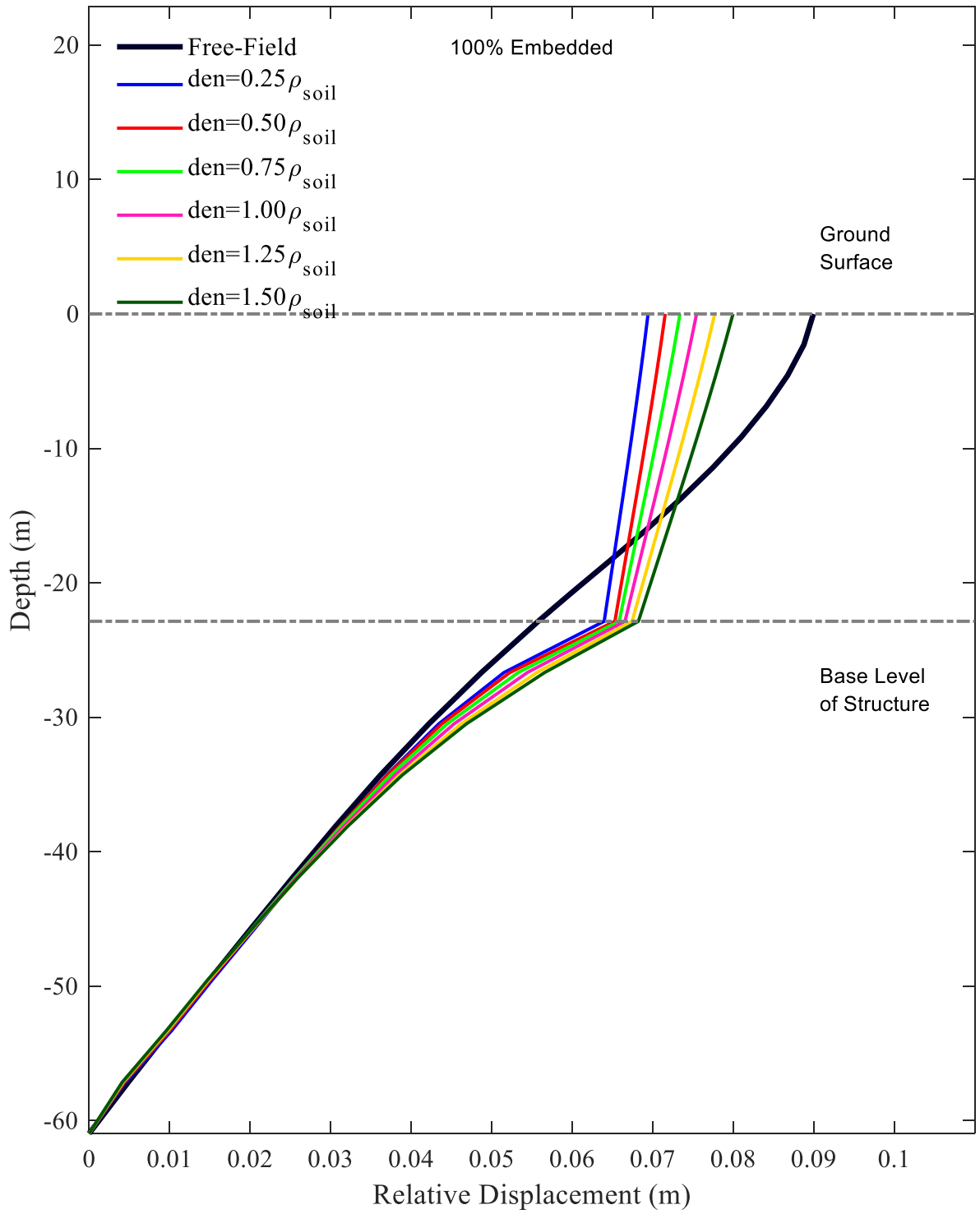

Figure C.11 Displacement profile at the instant of peak dynamic pressure for a fully embedded structure

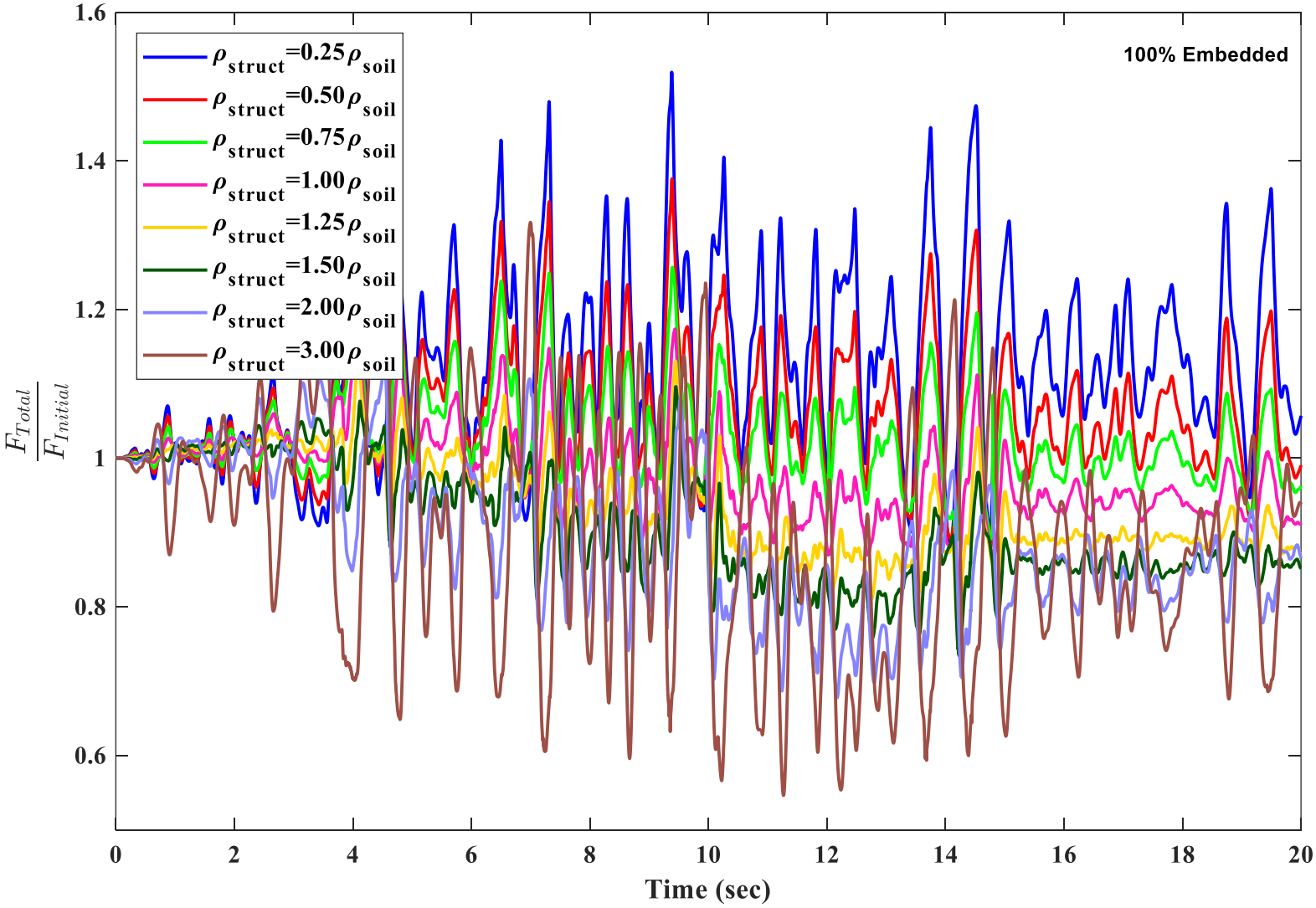

Figure C.12 Ratio of resultant force to initial resultant force on the wall of the structure at 180° orientation using an input motion scaled by 4 for fully embedded structure

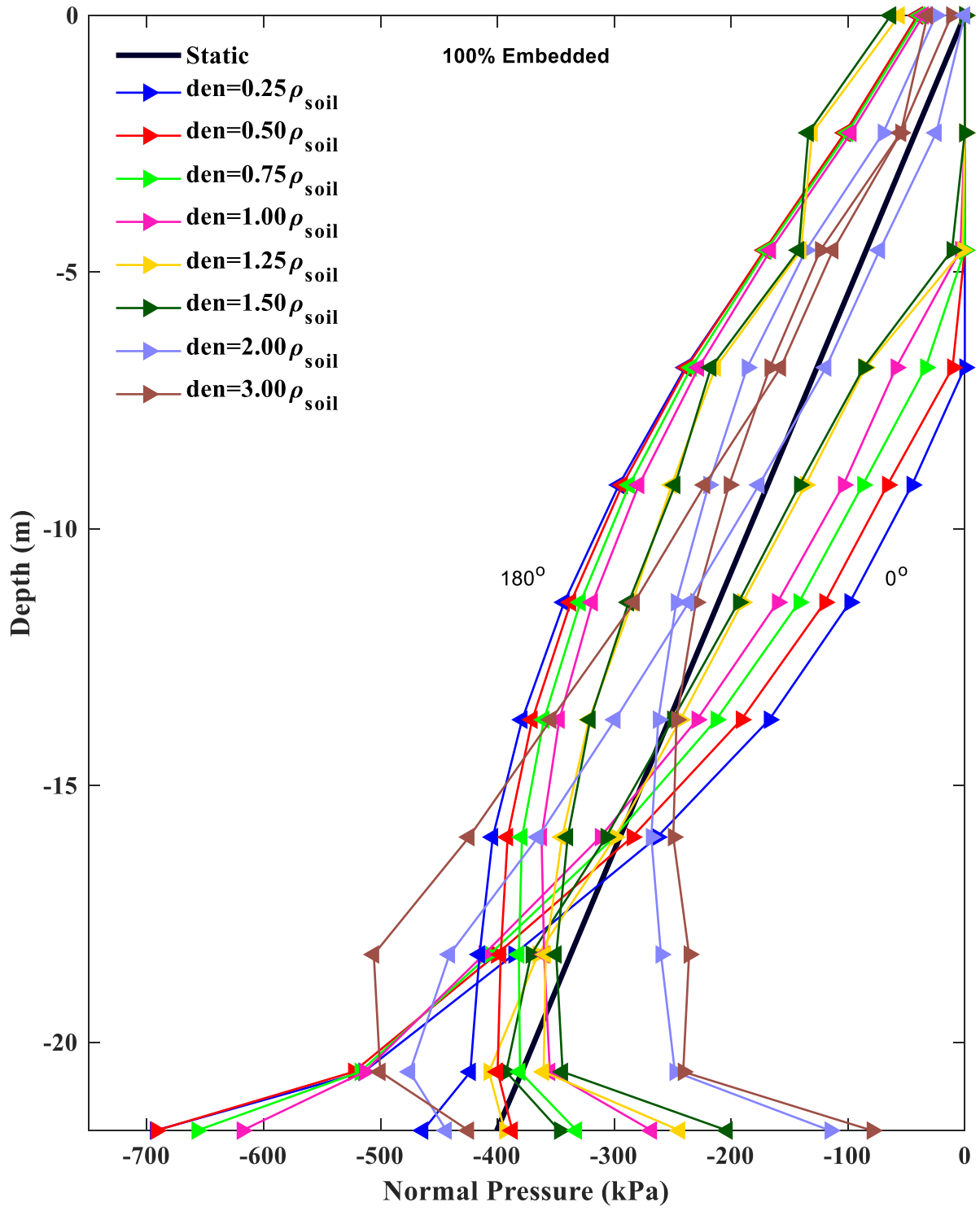

Figure C.13 Peak normal pressure along the perimeter of the structure for motion scaled by 4 for a fully embedded structure

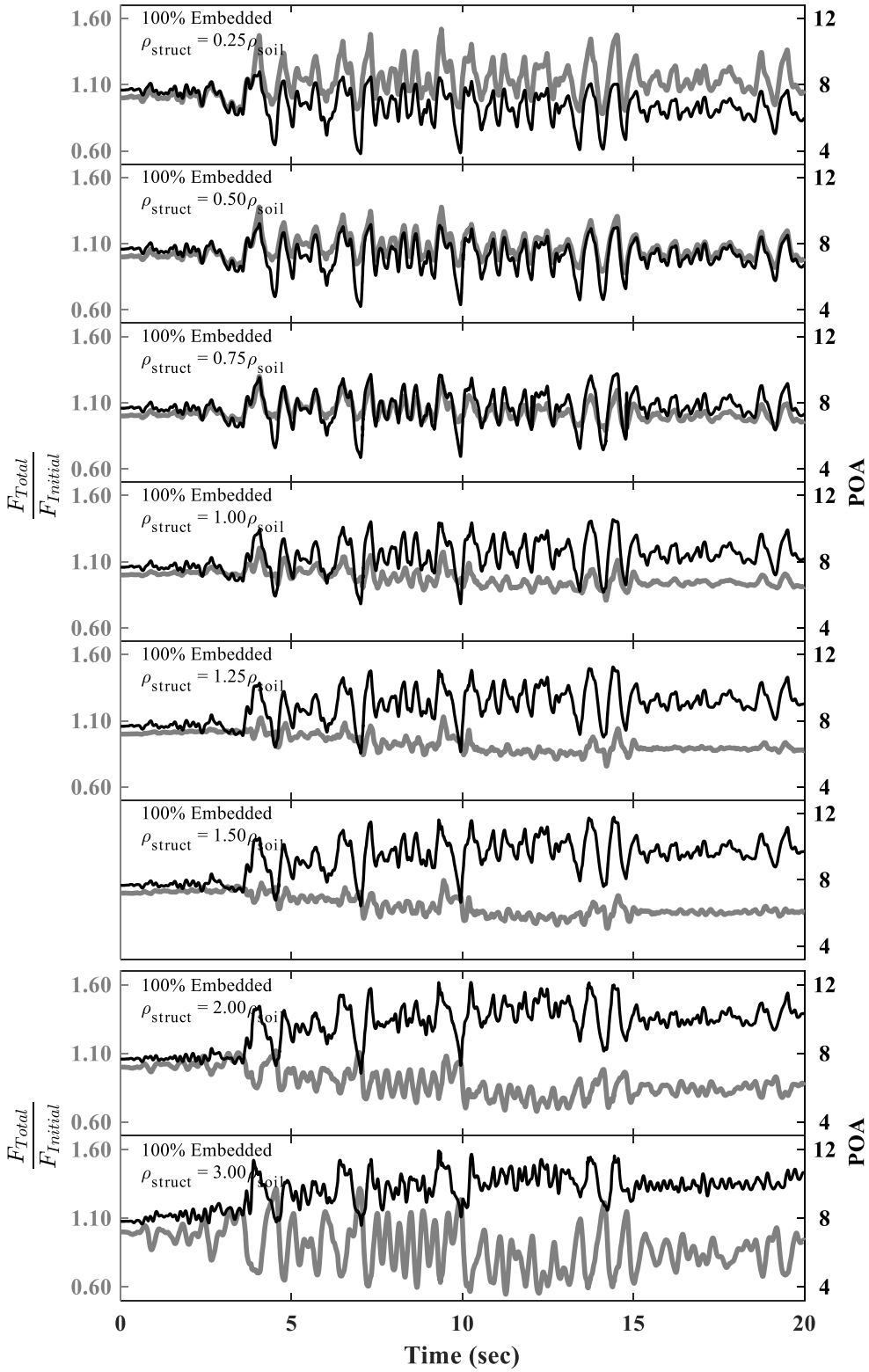

Figure C.14 Ratio of resultant force to initial resultant force and ratio of point of action to height of structure (22.68 m) on the wall of the structure for a 100% embedded structure

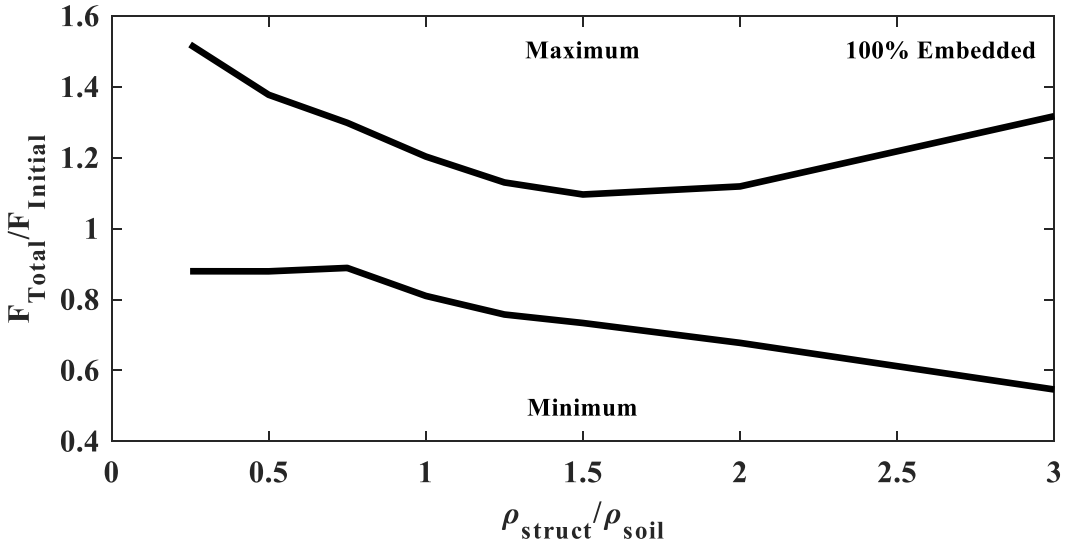

Figure C.15 Maximum resultant force and displacement versus density for 100% embedded structure

C.6 Embedment of Structure

To investigate the impact that embedment has on the overall response, another configuration was considered in which the structure was embedded 50% of it's total height as opposed to the previous fully embedded state. Besides the modifications to the embedded structure, all other properties were the same as the fully embedded structure as discussed in Chapter 5. Similar to the previous section (C.5), the density of the structure was adjusted and varied from 12.5% to 75% of the density of the soil. The density played a similar role as the fully embedded case except the previously observed trends were more strongly correlated. As was the case with the fully embedded structure (C.5), the acceleration (Figure C.16) and displacement (Figure C.17) of the structure lagged behind the free-field which was greatly reduced with the increase in the density (Figure C.18 - Figure C.19). Similarly, the spectral acceleration (Figure C.20) for the structure approached the free-field when the density was increased but with the high frequency response greatly diminished.

As was the case with the fully embedded structure, the relative displacement (Figure C.21) and force exerted on the walls of the embedded structure (Figure C.22 - Figure C.24) was reduced as the density of the structure was increased. The resulting force exerted on the structure was at its maximum (160% of the static stress) when the density of the structure was at its minimum (12.5% of the soil density). As the relative displacement and lag was diminished, there was a noticeable reduction in the resultant force up to around 62.5% of the soil density (Figure C.25).

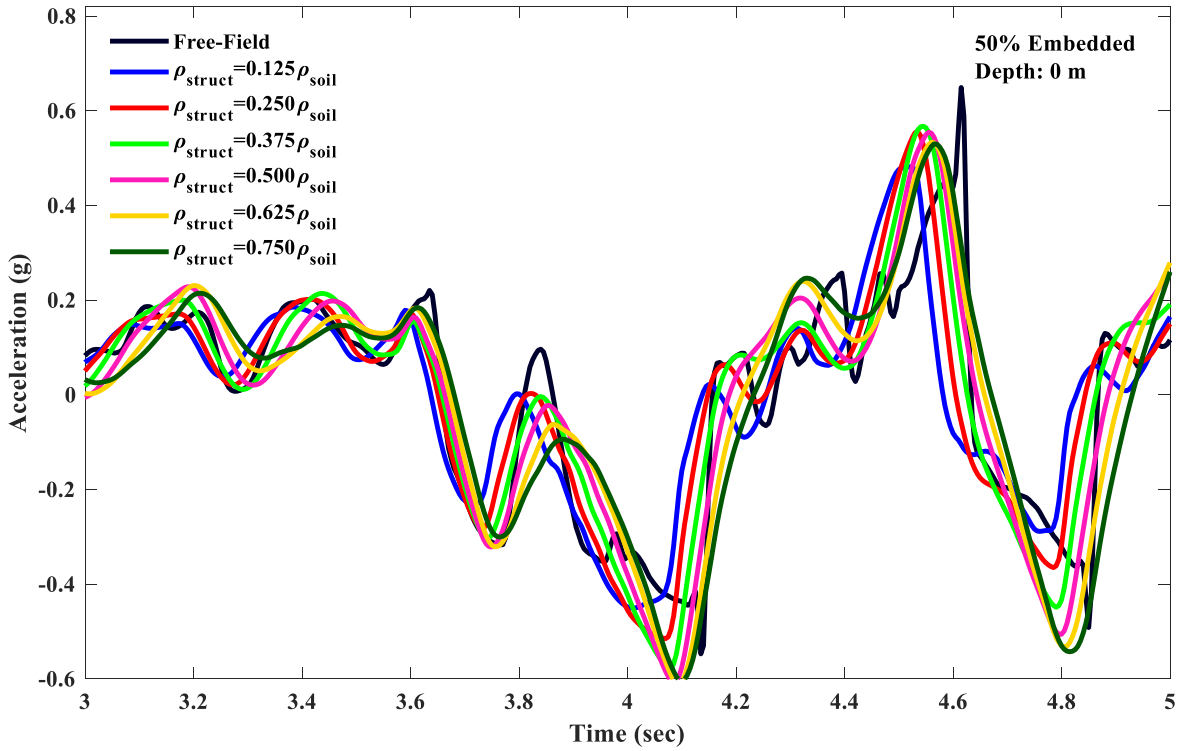

Figure C.16 Acceleration time history for 50% embedded structure at ground surface (0m)

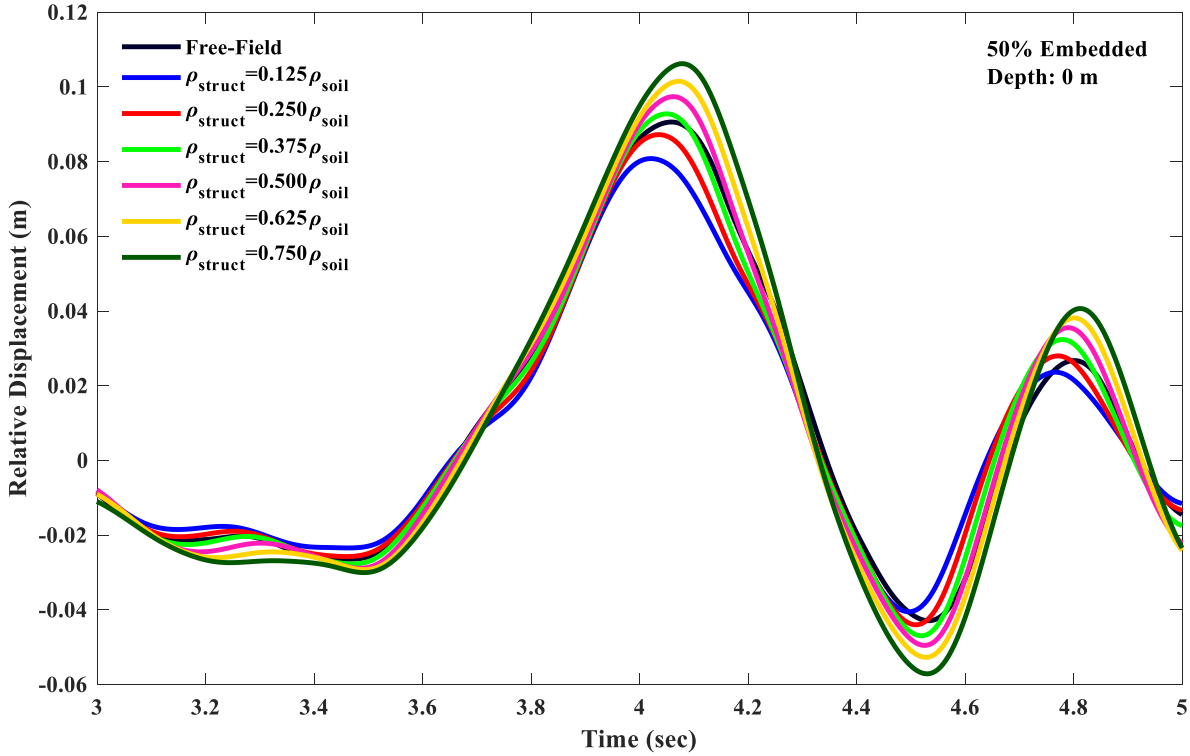

Figure C.17 Relative displacement time history for 50% embedded structure at ground surface (0m)

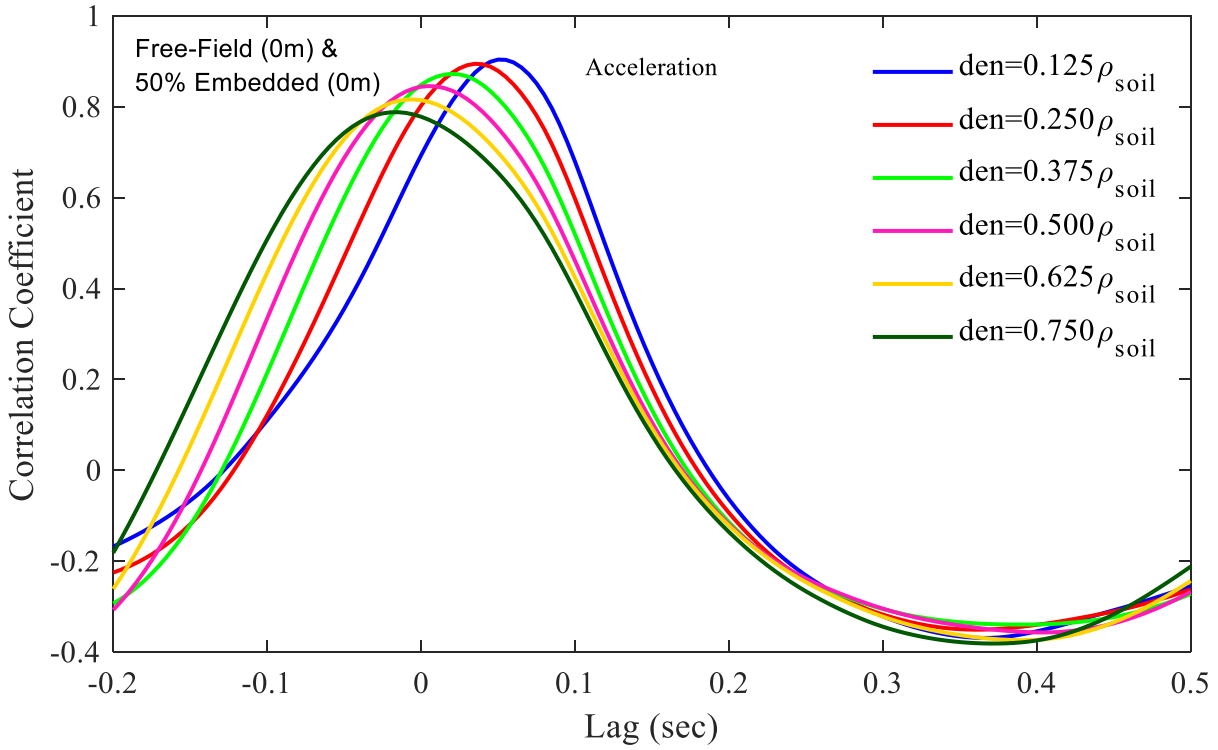

Figure C.18 Cross Correlation of acceleration of free-field and structure at ground surface (0m)

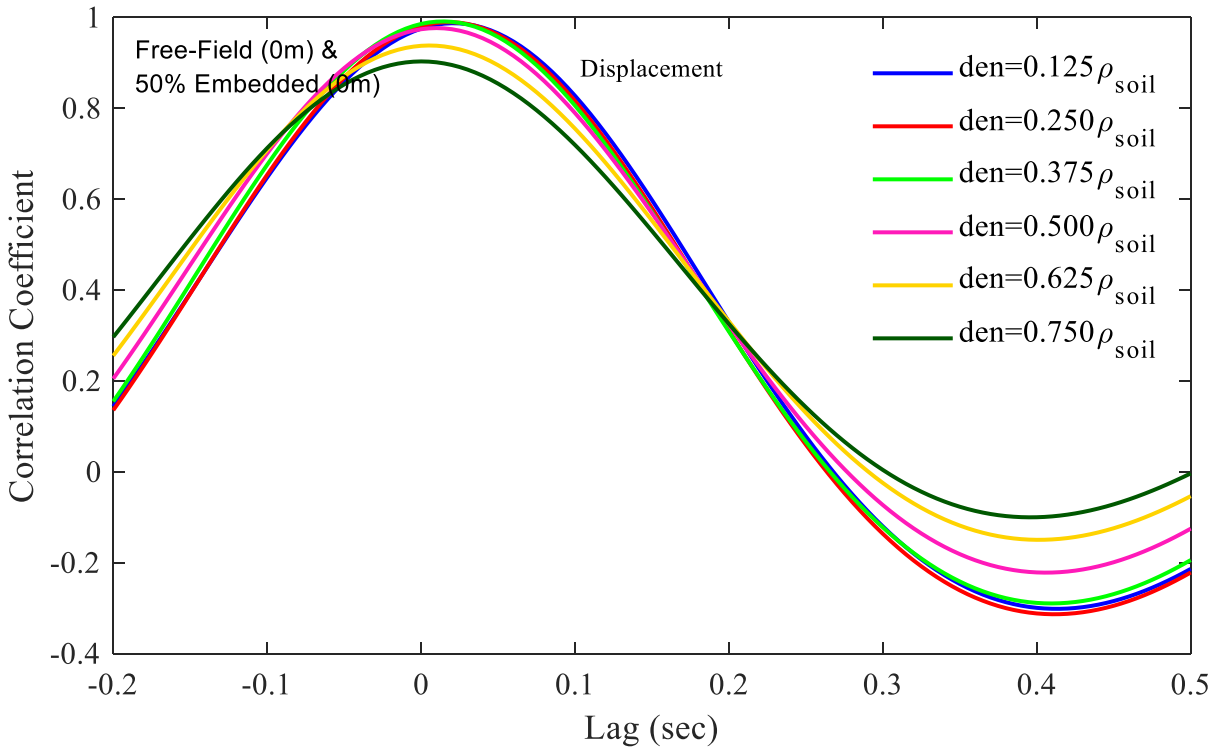

Figure C.19 Cross Correlation of displacement of free-field and structure at ground surface (0m)

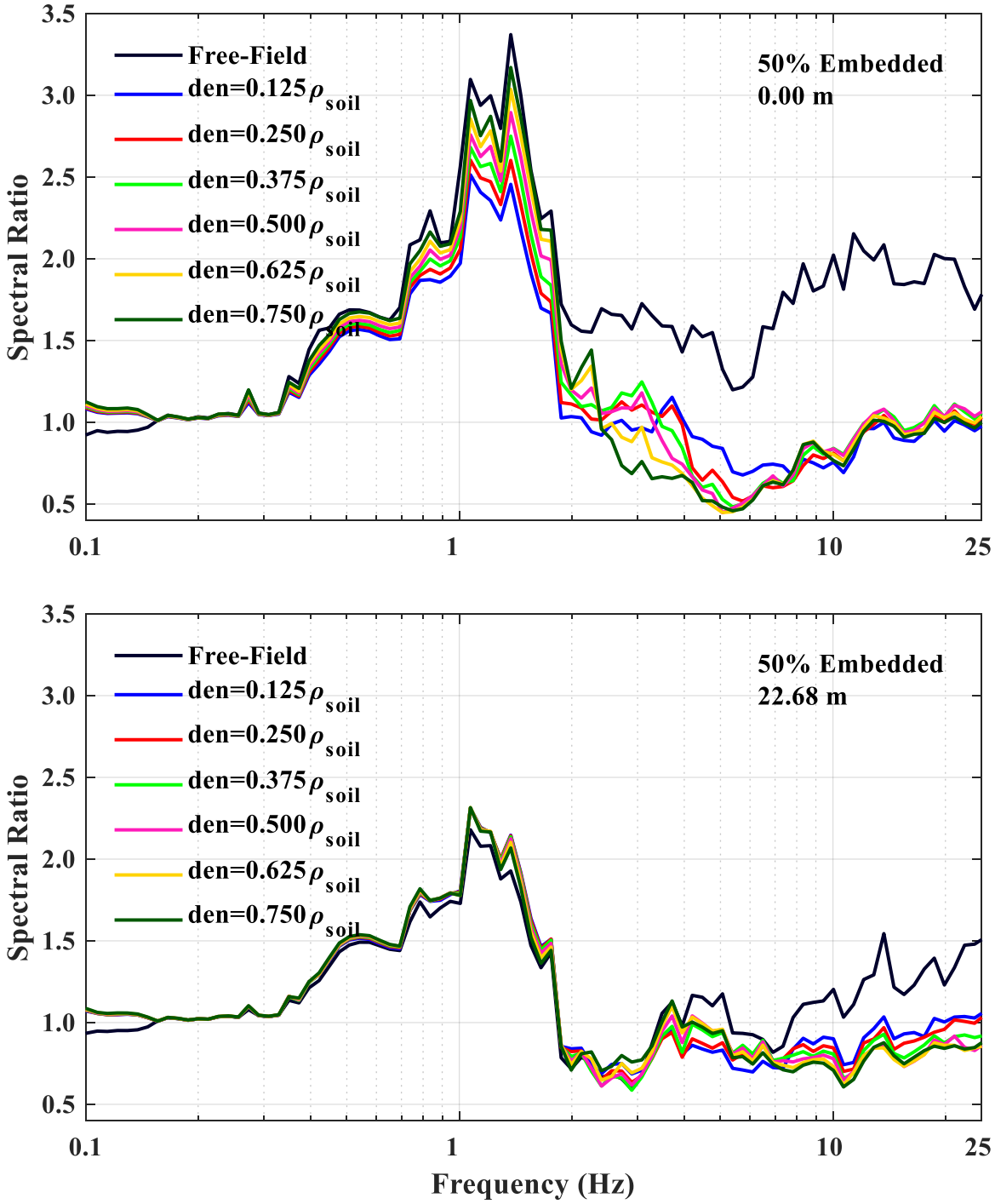

Figure C.20 Ratio of spectral acceleration at ground surface (0 m), and base level of structure (22.68 m) to motion at base of mesh at the structure for 50% embedded structure

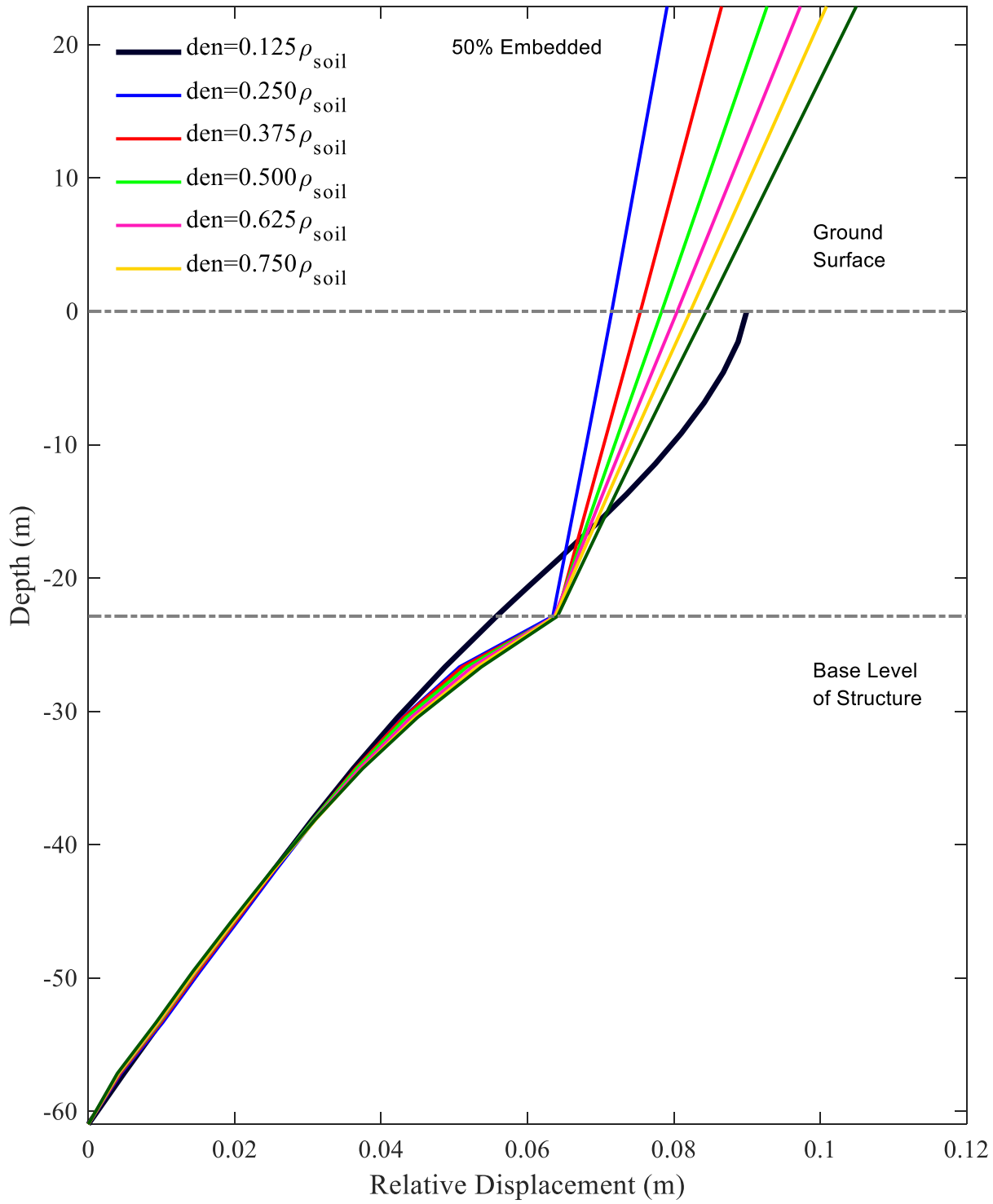

Figure C.21 Displacement profile at the instant of peak dynamic pressure for a 50% embedded structure

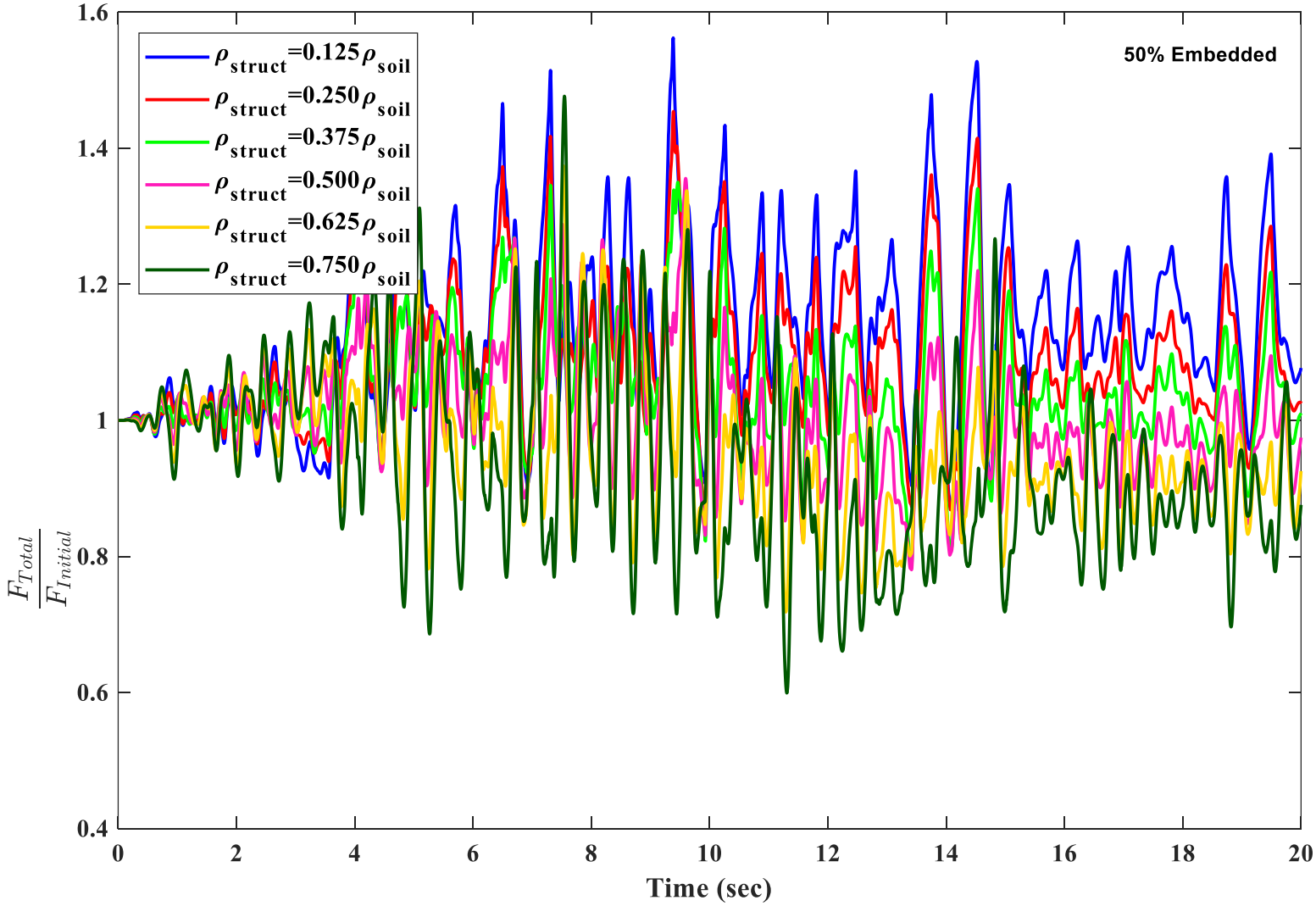

Figure C.22 Ratio of resultant force to initial resultant force on the wall of the structure at 180° orientation using an input motion scaled by 4 for 50% embedded structure

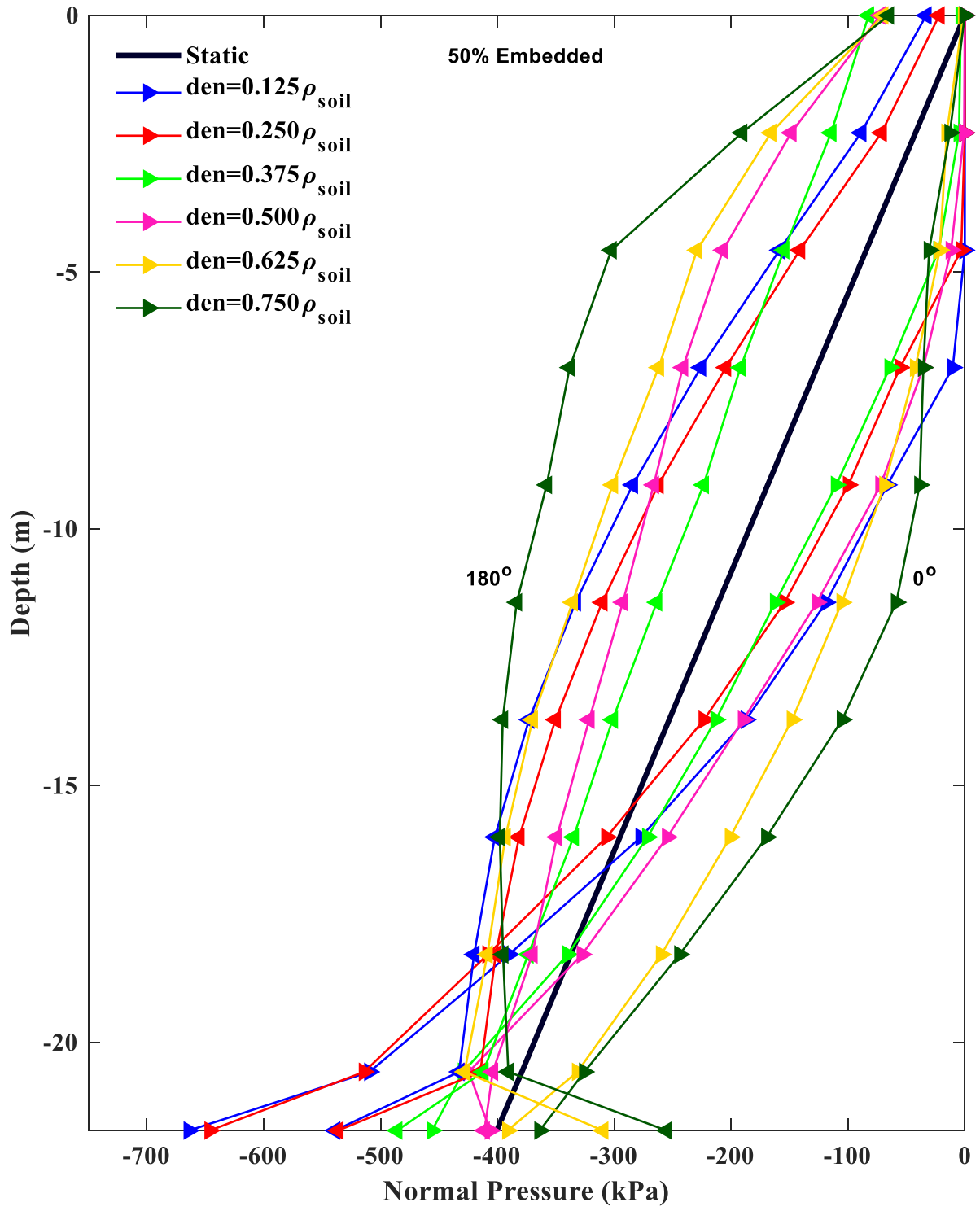

Figure C.23 Normal pressure along the perimeter of the structure for motion scaled by 4 for 50% embedded structure

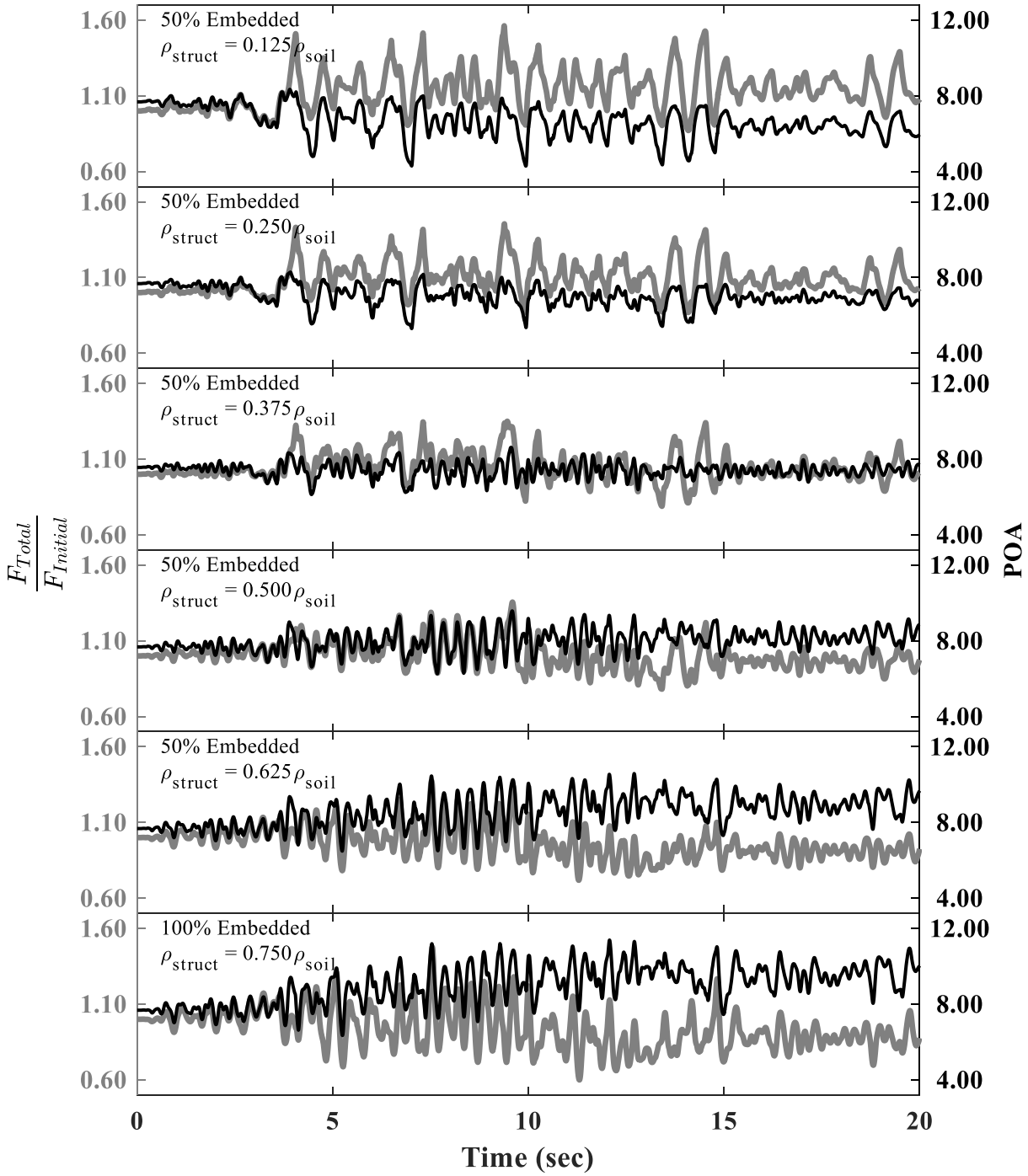

Figure C.24 Ratio of resultant force to initial resultant force and ratio of point of action to height of structure (22.68 m) on the wall of the structure for a 50% embedded structure

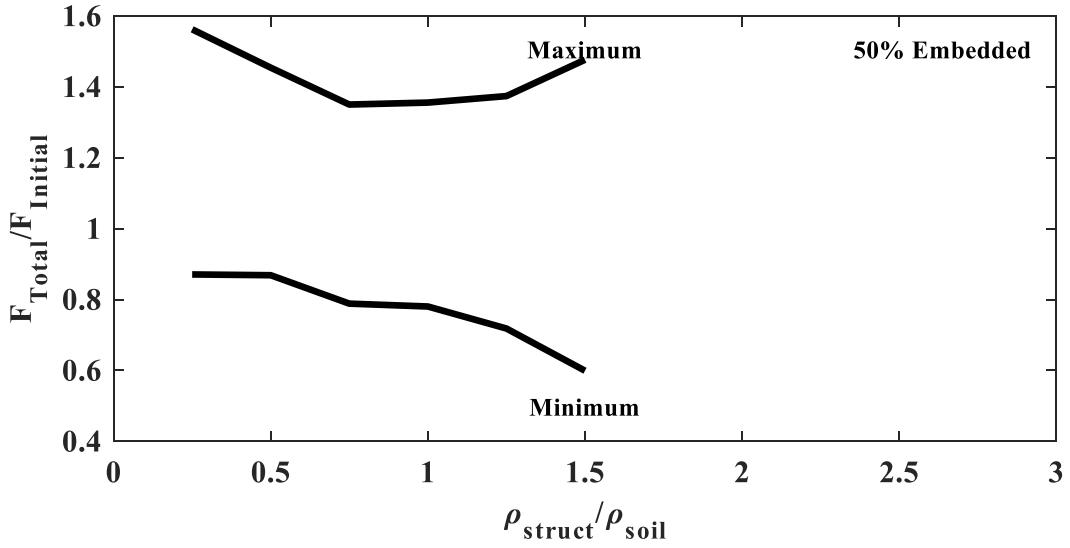

Figure C.25 Maximum resultant force and displacement versus density for 50% embedded structure